Development of 18F-labeled agonist radioligands for PET imaging of the high-affinity state of cerebral dopamine D2/3 receptors

Shalgunov, Vladimir

Printing of this thesis was financially supported by:

University of Groningen

University Medical Center Groningen

Research School of Behavioral
and Cognitive Neurosciences

Von Gahlen Nederland B.V.

Cover design: Julia Kurdi
Layout: Ekaterina Tsypina
Printing: Ridderprint BV, www.ridderprint.nl

ISBN: 978-90-367-9923-2 (hardcopy)
978-90-367-9922-5 (electronic version)

university of groningen

Development of ^{18}F-labeled agonist radioligands for PET imaging of the high-affinity state of cerebral dopamine $D_{2/3}$ receptors

PhD Thesis

to obtain the degree of PhD at the
University of Groningen
on the authority of the
Rector Magnificus Prof. E. Sterken
and in accordance with
the decision by the college of Deans.

This thesis will be defended in public on

Monday 10 July 2017 at 14.30 hours

by

Vladimir Shalgunov
born on 28 November 1986
in Moscow, Russia

Supervisors
Prof. P. H. Elsinga
Prof. J. Booij
Prof. R. A. J. O. Dierckx

Assessment committee
Prof. P. P. de Deyn
Prof. G.-M. Knudsen
Prof. A. D. Windhorst

CONTENTS

Chapter 1

Introduction

Dopaminergic system and its role in brain functioning

Dopamine is a neurotransmitter that plays a role in central nervous system (CNS) functions such as the regulation of movement, cognitive functions, emotions, motivation and reward [1]. Dopaminergic neurons originate in the midbrain, more specifically in the substantia nigra pars compacta and ventral tegmental area (Figure 1), and project from there into the dorsal striatum (nigrostriatal pathway), ventral striatum, amygdala, hippocampus (mesolimbic pathway), cortex (mesocortical pathway) and pituitary (tubero-infundibular pathway) [2]. At the ends of these projections, at interneuronal junctions called synapses, dopaminergic signaling takes place when dopamine is released from synaptic vesicles of the pre-synaptic neurons into the synaptic cleft, binds to dopamine receptors situated on the membrane of the post-synaptic neurons and activates them temporarily, launching the intracellular signaling cascade. The pre-synaptic membrane also contains dopamine "autoreceptors", the activation of which regulates dopamine release [3].

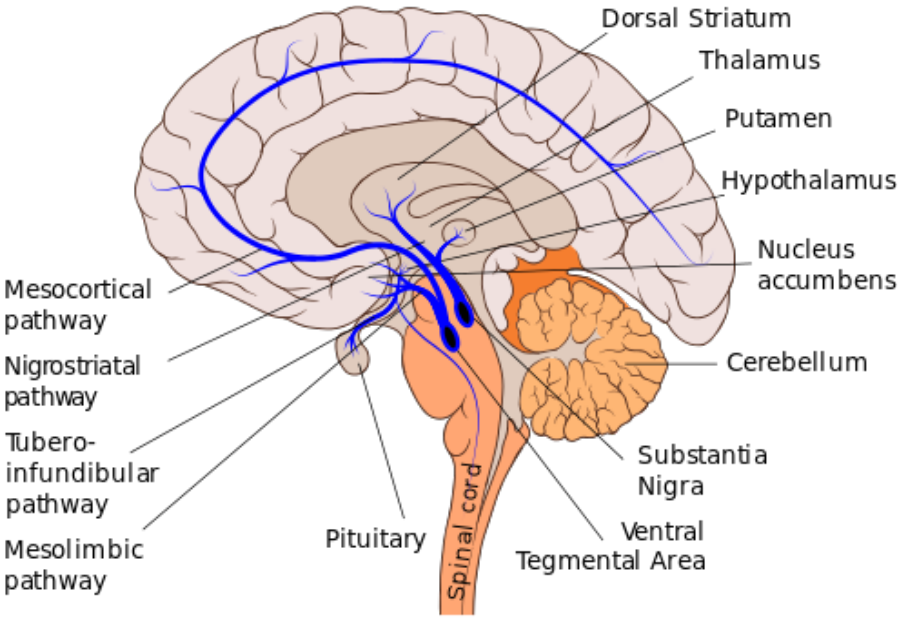

Figure 1. Dopaminergic pathways of the human brain.

Dopamine receptors belong to the superfamily of heptahelical transmembrane receptors called G-protein coupled receptors (GPCRs) and can be clas-

sified into 2 types: D_1-like, subdivided into D_1 and D_5 subtypes, and D_2-like, subdivided into D_2, D_3 and D_4 subtypes. At the secondary messenger level, D_1-like and D_2-like receptors have opposite pharmacological effects: D_1-like signaling stimulates cyclic adenosine monophosphate (cAMP) production while D_2-like signaling inhibits it [4].

In mammalian central nervous system, the highest densities of dopamine receptors, both D_1-like and D_2-like, are observed in the striatum, although D_4 and D_5 subtypes have higher densities in other regions, primarily cortical [5–10]. For D_2-like receptors, dorsal striatum tends to contain mainly the D_2 subtype while ventral striatum, pallidum and nucleus accumbens tend to have considerable densities of the D_3 subtype [11,12].

Dysregulation of dopamine signaling is implicated in many neurological disorders. Degeneration of nigrostriatal pathway is found in neurodegenerative diseases like Parkinson's disease and Huntington's disease [13,14]. Addictive substances like amphetamine, nicotine, and alcohol affect dopamine levels in the brain, and even the actions of opioids and nicotine are partially caused by the influence of these substances on dopaminergic signaling [15]. Dopaminergic signaling is also implicated in major depression [16,17]. Finally, an influential hypothesis of the pathogenesis of schizophrenia states that psychotic symptoms are caused by overactive dopaminergic signaling in the brain, stemming from elevated dopamine synthesis and intrasynaptic concentrations, increased dopamine receptor density or increased susceptibility of dopamine receptors to activation [18–20].

Radioactive tracers in clinical diagnostics

The studies of functional anatomy and physiology of living organisms are greatly facilitated by the use of radioactively labeled compounds (called radiopharmaceuticals when used in the clinic) which possess affinity to certain target biomolecules. Such compounds can be used as probes to assess the distribution and/or functionality or their targets in vivo. The advantage of the radioactive label is that it does not have to be extracted from the tissue for quantification, and the intensity and type of radioactive decay are independent of the environment. Some radioactive isotopes generate gamma photons upon their decay, which easily escape from the living tissue and can be detected externally, providing an opportunity to perform studies non-invasively and (with the right technology) obtain 3-dimensional images of the probe distribution in vivo. Isotopes that not only generate gamma photons

but also decay quickly (have half-lives on the order of minutes or hours, in a few cases – days) are especially good for non-invasive imaging in the clinic. Their short half-lives make it possible to administer relatively large amounts of radioactivity, which generate a lot of signal for the imaging but result in a low radiation burden for the patients.

Probes labeled with short-lived isotopes typically have high molar radioactivities (specific activities) and thus can be reliably detected at extremely low concentrations. Therefore, in non-invasive imaging experiments, probes are administered at very low dose levels. The idea is that the probe does not saturate or even significantly influence the physiological processes that are being imaged. Such probes are called tracers (or radiotracers), while the administered dose which is low enough to have no consequences on the functioning of the imaged organism is called a tracer dose.

Methods of non-invasive imaging with radioactive tracers

There are currently two major non-invasive imaging methods based on the detection of gamma-photons formed in radioactive decay: positron emission tomography (PET) and single photon emission computed tomography (SPECT) [21,22]. The latter relies on nuclei directly emitting gamma photons upon radioactive decay (with typical energies of 100–170 keV), while the former relies on isotopes that decay by emitting positrons and detects annihilation photons (511 keV) that are generated after positrons meet electrons (Figure 2).

Positron-emitting isotopes include light nonmetal elements like ^{11}C, ^{13}N, ^{15}O, ^{18}F as well as heavier nonmetals (^{76}Br, ^{124}I) and radiometals (^{64}Cu, ^{68}Ga, ^{89}Zr). Single-photon emitting isotopes are primarily radiometals (^{111}In, ^{67}Ga, ^{99m}Tc) and heavy nonmetals (^{123}I). Positron-emitting isotopes like ^{11}C, ^{13}N and ^{15}O correspond to elements naturally occurring in the majority of biomolecules and thus are, at least from the viewpoint of molecular design, especially suitable for the labeling of small-molecule tracers, where minor modification of chemical structure (including replacement of a single atom) can lead to significant changes in physico-chemical and biological properties. Other isotopes, both positron-emitting and single-photon emitting, can be introduced into novel small molecules specifically designed for the purpose; alternatively, they can be made part of prosthetic groups for the labeling of biologics that have high molecular weight and thus greater tolerance for chemical modification.

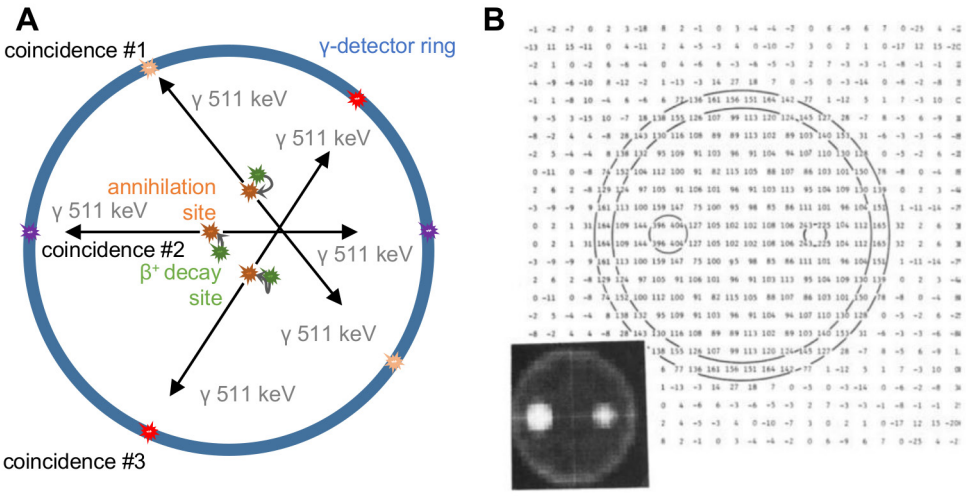

Figure 2. Principles of PET imaging.

A – positron-emitting isotopes decay, positrons travel from the decay site, lose their kinetic energy in the process and eventually annihilate upon encountering an electron, which generates two 511 keV gamma-photons emitted in opposite directions from the annihilation site. When gamma-photon capture is simultaneously registered at two detectors in the gamma-detector ring, a decay event can be assumed to have happened on a line connecting the two detectors (line of response). Regions with higher radioactivity concentrations will have more such lines passing through them.

B – Numerical (large picture) and graphical (inset) reconstructions of a scan performed on a "phantom" (artificial object with known amounts and distribution of radioactivity) in the first prototype PET camera reported in 1975. © The Radiological Society of North America (RSNA®). Reproduced from Ter-Pogossian M M, Phelps M E, Hoffman E J, et al. A positron-emission transaxial tomograph for nuclear imaging (PETT). Radiology 1975;114:89–98 [23].

PET technology has a number of important advantages over SPECT technology. First, the sensitivity of PET cameras is higher than that of SPECT cameras, because the latter need a collimator to form images, and the natural background of high-energy gamma photons used in PET is lower than for low-energy photons used in SPECT. Second, the reliance on two high-energy photons per decay event makes the PET signal more quantitative than the SPECT signal, although proper calibration of the detectors and correction for absorption and scattering are necessary in both cases. Third, dynamic imaging techniques, which make it possible to follow changes of radioactivity concentration in a region of interest on a second scale, are easier to implement, and therefore more developed, in PET than in SPECT. Finally, PET cameras used in the clinic typically have greater spatial resolution than clinical SPECT cameras (~5 mm vs ~10 mm). On the other hand, recent de-

velopments in SPECT technology allow, in some specific set-ups, imaging with spatial and temporal resolution comparable to or even exceeding those of PET [24,25]. Moreover, SPECT technology allows simultaneous imaging of more than one radiolabel: isotopes can be distinguished by their characteristic gamma photon energies, while annihilation photons used for PET are the same for all positron-emitting isotopes. Finally, PET technology is generally more expensive than SPECT technology, one of the reasons for this being that many isotopes PET relies on (see above) have to be produced in cyclotrons.

To sum up, both SPECT and PET are useful tools for both clinical and preclinical imaging, but high-end clinical diagnostics and fundamental as well as applied biomedical research tend to be carried out with PET. Tracers for PET imaging of the brain include enzyme substrates, receptor and transporter ligands and even simple water [26].

Outcome measures of PET and SPECT imaging experiments

When using tracers (radioligands) that reversibly bind to their targets (as usually happens with receptors or transporter proteins) one typically wants to know the target density in the tissue (B_{max}) and the affinity of the tracer for its target ($1/K_d$; the lower the dissociation constant, the higher the affinity). Measuring these parameters using data from a single tracer injection is impossible, because tracers have specific as well as non-specific binding. During in vitro binding assays, non-specific binding can be measured in a separate experiment where all specific binding is inhibited by a large excess of unlabeled "blocker" drug. However, the same cannot commonly be done in vivo, because high receptor occupancy by the "blocker" drug may result in unwanted, potentially toxic, pharmacological effects.

Therefore, the key outcome measure for in vivo imaging with reversibly binding tracers is the binding potential (BP) [27]. BP is a ratio equal to the product of B_{avail} and $1/K_d$. Here, B_{avail} is available target density. In vitro all receptors are available for binding, so $B_{avail} = B_{max}$, but in vivo receptors may be internalized or occupied by other ligands (including the endogenous neurotransmitter).

Because BP values are proportional to B_{avail}, they can be used as a measure of receptor availability for ligand binding in the living brain. Changes in BP reflect changes in overall receptor densities or in receptor occupancy by endogenous ligands (or both; note that it's impossible to say what are the

separate contributions of these two factors when only a single BP measurement is available). Receptor occupancy by exogenous drugs or by pharmacologically induced neurotransmitter release can also be calculated from BP values.

$$\mathrm{Occ} = \frac{\mathrm{BP}_{\mathrm{baseline}} - \mathrm{BP}_{\mathrm{challenge}}}{\mathrm{BP}_{\mathrm{baseline}}},$$

where $\mathrm{BP}_{\mathrm{baseline}}$ and $\mathrm{BP}_{\mathrm{challenge}}$ are BP values measured in the subject at baseline and after a "challenge", i.e. after administration of a drug that competes with the tracer for binding to receptors or that manipulates neurotransmitter levels.

Finally, available receptor density B_{avail} and tracer's in vivo affinity K_d can be estimated separately if the BPs are determined after at least two different injected tracer doses (see Chapter 2 for more details).

PET and SPECT imaging of the dopaminergic system

PET and SPECT radioligands make it possible to look at the functioning of the dopaminergic system from different angles. Synthesis and transport of L-dihydroxyphenylalanine (L-DOPA), a precursor for dopamine, can be imaged by PET using with 6-[^{18}F]fluoro-L-DOPA. The regional density of the dopamine transporter (DAT) which is responsible for the reuptake of dopamine from the synaptic cleft can be imaged with SPECT ligands like [^{123}I]FP-CIT (marketed as DaTSCAN®), [^{123}I]β-CIT, [^{123}I]PE2I and [^{99m}Tc]TRODAT-1 and PET ligands like [^{18}F]FP-CIT. The PET tracer [^{11}C]DTBZ can be used to image regional densities of the vesicular monoamine transporter (VMAT2), a protein that pumps dopamine into synaptic vesicles for future release. PET tracers for D_1-like receptors ([^{11}C]NNC112, [^{11}C]SCH23390) and both PET and SPECT tracers for D_2-like receptors ([^{11}C]raclopride, [^{18}F]fallypride, [^{123}I]IBZM) are available [28].

Imaging of these targets is relevant both for clinical diagnostics and for neuroscientific research. For instance, a profound decrease of dopamine biosynthesis and striatal DAT and VMAT2 availability was found in Parkinsonian patients by 6-[^{18}F]fluoro-L-DOPA, [^{11}C]DTBZ and [^{18}F]FP-CIT (PET) / [^{123}I]FP-CIT (SPECT) imaging [29–31]. Imaging with [^{11}C]NNC112 and [^{11}C]SCH23390 revealed alterations of cortical D_1 receptor availability in schizophrenia [32]. Finally, [^{123}I]IBZM and [^{11}C]raclopride, benzamide ligands for D_2 and D_3 receptors (together referred to as $D_{2/3}$), were found to be

sensitive to fluctuations in intrasynaptic dopamine levels [33,34]. This enabled studies of synaptic neurotransmission in both healthy subjects [35,36] and in pathological conditions such as schizophrenia, addiction and major depression [16,37–39]. Dopamine D_2-like receptors have been a very popular target in PET imaging for more than three decades (see Figure 3), and D_2-like receptor imaging by PET (as well as by SPECT) has become a clinical tool.

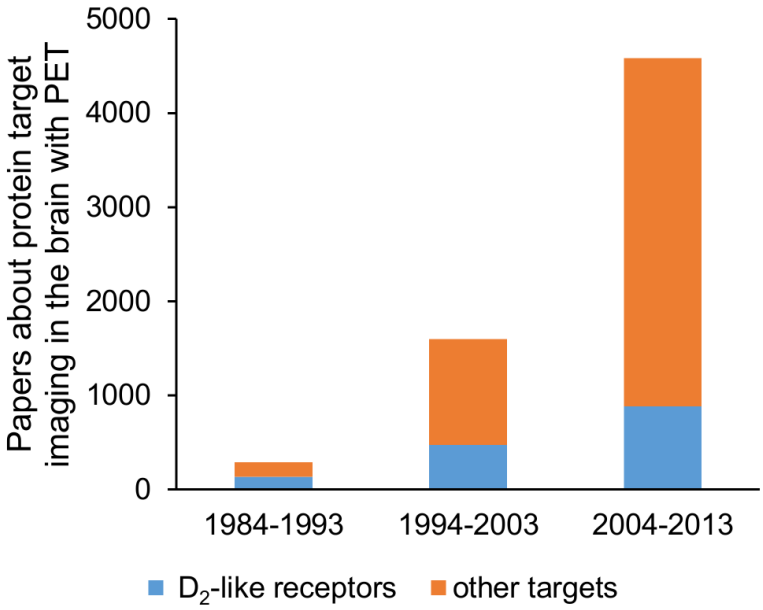

Figure 3. Publications about D_2-like receptor imaging related to the total number of publications about protein target imaging by PET.

Data for the three decades from 1984 to 2013 are presented. Based on literature search results reported in [26].

Affinity states of dopamine $D_{2/3}$ receptors

Dopamine receptors require heterotrimeric G-proteins in order to launch their signaling cascades after the receptors are activated by agonist ligands.

Models of GPCR signaling, of which there are many [40–43], postulate that there is positive cooperativity between receptor-G-protein (RG) and agonist-receptor (AR) binding, which means that agonist ligands (e.g. dopamine itself when we talk about dopamine receptors) have higher affinity toward RG complexes than towards free receptors, and G-proteins prefer to

couple with agonist-bound AR receptors. Indeed, this can be demonstrated in vitro by plotting a saturation curve for radiolabeled agonist or a competition curve for radiolabeled antagonist displaced by unlabeled agonist in receptor-containing membrane homogenates (Figure 4). In both cases, the levels of bound radioligand will change in a biphasic manner, showing that in a single receptor population, agonist recognizes two subsets with different affinities (affinity difference can be 100–1000 fold for potent agonists). On top of that, the difference in affinities of agonist drugs for the high and low affinity states of the D_2 receptor has been shown to correlate with their intrinsic activity [44].

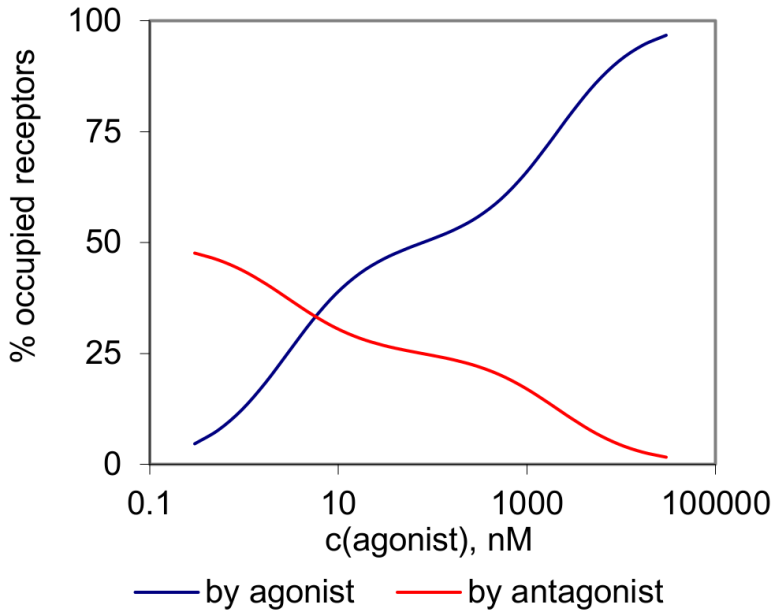

Figure 4. High- and low-affinity states visible on saturation (blue) and competition (red) curves.

The figure shows a numerical simulation of an in vitro experiment where an antagonist ligand, present at fixed concentration (2 nM), is displaced from the receptors by increasing concentrations (0.3 nM to 30 μM) of an agonist ligand. Percentage of total receptors occupied by the agonist (blue) and antagonist (red) is plotted against agonist concentration.

The antagonist ligand has an affinity of 2 nM to all receptors, the agonist has an affinity of 3 nM for receptors in the high-affinity state and 2100 nM for receptors in the low-affinity state, half of all receptors are in the high-affinity state. The graph is built in Excel using binding isotherm equation to model drug-receptor binding (see e.g. [45]).

In vivo imaging of the high-affinity state

The concept of the high-affinity state is potentially highly relevant for the in vivo imaging of dopamine $D_{2/3}$ receptors and other GPCRs. If some of the receptors are in the high-affinity state for the agonist while others are not, then agonist radioligands should be more sensitive to alterations in endogenous neurotransmitter levels than antagonist tracers, because they compete with the neurotransmitter for the same receptor subset.

Moreover, one can argue that receptors bound to G-proteins configured in the high-affinity state (Rhigh) represent the functional subpopulation of receptors, ready to launch the signaling cascade as soon as an agonist binds to them. Relative abundance of Rhigh can then be a measure of the system's sensitivity to neurotransmitter impulses, with more predictive value than total receptor density. Indeed, elevated percentages of $D_{2/3}$ receptors in the high-affinity state ($D_{2/3}$high, measured in vitro) were reported in animal models of psychosis, thought to be associated with hypersensitivity to dopamine [46]. By this reasoning, $D_{2/3}$-agonist tracers, which only recognize "functional" receptors instead of all receptors, as $D_{2/3}$ antagonists do, could be valuable tools for diagnostic purposes and investigation of pathological alterations in dopaminergic signaling.

New experimental evidence, which appeared while the research described in this thesis was being carried out, did not confirm the existence of alterations in $D_{2/3}$high relative abundance in neuropathological states [47,48], and cast doubt on the validity of the $D_{2/3}$high concept in vivo [49]. However, the greater vulnerability of $D_{2/3}$ agonist tracers to displacement by endogenous dopamine, compared to the "gold standard" $D_{2/3}$ antagonist tracer [^{11}C]raclopride, appears to hold in both pre-clinical [50–53] and clinical settings [54,55].

Tracers available for $D_{2/3}$ receptor imaging

For covalent labeling of brain SPECT tracers, iodine-123 is the isotope of choice. It has a half-life of 13.2 h. PET tracers for receptor imaging in the brain are usually labeled with carbon-11 or fluorine-18. The advantage of carbon-11 is that biomolecules can be labeled without a change of their structure, thus preserving all their properties. However, the very short half-life of carbon-11 (20.4 min) means ^{11}C-tracers can only be used in imaging centers that have an on-site cyclotron to produce the isotope.

Table 1. Properties of positron-emitting isotopes used for covalently labeled PET tracers.

Isotope	$T_{1/2}$, min	Positron energy, MeV	Mean range in water[a], mm	Max range in water, mm
Carbon-11	20.4	0.96	1.2	4.2
Nitrogen-13	10.0	1.19	1.8	5.5
Oxygen-15	2.1	1.73	3.0	8.4
Fluorine-18	109.8	0.63	0.6	2.4

Adapted from [60].
a Living tissue mostly consists of water, so presented values can be extrapolated to living tissue as well.

Since the half-life of fluorine-18 is 109.8 min, ^{18}F-labeled tracers can be distributed to "satellite" imaging centers within tens of (or even a few hundred) kilometers from the nearest production site [56]. Fluorine-18 also provides greater intrinsic resolution than carbon-11 because of the lower positron energy, and consequently shorter positron range (Table 1). The issue with fluorine-18 is that few relevant receptor ligands contain a fluorine atom naturally. Therefore, ^{18}F-labeled tracers are usually compounds specifically developed for the purpose by modification of existing fluorine-free ligands, an endeavor that often fails, because the highly electronegative fluorine atom can have dramatic influence on the properties (for instance, pKa and LogD) of the molecule into which it is introduced [57–59].

In SPECT, the antagonist [^{123}I]IBZM is the gold standard tracer for $D_{2/3}$ receptor imaging, but no agonist SPECT tracers for $D_{2/3}$ receptors are available. PET tracers available for $D_{2/3}$ receptor imaging include both agonists and antagonists. The high-affinity antagonist [^{11}C]N-methylspiperone (NMSP) was popular in the 1980s, but was later abandoned in favor of [^{11}C]raclopride, because NMSP has affinity to serotonin 5-HT_{2A} as well as to dopamine $D_{2/3}$ receptors and its binding is insensitive to endogenous dopamine levels. [^{18}F]Fallypride and [^{11}C]FLB457, antagonists with very high affinities towards $D_{2/3}$ receptors, are typically used for the imaging of extrastriatal regions, where the densities of $D_{2/3}$ receptors are low (binding of these traces in the striatum can be hard to quantify due to slow washout rates).

[^{18}F]des-methoxy-fallypride, a lower-affinity congener of fallypride, is suitable for the imaging of striatal $D_{2/3}$ receptors and can be considered an "^{18}F version" of [^{11}C]raclopride.

Agonist PET tracers used for $D_{2/3}$ receptor imaging in humans are [^{11}C](−)NPA, [^{11}C]MNPA and [^{11}C](+)PHNO. [^{11}C](−)NPA and [^{11}C]MNPA are based on the apomorphine scaffold, while [^{11}C](+)PHNO is a naphtoxazine (Figure 5). Apomorphines, naphtoxazines and aminotetralines are the most intensively investigated scaffolds in the development of $D_{2/3}$-agonist radioligands for PET [61].

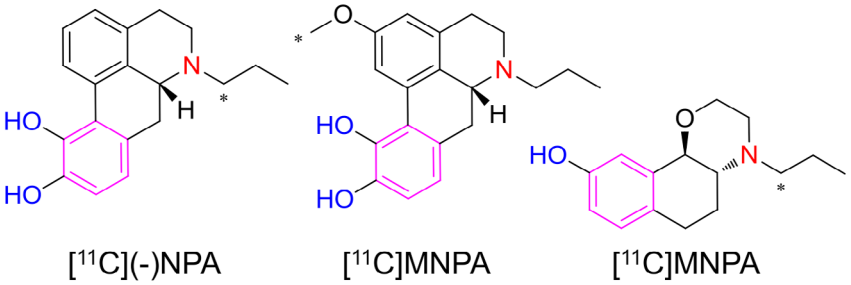

Figure 5. $D_{2/3}$ agonist PET tracers currently available for human studies.
Asterisks indicate ^{11}C-atoms. Note that each compound contains a phenethylamine motif, consisting of an aromatic ring, hydroxyl groups and a basic nitrogen two carbons away from the ring.

The first successful ^{18}F-fluorine labeled $D_{2/3}$ agonist [^{18}F]FPPAT, an aminotetraline, was reported as far back as 2004 [62], but was not developed further (until very recently – see [63]), probably due to its relatively low signal-to-noise ratio. [^{18}F]MCL-524, an apomorphine $D_{2/3}$ agonist structurally similar to [^{11}C]MNPA and [^{11}C]NPA, showed very promising results in preliminary evaluation, but has been developed only recently and is not yet in widespread use [64].

Aim and outline of the thesis

At the onset of the research described in this thesis, there were no known $D_{2/3}$ agonist SPECT tracers, and all $D_{2/3}$ agonist PET tracers used in humans were labeled with carbon-11, which limited their application for clinical research. Creation of ^{18}F-labeled $D_{2/3}$-agonist tracers with good signal-to-

noise ratios could greatly expand the potential area of application for the PET imaging of $D_{2/3}$high. Such tracers could be produced commercially and delivered to PET imaging centers without an on-site cyclotron. Development of a ^{123}I-labeled $D_{2/3}$ agonist would make SPECT imaging of $D_{2/3}$high possible.

Research described in this thesis, funded by the Dutch Technology Foundation (STW; grant number 10127), aimed to develop novel ^{18}F-labeled $D_{2/3}$ agonist tracers that would be suitable for PET imaging of the high-affinity state of the $D_{2/3}$ receptors in humans (development of potential ^{123}I-labeled SPECT tracers is described elsewhere [65]).

For this purpose, we selected a class of high-affinity $D_{2/3}$-agonists not previously used for tracer development, 2-aminomethylchroman-7-ols (AMCs) [66], and designed, prepared and evaluated a number of potential PET tracers based on this scaffold.

Chapter 2 of this thesis discusses the theoretical and practical aspects of GPCR high-affinity state imaging by PET. It provides an overview of experimental paradigms and available agonist tracers which may be used for this purpose and discusses experimental evidence for the existence of the high-affinity state of GPCRs in vivo.

Chapter 3 describes the design, preparation and pharmacological characterization of AMC derivatives as potential $D_{2/3}$ agonist tracers for PET. The affinities of tracer candidates to the high- and low-affinity states of D_2 receptors and to other dopamine receptor subtypes were measured in membrane homogenate competition assays, and the agonistic properties of AMCs at D_2 receptors were assessed in cell-based functional assays. Compounds with the highest affinities for D_2high, (*R*)-2-[(4-(4-fluorobutoxy)benzylamino) methyl]chroman-7-ol (**12a** or [^{18}F]FBu-AMC13) and (*R*) 1-(4-(2-[^{18}F]fluoroethoxy)phenyl)-4-(4-(7-hydroxychroman-2-yl)-3-azabutyl)-piperazine (**12d** or [^{18}F]FEt-AMC15), were labeled with fluorine-18 and evaluated by in vitro autoradiography in rat brain slices.

Chapter 4 is devoted to the preparation and evaluation of (*R*)-2-[(4-fluorobenzylamino)methyl]chroman-7-ol (AMC20), an additional aminomethyl chromane derivative with high affinity towards D_2high. This compound was synthesized and pharmacologically characterized later than other compounds mentioned in Chapter 3, but showed an order of magnitude higher affinity towards D_2high and therefore was given high priority in tracer devel-

opment. Chapter 4 contains data on the radiolabeling of [^{18}F]AMC20, confirmation of its preferential binding to the high-affinity state of $D_{2/3}$ receptors in rat brain slices, characterization of its distribution in living rat brain and proof of the $D_{2/3}$-specificity of its uptake in the striatum by pre-treatment of animals with non-radioactive raclopride.

Chapter 5 describes further optimization of AMC ligands that were selected for radiolabeling based on the pharmacological characterization presented in Chapter 3. A method for the optimization of the lipophilicity of [^{18}F]fluoroalkylated ligands by varying the length of the [^{18}F]fluoroalkyl chains is presented. Furthermore, the optimized ligands [^{18}F]FEt-AMC13 and [^{18}F]FEt-AMC15 were evaluated in vivo, using the same scheme as was employed for [^{18}F]AMC20. Most reported data concern [^{18}F]FEt-AMC13, as [^{18}F]FEt-AMC15 was found to not penetrate the blood-brain barrier.

Chapter 6 describes the automation of the synthesis of ^{18}F-labeled building blocks used to prepare AMC-based tracers, based on the use of an microfluidic radiosynthesis module. After this partial automation, azeotropic drying of [^{18}F]fluoride was no longer necessary and the production of ^{18}F-labeled tracers became much easier. It also resulted in decreased radioactivity exposure for researchers at late stages of the current project.

Chapter 7 presents a summary of our work on tracer development and discusses the findings of this research.

Finally, **Chapter 8** identifies steps that need to be taken for further development of AMC-based $D_{2/3}$ agonist tracers. The chapter ends with a discussion of the relevance of agonist tracers for neuroreceptor imaging and of possible approaches to further test the validity of the high-affinity state concept in vivo.

REFERENCES

1. Vallone D, Picetti R, Borrelli E. Structure and function of dopamine receptors. Neurosci. Biobehav. Rev. 2000;24:125–32.

2. Halász B, Fuxe K, Agnati LF, Kalia M, Goldstein M, Andersson K, et al. The Dopaminergic System. Berlin, Heidelberg: Springer Berlin Heidelberg; 1985.

3. Beaulieu J, Gainetdinov RR. The physiology, signaling, and pharmacology of dopamine receptors. Pharmacol. Rev. 2011;63:182–217.

4. Neve KA, Seamans JK, Trantham-Davidson H. Dopamine Receptor Signaling. J. Recept. Signal Transduct. Res. 2004;24:165–205.

5. Boyson SJ, McGonigle P, Molinoff PB, Molinoff B. Quantitative autoradiographic localization of the D_1 and D_2 subtypes of dopamine receptors in rat brain. J. Neurosci. 1986;6:3177–88.

6. Cortés R, Gueye B, Pazos A, Probst A, Palacios JM. Dopamine receptors in human brain: autoradiographic distribution of D_1 sites. Neuroscience. 1989;28:263–73.

7. Camps M, Cortés R, Gueye B, Probst A, Palacios JM. Dopamine receptors in human brain: autoradiographic distribution of D_2 sites. Neuroscience. 1989;28:275–90.

8. Primus RJ, Thurkauf A, Xu J, Yevich E, McInerney S, Shaw K, et al. II. Localization and characterization of dopamine D4 binding sites in rat and human brain by use of the novel, D_4 receptor-selective ligand [^{3}H]NGD 94-1. J. Pharmacol. Exp. Ther. 1997;282:1020–7.

9. Lahti RA, Roberts RC, Cochrane E V, Primus RJ, Gallager DW, Conley RR, et al. Direct determination of dopamine D_4 receptors in normal and schizophrenic postmortem brain tissue: a [^{3}H]NGD-94-1 study. Mol. Psychiatry. 1998;3:528–33.

10. Khan ZU, Gutiérrez A, Martín R, Peñafiel A, Rivera A, de la Calle A. Dopamine D_5 receptors of rat and human brain. Neuroscience. 2000;100:689–99.

11. Stanwood GD, Artymyshyn RP, Kung MP, Kung HF, Lucki I, McGonigle P. Quantitative autoradiographic mapping of rat brain dopamine D_3 binding with [^{125}I]7-OH-PIPAT: evidence for the presence of D_3 receptors on dopaminergic and nondopaminergic cell bodies and terminals. J. Pharmacol. Exp. Ther. 2000;295:1223–31.

12. Seeman P, Wilson A, Gmeiner P, Kapur S. Dopamine D_2 and D_3 receptors in human putamen, caudate nucleus, and globus pallidus. Synapse. 2006;60:205–11.

13. Bernheimer H, Birkmayer W, Hornykiewicz O, Jellinger K, Seitelberger F. Brain dopamine and the syndromes of Parkinson and Huntington Clinical, morphological and neurochemical correlations. J. Neurol. Sci. 1973;20:415–55.

14. Schwab LC, Garas SN, Drouin-Ouellet J, Mason SL, Stott SR, Barker RA. Dopamine and Huntington's disease. Expert Rev. Neurother. 2015;15:445–58.

15. Sulzer D. How Addictive Drugs Disrupt Presynaptic Dopamine Neurotransmission. Neuron. Elsevier Inc.; 2011;69:628–49.

16. Meyer JH, McNeely HE, Sagrati S, Boovariwala A, Martin K, Verhoeff NPLG, et al. Elevated putamen D_2 receptor binding potential in major depression with motor retardation: an [^{11}C]raclopride positron emission tomography study. Am. J. Psychiatry. 2006;163:1594–602.

17. Tatsumi M, Groshan K, Blakely RD, Richelson E. Pharmacological profile of antidepressants and related compounds at human monoamine transporters. Eur. J. Pharmacol. 1997;340:249–58.

18. van Rossum JM. The significance of dopamine-receptor blockade for the action of neuroleptic drugs. In: Brill H, Cole J, Deniker P, Hippius H, Bradley PB, editors. Neuropsychopharmacol. Proc 5th Coll. Int Neuropsychopharmacol. Excerpta Medica Foundation; 1967. p. 321–9.

19. van Kammen DP. The dopamine hypothesis of schizophrenia revisited. Psychoneuroendocrinology. 1979;4:37–46.

20. Seeman P. Are dopamine D2 receptors out of control in psychosis? Prog. Neuropsychopharmacol. Biol. Psychiatry. Elsevier B.V.; 2013;46:146–52.

21. Rahmim A, Zaidi H. PET versus SPECT: strengths, limitations and challenges. Nucl. Med. Commun. 2008;29:193–207.

22. Hicks RJ, Hofman MS. Is there still a role for SPECT-CT in oncology in the PET-CT era? Nat. Rev. Clin. Oncol. 2012;9:712–20.

23. Ter-Pogossian MM, Phelps ME, Hoffman EJ, Mullani N A. A positron-emission transaxial tomograph for nuclear imaging (PETT). Radiology. 1975;114:89–98.

24. Peterson TE, Furenlid LR. SPECT detectors: the Anger Camera and beyond. Phys. Med. Biol. 2011;56:R145–82.

25. Slomka PJ, Pan T, Berman DS, Germano G. Advances in SPECT and PET Hardware. Prog. Cardiovasc. Dis. Elsevier B.V.; 2015;57:566–78.

26. Gunn RN, Slifstein M, Searle GE, Price JC. Quantitative imaging of protein targets in the human brain with PET. Phys. Med. Biol. IOP Publishing; 2015;60:R363-411.

27. Mintun MA, Raichle ME, Kilbourn MR, Wooten GF, Welch MJ. A quantitative model for the in vivo assessment of drug binding sites with positron emission tomography. Ann. Neurol. 1984;15:217–27.

28. Dierckx RAJO, Otte A, de Vries EFJ, van Waarde A, Luiten PGM, editors. PET and SPECT of Neurobiological Systems. Berlin, Heidelberg: Springer Berlin Heidelberg; 2014.

29. Booij J, Tissingh G, Winogrodzka A, van Royen EA. Imaging of the dopaminergic neurotransmission system using single-photon emission tomography and positron emission tomography in patients with parkinsonism. Eur. J. Nucl. Med. Mol. Imaging. 1999;26:171–82.

30. Koeppe RA, Gilman S, Junck L, Wernette K, Frey KA. Differentiating Alzheimer's disease from dementia with Lewy bodies and Parkinson's disease with (+)-[^{11}C]dihydrotetrabenazine positron emission tomography. Alzheimers. Dement. 2008;4:S67-76.

31. Brooks DJ. Imaging approaches to Parkinson disease. J. Nucl. Med. 2010;51:596–609.

32. Abi-Dargham A, Moore H. Prefrontal DA transmission at D_1 receptors and the pathology of schizophrenia. Neuroscientist. 2003;9:404–16.

33. Laruelle M. Imaging synaptic neurotransmission with in vivo binding competition techniques: a critical review. J. Cereb. Blood Flow Metab. 2000;20:423–51.

34. Laruelle M. Measuring Dopamine Synaptic Transmission with Molecular Imaging and Pharmacological Challenges: The State of the Art. Neuromethods. 2012. p. 163–203.

35. Koepp MJ, Gunn RN, Lawrence AD, Cunningham VJ, Dagher A, Jones T, et al. Evidence for striatal dopamine release during a video game. Nature. 1998;393:266–8.

36. Kim J-H, Son Y-D, Kim H-K, Lee S-Y, Cho S-E, Kim Y-B, et al. Effects of age

on dopamine D_2 receptor availability in striatal subdivisions: a high-resolution positron emission tomography study. Eur. Neuropsychopharmacol. Elsevier B.V.; 2011;21:885–91.

37. Abi-Dargham A. Do we still believe in the dopamine hypothesis? New data bring new evidence. Int. J. Neuropsychopharmacol. 2004;7 Suppl 1:S1-5.

38. Abi-Dargham A, van de Giessen E, Slifstein M, Kegeles LS, Laruelle M. Baseline and amphetamine-stimulated dopamine activity are related in drug-naïve schizophrenic subjects. Biol. Psychiatry. Society of Biological Psychiatry; 2009;65:1091–3.

39. Volkow ND, Fowler JS, Wang G-J, Swanson JM. Dopamine in drug abuse and addiction: results from imaging studies and treatment implications. Mol. Psychiatry. 2004;9:557–69.

40. De Lean A, Stadel JM, Lefkowitz RJ. A ternary complex model explains the agonist-specific binding properties of the adenylate cyclase-coupled beta-adrenergic receptor. J. Biol. Chem. 1980;255:7108–17.

41. Kenakin T. Efficacy at G-protein-coupled receptors. Nat. Rev. Drug Discov. 2002;1:103–10.

42. Weiss J. The Cubic Ternary Complex Receptor–Occupancy Model I. Model Description. J. Theor. Biol. 1996;178:151–67.

43. Stein RSL, Ehlert FJ. A kinetic model of GPCRs: analysis of G protein activity, occupancy, coupling and receptor-state affinity constants. J. Recept. Signal Transduct. Res. 2014;0:1–15.

44. Lahti RA, Figur LM, Piercey MF, Ruppel PL, Evans DL. Intrinsic activity determinations at the dopamine D_2 guanine nucleotide-binding protein-coupled receptor: utilization of receptor state binding affinities. Mol. Pharmacol. ASPET; 1992;42:432–8.

45. Ruffolo RR. Review important concepts of receptor theory. J. Auton. Pharmacol. 1982;2:277–95.

46. Seeman P, Schwarz J, Chen J, Szechtman H, Perreault M, McKnight GS, et al. Psychosis pathways converge via D_2high dopamine receptors. Synapse. 2006;60:319–46.

47. Graff-Guerrero A, Mizrahi R, Agid O, Marcon H, Barsoum P, Rusjan P, et al. The dopamine D_2 receptors in high-affinity state and D_3 receptors in schiz-

ophrenia: a clinical [^{11}C]-(+)-PHNO PET study. Neuropsychopharmacology. 2009;34:1078–86.

48. Narendran R, Martinez D, Mason NS, Lopresti BJ, Himes ML, Chen C-M, et al. Imaging of dopamine $D_{2/3}$ agonist binding in cocaine dependence: A [^{11}C]NPA positron emission tomography study. Synapse. 2011;65:1344–9.

49. Skinbjerg M, Sibley DR, Javitch JA, Abi-Dargham A. Imaging the high-affinity state of the dopamine D_2 receptor in vivo: Fact or fiction? Biochem. Pharmacol. Elsevier Inc.; 2012;83:193–8.

50. Cumming P, Wong DF, Gillings N, Hilton J, Scheffel U, Gjedde A. Specific binding of [^{11}C]raclopride and N-[^{3}H]propyl-norapomorphine to dopamine receptors in living mouse striatum: occupancy by endogenous dopamine and guanosine triphosphate-free G protein. J. Cereb. Blood Flow Metab. 2002;22:596–604.

51. Narendran R, Hwang D-R, Slifstein M, Talbot PS, Erritzoe D, Huang Y, et al. In vivo vulnerability to competition by endogenous dopamine: comparison of the D_2 receptor agonist radiotracer (–)-N-[^{11}C]propyl-norapomorphine ([^{11}C]NPA) with the D_2 receptor antagonist radiotracer [^{11}C]-raclopride. Synapse. 2004;52:188–208.

52. Ginovart N, Galineau L, Willeit M, Mizrahi R, Bloomfield PM, Seeman P, et al. Binding characteristics and sensitivity to endogenous dopamine of [^{11}C]-(+)-PHNO, a new agonist radiotracer for imaging the high-affinity state of D_2 receptors in vivo using positron emission tomography. J. Neurochem. 2006;97:1089–103.

53. Gallezot JD, Kloczynski T, Weinzimmer D, Labaree D, Zheng MQ, Lim K, et al. Imaging Nicotine- and Amphetamine-Induced Dopamine Release in Rhesus Monkeys with [^{11}C]PHNO vs [^{11}C]raclopride PET. Neuropsychopharmacology. 2013;866–74.

54. Narendran R, Mason NS, Laymon CM, Lopresti BJ, Velasquez ND, May MA, et al. A comparative evaluation of the dopamine $D_{2/3}$ agonist radiotracer [^{11}C](–)-N-propyl-norapomorphine and antagonist [^{11}C]raclopride to measure amphetamine-induced dopamine release in the human striatum. J. Pharmacol. Exp. Ther. 2010;333:533–9.

55. Shotbolt P, Tziortzi AC, Searle GE, Colasanti A, van der Aart J, Abanades S, et al. Within-subject comparison of [^{11}C]-(+)-PHNO and [^{11}C]raclopride sensitivity to acute amphetamine challenge in healthy humans. J. Cereb. Blood Flow Metab. 2012;32:127–36.

56. Keng PY, Esterby M, Dam RM Van. Emerging Technologies for Decentralized Production of PET Tracers. In: Hsieh C-H, editor. Positron Emiss. Tomogr. – Curr. Clin. Res. Asp. InTech; 2012. p. 153–82.

57. Krohn KA, Mankoff DA, Muzi M, Link JM, Spence AM. True tracers: comparing FDG with glucose and FLT with thymidine. Nucl. Med. Biol. 2005;32:663–71.

58. Vasdev N, Seeman P, Garcia A, Stableford WT, Nobrega JN, Houle S, et al. Syntheses and in vitro evaluation of fluorinated naphthoxazines as dopamine D_2/D_3 receptor agonists: radiosynthesis, ex vivo biodistribution and autoradiography of [^{18}F]F-PHNO. Nucl. Med. Biol. 2007;34:195–203.

59. Kiesewetter DO, Brücke T, Finn RD. Radiochemical synthesis of [^{18}F]fluororaclopride. Int. J. Rad. Appl. Instrum. A. 1989;40:455–60.

60. Conti M, Eriksson L. Physics of pure and non-pure positron emitters for PET: a review and a discussion. EJNMMI Phys. EJNMMI Physics; 2016;3:8.

61. Finnema SJ, Bang-Andersen B, Wikström H V, Halldin C. Current state of agonist radioligands for imaging of brain dopamine D_2/D_3 receptors in vivo with positron emission tomography. Curr. Top. Med. Chem. 2010;10:1477–98.

62. Shi B, Narayanan TK, Christian BT, Chattopadhyay S, Mukherjee J. Synthesis and biological evaluation of the binding of dopamine D_2/D_3 receptor agonist, (R,S)-5-hydroxy-2-(N-propyl-N-(5'-[^{18}]F-fluoropentyl)aminotetralin ([^{18}]F-5-OH-FPPAT) in rodents and nonhuman primates. Nucl. Med. Biol. 2004;31:303–11.

63. Mukherjee J, Majji D, Kaur J, Constantinescu CC, Narayanan TK, Shi B, et al. PET radiotracer development for imaging high-affinity state of dopamine D_2 and D_3 receptors: Binding studies of fluorine-18 labeled aminotetralins in rodents. Synapse. 2016 Nov 19;1–15.

64. Finnema SJ, Stepanov V, Nakao R, Sromek AW, Zhang T, Neumeyer JL, et al. [^{18}F]-MCL-524, an ^{18}F-Labelled Dopamine D_2 and D_3 Receptor Agonist Sensitive to Dopamine: A Preliminary PET Study. J. Nucl. Med. 2014;55:1164–70.

65. van Wieringen J-P. Evaluation of potential agonist radioligands for imaging dopamine $D_{2/3}$ receptors. University of Amsterdam; 2015.

66. Mewshaw RE, Kavanagh J, Stack G, Marquis KL, Shi X, Kagan MZ, et al. New generation dopaminergic agents. 1. Discovery of a novel scaffold which embraces the D_2 agonist pharmacophore. Structure-activity relationships of a series of 2-(aminomethyl)chromans. J. Med. Chem. 1997;40:4235–56.

Chapter 2

Hunting for the high-affinity state of G-protein coupled receptors with agonist PET tracers: theoretical and practical considerations

1. Introduction

Non-invasive imaging of synaptic neurotransmitter receptors with positron emission tomography (PET) provides insights into the number of receptors expressed in the brain and the functioning of brain networks. Analysis of the imaging data yields information about the role of particular neurotransmitters in the functioning of the brain in health as well as in neuropsychiatric disorders, including syndromes characterized by cognitive dysfunctions.

Receptors that neurotransmitters bind to are either ligand-gated ion channels (LGICs) or G-protein coupled receptors (GPCRs). For some neurotransmitters, all receptors belong to a single receptor superfamily, e.g. all known dopamine receptors are GPCRs. Some bind to receptors from both superfamilies, e.g. there are LGIC-type and GPCR-type receptors of the neurotransmitters acetylcholine and glutamate.

The signaling mechanism of LGICs is comparatively simple and quick – neurotransmitter binding opens the ionic channel that the receptor itself forms. Quick (millisecond time scale) and usually short-lasting postsynaptic response is thus obtained. GPCRs, on the other hand, affect their downstream signaling pathways through mediation of trimeric proteins called G-proteins (Figure 1). The GPCR signaling mechanism is slower (second time scale) and more energy-consuming than that of LGICs, but longer lasting and much more versatile. Due to this versatility, GPCRs are the most popular targets for drugs used in clinical practice [1,2].

In vitro studies in membrane homogenates from cultured cells or isolated tissues have shown that in a single population of GPCRs to which antagonist drugs have single affinity, agonist drugs recognize two distinct receptor subpopulations: one for which they have high affinity and one for which they have low affinity. The existence of a receptor subpopulation that possesses high-affinity towards the agonists (dubbed “high-affinity state”, Rhigh) has been demonstrated for numerous neurotransmitter GPCRs including dopaminergic [3,4], serotonergic [5–7], muscarinic [8] and opioid receptors [9]. The high-affinity state is commonly thought to be composed of receptor molecules bound to G-proteins.

The relationship between G-protein coupling and high affinity towards the agonist gave rise to a hypothesis that the relative abundance of Rhigh may characterize the responsiveness of the synaptic signaling machinery to ago-

nist levels. Indeed, alterations of the fraction of receptors configured in the high-affinity state, as measured in membrane homogenates, were found in pathological states associated with dysregulation of neurotransmission. For instance, the relative abundance of the high affinity state of μ-opioid receptors was decreased in guinea pigs after chronic morphine treatment [10], while the high-affinity state of muscarinic M_1 receptors was downregulated in Alzheimer's disease [11,12]. Upregulation of the high-affinity state of dopamine D_2 receptors has been reported in several animal models of psychosis [13,14].

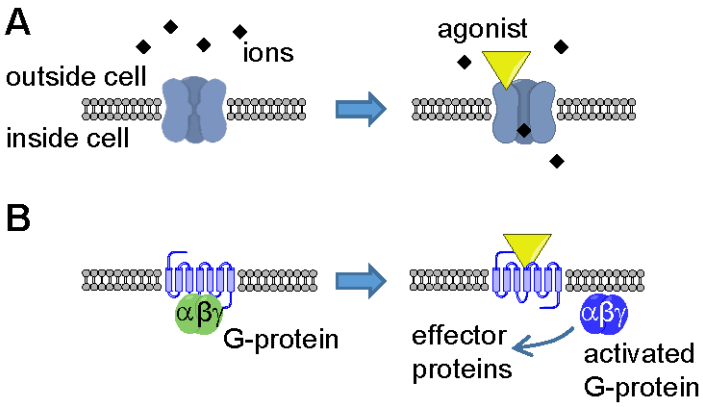

Figure 1. Simplified signaling mechanisms of ligand-gated ion channels (A) and G-protein coupled receptors (B).

Assessing the availability of Rhigh may, therefore, provide more valuable information about the state of neurotransmission in vivo than assessing the availability of total receptors. Given that agonists preferentially bind to Rhigh, this hypothesis spurred the development of agonist PET tracers and their use for neuroreceptor imaging.

In this chapter we will review and discuss the molecular basis of the high-affinity state, inherent advantages and shortcomings of agonist PET tracers stemming from their preferential binding to the high-affinity state, agonist PET tracers currently available for receptor imaging in vivo, experimental methods used for the imaging of high-affinity state in vivo and evidence collected with these methods.

2. Nature of the high-affinity state of GPCRs

2.1. G-protein-dependent high-affinity state

The canonical view of the nature of the high-affinity state is based on the so-called ternary complex model of G-protein signaling which originates from the studies of agonist binding to β-adrenergic receptors in membrane homogenates [15,16]. This model claims that in order to launch the G-protein signaling cascade, a "ternary" complex must form, consisting of agonist, receptor and G-protein. Positive cooperativity between receptor-agonist and receptor-G-protein binding creates the separation of the total receptor population into high and low-affinity states. For the agonist, receptors complexed with G-proteins form the high-affinity state, whereas free receptor molecules represent the low-affinity state. Indeed, the preference of agonist ligands for the G-protein-bound high-affinity state was found to correlate with their intrinsic activity [17–19].

Several newer and more sophisticated versions of the ternary complex model have been developed in order to account for such pharmacological phenomena as constitutive activity (presence of baseline signaling in the absence of agonists) and inverse agonism (existence of ligands that decrease rather than increase the level of signaling relative to baseline). These models imply the existence of more than two receptor species with different affinities for the agonist, but the main premise remains the same: G-protein binding is the main factor that determines the receptor's affinity towards the agonist [20,21].

An important feature of the G-protein dependent high-affinity state is its sensitivity to guanosine triphosphate (GTP). Indeed, the high-affinity state of GPCRs detected in membrane homogenates usually disappears upon GTP addition [3–9]. The reason for this is that the canonical G-protein signaling cascade involves the so-called GTP cycle (Figure 2). G-proteins are heterotrimers, and one of their subunits, Gα, has a binding site for guanosine nucleotide (this gives G-proteins their name). In an inactive G-protein, this site is occupied by guanosine diphosphate (GDP). Upon G-protein activation by an agonist-bound receptor, GDP is replaced by GTP from the cytoplasm, which leads to the dissociation of Gα-subunit from the Gβ and Gγ subunits (together referred to as Gβγ). The G-protein splits into two halves, which then activate downstream effectors. If the G-protein uncouples from the receptor, the receptor quickly relaxes into its inactive "low-affinity" state [22].

Eventual hydrolysis of GTP to GDP in the Gα subunit lets the G-protein reassemble and bind to the receptor again, which closes the cycle [23].

Therefore, the GTP cycle acts as a negative feedback loop, promoting G-protein decoupling from the receptors and their (temporary) conversion into the low-affinity state after agonist binding. Excess GTP shifts the equilibrium towards complete dissociation of G-proteins from the receptors.

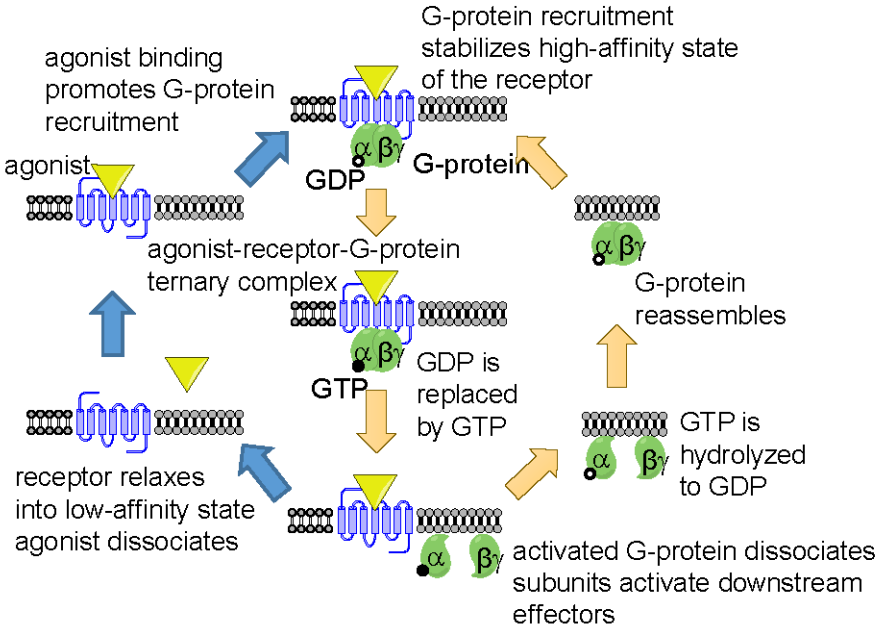

Figure 2. GPCR activation (left circuit) and GTP cycle (right circuit, light orange arrows).

2.2. Oligomerization-dependent high-affinity state

The growing amount of evidence on GPCR oligomerization in cultured cells and living tissues [24] and on the pharmacological relevance of such oligomerization (see [25] for review) has given rise to the concept of oligomerization-dependent high-affinity state. When the agonist interacts with a receptor oligomer, occupying and activating a single receptor unit within it, conformational changes in this receptor influence the conformation

of other receptors within the same oligomer and decrease their affinity for other agonist molecules (Figure 3). In other words, separation into high- and low-affinity states is caused by negative cooperativity effects in the agonist binding to oligomerized receptors [26].

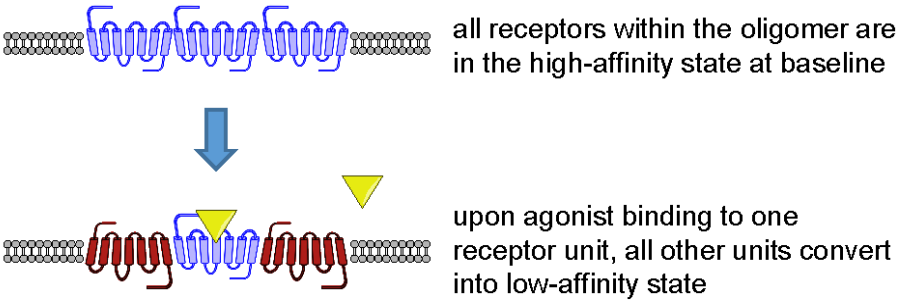

Figure 3. Oligomerization-dependent high-affinity state.

Receptor oligomerization is arguably mainly relevant for the explanation of the interplay between signaling pathways of different types of receptors [25]: interaction between oligomer subunits is conceptually simpler than interference of downstream cascades. However, among data from radioligand binding studies there are also some results that are better explained by oligomerization than by G-protein coupling, such as (i) GTP-insensitive high-affinity agonist binding to dopamine D_3 and serotonin 5-HT_{2A} receptors [27,28], (ii) detection of high- and low-affinity states of adenosine A_{2A} receptors by antagonist ligands [29] and (iii) detection of several (more than two) binding sites with different affinities to agonists in the muscarinic M_2 receptor population [30].

If there is cooperativity between receptor-agonist and receptor-receptor interaction, agonist binding might influence the degree of receptor oligomerization. Some studies indeed report such phenomena [31,32], but, in general, experimental data on the relationship between ligand binding and oligomerization are contradictory both in terms of whether ligand binding really promotes formation or dissociation of oligomers and whether this action is correlated with intrinsic activity (see [33,34] for review).

2.3. Influence of agonist binding on the high-affinity state

In both G-protein-coupling and oligomerization-dependent models of high-affinity state, agonist binding to the receptor influences receptor interaction with other molecules and thus can alter the relative abundance of the high-affinity state.

G-protein-dependent high-affinity state: Under conditions where no feedback loops are present, as is the case with in vitro binding studies with non-living material like membrane homogenates and tissue slices, the relationship between agonist concentration and percentage of receptors in the high-affinity state at equilibrium is straightforward. In the absence of GTP, agonist binding can only increase G-protein recruitment. Therefore, increasing agonist concentration will make the percentage of receptors in the "G-protein-dependent" high-affinity state grow from some "floor" value (see section 2.5) to the "ceiling" value, determined by receptor-G-protein stoichiometry in the system (100% if the number of available G-proteins is greater than or equal to the number of receptors). On the other hand, in the presence of excess GTP (or its analogs) and negligible GTP hydrolysis, all G-proteins activated by agonist-bound receptors will be dissociated and uncoupled from the receptors, so at any agonist concentration there will be no discernible high-affinity state.

In living cells and tissues, however, the GTP cycle plays the role of a negative feedback loop, which counteracts excess high-to-low or low-to-high conversion of affinity states caused by the agonist. Depending on the combination of concentrations and kinetic rates, either G-protein-recruiting or G-protein-dissociating effects of agonist can become dominant. Indeed, mathematical simulations of GPCR signaling have demonstrated the possibility of both agonist-induced increases and agonist-induced decreases in the relative abundance of the G-protein-dependent high-affinity state [21].

Oligomerization-dependent high-affinity state: Negative cooperativity in agonist binding to oligomerized receptors implies that increasing agonist concentration will bring more and more receptors into "low-affinity state". The percentage of receptors in the high-affinity state, equal to 100% in the absence of agonist, will decrease to 100% / N (N is the average number of receptors per oligomer) when the agonist occupies one receptor unit in each oligomer, converting all the other units to low-affinity state. When agonist concentration raises so high that agonists start to occupy receptors in the low-affinity state, the relative abundance of the high-affinity state will fall

even lower. There are no well described and widely accepted feedback loops for the oligomerization-dependent model of the high-affinity state.

2.4. Agonist-induced receptor internalization

Activation of GPCRs by agonists promotes not only G-protein binding to them, but also their phosphorylation by G-protein coupled receptor kinases (GRK) and internalization mediated by β-arrestins [35]. This provides an extra pathway through which the agonist can influence the relative abundance of the high-affinity state. Internalized receptors are de-coupled from G-proteins (coupled to β-arrestins instead) and removed from the cell surface to intracellular compartments, where the ionic environment and pH value can be different from extracellular conditions. This makes internalized receptors less accessible (especially for hydrophilic ligands) and possibly also alters their affinity towards their ligands.

In vitro, β-arrestin recruitment can happen within minutes [36,37]. Internalization of dopamine $D_{2/3}$ receptors was observed within the same timeframe in vivo and was shown to be dose-dependent [38]. Although it is not yet clear whether internalization mainly happens to receptors in the low- or in the high-affinity state [39,40], internalized $D_{2/3}$ receptors on intact cells and μ-opioid receptors incubated in a buffer imitating endosomal medium were shown to have decreased affinities towards their ligands [41,42].

Therefore, high concentrations of agonist can launch receptor internalization and change the number and relative abundances of receptor subpopulations with different affinities towards imaging radioligands. On the other hand, in internalization-deficient β-arrestin knockout mice, baseline binding of $D_{2/3}$ agonist and antagonist tracers was the same as in wild type-controls [43]. Perhaps, then, basal neurotransmitter levels in the living brain establish a dynamic equilibrium between receptor internalization and recycling.

2.5. Relative abundance of high-affinity state in the absence of the agonist

The oligomerization-dependent model of the high-affinity state implies that this is the state in which all receptors are configured in the absence of the agonist.

For the G-protein-dependent high-affinity state, its baseline relative abundance, that is, the degree to which G-proteins interact with the receptors in the absence of agonist, is a matter of debate (see [44,45] for review). One extreme view, called collision coupling (Figure 4A), states that in living cells G-proteins are not normally bound to the receptors, but instead interact with them transiently when receptors become activated [46]. Another extreme view (Figure 4B) states that G-proteins are always bound ("pre-coupled") to the receptors, and do not decouple even after activation, which happens through structural rearrangement of the G-protein rather than through dissociation [47–49].

On the one hand, collision coupling provides a straightforward interpretation of differences in intrinsic activities of the agonists: agonist efficacy is related to the number of different G-proteins that an agonist-bound receptor can bind and activate per unit of time. Decoupling of G-proteins from the receptors upon activation explains the disappearance of the high-affinity state upon GTP addition in membrane homogenates. On the other hand, receptors and G-proteins are known to be co-isolated by immunoprecipitation, and bioluminescence and fluorescence resonance energy transfer (BRET/FRET) experiments with mutated proteins incorporating fluorescent or bioluminescent probe demonstrate close contact between receptors and G-proteins in the absence of agonists [44]. Moreover, in BRET studies with α_2 adrenergic and δ-opioid receptors, these receptors were found to interact with G-proteins both before and after activation by agonist [48,49].

Middle courses between the extreme views are of course possible, where some G-proteins are bound to receptors at baseline but decoupled upon activation, or where G-proteins are uncoupled at baseline but become bound to receptors upon activation. Moreover, BRET and FRET experiments image the whole population of the receptors, so constant presence of a RET signal, while showing that a fraction of receptors is engaged with G-proteins, does not exclude the possibility of a rapid turnover of G-proteins with which these receptors interact.

2.6. Summary

The existence of high- and low-affinity states of GPCRs is commonly thought to be due to receptor interaction with G-proteins. Being a part of the canonical GPCR signaling cascade, receptor-G-protein coupling is directly related to the pharmacological activity of the agonists.

GPCR oligomerization (both homo- and hetero), with negative cooperativity in agonist binding within the oligomer, can be an alternative mechanism leading to the formation of receptor subpopulations with different affinities for the agonist. It is plausible that at least for some GPCRs oligomerization may contribute to the splitting of receptors into high- and low-affinity states instead of, or in addition to, G-protein coupling.

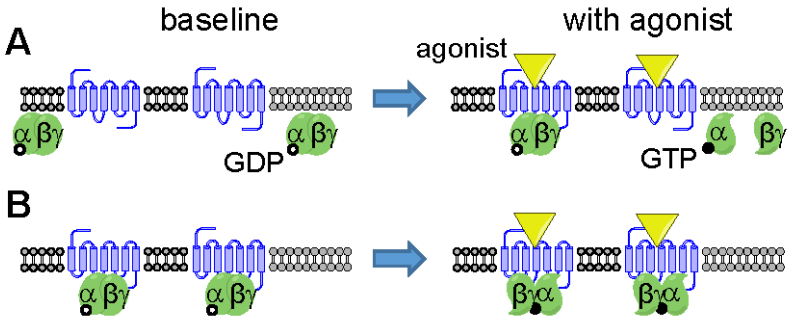

Figure 4. Two extreme modes of receptor-G-protein interaction.

In the collision-coupling model (A), G-proteins do not stably interact with receptors, but agonist action on the receptor promotes G-protein recruitment to and activation by the receptors, which results in the dissociation of G-proteins. In the pre-coupling model (B), G-proteins are stably bound to the receptors, and rearrange their structures upon activation instead of dissociating.

Both models of high-affinity state imply that agonists preferentially bind to receptors that are most ready to launch the signaling cascade, although in the oligomerization model it is so just because agonist binding makes unoccupied receptors “less ready”. Moreover, agonist binding can influence the relative abundance of the high-affinity state, potentially promoting its formation or disintegration and launching receptor internalization in intact cells and living tissues. Such influence is most directly demonstrated for the G-protein-dependent model of the high-affinity state.

3. Expected advantages and disadvantages of agonist tracers relative to antagonist tracers

From the notion that agonists preferentially bind to a high-affinity functional subset of receptors, one can logically infer a number of applications in which agonist tracers should be superior, at least in theory, to antagonist

tracers. Note that proposed advantages of agonist tracers mentioned below hold independently of whether the high-affinity state is G-protein-dependent or oligomerization-dependent.

3.1. Applications where agonist tracers have comparative advantage over antagonist tracers

3.1.1. Measurement of synaptic neurotransmission

An endogenous neurotransmitter is an agonist by definition, so it competes with the agonist tracer for the same subset of receptors – receptors configured in high-affinity state – while an antagonist tracer also binds to receptors in the low-affinity state that are "ignored" by the neurotransmitter except at very high concentrations. This means that a change in the concentration of neurotransmitter of a given magnitude will lead to a greater change in agonist tracer binding compared to antagonist tracer binding (Figure 5).

For receptors such as serotonin receptors where until recently no antagonist ligands appeared to be clearly sensitive to alterations of endogenous neurotransmitter levels [50], development of agonist ligands is considered a promising path to achieve the goal of measuring synaptic neurotransmission [51].

3.1.2. Studies of (pathological) alterations in receptor signaling

In Section 1, a few examples were given of how alterations of the percentage of receptors configured in the high-affinity state can accompany disease. Such findings indicate that the relative abundance of the high-affinity state may be a better marker of the "normality" of the receptor population than total receptor density. Agonist tracers should then be a convenient tool for pinpointing alterations of the availability of receptors configured in the high-affinity state in disease.

The results of some in vitro experiments with agonist and antagonist radioligands have supported the hypothesis that agonist tracers are superior to antagonists in detecting pathological changes in neuroreceptor signaling. In vitro binding of the serotonin 5-HT_{1A} agonists [^{18}F]F15599 and [^{18}F]F13640, but not of the antagonist [^{18}F]MPPF, in post-mortem brain sections of Alzheimer patients was decreased compared to control brains [52,53]. In unilateral 6-hydroxydopamine-induced lesions of the rat brain (exhibiting dopaminergic neurodegeneration similar to Parkinson's disease

in humans, where upregulation of Rhigh is hypothesized), the ex vivo binding of dopamine $D_{2/3}$ agonist [^{3}H]NPA was changed to a greater extent than the in vitro binding of $D_{2/3}$ antagonist [^{3}H]raclopride [54].

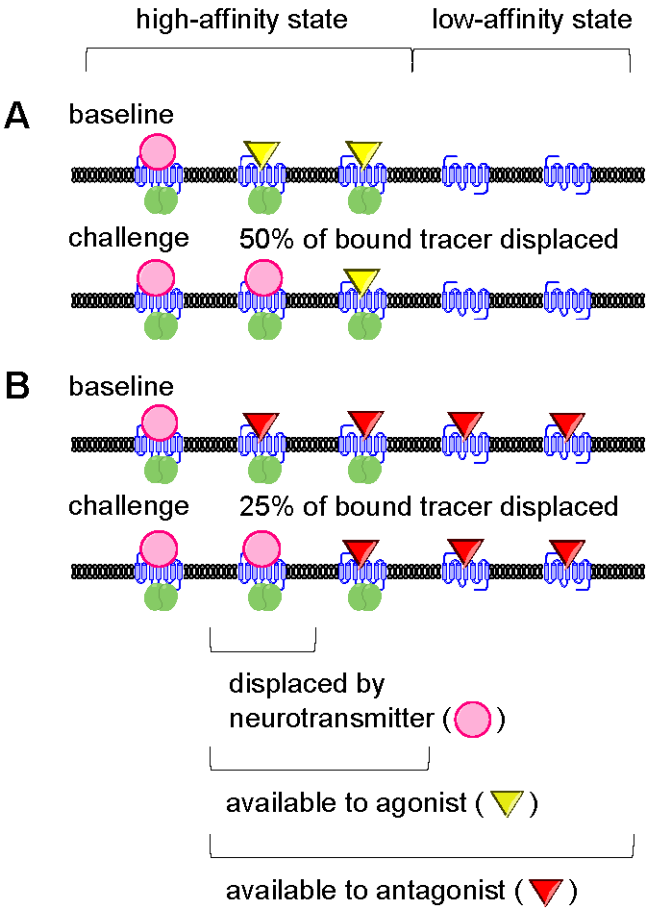

Figure 5. Greater sensitivity of agonist tracers to displacement ("challenge") by neurotransmitter.

Agonist tracers primarily bind to the receptors configured in the high-affinity state, as do neurotransmitters. Therefore, the same change in receptor occupancy by the neurotransmitter displaces greater fraction of bound agonist tracer (A) than of bound antagonist tracer (B).

3.1.3. Measurement of agonist drug occupancy

Many drugs owe their effect to their agonist activity at one or more kinds of receptors. For instance, many antiparkinsonian drugs are $D_{2/3}$ agonists

[55]; muscarinic receptor agonists like milameline were tried as treatment for Alzheimer's disease [56]; the mechanism of action of antipsychotics may include not only $D_{2/3}$ antagonism but also 5-HT_{1A} agonism [57,58]; the active metabolite of clozapine (also an atypical antipsychotic) acts as an agonist at muscarinic M_1 receptors [59]; opiate agonists are widely used as analgesics or antitussives and for treating diarrhea and opiate abuse [60].

Increased sensitivity of agonist tracers to displacement by agonist drugs can help in occupancy studies: opioid receptor antagonist [^{11}C]diprenorhin failed to detect receptor occupancy by clinically relevant doses of opioid agonists [61,62].

Agonist tracers can also complement antagonist tracers in the investigations of the affinity-state preference of new drugs. The sensitivities of agonist and antagonist tracers to the displacement by the drug can be compared: drugs preferring the high-affinity state will displace the agonist tracer more readily, while drugs not distinguishing between affinity states will show no difference in displacement efficacy. Two studies attempting this approach have been published [63,64], but both reported equal displacement of agonist and antagonist tracers by the drug, which can be interpreted in two ways: either the tested drugs were ideal antagonists, or the hypothesis of greater agonist tracer displacement by agonist drug does not hold.

3.2. Intrinsic shortcomings of agonist tracers

Though the preference for the high-affinity state makes agonist tracers potentially superior to antagonists in certain imaging applications, it also results in a number of specific difficulties associated with development and use of agonist tracers.

3.2.1. Lower signal-to-noise ratios

The signal-to-noise ratio of a PET tracer is proportional to the density of receptors the tracer can bind to in the brain (B_{avail}) and to the tracer's affinity towards these receptors ($1/K_d$). The density of receptors configured in the high-affinity state (and thus recognized by agonist tracers) is by definition lower than the total receptor density.

Moreover, in the G-protein dependent model of the high-affinity state, agonist binding to the receptor promotes eventual decoupling of G-protein and the relaxation of the receptor into the low-affinity state. Although, as men-

tioned above, the net effect of agonist binding on the relative abundance of the high-affinity state can be both positive and negative, negative feedback in the form of the GTP cycle can decrease effective affinity of the agonist towards the receptors relative to what is measured in membrane homogenates in the absence of GTP. Indeed, GTP depletion was shown to increase the affinity of agonist, but not antagonist ligands to opioid receptors in cultured cells [65].

Therefore, affinity and non-specific binding requirements for agonist tracers are stricter than for antagonists.

3.2.2. Greater likelihood of unwanted pharmacological effects

As agonist tracers preferentially bind to the functional subpopulation of the receptors, a lower dose of them is needed to induce significant physiological responses, which can distort the experimental results and cause discomfort to the patients.

Indeed, staying below the pharmacological dose range is a concern in opioid receptor imaging with agonist tracers [66–68]. It was also reported as a potential concern in serotonin 5-HT_{1A} receptor imaging with the agonist [^{11}C]CUMI-101 [69], even though first tests of the same compound in humans showed no adverse effects [70]. Exceeding the pharmacological threshold is especially easy with tracers that have complex labeling chemistry. For instance, the dopamine $D_{2/3}$ receptor agonist [^{11}C](+)PHNO was originally labeled via a four-step route, resulting in a relatively low achievable specific radioactivity [71]. As a consequence, a high incidence of nausea (emesis is a typical effect of D_2 agonism) was reported in patients injected with [^{11}C](+)PHNO [72], and it was later found that [^{11}C](+)PHNO human PET studies had frequently been performed under non-tracer conditions [73].

4. Existing PET agonist tracers for GPCR imaging in the central nervous system

The greatest number of agonist PET tracers has been developed for the imaging of dopamine $D_{2/3}$ receptors (see [74] for a review). Tracer development efforts in the last two decades have yielded a number of agonist radioligands for other receptors as well. The most promising agonist tracers developed for PET imaging of neuroreceptors are presented in Table 1.

4.1. Definition and properties of an agonist tracer

An agonist tracer is usually defined as "a tracer based on a compound that has agonist activity at the receptors it binds to". There are many ways to confirm and measure the degree of agonistic activity: behavioral or ex vivo studies examining the physiological effect of the drug, functional in vitro assays measuring the levels of certain secondary messengers or the recruiting of proteins involved in signaling cascades to the receptors.

Because of the known correlation between intrinsic activity and the ratio of agonist affinities towards high- and low-affinity receptor states, it is often assumed to be self-evident that agonists preferentially bind to the high-affinity state. However, due to the existence of non-canonical signaling pathways, agonism does not necessarily imply preferential binding to receptor-G-protein complexes. One example is cariprazine, a drug which was recently labeled with carbon-11 and evaluated as a dopamine $D_{2/3}$ receptor tracer. This compound showed partial $D_{2/3}$ agonist activity in secondary messenger assays, but did not recruit G-proteins in vitro [75–77]. Observations of G-protein recruitment may also differ between in vitro setups. For instance, [^{11}C]CUMI-101, a tracer for serotonin 5-HT_{1A} receptors, was defined as an agonist based on the [^{35}S]GTPγS assay (indirect measurement of G-protein recruiting to the receptors) in membrane homogenates from cell cultures expressing recombinant human receptors, but was later found to act as an antagonist when the same assay was done in primate and rat brain homogenates [78,79].

Therefore, the most certain proof of the agonist radioligand's preferential binding to the high-affinity state is directly demonstrating that it recognizes high- and low- affinity states of its receptor in natural tissue or in transfected cell culture. It is worth noting that for some agonist tracers, confirmation of preferential binding to Rhigh in vitro followed in vivo evaluation (compare [80] and [27]), while for some others the capability to discern affinity states in vitro was not assessed at all (see e.g. [81,82]).

4.2. In vivo evaluation of PET neuroreceptor tracers

Characteristics desirable for a PET tracer for brain imaging include the ability to pass the blood-brain-barrier, a low degree of metabolism, a high contrast between target (specific) and non-target (non-specific) binding, and pharmacokinetics that can be reliably quantified from a 60–90 minute-long PET scan (see e.g. [83–85] for review). Measuring synaptic neurotransmis-

sion is an important application in brain imaging, therefore neuroreceptor tracers are tested for the sensitivity of their binding to endogenous neurotransmitters, and agonists are supposed to be superior to antagonists in this regard.

Neuroreceptor tracers are usually evaluated in rodents or non-human primates before being moved to human studies. In non-human primates, one can investigate the binding of the tracers with high spatial detail using clinical PET cameras. Evaluation in rodents is cheaper and enables the use of more invasive methods, but differences in rodent and primate physiology can be a confounding factor when the results are extrapolated to humans. In addition, the small size of rodents forces the researchers to use dedicated non-clinical "micro-PET" cameras and does not permit to reliably image minor brain structures. In order to strike the right balance between controllability of the experimental conditions and image quality, tracers are sometimes evaluated in (relatively) large mammals, such as cats or pigs.

4.3. Availability of agonist PET neuroreceptor tracers

Of the available agonist PET tracers, three are actively used in clinical research: [^{11}C](+)PHNO for the imaging of dopamine $D_{2/3}$ receptors, [^{11}C]carfentanil for the imaging of μ-opioid receptors and [^{18}F]FP-TZTP for the imaging of muscarinic acetylcholinic M_2 receptors [71,86,87]. For all of them, however, agonism is not considered the primary advantage. [^{11}C](+)PHNO is the tracer currently considered the most sensitive to endogenous dopamine levels, for reasons probably related to its agonism, but it appears to be more prized for its preferential (though not selective) binding to D_3 receptors, compared to existing non-subtype-selective $D_{2/3}$ antagonist ligands like [^{11}C]raclopride [88]. [^{11}C]carfentanil and [^{18}F]TZTP are the only tracers available for the corresponding receptor subtypes, so there are no antagonist tracers with which they could be compared head-to-head.

Other agonist tracers for neuroreceptors can be separated into three categories. The first category includes tracers that have seen no or little use simply because they have been developed only recently. The biggest progress is achieved for the serotonin 5-HT_{1A} receptor tracer [^{11}C]CUMI-101, the 5-HT_{2A} receptor tracer [^{11}C]CIMBI-36 and the κ-opioid receptor tracer [^{11}C]GR103545, which have already been successfully evaluated in humans [89–93]. Other agonists are the dopamine $D_{2/3}$ tracer [^{18}F]MCL-524, the D_2-selective tracer [^{11}C]SV-III-130, the putatively D_3-selective tracer

[^{18}F]7-OH-FHXPAT, the serotonin 5-HT_{1A} receptor tracers [^{18}F]FECUMI-101, [^{18}F]F13714 and [^{18}F]F13640, the μ/κ opioid receptor tracers [^{11}C]PEO and [^{18}F]FE-PEO, and, finally, the κ-opioid tracers [^{11}C]FEKAP, [^{11}C]FKAP and ^{11}C]DKAP [94–104]. Note that this category includes a number of ^{18}F-versions of previously developed ^{11}C-tracers, because the longer half-life of fluorine-18 makes such tracers more suitable for wide scale clinical use.

The second category contains tracers with decent imaging properties that have been eclipsed by their newer more successful derivatives. Such are the $D_{2/3}$ tracers [^{11}C]5-OH-DPAT, [^{18}F]FPPAT, [^{11}C](−)NPA and [^{11}C]MNPA that are eclipsed by [^{11}C](+)PHNO, the 5-HT_{1A} tracer [^{18}F]F15599 which is considered inferior to [^{18}F]F13640 and [^{18}F]F13714, [^{11}C]CIMBI- 5 which is replaced by [^{11}C]CIMBI-36, and [^{18}F]sufentanil which was created as a longer half-life alternative to [^{11}C]carfentanil but was not developed further [80,105–111].

Tracers from the third category are tracers with issues that hamper their routine application for research. For instance, two known tracers for $D_{1/5}$ dopamine receptors, (*R*)-[^{11}C]SKF82957 and (*S*)-[^{11}C]N-methyl-NNC 01-0259 [112,113], form lipophilic metabolites that penetrate into the brain and confound the interpretation of the results, though this can be remedied by inhibiting catechol-O-methyl transferase activity [114]. Tests of (*S*)-[^{11}C]N-methyl-NNC 01-0259 sensitivity to endogenous dopamine levels yielded a negative result [115]. This halted further development of this tracer, although known $D_{1/5}$ antagonist tracers are also insensitive to dopamine levels [116]. The D_3-selective agonist tracer [^{18}F]LS-3-134 was shown to specifically bind to D_3 receptors in monkey brain, but specific binding was only measurable under dopamine depletion conditions [117]. The muscarinic M_1 receptor tracer [^{11}C]AF-150(*S*) showed both specific binding and sensitivity to endogenous acetylcholine levels in rats, but the low signal-to-noise ratios of this ligand cast doubt on its suitability for further research [118,119].

In order to demonstrate the preferential binding of agonist tracers to receptor high-affinity state, a head-to-head comparison with reference tracers binding to all receptors (i.e. antagonist tracers) is required. For $D_{1/5}$, $D_{2/3}$, 5-HT_{1A} and 5-HT_{2A} agonist tracers, counterpart antagonist tracers are available, which possess matching pharmacological selectivities (i.e. bind with similar relative affinities to the same receptor subtypes within the relevant region of interest as their “corresponding” agonist tracers) and, in case of $D_{2/3}$ and 5-HT_{2A} ligands, sensitivity to endogenous neurotransmitter levels [50,116,120,121]. The same is true for the κ-opioid agonist [^{11}C]GR103545,

which was developed along with its antagonist counterpart [^{11}C]LY2795050 [122], and for the μ/κ-opioid agonist [^{11}C]PEO, which can be used in conjunction with the μ-partial agonist and κ-antagonist [^{11}C]buprenorphine [101]. For the μ-opioid agonist [^{11}C]carfentanil, the M_2 agonist [^{18}F]FP-TZTP and the M_1 agonist [^{18}F]AF-150(*S*) there are no suitable antagonist counterparts [123,124]. In theory, non-selective antagonists can be used for head-to-head comparison with concomitant blockade of receptors to which the antagonist, but not the agonist, binds, but the reliability of such experimental schemes in vivo is questionable because of the possible pharmacological effects of such blockade.

In conclusion, agonist tracers with favorable imaging characteristics are available for dopamine $D_{2/3}$, serotonin 5-HT_{1A} and 5-HT_{2A}, μ and κ-opioid and muscarinic M_2 receptors. Agonist tracers for dopamine $D_{1/5}$ and muscarinic M_1 receptors have issues that make their use for PET imaging problematic. Preference for the high-affinity state in vitro has only been directly demonstrated for $D_{1/5}$ and $D_{2/3}$ tracers, some 5-HT_{1A} tracers and the M_1 tracer [^{18}F]AF-150(*S*). Agonist tracers for $D_{2/3}$, 5-HT_{1A}, 5-HT_{2A} and κ-opioid receptors can be matched with antagonist tracers binding to the same receptors for head-to-head comparisons.

Table 1. Agonist tracers developed for the imaging of high-affinity state of neuroreceptors.

Receptor(s)	Tracer name	In vitro evaluation		In vivo evaluation					Remarks
		ago-nism proven by[a,b]	preference for Rhigh proven by[c]	rodents	non-human primates	other animals	humans	sensitive to endogenous neurotrans-mitter levels[d]	
Dopamine $D_{1/5}$	(*S*)(+)[^{11}C]SKF82957	–[e]	COMP+[e] GTPdis+ [125]	rats [114, 126, 127]	–	–	–	rats – [114]	lipophilic metabolites in brain tissue
	(*S*)[^{11}C]NNC 01-0259	MESS+ [115]	–	–	[113, 128, 129]	–	–	primates – [115]	lipophilic metabolites in brain tissue
Dopamine $D_{2/3}$	[^{11}C]PHNO	–	GTPdis+ [130] COMP+ [131] SAT– [132]	rats [71, 133, 134]	[135]	cats [136]	[137] (first)	rats + [71, 133, 134] cats + [136] Primates + [138] humans + [139, 140]	now primarily used as D_3-selective tracer [88] derivation of ^{18}F-version unsuccessful [141]

(continued on the next page)

Table 1 (continuation). Agonist tracers developed for the imaging of high-affinity state of neuroreceptors.

Receptor(s)	Tracer name	In vitro evaluation		In vivo evaluation					Remarks
		ago-nism proven by[a,b]	preference for Rhigh proven by[c]	rodents	non-human primates	other animals	humans	sensitive to endogenous neurotrans-mitter levels[d]	
Dopamine $D_{2/3}$	[^{11}C]NPA	–	COMP+ [55, 131]	rats [107]	[107, 142, 143]	cats [136] pigs [144]	[145] (first)	cats + [136] primates + [143] humans + [146]	relatively difficult radiosynthesis
	[^{11}C]MNPA	–	COMP+ [27] SAT– [132]	mice [43, 147] rats [148]	[80, 149–153]		[154] (first)	rats + [148] mice + [43] primates + [152]	lowest signal-to-noise among $D_{2/3}$ tracers used in humans
	[^{18}F]MCL-524	–	COMP+ [155]	–	[94]	–	–	primates + [94]	structurally related to NPA and MNPA
Dopamine D_2	[^{11}C]SV-III-130	MESS+ [95]	–	–	[95]	–	–	primates + [95]	possible 5-HT_{1A} binding

(continued on the next page)

Table 1 (continuation). Agonist tracers developed for the imaging of high-affinity state of neuroreceptors.

Receptor(s)	Tracer name	In vitro evaluation		In vivo evaluation					Remarks
		ago-nism proven by[a,b]	preference for Rhigh proven by[c]	rodents	non-human primates	other animals	humans	sensitive to endogenous neurotrans-mitter levels[d]	
Dopamine D_3	[^{18}F]LS-3-134	MESS+ [117]	COMP– [156]	–	[117]	–	–	primates + [117]	specific binding seen only after dopamine depletion
	[^{18}F]7-OH-FHXPAT	–	GTPdis+ [96]	mice, rats [96]	–	–	–	–	D_3-over-D_2 selectivity not fully characterized
Serotonin 5-HT_{1A}	[^{11}C]CUMI-101	GT-Prec– [79] GTPrec± [78]	–	–	[69, 157]	–	[70, 89]	rodents – [158] primates + [159] humans – [160] humans ± [161]	agonist at human recombinant receptors, antagonist at native rat receptors [78] possibly binds adrenoceptors [79] derivation of ^{18}F-version successful [97, 162]

(continued on the next page)

Table 1 (continuation). Agonist tracers developed for the imaging of high-affinity state of neuroreceptors.

Receptor(s)	Tracer name	In vitro evaluation		In vivo evaluation					Remarks
		ago-nism proven by[a,b]	preference for Rhigh proven by[c]	rodents	non-human primates	other animals	humans	sensitive to endogenous neurotrans-mitter levels[d]	
Serotonin 5-HT$_{1A}$	[^{18}F]F13714	GTPrec+ MESS+ [163]	GTPdis+ [98]	rats [98]	[99]	cats [98] marmo-sets [164]	–	–	specific binding is irreversible
	[^{18}F]F13640	GTPrec+ [165]	–	rats [100]	–	cats [100]	–	–	
Serotonin 5-HT$_{2A}$	[^{11}C]CIMBI-36	MESS+ [81]	–	rats, mice (only safety) [166]	[167]	pigs [81]	[90, 91]	pigs + [168]	also binds 5-HT$_{2C}$ [167] derivation of ^{18}F-version unsuccessful [169]
k-opioid	[^{11}C]GR103545 also known as (*R*)-[^{11}C]GR89696	PHYS+ (for k	COMP± [170]	mice [171] (race-mate) [172] (euto-mer)	[67, 68, 173]	–	[92,93]	–	competition assay shows biphasic binding, but this may reflect different affinities for k

(continued on the next page)

Table 1 (continuation). Agonist tracers developed for the imaging of high-affinity state of neuroreceptors.

Receptor(s)	Tracer name	In vitro evaluation		In vivo evaluation					Remarks
		ago-nism proven by[a,b]	preference for Rhigh proven by[c]	rodents	non-human primates	other animals	humans	sensitive to endogenous neurotrans-mitter levels[d]	
μ-opioid	[^{11}C]carfentanil (mu-OR)	PHYS+ [174]	–	mice [175] rats [42]	[86]	–	[86] (first)	rats + [42] humans + [176–178] humans – [179]	derivation of ^{18}F-version successful, no follow-up [110]
μ/k-opioid	[^{11}C]PEO	GTPrec+ [101]	–	rats [101]	–	–	–	–	derivation of ^{18}F-version successful [102, 180]
Muscarinic M_1	[^{11}C]AF-150(*S*)	–	COMP+ [19]	rats [118, 119]	–	–	–	rats ± [119]	low signal-to-noise ratios
Muscarinic M_2	[^{18}F]FP-TZTP	PHYS+ [181]	–	mice [182] rats [87, 183, 184]	pri-mates, [183]	–	[185] (first)	primates + [186]	^{11}C version created, no follow-up [187]

(continued on the next page)

Table 1 (continuation). Agonist tracers developed for the imaging of high-affinity state of neuroreceptors.

a Coding of experimental paradigms aiming to confirm agonism: MESS – monitoring secondary messenger levels in functional assays in vitro; GTPrec –monitoring GTP recruitment to G-proteins in vitro; PHYS – monitoring physiological or behavioral effects of the compound in vivo or ex vivo.
b Works confirming functional agonism are cited only if the preference for Rhigh has not been directly confirmed.
c Coding of experimental paradigms aiming to confirm preferential binding to Rhigh: COMP – obtaining a biphasic competition curve in vitro; SAT –obtaining a biphasic saturation curve in vitro; GTPdis – detecting the loss of specific binding upon GTP or GppNHp addition in vitro.
d Coding of the outcomes of studies confirming sensitivity to endogenous neurotransmitter levels (and also agonism and Rhigh preference): + positive outcome, – negative outcome, ± ambiguous results.
e No data available.

5. Proving the existence of the high-affinity state in vivo

5.1. Outcome measures of in vivo experiments

In vivo experiments with neuroreceptor radioligands measure the availability of the receptors and changes in this availability in response to alterations of endogenous neurotransmitter levels or administration of exogenous drugs. Binding potentials and target/nontarget ratios are "raw" measures representing receptor availability, which can later be recalculated to receptor densities or occupancies.

5.1.1. Binding potentials

The typical outcome measure of in vivo imaging experiments is the binding potential (BP), which is derived from the time-activity curves measured for the tissue of interest and blood plasma or other reference tissue using kinetic modeling approaches [188]. Binding potential represents a product of available binding site density (B_{max}) and radioligand affinity to the binding sites (inverse of the dissociation constant, $1/K_d$) and is equal to the ratio of the concentrations of specifically bound and free ligand in the tissue at equilibrium provided that radioligand dose is low enough (see Appendix for more explanation). Note that in vivo not all receptors may be available for binding, as they can be internalized, converted into low-affinity state (for an agonist) or occupied by neurotransmitter, so in the in vivo context the term B_{avail} is more suitable than B_{max}.

Given the difficulty of determining the true concentration of the free ligand in the living tissue, other concentrations proportional to free ligand concentration in tissue are substituted in its place. Specifically bound concentration is related to free plasma concentration (BP_F), total plasma concentration (BP_P) or "non-displaceable" concentration (BP_{ND}), i.e. total concentration of free and non-specifically bound ligand in the tissue [189]. It is reasonable to assume that free ligand concentrations in the plasma and in the interstitial liquid of the brain tissue are equal at equilibrium, so BP_F can be considered the "true" BP.

5.1.2. Target/non-target ratios

When regions of interest are small relative to the PET camera resolution (i.e. subsections of rodent brain) it is often hard to obtain a reliable time-activity curve with high temporal resolution. Also, in situations when a lot

of experimental conditions have to be tested and compared, it is often infeasible to obtain time-activity curves by PET or by killing large groups of animals at different time points. In such situations, one can take advantage of the "pseudo-equilibrium" state, when the concentration ratios between receptor-rich and receptor-free tissues remain constant even as absolute concentrations are changing. For a typical neuroreceptor ligand, one can reasonably expect the pseudo-equilibrium state to be reached within half an hour after injection. Once the time range in which the pseudo-equilibrium exists is validated, specific binding can be quantified from tissue concentrations at a single time point within this time range. Such concentrations can be obtained by ex vivo dissection and radioactivity counting or from a static PET scan. Target/non-target concentration ratios can be used as is or be recalculated to specific binding ratios (SBRs):

$$SBR = \frac{T - NT}{NT} = \frac{T}{NT} - 1,$$

where T and NT are radioligand concentrations in receptor-rich ("target") and receptor-poor ("non-target") regions of interest. Note that in the absence of specific binding SBR = 0, while T/NT = 1.

"Raw" specific binding, i.e. the difference between radioligand concentrations in receptor-poor and receptor-rich regions can also be used as an outcome measure. However, when specific binding is not normalized to the non-specific binding at the same time point, its value is prone to intra-subject variations in pharmacokinetics. Therefore, the use of binding ratios is preferred.

5.1.3. Available receptor density

Available receptor density (B_{avail}) can be estimated in a saturation experiment. Specific binding of a radioligand is determined by two parameters: the density of binding sites in the region of interest (B_{avail}) and the affinity of the radioligand towards these receptors (K_d). To independently estimate these two parameters, specific binding of the ligand (i.e. binding potential or target/non-target ratio) has to be measured at least at two different injected doses (for radiotracers, injected dose is usually varied by changing molar radioactivity). B_{avail} can then be quantified by regression analysis.

5.1.4. Receptor occupancy

Displacement of a tracer from the receptors by a competing ligand can be represented as a decrease in binding site density available to the tracer (B_{avail}). B_{avail} is proportional to BP, so receptor occupancy by unlabeled agonist drug can be calculated as the change in binding potential or target-non-target ratio after drug administration, relative to baseline. The same holds for the occupancy of the receptors by endogenous neurotransmitter, when drugs stimulating neurotransmitter release or depletion are administered.

5.2. Experimental paradigms used to demonstrate the existence of high-affinity state in vivo

In order to demonstrate that agonist tracers preferentially bind to a certain "high-affinity" subset of receptors in vivo three approaches have been used (summarized in Table 2). One approach is to directly measure the available binding site densities for agonist and antagonist tracers and demonstrate that the binding site density available to the agonist is lower. Another is to infer the ratio of high-affinity binding site density to total binding site density from the results of experiments where tracers compete for binding to the receptors with unlabeled ligands. A third approach is to demonstrate that agonist, but not antagonist, binding can be influenced by manipulations of receptor-G-protein coupling.

It is important to emphasize that, in order to compare agonist and antagonist tracers with each other, their pharmacological selectivity profiles (i.e. relative binding affinities towards different receptor subtypes) should be identical within the region of interest used for comparison. Otherwise any detected difference in binding behavior could be attributed to the relative preference of one of the tracers towards a certain receptor subtype.

In principle, all experiments described below can be performed not only with PET tracers labeled with short-lived positron-emitting isotopes, but also with radioligands labeled with long-lived isotopes such as tritium ^{3}H. On the one hand, this makes the experimental paradigm non-translatable to the clinical setup. On the other hand, this enables the use of elegant approaches like the double-tracer study, where radioligands labeled with short-lived (e.g. ^{11}C) and long-lived (e.g. ^{3}H) isotopes are compared head-to-head in the same group of animals [190,191].

Table 2. Experimental paradigms used for the detection of high-affinity state in vivo.

Approach	Experimental paradigm	Minimum ligand set necessary	Minimum number of experimental conditions	Result confirming the presence of high-affinity state in vivo	Shortcomings		Examples
					Risk of pharmacological effects	Other	
binding site density comparison	saturation experiment	labeled antagonist + labeled agonist	4 minimum 2 dose levels per radioligand	lower B_{avail} value for agonist tracer than for antagonist tracer	Y		[136, 158, 192]
	$B_{avail} = BP_F \times K_d$	labeled antagonist + labeled agonist	2 single dose level per radioligand	lower B_{avail} value for agonist tracer than for antagonist tracer	N	requires arterial input with free fraction in plasma, in vitro K_d is likely not equal to in vivo K_d	[69]
	correlation analysis	labeled antagonist + labeled agonist	2 single dose level per radioligand	presence of the main trend with upward or downward deviations from it for certain regions of interests	N	see main text	[69, 91, 164, 167]
	imaging in disorders	labeled antagonist + labeled agonist	4 single dose level per radioligand, imaging in healthy and diseased state	same specific binding for antagonist tracer in control and diseased state, different specific binding for agonist tracer	N	up- or downregulation of high-affinity state has to be demonstrated in vitro	[147, 191]

(continued on the next page)

Table 2 (continuation). Experimental paradigms used for the detection of high-affinity state in vivo.

Approach	Experimental paradigm	Minimum ligand set necessary	Minimum number of experimental conditions	Result confirming the presence of high-affinity state in vivo	Shortcomings		Examples
					Risk of pharmacological effects	Other	
competition studies	in vivo displacement curves	labeled antagonist + unlabeled agonist	5 minimum number of dose levels to distinguish between mono- and bi-phasic curves	displacement curve better explained by biphasic than by monophasic model	Y	large number of dose levels to test	[132, 190, 193, 194]
	neurotransmitter challenge	labeled antagonist + labeled agonist + stimulator of neurotransmitter release or depletion	4 single dose level per radioligand, imaging before and after challenge	greater displacement of agonist tracer by the challenge of same magnitude	Y	see main text	[136, 142, 149]
	exogenous drug challenge	labeled antagonist + labeled agonist + unlabeled agonist	4 single dose level per radioligand, imaging before and after challenge	greater displacement of agonist tracer by the challenge of same magnitude	Y		[132, 150, 190, 195, 196]

(continued on the next page)

Table 2 (continuation). Experimental paradigms used for the detection of high-affinity state in vivo.

Approach	Experimental paradigm	Minimum ligand set necessary	Minimum number of experimental conditions	Result confirming the presence of high-affinity state in vivo	Shortcomings		Examples
					Risk of pharmacological effects	Other	
probing the nature of the high-affinity state	sensitivity to G-protein coupling	labeled antagonist + labeled agonist + agent for G-protein decoupling	4 single dose level per radioligand, imaging before and after G-protein decoupling	G-protein decoupling decreases specific binding for the agonist but not for the antagonist radioligand	N	requires intrathecal or intracerebral injections, does not look at what fraction of total receptors are in the high-affinity state	proof-of-concept presented in [197]

5.2.1. Approach 1: Comparing binding site densities

Saturation study

As explained above, a minimum of two different radioligand doses needs to be tested to estimate binding site density (B_{avail}). More doses will add precision and can reveal potential cooperativity effects or the presence of multiple binding sites with different affinities (e.g. receptor affinity states), provided that radioligand binding to all these sites is distinguishable from non-specific binding. However, published PET studies comparing binding site densities of agonist and antagonist tracers were restricted to two doses [136,192]. Another study used single-timepoint SBRs as outcome measure and built "real" 9–10-point saturation curves [158].

In two-dose PET-based experiments for B_{avail} quantification, the low dose corresponds to the minimum radioligand amount that can be injected, i.e. the "tracer dose", which should occupy 10% or fewer receptors. The high dose is chosen to occupy about two thirds of all receptors [136,192].

Extracting density values from true binding potential measurements

It should be noted that performing a saturation assay with agonist radioligands can lead to unwanted and dangerous pharmacological effects, especially in the case of opioid ligands [67,68].

In a head-to-head comparison of 5-HT_{1A} agonist and antagonist tracers [69], Kumar and co-workers attempted to circumvent this problem by comparing the "true" binding potentials (BP_F) for the two tracers at low injected dose instead of performing a second high-dose scan to independently measure B_{avail} and K_d. Given that $BP_F = B_{avail}/K_d$, B_{avail} can arguably be calculated from the BP_F value using in vitro K_d value for the corresponding tracer. However, there are two problems with this approach. First, in order to calculate BP_F, one needs to obtain arterial input curve and free fraction in plasma for the investigated radioligand, in addition to time-activity curve for the region of interest. Such a large amount of input data makes BP_F prone to experimental errors and biases. Second, the in vivo K_d of the radioligand is not necessarily equal to the in vitro K_d, especially if the latter is measured for receptors from a different animal species or in transfected cells.

Studying correlation between regional binding of agonist and antagonist

Another approach to obtain insight into the relationship between available binding site densities for agonist and antagonist tracers while staying below the "tracer" threshold is to plot the binding potentials or target/non-target ratios measured for an agonist tracer in various brain regions against the corresponding measurements for an antagonist tracer and look at the correlation.

If agonist binding in a certain brain region lies above the main trend on the correlation graph, it suggests that the relative abundance of receptors in the high-affinity state in this region is higher than average, and vice versa.

This approach, however, has many limitations. If the relative abundance of the high-affinity state is drastically different in each region, the correlation graph will be meaningless: there will be no main trend to pinpoint deviations from. If the relative abundance of the high-affinity state is the same in all regions, the correlation graph will be a straight line, revealing no differences in agonist and antagonist binding, and thus no evidence in favor of the existence of the high-affinity state. Therefore, analysis of the correlation between agonist and antagonist binding cannot be the sole method of looking for the existence of high-affinity state, but can be an extra piece of data analysis in experiments based on other paradigms.

Studying agonist binding in disorders presumably caused by high-affinity state dysregulation

In vitro experiments in membrane homogenates suggest that some neurological disorders are accompanied by alterations in the relative abundance of the high-affinity state in a given receptor population, while changes in overall receptor density relative to the healthy condition are either absent or much less pronounced. One example is animal models of psychosis where the high-affinity state of $D_{2/3}$ receptors is upregulated [13,198].

Therefore, another way to demonstrate the existence of high-affinity state in vivo is to show that its upregulation (or downregulation) can be non-invasively detected by agonist tracers. If the relative abundance of high-affinity state is altered, but the overall receptor density remains (relatively) constant, the binding of the agonist, but not of the antagonist tracer will be different in the diseased state relative to the healthy healthy state. Ratios of

BP or SBR values for agonist and antagonist tracers can be used as outcome measures to normalize for possible concomitant alterations in total receptor density [199].

In this paradigm, the binding of each tracer only has to be assessed at a low pharmacologically inactive dose. However, one has to demonstrate that the relative abundance of high-affinity state really differs between healthy and diseased states, using experimental approaches other than PET (typically, in vitro assays). Moreover, in the diseased state, alteration of the relative abundance of the high-affinity state may be accompanied by alterations in other parameters relevant for radioligand binding. For instance, changes in baseline neurotransmitter levels also differentially affect the binding of agonist and antagonist tracers (agonist binding is changed to a greater extent). Concomitant changes in several parameters pressing agonist tracer binding in different directions can offset each other, leading to little or no change in overall apparent receptor availability to the agonist tracer compared to the healthy state.

5.2.2. Approach 2: Studying tracer vulnerability to displacement by unlabeled competitor

One important difference between tracer-drug competition experiments in vitro and in vivo is that in the latter case the concentration of both tracer and drug at the receptors is not constant. While for the radioligand a true equilibrium between its concentrations in blood and brain tissue can be achieved by using bolus-plus-infusion injection scheme, the same is virtually infeasible for the unlabeled drug (tissue concentrations of which are much harder to monitor). Nevertheless, one can usually safely assume that the pharmacokinetics of the competing drug are dose-linear within the investigated dose range, so the degree of displacement of the tracer by the drug, ceteris paribus, is also dose-linear.

Building in vivo displacement curves

In vitro, the high-affinity state is detected by displacing an antagonist radioligand with ever increasing concentrations of unlabeled agonist drug. When the remaining specific binding of the radioligand is plotted against unlabeled agonist concentrations, the displacement is shown to proceed in two phases: agonist first displaces the radioligand from high-affinity sites,

then from low-affinity sites. The same displacement curve can be built in vivo by plotting binding potentials or target/non-target ratios for an antagonist tracer against administered dose of unlabeled agonist drug.

The advantage of this paradigm is that it does not require an agonist radioligand. Antagonist radioligands are much more numerous than agonist radioligands, so displacement curve paradigm is currently applicable to a wider range of receptors than other paradigms mentioned below.

The downside, however, is that the generation of a displacement curve is a laborious undertaking. The shape of the biphasic curve is determined by five parameters: maximum binding level (at no displacement), minimum binding level (full displacement), agonist affinities for high- and low-affinity states and the percentage of receptors in the investigated population configured in the high-affinity state. This means that at least five different dose levels (including zero) have to be used in order to test whether the obtained curve is mono- or biphasic.

Therefore, studies that employed the displacement curve approach typically used specific binding ratios obtained ex vivo at a single time point from large numbers of rodents [132,190], though the use of PET scanning in primates is also reported [193,194]. The actual number of dose levels tested was 6–9 in rodent and 9 in primates.

Comparing vulnerability to displacement by unlabeled agonist

An agonist tracer should be more vulnerable than an antagonist tracer to displacement (or "challenge") by other agonists, because it competes with them for the same subpopulation of receptors. Displacement can be elicited by administering an appropriate agonist drug or by stimulating endogenous neurotransmitter release.

The advantage of using exogenous agonist drugs for displacement is that these drugs can be selected to be subtype-specific and to only occupy the receptor population that is being imaged (or even a defined subset of this population if the tracer binds to more than one receptor subtype).

On the other hand, manipulating neurotransmitter levels has the advantage of being "natural": one looks at the competition of the tracer with the endogenous ligand, the action of which on the receptors is thought to govern the functioning of the brain (see [116] and [50] for reviews). One can also

reasonably expect that the competition will only happen at receptors that are really situated in the synapses. Moreover, neurotransmitter levels can be both increased and decreased relative to the baseline. In the latter case, the expected result is greater increase, rather than greater decrease, of binding for the agonist tracer. However, manipulating neurotransmitter release has its downsides, too. First, the effect-vs-time relationship between the administration of the drug that stimulates a rise or fall in endogenous neurotransmitter level and synaptic receptor occupancy is more complex than when receptors are occupied with exogenous agonist. Second, the released neurotransmitter can act on other receptor subtypes beyond the one being imaged. Third, some drugs used to manipulate neurotransmitter levels are known to manipulate levels of several neurotransmitters at once (e.g., amphetamine stimulates both dopamine and norepinephrine release). The lack of selectivity regarding what neurotransmitter is manipulated and which receptors are occupied can confound the interpretation of cause-and-effect relationships.

If the "tracer condition" is satisfied (radioligands occupy a negligible fraction of all receptors), the ratio of agonist and antagonist radioligand vulnerabilities to displacement by a challenge is a constant value as long as less than 100% of the high-affinity state is occupied as a result of the challenge (Figure 6). Therefore, in theory, a single dose of agonist drug or neurotransmitter level manipulator should provide enough information to compare the vulnerability of agonist and antagonist tracers. In practice, because the actual percentage of receptors in the high-affinity state is unknown, several challenge magnitudes are often tested, resulting in occupancies of up to 100% [132,136,150,190], except in the human studies where the maximum challenge magnitude is limited by ethical considerations [139,146].

An important limitation of the vulnerability comparison paradigm is that the preference for the high-affinity state is not the only factor influencing the vulnerability of the radioligand to displacement by unlabeled drugs. For instance, many preclinical in vivo tracer binding experiments are performed in anesthetized animals, and isoflurane and ketamine anesthesia were found to increase the baseline binding of agonist $D_{2/3}$ tracers, exaggerating the vulnerability of agonist tracers relative to antagonists [152,200]. The mechanism of such selective influence is unclear, although there are reports that anesthetics interfere with receptor-G-protein (un)coupling [201,202] and alter endogenous neurotransmitter levels [203,204]. Furthermore,

$D_{2/3}$-antagonist tracers are known to differ between themselves in the sensitivity to changes in dopamine levels [116,205]. The underlying reasons may be more or less favorable receptor binding kinetics (see [50,206] for discussion) or differences in affinity towards surface and internalized receptors [207,208]. Although a head-to-head comparison of $D_{2/3}$-agonist [^{11}C]MNPA and $D_{2/3}$-antagonist [^{18}F]fallypride in internalization-deficient mice demonstrated that competition with the neurotransmitter is sufficient to explain short-term (though not long-term) changes in binding for both tracers [43], situation can be different for other receptor types [42].

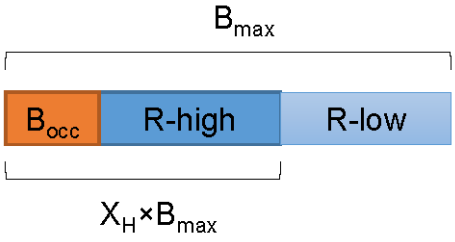

$$\left.\begin{aligned}\Delta B_{Ag} &= 100\% \times \left(-\frac{B_{occ}}{X_H B_{max}}\right), B_{occ} < X_H B_{max} \\ \Delta B_{An} &= 100\% \times \left(-\frac{B_{occ}}{B_{max}}\right)\end{aligned}\right\} \Rightarrow \frac{\Delta B_{Ag}}{\Delta B_{An}} = \frac{1}{X_H}$$

Figure 6. Relationship between agonist and antagonist tracer displacement and the fraction of receptors occupied by competing agonist drug or neurotransmitter.

B_{max} is the total receptor density available at baseline, X_H is the fraction of receptors configured in the high-affinity state, B_{occ} is the amount of receptors occupied as a result of the challenge. Binding potentials or target/nontarget ratios of tracer binding can be considered proportional to the density of receptors not occupied by competitor. If $B_{occ} < X_H B_{max}$, i.e. not all high-affinity state receptors become occupied, the ratio of relative decreases of agonist and antagonist tracer binding is constant and equal to $1/X_H$.

5.2.3. Approach 3: Studying vulnerability to G-protein uncoupling in vivo

Addition of GTP or its analogs decreases specific binding of agonist but not antagonist ligands in vitro, so uncoupling of G-proteins induced in vivo should lead to the same effects.

Seeman demonstrated that GTP addition to tissues extracted from an animal after $D_{2/3}$ agonist radioligand injection accelerates radioligand dissociation from $D_{2/3}$ receptors in the tissue [197] and proposed the use of pertussis toxin to promote G-protein decoupling from the receptors in vivo. Indeed, physiological effects of dopamine and opioid receptor agonists were inhibited by pertussis toxin injections [209–211].

This approach probes the nature of the high-affinity state, that is, it seeks an answer to the question "is G-protein binding to the receptor significant for agonist binding to the receptor?" However, this question is not the same as "do agonists bind to a subset of all receptors?", which is addressed in other paradigms. As discussed in Section 2, all receptors may be pre-coupled to G-proteins. Moreover, G-protein decoupling agents (pertussis toxin or anything else) will have to be introduced locally into the region of interest rather than systemically through intravenous, intraperitoneal or subcutaneous injections. For brain imaging, that means that intrathecal and intracerebral injections will have to be used. Such injections are technically challenging and hardly (if anyhow) translatable to the clinic. Therefore, this paradigm has not yet been used for head-to-head comparisons of agonist and antagonist radioligands.

5.3. Current evidence on the existence of high-affinity state in vivo

5.3.1. Dopamine receptors

The majority of studies attempting to demonstrate the existence of high-affinity state in vivo has concerned dopamine $D_{2/3}$ receptors. Agonists [^{11}C](−)NPA, [^{11}C]MNPA and [^{11}C](+)PHNO were compared with antagonists [^{11}C]raclopride and [^{18}F]fallypride. In some studies these compounds were used in their unlabeled or ^{3}H-labeled forms. A large portion of these studies failed to demonstrate the existence in vivo of the subpopulation of $D_{2/3}$ receptors configured in the high-affinity state (see [212] for review).

Binding site densities for $D_{2/3}$ agonist and antagonist tracers were found to be equal in one study [136], while in another study the average relative abundance of $D_{2/3}$high was found to be 79% [192], which is close to the upper extreme of such percentages determined in vitro [213]. Saturation of [^{11}C](+)PHNO binding in monkey brain was found to be biphasic, but the two binding sites most probably corresponded to D_2 and D_3 receptor subtypes rather than to high- and low- affinity states [214].

In rats with brain lesions induced by 6-hydroxydopamine, binding levels of $D_{2/3}$ antagonist [^{11}C]raclopride and of $D_{2/3}$ agonist [^{3}H]PHNO were increased to the same extent [191]. No difference in baseline agonist binding relative to the healthy condition was found in dopamine beta-hydroxylase knockout (Dβh-KO) mice [147], in rats withdrawn from chronic ethanol and in amphetamine-sensitized rats [191]. In these three animal models, an upregulation of $D_{2/3}$high was previously demonstrated in vitro by the group of Seeman [198,215–217]. However, in vitro measurements of elevated striatal $D_{2/3}$high in Dβh-KO mice could not be replicated by the group that performed the in vivo imaging study [147]. Moreover, most of the data on the elevation of $D_{2/3}$high in ethanol-withdrawn rats is based on comparison of B_{max} values for antagonist radioligands in the presence and absence of GppNHp [198,216]. This is an indirect method of assessing $D_{2/3}$-high abundance, shortcomings of which are discussed in a recent review [213].

In clinical studies of diseases where alteration of $D_{2/3}$high was suspected, binding potentials of agonist tracers in healthy and diseased subjects were identical [199,218–221].

The dopamine $D_{2/3}$ antagonist radioligand raclopride (^{11}C- or ^{3}H-labeled) was displaced by $D_{2/3}$ agonist drugs in a monophasic manner [132,190,193]. In a more recent study, up to 70% of [^{11}C]raclopride binding was displaced by $D_{2/3}$ agonist quinpirole without any evidence of biphasicity [38].

The majority of studies comparing agonist and antagonist tracers' vulnerability to displacement by agonist drugs found no difference in vulnerabilities [132,150,190], though some reports confirming greater vulnerability of agonist tracers do exist [195,196] and the relative timing of tracer and drug administration was claimed to be important [196].

Nevertheless, $D_{2/3}$ agonists did prove to be more sensitive than antagonists to endogenous dopamine levels in anesthetized rodents [43], cats [136] and non-human primates [138,142,149] as well as in awake humans [139,146], though not in awake rodents [132,190,191,200], with a single exception [195]. However, lack of consistency in preclinical data on neurotransmitter and agonist drug challenge raises a question whether this advantage of the agonists stems from their preference for the high-affinity state or from other factors (see 5.2.2).

For dopamine $D_{1/5}$ receptors, an in vivo displacement curve was built in baboons using the D_1 antagonist [^{11}C]NNC-112 and the D_1 agonist drug

DAR-0100A [194]. Occupancies above 40% were not investigated, but the best-fit curve was monophasic, not supporting the existence of a high-affinity receptor subpopulation.

5.3.2. Serotonin receptors

A few head-to-head agonist-antagonist comparisons done with serotonin receptor radioligands yielded ambiguous results.

Two studies found that about 80–90% of the specific binding of antagonist 5-HT_{1A} ligand [^{11}C]WAY-100635 could be displaced by the 5-HT_{1A} agonist 8-OH-DPAT [222,223], but in both cases only a single dose of the agonist was tried, so it's impossible to say whether 8-OH-DPAT displaces [^{11}C]WAY-100635 in a monophasic or a biphasic manner. In an ex vivo saturation study, the binding site density of 5-HT_{1A} agonist [^{3}H]CUMI-101 was 33% lower than that of the antagonist [^{3}H]MPPF in rat frontal cortex, but 82% higher in rat hippocampus [158]. BP_F values for [^{11}C]CUMI-101 across the baboon brain were about 45% of BP_F values for 5-HT1A antagonist [^{11}C]WAY100635 [69], while in vitro K_d values for the two tracers were comparable, but these findings should be interpreted with caution for reasons described in Section 5.2.1. Yet another study found considerable differences between the binding patterns of 5-HT1A agonist [^{18}F]F13174 and 5-HT_{1A} antagonist [^{18}F]MPPF in marmosets: regional BP_{ND} values even did not correlate when animals were imaged without the use of anesthesia [164]. However, the variability of data (especially for [^{18}F]F13174) was high, so it is hard to draw any firm conclusions regarding the existence of separate 5-HT_{1A} receptor subpopulations recognized by [^{18}F]F13174 and [^{18}F]MPPF from this study.

Regional BP_{ND} values of the 5-HT_{2A} agonist [^{11}C]CIMBI-36 were compared with regional BP_{ND} values of the 5-HT_{2A} antagonist [^{11}C]MDL100907 in monkeys [167] and regional BP_{ND} values of another 5-HT_{2A} antagonist [^{18}F]altanserin in humans [91]. Both analyses did yield deviations from linear correlation in the hippocampus and choroid plexus, but these could all be explained by the binding of [^{11}C]CIMBI-36 to 5-HT_{2C} receptors.

To sum up, the majority of data, both for dopamine and serotonin receptors, do not support the existence of a receptor subpopulation in vivo to which agonists preferentially bind. There are some indisputable differences in the behavior of agonist tracers and antagonist tracers, such as specific sensitivity of the former to anesthesia and greater sensitivity to synaptic neurotransmitter levels, but the reason for these differences is not clear.

5.4. Experimental data in the light of the nature of the high-affinity state

Though some instances of failed attempts to detect the high-affinity state in vivo may have resulted from insufficient characterization of the selectivity and intrinsic activity of agonist radioligands [78,79,224], the nature and functioning of the high-affinity state have remained complex and elusive.

Two explanations of the failure to detect high- and low-affinity states in vivo have been put forward. One explanation proposes that all, or almost all, receptors are configured in the high-affinity state in vivo [132] and permanently pre-coupled to G-proteins, so that these G-proteins, at least their Gα subunits, do not dissociate from the receptors after activation [212]. Another explanation states that, whatever the baseline degree of receptor-G-protein pre-coupling, receptors can and do recruit new G-proteins when occupied by agonists, so high agonist concentrations eventually make all receptors bind G-proteins and thus convert to the high-affinity state [190,194]. Indeed, receptors have been subjected to high agonist (drug or neurotransmitter) concentrations in virtually all experimental paradigms used for in vivo detection of the high-affinity state (Table 2). In vivo imaging experiments last for tens of minutes, while time constants for receptor and G-protein activation and for receptor-ligand and receptor-G-protein binding vary from tens of milliseconds to a few seconds [36]. Gradual G-protein recruitment in response to agonist binding can thus confound experimental outcomes in currently used paradigms and can "inflate" the apparent relative abundance of the high-affinity state in vivo. Indeed, in studies comparing the vulnerability of dopamine $D_{2/3}$ agonist and antagonist tracers to drug challenge, the lowest doses of $D_{2/3}$ agonist drugs and the dopamine release stimulator amphetamine (resulting in the lowest receptor occupancies and therefore minimal G-protein recruitment) tended to produce the greatest relative difference between agonist and antagonist tracer displacement (Figure 7). In three such studies, the lowest doses of challenge drugs resulted in zero or negative displacement of the antagonist [^{11}C]/[^{3}H]raclopride but positive (though small and not statistically significant) displacement of agonist tracers [^{11}C]/[^{3}H](+)PHNO and [^{11}C]/[^{3}H]MNPA [132,150,190]. Superior sensitivity of $D_{2/3}$ agonists to amphetamine-induced dopamine release in humans compared to the $D_{2/3}$ antagonist [^{11}C]raclopride was demonstrated at receptor occupancies of 22% or lower [139,146]. Finally, the $D_{2/3}$ agonist [^{3}H]PHNO was found to be more vulnerable than [^{3}H]raclopride to displacement by the ago-

nist (–)NPA when this agonist was co-injected with the radioligands instead of being injected some time before their administration, although this work used non-normalized "raw" specific binding as outcome measure [196].

Comparison of the in vivo imaging results with available in vitro data on detection of the high-affinity state raises even more questions. There are no systematic reviews of in vitro studies assessing the percentage of receptors configured in the high-affinity state for non-dopaminergic receptors. However, recently published reviews dedicated to the affinity states of $D_{2/3}$ receptors [213,225] demonstrate not only the lack of agreement, but also the absence of a trend in the assessments of the abundance of the high-affinity state of $D_{2/3}$ receptors in different set-ups (Figure 8):

(i) Experiments in membrane homogenates from transfected cells and isolated tissues consistently showed that a significant portion of $D_{2/3}$ receptors is configured in the low-affinity state. Only about 20% of dopamine $D_{2/3}$ receptors receptors in the rodent brain and about 30% in the human brain are in the high-affinity state [213].

(ii) No high-affinity state of $D_{2/3}$ receptors could be detected on intact cells. In bovine pituitary membranes, 55% of $D_{2/3}$ receptors were in the high-affinity state, but intact dispersed pituitary cells had only low-affinity state [226]. Similar results were demonstrated with transfected HEK293T and T-REx-293 cells expressing D_2 receptors [27,41]. One study found 16% of D_2 receptors on cultured rat pituitary adenoma cells configured in the high-affinity state using [^{3}H]domperidone as a radioligand [227], but these results have yet to be replicated.

(iii) Autoradiographic studies comparing binding site densities for agonist and antagonist radioligands in tissue slices again revealed the presence of a high-affinity subset of $D_{2/3}$ receptors, but the majority of antagonist radioligand vs agonist drug displacement experiments demonstrated a single high-affinity population of $D_{2/3}$ receptors in tissue slices in vitro [225]. This is in agreement with the data from in vivo imaging (see Section 5.3.1).

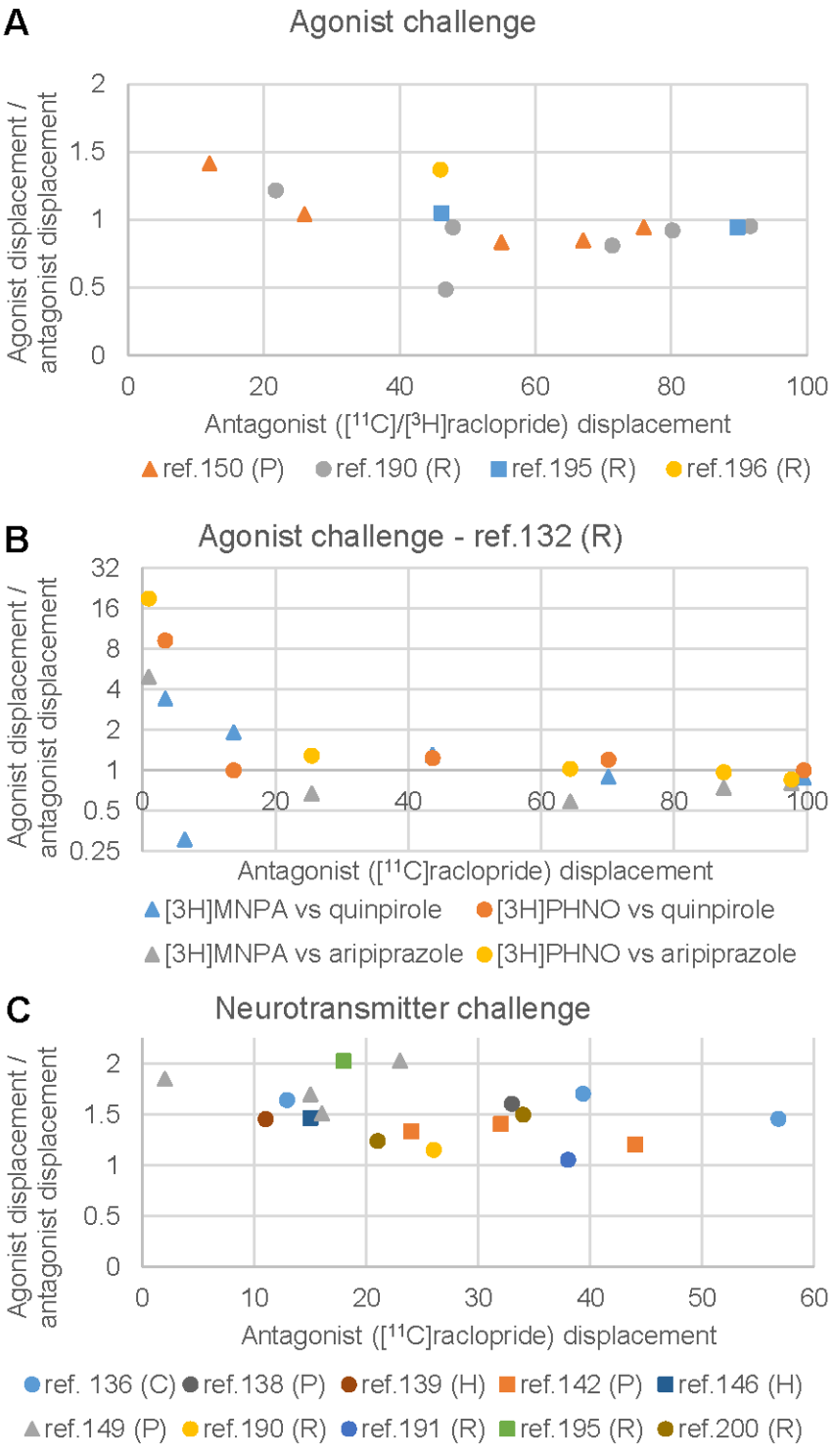
A
Agonist challenge
Agonist displacement / antagonist displacement
2
1.5
1
0.5
0
0
20
40
60
80
100
Antagonist ([11C]/[3H]raclopride) displacement
ref.150 (P)
ref.190 (R)
ref.195 (R)
ref.196 (R)
B
Agonist challenge - ref.132 (R)
Agonist displacement / antagonist displacement
32
16
8
4
2
1
0.5
0.25
0
20
40
60
80
100
Antagonist ([11C]raclopride) displacement
[3H]MNPA vs quinpirole
[3H]PHNO vs quinpirole
[3H]MNPA vs aripiprazole
[3H]PHNO vs aripiprazole
C
Neurotransmitter challenge
Agonist displacement / antagonist displacement
2
1.5
1
0.5
0
0
10
20
30
40
50
60
Antagonist ([11C]raclopride) displacement
ref. 136 (C)
ref.138 (P)
ref.139 (H)
ref.142 (P)
ref.146 (H)
ref.149 (P)
ref.190 (R)
ref.191 (R)
ref.195 (R)
ref.200 (R)

Figure 7 (previous page). Relationship between $D_{2/3}$ receptor occupancy achieved by challenges in vulnerability comparison experiments and the relative difference in displacement of agonist and antagonist tracers in these studies.

A – summary of agonist challenge experiments except [132], B – summary of agonist challenge experiments in [132], C – summary of neurotransmitter (dopamine) challenge experiments. Agonist tracers are [^{11}C]/[^{3}H](–)NPA (squares), [^{11}C]/[^{3}H]MNPA (triangles) and [^{11}C]/[^{3}H](+)PHNO (circles). Experiments were done in rodents (R), cats (C), non-human primates (P) and humans (H).

Data from [132] could not be merged with the other data, because SBRs from control rats in that study were consistently lower than SBRs from rats injected with the lowest doses of displacing drugs, resulting in "negative" displacement values. For graph B, displacement values reported in [132] were zero-corrected by distracting from them the lowest displacement value observed in the whole study.

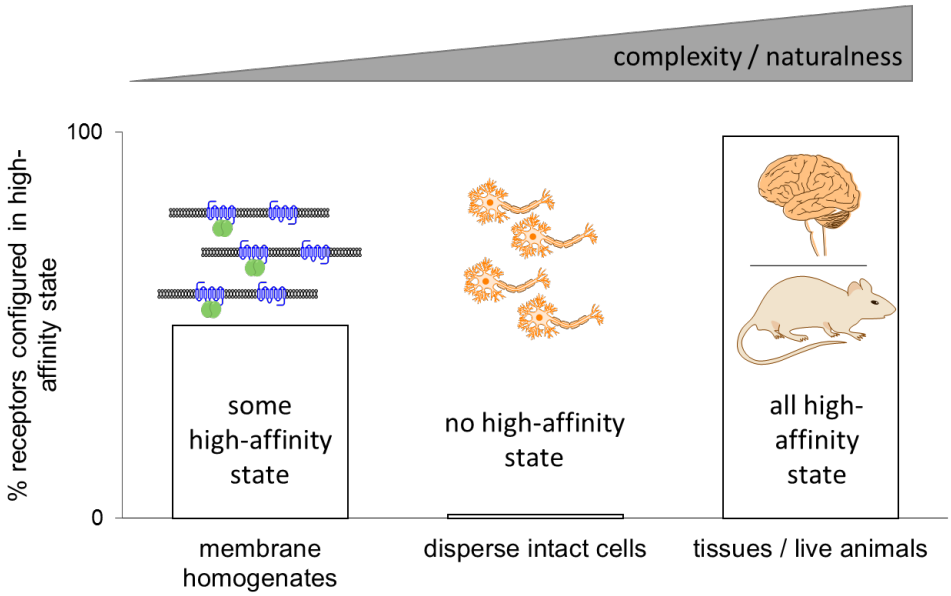

Figure 8. Lack of agreement and contiguousness between assessments of the abundance of receptors configured in high-affinity state in different setups.

For $D_{2/3}$ receptors, a certain percentage of receptors (considerably less than 100%) is known to exist in high-affinity state in membrane homogenates [213]. However, no high-affinity state can be detected at equilibrium in intact cells [27,41,226], while in tissues and living animals all receptors appear to be configured in the high-affinity state [212,225].

In order to explain the low relative abundance of the high-affinity state in membrane homogenates within the pre-coupling model of receptor-G-protein interaction, one can assume that a partial damage of pre-assem-

bled receptor-G-protein complexes happens during membrane preparation, but the exact mechanism of such damage is hard to define. Alternatively, one can assume the existence of a large intracellular reserve of receptors in the high-affinity state. In transfected cells, the affinity of agonist ligands used as PET tracers towards internalized $D_{2/3}$ receptors was shown to be about 2-fold lower than towards surface receptors [41] – a change that would hardly be noticeable in saturation or competition curves. However, the total densities of $D_{2/3}$ receptors measured in membrane homogenates by radioligand binding saturation and in vivo by PET are in good agreement [225], which does not support the existence of extra $D_{2/3}$ receptors that are detectable in vivo but aren't found in membrane homogenates.

The collision coupling model of receptor-G-protein interaction can be reconciled with measurements of the high-affinity state in membrane homogenates if one assumes that in these homogenates only a fraction of the total G-protein pool of the cell is available for recruitment to the receptors. Indeed, the number of G-proteins in living cells is likely equal to or much greater than the number of their cognate receptors [44,228,229]. However, given that G-proteins are anchored to the lipid bilayer [230], it is not clear how such G-protein reserve can both be easily accessible in the living tissue and become inaccessible or lost in membrane homogenates. Especially the findings of Seeman [196] are puzzling in this regard. Seeman reported that the IC_{50} values of (−)NPA in the displacement of bound [^{3}H](+)PHNO and [^{3}H]raclopride in striatal membrane homogenates (with 2-hour equilibration at room temperature before readout) differed much more (~7-fold) when radioligands and (−)NPA were added simultaneously to the membranes than when membranes were pre-incubated with (−)NPA for 30 minutes (~2-fold). Equal vulnerabilities of [^{3}H]raclopride and [^{3}H](+)PHNO in the case of (−)NPA pre-incubation imply that (−)NPA can and does stimulate G-protein recruitment to all or almost all receptors in the membranes, while greater vulnerability of [^{3}H](+)PHNO in case of simultaneous addition implies that in the absence of an agonist, only some receptors are G-protein-bound and therefore accessible to [^{3}H](+)PHNO. However, even in the case of simultaneous addition there is enough time during the equilibration for (−)NPA to elicit recruitment of "spare" G-proteins to the receptors.

The absence of the high-affinity state of $D_{2/3}$ receptors in isolated intact cells [27,41,226] is even harder to reconcile with either of the two models mentioned above. Collision coupling at least provides a theoretical expla-

nation of the disappearance of high-affinity state upon agonist addition due to a high level of GTP in living cells. Still it remains puzzling why an agonist forces $D_{2/3}$ receptors in dispersed cells from a natural tissue (bovine pituitary) to uncouple from G-proteins (convert into the low-affinity state), but promotes G-protein recruitment (conversion to the high-affinity state) when it is acting on the same receptors in intact tissue.

Switching from the G-protein-dependent high-affinity state model to the oligomerization-dependent model leaves the same questions open: it is not clear how the degrees of receptor oligomerization can be different in membranes, dispersed cells and living tissues. Moreover, observation of almost all receptors configured in high-affinity state in vivo is hard to reconcile with the oligomerization-dependent model. At full oligomerization and full agonist occupancy, cooperativity-induced high-affinity state can have relative abundance of no more than 50% (in the case of dimers), and higher values imply that few, if any, receptors are oligomerized.

6. Conclusion

The concept of the high-affinity state postulates that a certain subset of receptors in the living brain is primarily responsible for receptor signaling. Assessing the abundance of this subset is thus potentially very relevant for studies concerning the responses of neurotransmission to pharmacological or physical stimuli and the dysregulation of neurotransmission in neurological disorders.

A number of experimental paradigms has been developed for the estimation of the relative abundance of receptors configured in the high-affinity state. The high-affinity state is preferentially recognized by agonists in vitro, so development of agonist PET tracers as tools for the non-invasive imaging of the high-affinity state has become popular in recent decades.

The greatest number of agonist tracers has been developed for dopamine $D_{2/3}$ receptors, but agonist tracers for dopamine D_1, κ-opioid and muscarinic M_2 receptors are also known, and in recent years, radiolabeled agonists for serotonin 5-HT_{1A} and 5-HT_{2A}, κ-opioid and muscarinic M_1 receptors have appeared. It should be noted, however, that for many of the non-dopaminergic tracers the actual preference for the high-affinity state has not been directly tested, because functional agonism is often assumed to be combined with preferential binding to the high-affinity state.

For dopamine, serotonin and κ-opioid receptors, head-to-head comparisons of agonist and antagonist tracers are now possible, while matching antagonist tracers for muscarinic M_2 and μ-opioid receptors have yet to be developed. Given that, beyond head-to-head agonist-antagonist comparisons, antagonist tracers are also suitable for experiments like displacement curve generation (see Section 5.2.2), development of new antagonist tracers for M_2 muscarinic and μ-opioid receptors with a pharmacological selectivity matching that of existing agonist tracers will arguably be more useful for the assessment of the affinity states of these receptors than development of new agonist tracers.

Agonist tracers appear to be more sensitive to endogenous neurotransmitter challenge, as was originally expected. However, other expectations regarding agonist tracers have not been fulfilled. Agonist imaging did not reveal alterations in the relative abundance of the high-affinity state in neurological disorders. The benefits of agonist tracers for the imaging of receptor occupancies by drugs have also not been proven.

Moreover, though separation of GPCRs into subsets with high- and low-affinity state is consistently observed in membrane homogenates in vitro, data from preclinical and clinical experiments does not support the existence of the high- and low-affinity states in vivo. The majority of these data concerns dopamine $D_{2/3}$ receptors, but some recent results on serotonin receptors paint the same picture.

The relative abundance of the high-affinity state may simply be close to (or equal to) 100%, making the detection of low-affinity state unfeasible. Alternatively, agonist drugs or tracers used for in vivo experiments may inflate the relative abundance of the high-affinity state.

Critical revision of experimental approaches and collection of experimental evidence for non-dopaminergic receptors will help clarify whether the high-affinity state of GPCRs exists in vivo and whether agonist tracers really have advantages over antagonist tracers because of their preferential binding to the high- affinity state.

APPENDIX

Calculation of binding potentials

The ratio of the concentrations of specifically bound tracer (B) and free tracer (F) in the tissue at equilibrium is equal to the ratio of available receptor density and ligand-receptor affinity (B_{max}/K_d) when the tracer only occupies a negligible fraction of all receptors (Figure A1). Therefore, radioligand doses are selected to occupy no more than 10% (preferably less than 1%) of all receptors.

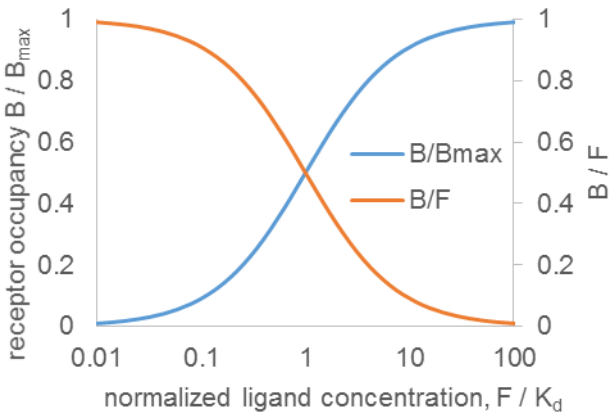

Figure A1. Relationship between the fraction of ligand-occupied receptors and B/F ratio.

At equilibrium, $\frac{BP}{B_{max}} = \frac{F}{F + K_d}$, therefore $\frac{B}{F} = \frac{B_{max}}{F + K_d}$. If $F << K_d$, which inevitably means that $B << B_{max}$, then $\frac{B}{F} \approx \frac{B_{max}}{K_d}$. Note that at low concentrations ($F/K_d << 1$), the ligand occupies only a small part of total receptor population, and the B/F ratio (binding potential) is stable (left part of the graph).

In practice, specifically bound tracer concentration B is often calculated as a difference between tracer concentrations in receptor-rich region of interest and receptor-poor reference region. Free tracer concentration, on the other hand, is replaced with directly measurable concentrations that are linearly dependent on “true” F at equilibrium [189]. These concentrations can be:

– free tracer concentration in plasma (equal to F if the tracer is transferred from tissue to plasma by passive diffusion);

– total, i.e. free and protein-bound, tracer concentration in plasma;

– nondisplaceable, i.e. free and non-specifically bound, tracer concentration in tissue.

To determine tracer concentration in plasma (whether free or total) one needs to obtain arterial plasma samples, which is an invasive procedure. Therefore, the last option is the most popular: tracer concentration in receptor-rich tissue is related to tracer concentration in receptor-poor tissue.

Binding potentials are defined at equilibrium. Plasma and tissue concentrations of a tracer can be directly equilibrated with each other by administering the tracer in an infusion, but such paradigms are hard to implement. Therefore, in most PET and SPECT studies tracer is administered via a simple bolus injection. In that case, in order to calculate binding potentials, time-activity curves for regions of interest are used as input data for so-called kinetic modelling. Tracer distribution is described in terms of its transfer between virtual compartments (like “free tracer”, “non-specifically bound tracer”, “specifically bound tracer”) in accordance with the law of mass action. Compartmental models are then integrated to obtain general equations describing the time course of tracer concentration in each compartment, and the values of individual kinetic parameters or their combinations are determined by curve fitting. Fewer fitting parameters often mean a more robust fit, so many simplifying assumptions are often made. Graphical analyses, simplifying the fitting process to linear regression, are also widely used [231,232]. Fitted parameters are then used to obtain binding potentials, essentially by extrapolating the kinetics observed in the imaging experiments to the situation of equilibrium.

REFERENCES

1. Overington JP, Al-Lazikani B, Hopkins AL. How many drug targets are there? Nat. Rev. Drug Discov. 2006;5:993–6.

2. Deupi X, Standfuss J. Structural insights into agonist-induced activation of G-protein-coupled receptors. Curr. Opin. Struct. Biol. 2011;21:541–51.

3. Sibley DR, De Lean A, Creese I. Anterior pituitary dopamine receptors. Demonstration of interconvertible high and low affinity states of the D_2 dopamine receptor. J. Biol. Chem. 1982;257:6351–61.

4. Leff SE, Hamblin MW, Creese I. Interactions of dopamine agonists with brain D_1 receptors labeled by ^{3}H-antagonists. Evidence for the presence of high and low affinity agonist-binding states. Mol. Pharmacol. 1985;27:171–83.

5. Battaglia G, Shannon M, Titeler M. Guanyl nucleotide and divalent cation regulation of cortical S_2 serotonin receptors. J. Neurochem. 1984;43:1213–9.

6. Gozlan H, Thibault S, Laporte AM, Lima L, Hamon M. The selective 5-HT_{1A} antagonist radioligand [^{3}H]WAY 100635 labels both G-protein-coupled and free 5-HT_{1A} receptors in rat brain membranes. Eur. J. Pharmacol. 1995;288:173–86.

7. Watson J, Collin L, Ho M, Riley G, Scott C, Selkirk J V, et al. 5-HT_{1A} receptor agonist-antagonist binding affinity difference as a measure of intrinsic activity in recombinant and native tissue systems. Br. J. Pharmacol. 2000;130:1108–14.

8. Ehlert FJ. The relationship between muscarinic receptor occupancy and adenylate cyclase inhibition in the rabbit myocardium. Mol. Pharmacol. 1985;28:410–21.

9. Law P, Hom DS, Lohs HH. Multiple Affinity States of Opiate Receptor in Neuroblastoma X Glioma NG108-15 Hybrid Cells. 1985;260.

10. Werling LL, McMahon PN, Cox BM. Selective changes in mu opioid receptor properties induced by chronic morphine exposure. Proc. Natl. Acad. Sci. U. S. A. 1989;86:6393–7.

11. Flynn DD, Weinstein DA, Mash DC. Loss of high-affinity agonist binding to M_1 muscarinic receptors in Alzheimer's disease: implications for the failure of cholinergic replacement therapies. Ann. Neurol. 1991;29:256–62.

12. Ladner CJ, Lee JM. Reduced high-affinity agonist binding at the M_1 muscarinic receptor in Alzheimer's disease brain: differential sensitivity to agonists and divalent cations. Exp. Neurol. 1999;158:451–8.

13. Seeman P, Schwarz J, Chen J, Szechtman H, Perreault M, McKnight GS, et al. Psychosis pathways converge via D_2high dopamine receptors. Synapse. 2006;60:319–46.

14. Seeman P. All roads to schizophrenia lead to dopamine supersensitivity and elevated dopamine D_2high receptors. CNS Neurosci. Ther. 2011;17:118–32.

15. De Lean A, Stadel JM, Lefkowitz RJ. A ternary complex model explains the agonist-specific binding properties of the adenylate cyclase-coupled beta-adrenergic receptor. J. Biol. Chem. 1980;255:7108–17.

16. Kent RS, De Lean A, Lefkowitz RJ. A quantitative analysis of beta-adrenergic receptor interactions: resolution of high and low affinity states of the receptor by computer modeling of ligand binding data. Mol. Pharmacol. 1980;17:14–23.

17. Lahti RA, Figur LM, Piercey MF, Ruppel PL, Evans DL. Intrinsic activity determinations at the dopamine D_2 guanine nucleotide-binding protein-coupled receptor: utilization of receptor state binding affinities. Mol. Pharmacol. ASPET; 1992;42:432–8.

18. Fitzgerald LW, Conklin DS, Krause CM, Marshall AP, Patterson JP, Tran DP, et al. High-affinity agonist binding correlates with efficacy (intrinsic activity) at the human serotonin 5-HT_{2A} and 5-HT_{2C} receptors: evidence favoring the ternary complex and two-state models of agonist action. J. Neurochem. 1999;72:2127–34.

19. Fisher A, Heldman E, Gurwitz D, Haring R, Meshulam H, Brandeis R, et al. New M_1 Agonists: Selective Signaling, Neurotrophic-Like and Cognitive Effects — Implications in the Treatment of Alzheimer's Disease. Alzheimer's Park. Dis. 1995. p. 449–55.

20. Christopoulos A, Kenakin T. G protein-coupled receptor allosterism and complexing. Pharmacol. Rev. 2002;54:323–74.

21. Stein RSL, Ehlert FJ. A kinetic model of GPCRs: analysis of G protein activity, occupancy, coupling and receptor-state affinity constants. J. Recept. Signal Transduct. Res. 2014;0:1–15.

22. Rosenbaum DM, Zhang C, Lyons JA, Holl R, Aragao D, Arlow DH, et al. Structure and function of an irreversible agonist-β_2 adrenoceptor complex. Nature. 2011;469:236–40.

23. Birnbaumer L, Birnbaumer M. Signal transduction by G proteins: 1994 edition. J. Recept. Signal Transduct. Res. 1995;15:213–52.

24. Khelashvili G, Dorff K, Shan J, Camacho-Artacho M, Skrabanek L, Vroling B, et al. GPCR-OKB: The G protein coupled receptor oligomer knowledge base. Bioinformatics. 2010;26:1804–5.

25. Ferré S, Casadó V, Devi LA, Filizola M, Jockers R, Lohse MJ, et al. G protein-coupled receptor oligomerization revisited: functional and pharmacological perspectives. Pharmacol. Rev. 2014;66:413–34.

26. Casadó V, Cortés A, Ciruela F, Mallol J, Ferré S, Lluis C, et al. Old and new ways to calculate the affinity of agonists and antagonists interacting with G-protein-coupled monomeric and dimeric receptors: The receptor-dimer co-operativity index. Pharmacol. Ther. 2007;116:343–54.

27. Skinbjerg M, Namkung Y, Halldin C, Innis RB, Sibley DR. Pharmacological characterization of 2-methoxy-N-propylnorapomorphine's interactions with D_2 and D_3 dopamine receptors. Synapse. 2009;63:462–75.

28. Lopez-Gimenez JF, Villazon M, Brea J, Loza MI, Palacios JM, Mengod G, et al. Multiple Conformations of Native and Recombinant Human 5-Hydroxytryptamine-2A Receptors Are Labelled by Agonists and Discriminated by Antagonists. Mol. Pharmacol. 2001;60:690–9.

29. Orru M, Bakešová J, Brugarolas M, Quiroz C, Beaumont V, Goldberg SR, et al. Striatal pre- and postsynaptic profile of adenosine A_{2A} receptor antagonists. PLoS One. 2011;6.

30. Chidiac P, Green MA, Pawagi AB, Wells JW. Cardiac Muscarinic Receptors. Cooperativity as the Basis for Multiple States of Affinity. Biochemistry. 1997;36:7361–79.

31. Grant M, Collier B, Kumar U. Agonist-dependent dissociation of human somatostatin receptor 2 dimers: a role in receptor trafficking. J. Biol. Chem. 2004;279:36179–83.

32. Patel RC, Kumar U, Lamb DC, Eid JS, Rocheville M, Grant M, et al. Ligand binding to somatostatin receptors induces receptor-specific oligomer formation in live cells. Proc. Natl. Acad. Sci. U. S. A. 2002;99:3294–9.

33. Cottet M, Faklaris O, Maurel D, Scholler P, Doumazane E, Trinquet E, et al. BRET and time-resolved FRET strategy to study GPCR oligomerization: From cell lines toward native tissues. Front. Endocrinol. (Lausanne). 2012;3.

34. Scarselli M, Annibale P, McCormick PJ, Kolachalam S, Aringhieri S, Radenovic A, et al. Revealing G-protein-coupled receptor oligomerization at the

single-molecule level through a nanoscopic lens: methods, dynamics and biological function. FEBS J. 2016;283:1197–217.

35. Gainetdinov RR, Premont RT, Bohn LM, Lefkowitz RJ, Caron MG. Desensitization of G Protein–Coupled Receptors and Neuronal Functions. Annu. Rev. Neurosci. 2004;27:107–44.

36. Lohse MJ, Nuber S, Hoffmann C. Fluorescence/bioluminescence resonance energy transfer techniques to study G-protein-coupled receptor activation and signaling. Pharmacol. Rev. 2012;64:299–336.

37. Krasel C, Vilardaga J-P, Bünemann M, Lohse MJ. Kinetics of G-protein-coupled receptor signalling and desensitization. Biochem. Soc. Trans. 2004;32:1029–31.

38. Sander CY, Hooker JM, Catana C, Rosen BR, Mandeville JB. Imaging Agonist-Induced D_2/D_3 Receptor Desensitization and Internalization In Vivo with PET/fMRI. Neuropsychopharmacology. 2016;41:1427–36.

39. Ko F, Seeman P, Sun WS, Kapur S. Dopamine D2 receptors internalize in their low-affinity state. Neuroreport. 2002;13:1017–20.

40. Sun W, Ginovart N, Ko F, Seeman P, Kapur S. In vivo evidence for dopamine-mediated internalization of D_2-receptors after amphetamine: differential findings with [^{3}H]raclopride versus [^{3}H]spiperone. Mol. Pharmacol. 2003;63:456–62.

41. Guo N, Guo W, Kralikova M, Jiang M, Schieren I, Narendran R, et al. Impact of D_2 receptor internalization on binding affinity of neuroimaging radiotracers. Neuropsychopharmacology. Nature Publishing Group; 2010;35:806–17.

42. Quelch DR, Katsouri L, Nutt DJ, Parker CA, Tyacke RJ. Imaging endogenous opioid peptide release with [^{11}C]carfentanil and [^{3}H]diprenorphine: influence of agonist-induced internalization. J Cereb Blood Flow Metab. 2014;34:1604–12.

43. Skinbjerg M, Liow J-S, Seneca N, Hong J, Lu S, Thorsell A, et al. D_2 dopamine receptor internalization prolongs the decrease of radioligand binding after amphetamine: a PET study in a receptor internalization-deficient mouse model. Neuroimage. Elsevier B.V.; 2010;50:1402–7.

44. Hein P, Bünemann M. Coupling mode of receptors and G proteins. Naunyn. Schmiedebergs. Arch. Pharmacol. 2009;379:435–43.

45. Oldham WM, Hamm HE. Heterotrimeric G protein activation by G-protein-coupled receptors. Nat. Rev. Mol. Cell Biol. 2008;9:60–71.

46. Tolkovsky AM, Levitzki A. Mode of coupling between the β-adrenergic receptor and adenylate cyclase in turkey erythrocytes. Biochemistry. 1978;17:3795–810.

47. Bünemann M, Frank M, Lohse MJ, Bu M. G_i protein activation in intact cells involves subunit rearrangement rather than dissociation. Proc. Natl. Acad. Sci. U. S. A. 2003;100:16077–82.

48. Galés C, Van Durm JJJ, Schaak S, Pontier S, Percherancier Y, Audet M, et al. Probing the activation-promoted structural rearrangements in preassembled receptor-G protein complexes. Nat. Struct. Mol. Biol. 2006;13:778–86.

49. Audet N, Galés C, Archer-Lahlou E, Vallières M, Schiller PW, Bouvier M, et al. Bioluminescence resonance energy transfer assays reveal ligand-specific conformational changes within preformed signaling complexes containing delta-opioid receptors and heterotrimeric G proteins. J. Biol. Chem. 2008;283:15078–88.

50. Finnema SJ, Scheinin M, Shahid M, Lehto J, Borroni E, Bang-Andersen B, et al. Application of cross-species PET imaging to assess neurotransmitter release in brain. Psychopharmacology (Berl). 2015;232:4129–57.

51. Paterson LM, Tyacke RJ, Nutt DJ, Knudsen GM. Measuring endogenous 5-HT release by emission tomography: promises and pitfalls. J. Cereb. Blood Flow Metab. Nature Publishing Group; 2010;30:1682–706.

52. Becker G, Streichenberger N, Billard T, Newman-Tancredi A, Zimmer L. A postmortem study to compare agonist and antagonist 5-HT_{1A} receptor-binding sites in Alzheimer's disease. CNS Neurosci. Ther. 2014;20:930–4.

53. Vidal B, Sebti J, Verdurand M, Fieux S, Billard T, Streichenberger N, et al. Agonist and antagonist bind differently to 5-HT_{1A} receptors during Alzheimer's disease: A post-mortem study with PET radiopharmaceuticals. Neuropharmacology. Elsevier Ltd; 2016;109:88–95.

54. Palner M, Kjaerby C, Knudsen GM, Cumming P. Effects of unilateral 6-OHDA lesions on [^{3}H]-N-propylnorapomorphine binding in striatum ex vivo and vulnerability to amphetamine-evoked dopamine release in rat. Neurochem. Int. Elsevier Ltd; 2011;58:243–7.

55. Seeman P. Antiparkinson therapeutic potencies correlate with their affinities at dopamine D_2High receptors. Synapse. Wiley Online Library; 2007;61:1013–8.

56. Heidrich A, Rösler M. Milameline: Nonselective, Partial Muscarinic Receptor Agonist for the Treatment of Alzheimer's Disease? CNS Drug Rev. 2006;5:93–104.

57. Bruins Slot LA, Kleven MS, Newman-Tancredi A. Effects of novel antipsychotics with mixed D_2 antagonist/5-HT_{1A} agonist properties on PCP-induced social interaction deficits in the rat. Neuropharmacology. 2005;49:996–1006.

58. Newman-Tancredi A, Gavaudan S, Conte C, Chaput C, Touzard M, Verrièle L, et al. Agonist and antagonist actions of antipsychotic agents at 5-HT_{1A} receptors: a [^{35}S]GTPγS binding study. Eur. J. Pharmacol. 1998;355:245–56.

59. Raedler TJ, Bymaster FP, Tandon R, Copolov D, Dean B. Towards a muscarinic hypothesis of schizophrenia. Mol. Psychiatry. 2007;12:232–46.

60. Lever JR. PET and SPECT imaging of the opioid system: receptors, radioligands and avenues for drug discovery and development. Curr. Pharm. Des. 2007;13:33–49.

61. Melichar JK, Hume SP, Williams TM, Daglish MRC, Taylor LG, Ahmad R, et al. Using [^{11}C]diprenorphine to image opioid receptor occupancy by methadone in opioid addiction: clinical and preclinical studies. J. Pharmacol. Exp. Ther. 2005;312:309–15.

62. Hume SP, Lingford-Hughes AR, Nataf V, Hirani E, Ahmad R, Davies AN, et al. Low sensitivity of the positron emission tomography ligand [^{11}C]diprenorphine to agonist opiates. J. Pharmacol. Exp. Ther. 2007;322:661–7.

63. Kodaka F, Ito H, Takano H, Takahashi H, Arakawa R, Miyoshi M, et al. Effect of risperidone on high-affinity state of dopamine D_2 receptors: a PET study with agonist ligand [^{11}C](*R*)-2-CH_3O-N-n-propylnorapomorphine. Int. J. Neuropsychopharmacol. 2011;14:83–9.

64. Seneca N, Finnema SJ, Laszlovszky I, Kiss B, Horváth A, Pásztor G, et al. Occupancy of dopamine D_2 and D_3 and serotonin 5-HT_{1A} receptors by the novel antipsychotic drug candidate, cariprazine (RGH-188), in monkey brain measured using positron emission tomography. Psychopharmacology (Berl). 2011;579–87.

65. Yabaluri N, Medzihradsky F. Reversible modulation of opioid receptor binding in intact neural cells by endogenous guanosine triphosphate. Mol. Pharmacol. 1995;48:690–5.

66. Zubieta JK, Smith YR, Bueller JA, Xu Y, Kilbourn MR, Jewett DM, et al. Regional mu opioid receptor regulation of sensory and affective dimensions of pain. Science. 2001;293:311–5.

67. Talbot PS, Narendran R, Butelman ER, Huang Y, Ngo K, Slifstein M, et al. A Radiotracer for Imaging -Opioid Receptors In Vivo with PET : Synthesis and Evaluation in Baboons. 2005;46:484–94.

68. Tomasi G, Nabulsi N, Zheng M-Q, Weinzimmer D, Ropchan J, Blumberg L, et al. Determination of in vivo B_{max} and K_d for [^{11}C]-GR103545, an agonist PET tracer for κ-opioid receptors: a study in nonhuman primates. J. Nucl. Med. 2013;54:600–8.

69. Kumar JSD, Milak MS, Majo VJ, Prabhakaran J, Mali P, Savenkova L, et al. Comparison of High and Low Affinity Serotonin 1A Receptors by PET In Vivo in Nonhuman Primates. J. Pharmacol. Sci. 2012;0:1–4.

70. Hines CS, Liow J-S, Zanotti-Fregonara P, Hirvonen J, Morse C, Pike VW, et al. Human Biodistribution and Dosimetry of [^{11}C]CUMI-101, an Agonist Radioligand for Serotonin-1A Receptors in Brain. PLoS One. 2011;6:e25309.

71. Wilson AA, McCormick P, Kapur S, Willeit M, Garcia A, Hussey D, et al. Radiosynthesis and evaluation of [^{11}C]-(+)-4-propyl-3,4,4a,5,6,10b-hexahydro-2H-naphtho[1,2-b][1,4]oxazin-9-ol as a potential radiotracer for in vivo imaging of the dopamine D_2 high-affinity state with positron emission tomography. J. Med. Chem. 2005;48:4153–60.

72. Mizrahi R, Houle S, Vitcu I, Ng A, Wilson AA. Side effects profile in humans of [^{11}C]-(+)-PHNO, a dopamine $D_{2/3}$ agonist ligand for PET. J. Nucl. Med. 2010;51:496–7.

73. Searle GE, Beaver JD, Tziortzi A, Comley RA, Bani M, Ghibellini G, et al. Mathematical modelling of [^{11}C]-(+)-PHNO human competition studies. Neuroimage. Elsevier Inc.; 2013;68:119–32.

74. Finnema SJ, Bang-Andersen B, Wikström H V, Halldin C. Current state of agonist radioligands for imaging of brain dopamine D_2/D_3 receptors in vivo with positron emission tomography. Curr. Top. Med. Chem. 2010;10:1477–98.

75. Kiss B, Horvath A, Nemethy Z, Schmidt E, Laszlovszky I, Bugovics G, et al. Cariprazine (RGH-188), a Dopamine D_3 Receptor-Preferring, D_3/D_2 Dopamine Receptor Antagonist-Partial Agonist Antipsychotic Candidate: In Vitro and Neurochemical Profile. J. Pharmacol. Exp. Ther. 2010;333:328–40.

76. Tadori Y, Forbes RA, McQuade RD, Kikuchi T. In vitro pharmacology of aripiprazole, its metabolite and experimental dopamine partial agonists at human dopamine D_2 and D_3 receptors. Eur. J. Pharmacol. Elsevier B.V.; 2011;668:355–65.

77. Tóth M, Varrone A, Steiger C, Laszlovszky I, Horváth A, Kiss B, et al. Brain uptake and distribution of the dopamine D_3/D_2 receptor partial agonist [^{11}C]cariprazine: An in vivo positron emission tomography study in nonhuman primates. Synapse. 2013;67:258–64.

78. Hendry N, Christie I, Rabiner EA, Laruelle M, Watson J. In vitro assessment of the agonist properties of the novel 5-HT_{1A} receptor ligand, CUMI-101 (MMP), in rat brain tissue. Nucl. Med. Biol. Elsevier Inc.; 2011;38:273–7.

79. Shrestha SS, Liow J-S, Lu S, Jenko K, Gladding RL, Svenningsson P, et al. [^{11}C]-CUMI-101, a PET radioligand, behaves as a serotonin 1A receptor antagonist and also binds to α_1 adrenoceptors in brain. J. Nucl. Med. 2014;55:141–6.

80. Finnema SJ, Seneca N, Farde L, Shchukin E, Sóvágó J, Gulyás B, et al. A preliminary PET evaluation of the new dopamine D_2 receptor agonist [^{11}C]MNPA in cynomolgus monkey. Nucl. Med. Biol. 2005;32:353–60.

81. Ettrup A, Hansen M, Santini MA, Paine J, Gillings N, Palner M, et al. Radiosynthesis and in vivo evaluation of a series of substituted 11C-phenethylamines as 5-HT_{2A} agonist PET tracers. Eur. J. Nucl. Med. Mol. Imaging. 2011;38:681–93.

82. Finnema SJ, Bang-Andersen B, Jørgensen M, Christoffersen CT, Gulyás B, Wikström H V, et al. The dopamine D_1 receptor agonist (*S*)-[^{11}C]N-methyl-NNC 01-0259 is not sensitive to changes in dopamine concentration – A positron emission tomography examination in the monkey brain. Synapse. 2013;0.

83. Wong D. Predicting the success of a radiopharmaceutical for in vivo imaging of central nervous system neuroreceptor systems. Mol. Imaging Biol. 2003;5:350–62.

84. Pike VW. PET radiotracers: crossing the blood-brain barrier and surviving metabolism. Trends Pharmacol. Sci. 2009;30:431–40.

85. Van de Bittner GC, Ricq EL, Hooker JM. A philosophy for CNS radiotracer design. Acc. Chem. Res. 2014;47:3127–34.

86. Frost JJ, Wagner HN, Dannals RF, Ravert HT, Links JM, Wilson AA, et al. Imaging opiate receptors in the human brain by positron tomography. J. Comput. Assist. Tomogr. 1985;9:231–6.

87. Kiesewetter DO, Lee J, Lang L, Park SG, Paik CH, Eckelman WC. Preparation of ^{18}F-labeled muscarinic agonist with M_2 selectivity. J. Med. Chem. 1995;38:5–8.

88. Boileau I, Nakajima S, Payer D. Imaging the D_3 dopamine receptor across behavioral and drug addictions: Positron emission tomography studies with [^{11}C]-(+)-PHNO. Eur. Neuropsychopharmacol. Elsevier; 2015;25:1410–20.

89. Milak MS, DeLorenzo C, Zanderigo F, Prabhakaran J, Kumar JSD, Majo VJ, et al. In vivo quantification of human serotonin 1A receptor using [^{11}C]-CUMI-101, an agonist PET radiotracer. J. Nucl. Med. 2010;51:1892–900.

90. Ettrup A, da Cunha-Bang S, McMahon B, Lehel S, Dyssegaard A, Skibsted AW, et al. Serotonin 2A receptor agonist binding in the human brain with [^{11}C]Cimbi-36. J. Cereb. Blood Flow Metab. 2014;34:1188–96.

91. Ettrup A, Svarer C, McMahon B, da Cunha-Bang S, Lehel S, Møller K, et al. Serotonin 2A receptor agonist binding in the human brain with [^{11}C]Cimbi-36: Test-retest reproducibility and head-to-head comparison with the antagonist [^{18}F]altanserin. Neuroimage. Elsevier B.V.; 2016;130:167–74.

92. Tomasi G, Zheng M-Q, Weinzimmer D, Lin S, Nabulsi N, Williams W, et al. Kinetic modeling of the kappa agonist tracer [^{11}C]GR103545 in humans. J. Nucl. Med. 2010;51:1293.

93. Naganawa M, Jacobsen LK, Zheng M-Q, Lin S-F, Banerjee A, Byon W, et al. Evaluation of the agonist PET radioligand [^{11}C]GR103545 to image kappa opioid receptor in humans: Kinetic model selection, test–retest reproducibility and receptor occupancy by the antagonist PF-04455242. Neuroimage. 2014;99:69–79.

94. Finnema SJ, Stepanov V, Nakao R, Sromek AW, Zhang T, Neumeyer JL, et al. [^{18}F]-MCL-524, an ^{18}F-Labelled Dopamine D_2 and D_3 Receptor Agonist Sensitive to Dopamine: A Preliminary PET Study. J. Nucl. Med. 2014;55:1164–70.

95. Xu J, Vangveravong S, Li S, Fan J, Jones LA, Cui J, et al. Positron emission tomography imaging of dopamine D_2 receptors using a highly selective radiolabeled D_2 receptor partial agonist. Neuroimage. Elsevier Inc.; 2013;71:168–74.

96. Mukherjee J, Majji D, Kaur J, Constantinescu CC, Narayanan TK, Shi B, et al. PET radiotracer development for imaging high-affinity state of dopamine D_2 and D_3 receptors: Binding studies of fluorine-18 labeled aminotetralins in rodents. Synapse. 2016 Nov 19;1–15.

97. Majo VJ, Milak MS, Prabhakaran J, Mali P, Savenkova L, Simpson NR, et al. Synthesis and in vivo evaluation of [^{18}F]2-(4-(4-(2-(2-fluoroethoxy)phenyl)piperazin-1-yl)butyl)-4-methyl-1,2,4-triazine-3,5(2H,4H)-dione ([^{18}F]FECUMI-101) as an imaging probe for 5-HT_{1A} receptor agonist in nonhuman primates. Bioorg. Med. Chem. Elsevier Ltd; 2013;21:5598–604.

98. Lemoine L, Becker G, Vacher B, Billard T, Lancelot S, Newman-Tancredi A, et al. Radiosynthesis and preclinical evaluation of [^{18}F]-F13714 as a fluorinated 5-HT_{1A} receptor agonist radioligand for PET neuroimaging. J. Nucl. Med. 2012;53:969–76.

99. Tavares A, Becker G, Barret O, Morley T, Alagille D, Vacher B, et al. Initial evaluation of [^{18}F]F13714, a novel 5-HT_{1A} receptor agonist in non-human primates. Annu. Congr. Eur. Assoc. Nucl. Med. 2013.

100. Vidal B, Fieux S, Billard T, Newman-Tancredi A, Zimmer L. Radiopharmacological evaluation of [^{18}F]F13640, a novel 5-HT_{1A} receptor agonist. J. Nucl. Med. 2014;55:1100.

101. Marton J, Schoultz BW, Hjørnevik T, Drzezga A, Yousefi BH, Wester H-J, et al. Synthesis and evaluation of a full-agonist orvinol for PET-imaging of opioid receptors: [^{11}C]PEO. J. Med. Chem. 2009;52:5586–9.

102. Riss PJ, Hong YT, Marton J, Caprioli D, Williamson DJ, Ferrari V, et al. Synthesis and evaluation of [^{18}F]-FE-PEO in rodents: an 18F-labeled full agonist for opioid receptor imaging. J. Nucl. Med. 2013;54:299–305.

103. Li S, Zheng M-Q, Lin S, Tabriz M, Kim SJ, Carson R, et al. Discovery and in vivo evaluation of novel kappa opioid receptor agonists as PET imaging tracers. J. Nucl. Med. . 2014;55:552.

104. Li S, Zheng M-Q, Lin S, Naganawa M, Gao H, Lara-Jaime T, et al. Novel kappa opioid receptor agonists as improved PET radiotracers: Development and in vivo evaluation. J. Nucl. Med. . 2015;56:5.

105. Mukherjee J, Narayanan TK, Christian BT, Shi B, Dunigan KA, Mantil J. In vitro and in vivo evaluation of the binding of the dopamine D_2 receptor agonist [^{11}C]-(R,S)-5-hydroxy-2-(di-n-propylamino)tetralin in rodents and nonhuman primate. Synapse. 2000;37:64–70.

106. Shi B, Narayanan TK, Christian BT, Chattopadhyay S, Mukherjee J. Synthesis and biological evaluation of the binding of dopamine D_2/D_3 receptor agonist, (R,S)-5-hydroxy-2-(N-propyl-N-(5'-[^{18}F]-fluoropentyl)aminotetralin

([^{18}F]-5-OH-FPPAT) in rodents and nonhuman primates. Nucl. Med. Biol. 2004;31:303–11.

107. Hwang DR, Kegeles LS, Laruelle M. (–)-N-[^{11}C]propyl-norapomorphine: a positron-labeled dopamine agonist for PET imaging of D_2 receptors. Nucl. Med. Biol. 2000;27:533–9.

108. Lemoine L, Verdurand M, Vacher B, Blanc E, Le Bars D, Newman-Tancredi A, et al. [^{18}F]F15599, a novel 5-HT_{1A} receptor agonist, as a radioligand for PET neuroimaging. Eur. J. Nucl. Med. Mol. Imaging. 2010;37:594–605.

109. Ettrup A, Palner M, Gillings N, Santini MA, Hansen M, Kornum BR, et al. Radiosynthesis and evaluation of [^{11}C]-CIMBI-5 as a 5-HT_{2A} receptor agonist radioligand for PET. J. Nucl. Med. 2010;51:1763–70.

110. Henriksen G, Platzer S, Marton J, Hauser A, Berthele A, Schwaiger M, et al. Syntheses, biological evaluation, and molecular modeling of ^{18}F-labeled 4-anilidopiperidines as mu-opioid receptor imaging agents. J. Med. Chem. 2005;48:7720–32.

111. Henriksen G, Platzer S, Hauser A, Willoch F, Berthele A, Schwaiger M, et al. ^{18}F-Labelled sufentanil for PET-imaging of μ-opioid receptors. Bioorg. Med. Chem. Lett. 2005;15:1773–7.

112. DaSilva JN, Wilson AA, Nobrega JN, Jiwa D, Houle S. Synthesis and autoradiographic localization of the dopamine D_1 agonists [^{11}C]SKF 75670 and [^{11}C]SKF 82957 as potential PET radioligands. Appl. Radiat. Isot. 1996;47:279–84.

113. Foged C, Halldin C, Lundkvist C, Karlsson P, Olsson H, Swahn CG, et al. Preparation of the dopamine D_1 agonists [^{11}C]SKF 82957 and [^{11}C]N-methyl-NNC 01–0259 and PET studies in monkeys. J. Label. Compd. Radiopharm. 1997;40:571–3.

114. Palner M, McCormick P, Parkes J, Knudsen GM, Wilson AA. Systemic catechol-O-methyl transferase inhibition enables the D_1 agonist radiotracer R-[^{11}C]SKF 82957. Nucl. Med. Biol. Elsevier Inc.; 2010;37:837–43.

115. Finnema SJ, Bang-Andersen B, Jørgensen M, Christoffersen CT, Gulyás B, Wikström H V, et al. The dopamine D_1 receptor agonist (*S*)-[^{11}C]N-methyl-NNC 01-0259 is not sensitive to changes in dopamine concentration--a positron emission tomography examination in the monkey brain. Synapse. 2013;67:586–95.

116. Laruelle M. Imaging synaptic neurotransmission with in vivo binding competition techniques: a critical review. J. Cereb. Blood Flow Metab. 2000;20:423–51.

117. Mach RH, Tu Z, Xu J, Li S, Jones LA, Taylor M, et al. Endogenous dopamine (DA) competes with the binding of a radiolabeled D_3 receptor partial agonist in vivo: a positron emission tomography study. Synapse. 2011;65:724–32.

118. Buiter H, Leysen J, Fisher A, Huisman M, Knol D, Lammertsma AA, et al. [^{11}C]AF150(*S*): An agonist PET ligand for the M1 muscarinic acetylcholine receptor. J. Nucl. Med. 2010;51:29.

119. Buiter HJ, Windhorst AD, Huisman MC, Yaqub M, Knol DL, Fisher A, et al. [^{11}C]AF150(*S*), an agonist PET ligand for M1 muscarinic acetylcholine receptors. EJNMMI Res. 2013;3:19.

120. Elsinga PH, Hatano K, Ishiwata K. PET tracers for imaging of the dopaminergic system. Curr. Med. Chem. 2006;13:2139–53.

121. Paterson LM, Kornum BR, Nutt DJ, Pike VW, Knudsen GM. 5-HT radioligands for human brain imaging with PET and SPECT. Med. Res. Rev. 2013;33:54–111.

122. Zheng M-Q, Nabulsi N, Kim SJ, Tomasi G, Lin S-F, Mitch C, et al. Synthesis and evaluation of [^{11}C]-LY2795050 as a κ-opioid receptor antagonist radiotracer for PET imaging. J. Nucl. Med. 2013;54:455–63.

123. Tsukada H. PET Imaging of Muscarinic Receptors. PET SPECT Neurobiol. Syst. Berlin, Heidelberg: Springer Berlin Heidelberg; 2014. p. 445–64.

124. van Waarde A, Absalom AR, Visser AKD, Dierckx RAJO. Positron Emission Tomography (PET) Imaging of Opioid Receptors. PET SPECT Neurobiol. Syst. Berlin, Heidelberg: Springer Berlin Heidelberg; 2014. p. 585–623.

125. Neumeyer JL, Baindur N, Niznik HB, Guan HC, Seeman P. (+-)-3-Allyl-6-bromo-7,8-dihydroxy-1-phenyl-2,3,4,5-tetrahydro-1H-3-benzazepine, a new high affinity D_1 dopamine receptor ligand: synthesis and structure-activity relationship. J. Med. Chem. 1991;34:3366–71.

126. DaSilva JN, Wilson AA, Valente CM, Hussey D, Wilson D, Houle S. In vivo binding of [^{11}C]SKF 75670 and [^{11}C]SKF 82957 in rat brain: two dopamine D_1 receptor agonist ligands. Life Sci. 1996;58:1661–70.

127. DaSilva JN, Schwartz RA, Greenwald ER, Lourenco CM, Wilson AA, Houle S. Dopamine D_1 agonist R-[^{11}C]SKF 82957: synthesis and in vivo characterization in rats. Nucl. Med. Biol. 1999;26:537–42.

128. Finnema S, Bang-Andersen B, Farde L, Jørgensen M, Gulyás B, Foged C, et al. PET evaluation of the partial dopamine D_1 receptor agonist radioligands R- and S-[^{11}C]N-Methyl-NNC 01-0259. Neuroimage. 2006;31:T114.

129. Finnema SJ, Bang-Andersen B, Jørgensen M, Gulyás B, Farde L, Wikström HV, et al. COMT inhibition prevents the formation of lipophilic radiometabolites of catechols, — An example with (*S*)-[^{11}C]N-methyl-NNC 01-0259. Neuroimage. 2008;41:T91.

130. Seeman P, Ulpian C, Larsen RD, Anderson PS. Dopamine receptors labeled by PHNO. Synapse. 1993;14:254–62.

131. Seeman P, Ko F, Willeit M, McCormick P, Ginovart N. Antiparkinson concentrations of pramipexole and PHNO occupy dopamine D_2high and D_3high receptors. Synapse. 2005;58:122–8.

132. Peng T, Zysk J, Dorff P, Elmore CS, Ström P, Malmquist J, et al. D_2 receptor occupancy in conscious rat brain is not significantly distinguished with [^{3}H]-MNPA, [^{3}H]-(+)-PHNO, and [^{3}H]-raclopride. Synapse. 2010;64:624–33.

133. Galineau L, Wilson AA, Garcia A, Houle S, Kapur S, Ginovart N. In vivo characterization of the pharmacokinetics and pharmacological properties of [^{11}C]-(+)-PHNO in rats using an intracerebral beta-sensitive system. Synapse. 2006;60:172–83.

134. Egerton A, Hirani E, Ahmad R, Turton DR, Brickute D, Rosso L, et al. Further evaluation of the carbon-11-labeled $D_{2/3}$ agonist PET radiotracer PHNO: Reproducibility in tracer characteristics and characterization of extrastriatal binding. Synapse. 2010;64:301–12.

135. Narendran R, Slifstein M, Guillin O, Hwang Y, Hwang D, Scher E, et al. Dopamine ($D_{2/3}$) receptor agonist positron emission tomography radiotracer [^{11}C]-(+)-PHNO is a D_3 receptor preferring agonist in vivo. Synapse. 2006;60:485–95.

136. Ginovart N, Galineau L, Willeit M, Mizrahi R, Bloomfield PM, Seeman P, et al. Binding characteristics and sensitivity to endogenous dopamine of [^{11}C]-(+)-PHNO, a new agonist radiotracer for imaging the high-affinity state of D_2 receptors in vivo using positron emission tomography. J. Neurochem. 2006;97:1089–103.

137. Willeit M, Ginovart N, Kapur S, Houle S, Hussey D, Seeman P, et al. High-affinity states of human brain dopamine $D_{2/3}$ receptors imaged by the agonist [^{11}C]-(+)-PHNO. Biol. Psychiatry. 2006;59:389–94.

138. Gallezot JD, Kloczynski T, Weinzimmer D, Labaree D, Zheng MQ, Lim K, et al. Imaging Nicotine- and Amphetamine-Induced Dopamine Release in Rhesus Monkeys with [^{11}C]PHNO vs [^{11}C]raclopride PET. Neuropsychopharmacology. 2013;866–74.

139. Shotbolt P, Tziortzi AC, Searle GE, Colasanti A, van der Aart J, Abanades S, et al. Within-subject comparison of [^{11}C]-(+)-PHNO and [^{11}C]raclopride sensitivity to acute amphetamine challenge in healthy humans. J. Cereb. Blood Flow Metab. 2012;32:127–36.

140. Graff-Guerrero A, Willeit M, Ginovart N, Mamo D, Mizrahi R, Rusjan P, et al. Brain region binding of the $D_{2/3}$ agonist [^{11}C]-(+)-PHNO and the $D_{2/3}$ antagonist [^{11}C]raclopride in healthy humans. Hum. Brain Mapp. 2008;29:400–10.

141. Vasdev N, Seeman P, Garcia A, Stableford WT, Nobrega JN, Houle S, et al. Syntheses and in vitro evaluation of fluorinated naphthoxazines as dopamine D_2/D_3 receptor agonists: radiosynthesis, ex vivo biodistribution and autoradiography of [^{18}F]F-PHNO. Nucl. Med. Biol. 2007;34:195–203.

142. Narendran R, Hwang D-R, Slifstein M, Talbot PS, Erritzoe D, Huang Y, et al. In vivo vulnerability to competition by endogenous dopamine: comparison of the D2 receptor agonist radiotracer (–)-N-[^{11}C]propyl-norapomorphine ([^{11}C]NPA) with the D_2 receptor antagonist radiotracer [^{11}C]-raclopride. Synapse. 2004;52:188–208.

143. Narendran R, Slifstein M, Hwang D-R, Hwang Y, Scher E, Reeder S, et al. Amphetamine-induced dopamine release: duration of action as assessed with the $D_{2/3}$ receptor agonist radiotracer (–)-N-[^{11}C]propyl-norapomorphine ([^{11}C]NPA) in an anesthetized nonhuman primate. Synapse. 2007;61:106–9.

144. Cumming P, Gillings NM, Jensen SB, Bjarkam C, Gjedde A. Kinetics of the uptake and distribution of the dopamine $D_{2/3}$ agonist (*R*)-N-(1-[^{11}C])n-propylnorapomorphine in brain of healthy and MPTP-treated Göttingen miniature pigs. Nucl. Med. Biol. 2003;30:547–53.

145. Narendran R, Frankle WG, Mason NS, Laymon CM, Lopresti BJ, Price JC, et al. Positron emission tomography imaging of $D_{2/3}$ agonist binding in healthy human subjects with the radiotracer [^{11}C]-N-propyl-norapomorphine: preliminary evaluation and reproducibility studies. Synapse. 2009;63:574–84.

146. Narendran R, Mason NS, Laymon CM, Lopresti BJ, Velasquez ND, May MA, et al. A comparative evaluation of the dopamine $D_{2/3}$ agonist radiotracer

[^{11}C](–)-N-propyl-norapomorphine and antagonist [^{11}C]raclopride to measure amphetamine-induced dopamine release in the human striatum. J. Pharmacol. Exp. Ther. 2010;333:533–9.

147. Skinbjerg M, Seneca N, Liow J-S, Hong J, Weinshenker D, Pike VW, et al. Dopamine beta-hydroxylase-deficient mice have normal densities of D_2 dopamine receptors in the high-affinity state based on in vivo PET imaging and in vitro radioligand binding. Synapse. 2010;64:699–703.

148. Seneca N, Zoghbi SS, Skinbjerg M, Liow J-S, Hong J, Sibley DR, et al. Occupancy of dopamine $D_{2/3}$ receptors in rat brain by endogenous dopamine measured with the agonist positron emission tomography radioligand [^{11}C]MNPA. Synapse. 2008;62:756–63.

149. Seneca N, Finnema SJ, Farde L, Gulyás B, Wikström H V, Halldin C, et al. Effect of amphetamine on dopamine D_2 receptor binding in nonhuman primate brain: a comparison of the agonist radioligand [^{11}C]MNPA and antagonist [^{11}C]raclopride. Synapse. 2006;59:260–9.

150. Finnema SJ, Halldin C, Bang-Andersen B, Gulyás B, Bundgaard C, Wikström H V, et al. Dopamine $D_{2/3}$ receptor occupancy of apomorphine in the nonhuman primate brain - a comparative PET study with [^{11}C]raclopride and [^{11}C]MNPA. Synapse. 2009;63:378–89.

151. Seneca N, Skinbjerg M, Zoghbi SS, Liow J, Gladding RL, Hong J, et al. Kinetic brain analysis and whole-body imaging in monkey of [^{11}C]MNPA: a dopamine agonist radioligand. Synapse. 2008;62:700–9.

152. Ohba H, Harada N, Nishiyama S, Kakiuchi T, Tsukada H. Ketamine/xylazine anesthesia alters [^{11}C]MNPA binding to dopamine D_2 receptors and response to methamphetamine challenge in monkey brain. Synapse. 2009;63:534–7.

153. Tsukada H, Ohba H, Nishiyama S, Kakiuchi T. Differential effects of stress on [^{11}C]raclopride and [^{11}C]MNPA binding to striatal D_2/D_3 dopamine receptors: A PET study in conscious monkeys. Synapse. 2011;65:84–9.

154. Otsuka T, Ito H, Halldin C, Takahashi H, Takano H, Arakawa R, et al. Quantitative PET analysis of the dopamine D_2 receptor agonist radioligand [^{11}C]-(*R*)-2-CH_3O-N-n-propylnorapomorphine in the human brain. J. Nucl. Med. 2009;50:703–10.

155. Sromek AW, Si Y-G, Zhang T, George SR, Seeman P, Neumeyer JL. Synthesis and Biological Evaluation of N-Fluoroalkyl and 2-Fluoroalkoxy Substituted

Aporphines: Potential PET Ligands for Dopamine D_2 Receptors. ACS Med. Chem. Lett. ACS Publications; 2011;2:189–94.

156. Rangel-Barajas C, Malik M, Taylor M, Neve KA, Mach RH, Luedtke RR. Characterization of [^{3}H]LS-3-134, a novel arylamide phenylpiperazine D_3 dopamine receptor selective radioligand. J. Neurochem. 2014;131:418–31.

157. Kumar JSD, Prabhakaran J, Majo VJ, Milak MS, Hsiung S-C, Tamir H, et al. Synthesis and in vivo evaluation of a novel 5-HT_{1A} receptor agonist radioligand (O-methyl-[^{11}C])2-(4-(4-(2-methoxyphenyl)piperazin-1-yl)butyl)-4-methyl-1,2,4-triazine-3,5(2H,4H)dione in nonhuman primates. Eur. J. Nucl. Med. Mol. Imaging. 2007;34:1050–60.

158. Palner M, Underwood MD, Kumar DJS, Arango V, Knudsen GM, John Mann J, et al. Ex vivo evaluation of the serotonin 1A receptor partial agonist [^{3}H]CUMI-101 in awake rats. Synapse. 2011;65:715–23.

159. Milak MS, Severance AJ, Prabhakaran J, Kumar JSD, Majo VJ, Ogden RT, et al. In vivo serotonin-sensitive binding of [^{11}C]CUMI-101: a serotonin 1A receptor agonist positron emission tomography radiotracer. J. Cereb. Blood Flow Metab. Nature Publishing Group; 2011;31:243–9.

160. Pinborg LH, Feng L, Haahr ME, Gillings N, Dyssegaard A, Madsen J, et al. No change in [^{11}C]CUMI-101 binding to 5-HT_{1A} receptors after intravenous citalopram in human. Synapse. 2012;66:880–4.

161. Selvaraj S, Turkheimer F, Rosso L, Faulkner P, Mouchlianitis E, Roiser JP, et al. Measuring endogenous changes in serotonergic neurotransmission in humans: a [^{11}C]CUMI-101 PET challenge study. Mol. Psychiatry. Nature Publishing Group; 2012;17:1254–60.

162. Kumar JSD, Underwood MD, Simpson NR, Kassir SA, Prabhakaran J, Majo VJ, et al. Autoradiographic Evaluation of [^{18}F]FECUMI-101, a High Affinity 5-HT_{1A}R Ligand in Human Brain. ACS Med. Chem. Lett. 2016;7:482–6.

163. Koek W, Vacher B, Cosi C, Assié MB, Patoiseau JF, Pauwels PJ, et al. 5-HT_{1A} receptor activation and antidepressant-like effects: F 13714 has high efficacy and marked antidepressant potential. Eur. J. Pharmacol. 2001;420:103–12.

164. Yokoyama C, Mawatari A, Kawasaki A, Takeda C, Onoe K, Doi H, et al. Marmoset Serotonin 5-HT_{1A} Receptor Mapping with a Biased Agonist PET Probe [^{18}F]F13714: Comparison with an Antagonist Tracer 18F-MPPF in Awake and Anesthetized States. Int. J. Neuropsychopharmacol. 2016;pyw079.

165. Maurel JL, Autin JM, Funes P, Newman-Tancredi A, Colpaert F, Vacher B. High-efficacy 5-HT_{1A} agonists for antidepressant treatment: A renewed opportunity. J. Med. Chem. 2007;50:5024–33.

166. Ettrup A, Holm S, Hansen M, Wasim M, Santini MA, Palner M, et al. Preclinical safety assessment of the 5-HT_{2A} receptor agonist PET radioligand [^{11}C]Cimbi-36. Mol. Imaging Biol. 2013;15:376–83.

167. Finnema SJ, Stepanov V, Ettrup A, Nakao R, Amini N, Svedberg M, et al. Characterization of [^{11}C]Cimbi-36 as an agonist PET radioligand for the 5-HT_{2A} and 5-HT_{2C} receptors in the nonhuman primate brain. Neuroimage. 2014;84:342–53.

168. Jorgensen LM, Weikop P, Villadsen J, Visnapuu T, Ettrup A, Hansen HD, et al. Cerebral 5-HT release correlates with [^{11}C]Cimbi36 PET measures of 5-HT_{2A} receptor occupancy in the pig brain. J. Cereb. Blood Flow Metab. 2016;

169. Herth MM, Petersen IN, Hansen HD, Hansen M, Ettrup A, Jensen AA, et al. Synthesis and evaluation of ^{18}F-labeled 5-HT_{2A} receptor agonists as PET ligands. Nucl. Med. Biol. 2016;43:455–62.

170. Caudle RM, Mannes AJ, Iadarola MJ. GR89,696 is a kappa-2 opioid receptor agonist and a kappa-1 opioid receptor antagonist in the guinea pig hippocampus. J. Pharmacol. Exp. Theraupeutics. 1997;283:1342–9.

171. Ravert HT, Mathews WB, Musachio JL, Scheffel U, Finley P, Dannals RF. [^{11}C]-methyl 4-[(3,4-dichlorophenyl)acetyl]-3-[(1-pyrrolidinyl)methyl]-1-piperazinecarboxylate ([^{11}C]GR89696): synthesis and in vivo binding to kappa opiate receptors. Nucl. Med. Biol. 1999;26:737–41.

172. Ravert HT, Scheffel U, Mathews WB, Musachio JL, Dannals RF. [^{11}C]-GR89696, a potent kappa opiate receptor radioligand; in vivo binding of the R and S enantiomers. Nucl. Med. Biol. 2002;29:47–53.

173. Schoultz BW, Hjornevik T, Willoch F, Marton J, Noda A, Murakami Y, et al. Evaluation of the kappa-opioid receptor-selective tracer [^{11}C]GR103545 in awake rhesus macaques. Eur. J. Nucl. Med. Mol. Imaging. 2010;37:1174–80.

174. Leysen J, Tollenaere JP, Koch MH, Laduron P. Differentiation of opiate and neuroleptic receptor binding in rat brain. Eur. J. Pharmacol. 1977;43:253–67.

175. Saji H, Tsutsumi D, Magata Y, Iida Y, Konishi J, Yokoyama A. Preparation and biodistribution in mice of [^{11}C]carfentanil: a radiopharmaceutical for study-

ing brain mu-opioid receptors by positron emission tomography. Ann. Nucl. Med. 1992;6:63–7.

176. Henriksen G, Willoch F, Library L, Livermore L. Imaging of opioid receptors in the central nervous system. Brain. 2008;131:1171–96.

177. Colasanti A, Searle GE, Long CJ, Hill SP, Reiley RR, Quelch D, et al. Endogenous opioid release in the human brain reward system induced by acute amphetamine administration. Biol. Psychiatry. Elsevier Inc.; 2012;72:371–7.

178. Mick I, Myers J, Stokes PRA, Erritzoe D, Colasanti A, Bowden-Jones H, et al. Amphetamine induced endogenous opioid release in the human brain detected with [^{11}C]carfentanil PET: replication in an independent cohort. Int. J. Neuropsychopharmacol. 2014;17:2069–74.

179. Guterstam J, Jayaram-Lindström N, Cervenka S, Frost JJ, Farde L, Halldin C, et al. Effects of amphetamine on the human brain opioid system--a positron emission tomography study. Int. J. Neuropsychopharmacol. 2013;16:763–9.

180. Schoultz BW, Hjørnevik T, Reed BJ, Marton J, Coello CS, Willoch F, et al. Synthesis and Evaluation of Three Structurally Related ^{18}F-Labelled Orvinols of Different Intrinsic Activities: 6-O-[^{18}F]Fluoroethyl-diprenorphine ([^{18}F]FDPN), 6-O-[^{18}F]Fluoroethyl-buprenorphine ([^{18}F]FBPN), and 6-O-[^{18}F]Fluoroethyl-phenethyl-orvinol ([^{18}F]FPEO]). J. Med. Chem. 2014;57:5464–9.

181. Sauerberg P, Olesen PH, Nielsen S, Treppendahl S, Sheardown MJ, Honoré T, et al. Novel functional M_1 selective muscarinic agonists. Synthesis and structure-activity relationships of 3-(1,2,5-thiadiazolyl)-1,2,5,6-tetrahydro-1-methylpyridines . J. Med. Chem. 1992;35:2274–83.

182. Jagoda EM, Kiesewetter DO, Shimoji K, Ravasi L, Yamada M, Gomeza J, et al. Regional brain uptake of the muscarinic ligand, [^{18}F]FP-TZTP, is greatly decreased in M_2 receptor knockout mice but not in M_1, M_3 and M_4 receptor knockout mice. Neuropharmacology. 2003;44:653–61.

183. Kiesewetter DO, Carson RE, Jagoda EM, Herscovitch P, Eckelman WC. In vivo muscarinic binding of 3-(alkylthio)-3-thiadiazolyl tetrahydropyridines. Synapse. 1999;31:29–40.

184. Ravasi L, Tokugawa J, Nakayama T, Seidel J, Sokoloff L, Eckelman WC, et al. Imaging of the muscarinic acetylcholine neuroreceptor in rats with the M2 selective agonist [^{18}F]FP-TZTP. Nucl. Med. Biol. Elsevier B.V.; 2011;

185. Podruchny TA, Connolly C, Bokde A, Herscovitch P, Eckelman WC, Kiesewet-

ter DO, et al. In vivo muscarinic 2 receptor imaging in cognitively normal young and older volunteers. Synapse. 2003;48:39–44.

186. Carson RE, Kiesewetter DO, Jagoda E, Der MG, Herscovitch P, Eckelman WC. Muscarinic cholinergic receptor measurements with [^{18}F]FP-TZTP: control and competition studies. J. Cereb. Blood Flow Metab. 1998;18:1130–42.

187. Reid AE, Ding Y-S, Eckelman WC, Logan J, Alexoff D, Shea C, et al. Comparison of the pharmacokinetics of different analogs of ^{11}C-labeled TZTP for imaging muscarinic M_2 receptors with PET. Nucl. Med. Biol. 2008;35:287–98.

188. Mintun MA, Raichle ME, Kilbourn MR, Wooten GF, Welch MJ. A quantitative model for the in vivo assessment of drug binding sites with positron emission tomography. Ann. Neurol. 1984;15:217–27.

189. Innis RB, Cunningham VJ, Delforge J, Fujita M, Gjedde A, Gunn RN, et al. Consensus nomenclature for in vivo imaging of reversibly binding radioligands. J. Cereb. Blood Flow Metab. 2007;27:1533–9.

190. McCormick PN, Kapur S, Seeman P, Wilson AA. Dopamine D2 receptor radiotracers [^{11}C](+)-PHNO and [^{3}H]raclopride are indistinguishably inhibited by D_2 agonists and antagonists ex vivo. Nucl. Med. Biol. 2008;35:11–7.

191. McCormick PN, Kapur S, Reckless G, Wilson AA. Ex vivo [^{11}C]-(+)-PHNO binding is unchanged in animal models displaying increased high-affinity states of the D_2 receptor in vitro. Synapse. 2009;63:998–1009.

192. Narendran R, Hwang D-R, Slifstein M, Hwang Y, Huang Y, Ekelund J, et al. Measurement of the proportion of D_2 receptors configured in state of high affinity for agonists in vivo: a positron emission tomography study using [^{11}C]N-propyl-norapomorphine and [^{11}C]raclopride in baboons. J. Pharmacol. Exp. Ther. 2005;315:80–90.

193. Kortekaas R, Maguire RP, Cremers TI, Dijkstra D, van Waarde A, Leenders KL. In vivo binding behavior of dopamine receptor agonist (+)-PD 128907 and implications for the "ceiling effect" in endogenous competition studies with [^{11}C]raclopride-a positron emission tomography study in Macaca mulatta. J. Cereb. Blood Flow Metab. 2004;24:531–5.

194. Slifstein M, Suckow RF, Javitch JA, Cooper T, Lieberman J, Abi-Dargham A. Characterization of in vivo pharmacokinetic properties of the dopamine D_1 receptor agonist DAR-0100A in nonhuman primates using PET with [^{11}C] NNC112 and [^{11}C] raclopride. J. Cereb. Blood Flow Metab. 2011;31:293–304.

195. Cumming P, Wong DF, Gillings N, Hilton J, Scheffel U, Gjedde A. Specific binding of [^{11}C]raclopride and N-[^{3}H]propyl-norapomorphine to dopamine receptors in living mouse striatum: occupancy by endogenous dopamine and guanosine triphosphate-free G protein. J. Cereb. Blood Flow Metab. 2002;22:596–604.

196. Seeman P. Dopamine D2High receptors measured ex vivo are elevated in amphetamine-sensitized animals. Synapse. 2009;63:186–92.

197. Seeman P. All Roads to Schizophrenia Lead to Dopamine Supersensitivity and Elevated Dopamine D_2High Receptors The Common Target for Antipsychotics Is the Dopamine D_2 Receptor . Neuroscience. 2011;17:118–32.

198. Seeman P, Weinshenker D, Quirion R, Srivastava LK, Bhardwaj SK, Grandy DK, et al. Dopamine supersensitivity correlates with D_2High states, implying many paths to psychosis. Proc. Natl. Acad. Sci. U. S. A. 2005;102:3513–8.

199. Narendran R, Martinez D, Mason NS, Lopresti BJ, Himes ML, Chen C-M, et al. Imaging of dopamine $D_{2/3}$ agonist binding in cocaine dependence: A [^{11}C]NPA positron emission tomography study. Synapse. 2011;65:1344–9.

200. McCormick PN, Ginovart N, Wilson AA. Isoflurane anaesthesia differentially affects the amphetamine sensitivity of agonist and antagonist D_2/D_3 positron emission tomography radiotracers: implications for in vivo imaging of dopamine release. Mol. Imaging Biol. 2011;13:737–46.

201. Aronstam RS, Dennison RL. Anesthetic effects on muscarinic signal transduction. Int. Anesthesiol. Clin. 1989;27:265–72.

202. Ishizawa Y. Mechanisms of anesthetic actions and the brain. J. Anesth. 2007;21:187–99.

203. Finnema SJ, Hughes ZA, Haaparanta-Solin M, Stepanov V, Nakao R, Varnäs K, et al. Amphetamine decreases α_{2C}-adrenoceptor binding of [^{11}C]ORM-13070: a PET study in the primate brain. Int. J. Neuropsychopharmacol. 2014;18:1–10.

204. Whittington RA, Virág L. Isoflurane decreases extracellular serotonin in the mouse hippocampus. Anesth. Analg. 2006;103:92–8, table of contents.

205. Laruelle M. Measuring Dopamine Synaptic Transmission with Molecular Imaging and Pharmacological Challenges: The State of the Art. Neuromethods. 2012. p. 163–203.

206. Morris ED, Yoder KK. Positron emission tomography displacement sensitivity: predicting binding potential change for positron emission tomogra-

phy tracers based on their kinetic characteristics. J. Cereb. Blood Flow Metab. 2007;27:606–17.

207. Ginovart N. Imaging the dopamine system with in vivo [^{11}C]raclopride displacement studies: understanding the true mechanism. Mol. Imaging Biol. 2005;7:45–52.

208. Quelch DR, Withey SL, Nutt DJ, Tyacke RJ, Parker CA. The influence of different cellular environments on PET radioligand binding: An application to $D_{2/3}$-dopamine receptor imaging. Neuropharmacology. 2014;85:305–13.

209. Wong CS, Su YF, Chang KJ, Watkins WD. Intrathecal pertussis toxin treatment attenuates opioid antinociception and reduces high-affinity state of opioid receptors. Anesthesiology. 1992;77:691–9.

210. Self DW, Terwilliger RZ, Nestler EJ, Stein L. Inactivation of G_i and G_o proteins in nucleus accumbens reduces both cocaine and heroin reinforcement. J. Neurosci. 1994;14:6239–47.

211. Fujita N, Nakahiro M, Fukuchi I, Saito K, Yoshida H. Effects of pertussis toxin on D_2-dopamine receptor in rat striatum: evidence for coupling of N_i regulatory protein with D_2-receptor. Brain Res. 1985;333:231–6.

212. Skinbjerg M, Sibley DR, Javitch JA, Abi-Dargham A. Imaging the high-affinity state of the dopamine D_2 receptor in vivo: Fact or fiction? Biochem. Pharmacol. Elsevier Inc.; 2012;83:193–8.

213. van Wieringen J-P, Booij J, Shalgunov V, Elsinga P, Michel MC. Agonist high- and low-affinity states of dopamine D_2 receptors: methods of detection and clinical implications. Naunyn. Schmiedebergs. Arch. Pharmacol. 2013;386:135–54.

214. Gallezot J-D, Beaver JD, Gunn RN, Nabulsi N, Weinzimmer D, Singhal T, et al. Affinity and selectivity of [^{11}C]-(+)-PHNO for the D_3 and D_2 receptors in the rhesus monkey brain in vivo. Synapse. 2012;66:489–500.

215. Seeman P, Tallerico T, Ko F, Tenn C, Kapur S. Amphetamine-sensitized animals show a marked increase in dopamine D_2high receptors occupied by endogenous dopamine, even in the absence of acute challenges. Synapse. 2002;46:235–9.

216. Seeman P, Tallerico T, Ko FF. Alcohol-withdrawn animals have a prolonged increase in dopamine D_2high receptors, reversed by general anesthesia: relation to relapse? Synapse. 2004;52:77–83.

217. Seeman P, McCormick PN, Kapur S. Increased dopamine D_2High receptors in amphetamine-sensitized rats, measured by the agonist [^{3}H](+)PHNO. Synapse. Wiley Online Library; 2007;61:263–7.

218. Graff-Guerrero A, Mizrahi R, Agid O, Marcon H, Barsoum P, Rusjan P, et al. The dopamine D_2 receptors in high-affinity state and D_3 receptors in schizophrenia: a clinical [^{11}C]-(+)-PHNO PET study. Neuropsychopharmacology. 2009;34:1078–86.

219. Suridjan I, Rusjan P, Addington J, Wilson AA, Houle S, Mizrahi R. Dopamine D_2 and D_3 binding in people at clinical high risk for schizophrenia, antipsychotic-naive patients and healthy controls while performing a cognitive task. J. Psychiatry Neurosci. 2013;38:98–106.

220. Boileau I, Payer D, Chugani B, Lobo D, Behzadi A, Rusjan PM, et al. The $D_{2/3}$ dopamine receptor in pathological gambling: a positron emission tomography study with [^{11}C]-(+)-propyl-hexahydro-naphtho-oxazin and [^{11}C]raclopride. Addiction. 2013;108:953–63.

221. Mizrahi R, Suridjan I, Kenk M, George TP, Wilson A, Houle S, et al. Dopamine response to psychosocial stress in chronic cannabis users: a PET study with [^{11}C]-(+)-PHNO. Neuropsychopharmacology. 2013;38:673–82.

222. Farde L, Ginovart N, Ito H, Lundkvist C, Pike VW, McCarron JA, et al. PET-characterization of (carbonyl-[^{11}C])WAY-100635 binding to 5-HT_{1A} receptors in the primate brain. Psychopharmacology (Berl). 1997;133:196–202.

223. Mathis CA, Simpson NR, Mahmood K, Kinahan PE, Mintun MA. [^{11}C]WAY 100635: a radioligand for imaging 5-HT_{1A} receptors with positron emission tomography. Life Sci. 1994;55:PL403-7.

224. Seeman P. Dopamine agonist radioligand binds to both D_2High and D_2Low receptors, explaining why alterations in D_2High are not detected in human brain scans. Synapse. 2012;66:88–93.

225. Cumming P. Absolute abundances and affinity states of dopamine receptors in mammalian brain: A review. Synapse. 2011;65:892–909.

226. Sibley DR, Mahan LC, Creese I. Dopamine receptor binding on intact cells. Absence of a high-affinity agonist-receptor binding state. Mol. Pharmacol. 1983;23:295–302.

227. Seeman P. Dopamine D_2High Receptors on Intact Cells. Synapse. 2008;318:314–8.

228. Ostrom RS, Post SR, Insel PA. Stoichiometry and compartmentation in G protein-coupled receptor signaling: implications for therapeutic interventions involving G_s. J. Pharmacol. Exp. Ther. 2000;294:407–12.

229. González-Maeso J, Rodríguez-Puertas R, Meana JJ. Quantitative stoichiometry of G-proteins activated by mu-opioid receptors in postmortem human brain. Eur. J. Pharmacol. 2002;452:21–33.

230. Gilman AG. G proteins: transducers of receptor-generated signals. Annu. Rev. Biochem. 1987;56:615–49.

231. Logan J, Fowler JS, Volkow ND, Wolf AP, Dewey SL, Schlyer DJ, et al. Graphical analysis of reversible radioligand binding from time-activity measurements applied to (N-[^{11}C]-methyl)-(–)-cocaine PET studies in human subjects. J. Cereb. Blood Flow Metab. 1990;10:740–7.

232. Ichise M, Liow J-S, Lu J-Q, Takano A, Model K, Toyama H, et al. Linearized reference tissue parametric imaging methods: application to [^{11}C]DASB positron emission tomography studies of the serotonin transporter in human brain. J. Cereb. Blood Flow Metab. 2003;23:1096–112.

Chapter 3

Synthesis and Characterization of a Novel Series of Agonist Compounds as Potential Radiopharmaceuticals for Imaging Dopamine $D_{2/3}$ Receptors in Their High-Affinity State

Jan-Peter van Wieringen[1]*, Vladimir Shalgunov[2]*, Henk M. Janssen[3], P. Michel Fransen[3], Anton M.G. Janssen[4], Martin C. Michel[5], Jan Booij[1] and Philip H. Elsinga[2]

1 Department of Nuclear Medicine, Academic Medical Center, University of Amsterdam, Amsterdam, The Netherlands

2 Department of Nuclear Medicine and Molecular Imaging, University Medical Center Groningen, University of Groningen, Groningen, The Netherlands

3 SyMO-Chem BV, Eindhoven, The Netherlands

4 GE Healthcare, Eindhoven, The Netherlands

5 Department of Pharmacology, Johannes Gutenberg University, Mainz, Germany

* These authors contributed equally to this work

(Journal of Medicinal Chemistry 2014;57:391–410)

LIST OF ABBREVIATIONS

AMC – 2-aminomethylchromane

DIPEA – diisopropylethylamine

moleq – molar equivalent

UPLC – ultra performance liquid chromatography

ABSTRACT

Imaging of dopamine $D_{2/3}$ receptors ($D_{2/3}R$) can shed light on the nature of several neuropsychiatric disorders, since $D_{2/3}R$ receptors are involved in these disorders. Agonist $D_{2/3}$ tracers for PET/SPECT imaging are considered superior to antagonists because they are more sensitive to dopamine concentrations and may selectively label the high-affinity receptor state. Carbon-11-labeled $D_{2/3}R$ agonists have been developed but these short-living tracers can only be used in centers with a cyclotron. Here, we report on the development of a series of novel D_2R agonist compounds, based on the 2-aminomethylchroman (AMC) scaffold, which provides ample opportunities for the introduction of the longer living fluorine-18 or iodine-123. Binding experiments showed that several AMC-compounds have high affinity and selectivity for $D_{2/3}R$ and showed agonism. Two fluorinated compounds were ^{18}F-labeled to enable in vitro autoradiography studies in rats, and both displayed specific binding to striatal $D_{2/3}R$. These findings encourage further in vivo evaluations.

INTRODUCTION

A disturbed dopamine system plays a central role in several neuropsychiatric disorders, including Parkinson's disease (PD) [1], dementia with Lewy bodies [2], schizophrenia [3], and drug addiction [4]. The prevalence of PD and schizophrenia is about 1% of the total population [5, 6] while the prevalence of (alcohol) addiction may be even higher [7] creating a large disease burden. For dementia with Lewy body pathology the prevalence among people above the age of 65 years is about 10% [8].

Dopamine receptors belong to the superfamily of G-protein coupled receptors (GPCRs) and are divided into 2 subfamilies based on their action on adenylyl cyclase (AC). The dopamine D_1-like (D_1 and D_5) subfamily stimulates AC to produce the second messenger cyclic adenosine monophosphate (cAMP), while D_2-like receptors (D_2, D_3, D_4) inhibit cAMP production by AC [9,10]. The D_2 and D_3 receptor subtypes are highly involved in the pathophysiology and treatment of PD and schizophrenia and, like other GPCRs, they typically exhibit interconvertible high- and low-affinity states for agonists in vitro [11–13] In the high-affinity state, the receptors are coupled to the G-protein, and this state is considered to be the active form of the receptor [14]. In the low-affinity state, receptors are uncoupled from the G-proteins and, as a result, inactive. There is substantial evidence that alterations in the density of $D_{2/3}$ receptors in the high-affinity state may be more relevant to the pathophysiology of neuropsychiatric disorders than alterations in the total receptor density. This is supported mostly by data from Seeman and co-workers [13]. In several animal models of neuropsychiatric disorders, including psychosis, increases in striatal $D_{2/3}$ high-affinity receptors of up to 9-fold were registered as compared to control animals, while total receptor numbers did not increase [15]. While agonists are selective for the high-affinity state, antagonists bind with equal affinity to the low- and high-affinity states of a receptor [16]. Therefore, antagonist radioligands cannot distinguish a shift in the state of receptors from low- to high-affinity [17]. Numerous compounds have been synthesized and characterized as agonist tracers for the imaging of $D_{2/3}$ in the high-affinity state by means of positron emission tomography (PET) [18]. These compounds are of different chemical classes, including ergolines, aporphines, 2-aminotetralins, benzoquinolines and naphthoxazines. The aporphines [^{11}C]NPA (N-propylnorapomorphine), [^{11}C]MNPA (2-methoxy-N-propylnorapomorphine) and the naphthoxazine [^{11}C]PHNO (4-propyl-9-hydroxynaphthoxazine) turned out to be the most successful and have also been evaluated as PET tracers in man [19,20].

In humans, the agonists [^{11}C]PHNO and [^{11}C]NPA showed better sensitivity for the detection of endogenous dopamine release than the antagonist [^{11}C]raclopride [21–24]. All three mentioned tracers also performed better than [^{11}C]raclopride in dopamine release measurement in rodents, pigs, cats and non-human primates [25]. This corroborates the notion that agonist radiotracers are more prone to detect changes in neurotransmitter concentrations than antagonist tracers. On the other hand, all $D_{2/3}$ agonist PET ligands successfully evaluated in humans are ^{11}C-labeled [19,20]. Because of the short half-life (20.4 minutes) of carbon-11, these radioligands can only be used when a cyclotron is present on-site. This expensive device is however available in only the minority of hospitals. To increase the worldwide availability of such agonist tracers, we are developing fluorine-18-labeled PET tracers (half-life 109.8 min) or iodine-123-labeled (half-life 13.2 h) agonist dopamine $D_{2/3}$ receptor tracers for single photon emission computed tomography (SPECT) imaging. Accordingly, we have prepared and evaluated a new series of agonist compounds based on the 2-aminomethylchroman-7-ol (AMC) scaffold. Structure-activity relationships for this class of compounds and classes related to it [27–31] including the preference for the high-affinity vs low-affinity state of D_2 receptor and selectivity for the D_2 receptor over other potential monoamine receptors such as the serotonin 1A (5-HT_{1A}) and α_1 adrenergic receptor, have already been examined in detail by Mewshaw and co-workers [26]. Importantly, the D_2-affinity and agonism of AMCs shows considerable tolerance to structural modifications in the moiety attached to the nitrogen atom of AMC core, which provides ample opportunities for the introduction of the ^{18}F or ^{123}I-label into the structure without compromising the necessary pharmacological properties. We have used data from the Mewshaw studies to design our AMCs that either bear an iodide or a fluorine atom, see Chart 1. We have included the non-halogenated reference compounds **10a-b** that were already evaluated in vitro by Mewshaw [26], as this enables us to put receptor binding data on the new iodinated (**11**) and fluorinated (**12**) series of compounds into perspective. Introduction of the piperazine group in some of the AMC-structures was inspired by studies on pramipexole [32] and 5-OH-DPAT [33], piperazines that have shown potent and selective D_3-receptor binding, as well as by several Mewshaw studies [27–31].

Chart 1: The (*R*) 2-aminomethylchroman-7-ols (AMCs) that are investigated in this study: reference compounds **10**, the iodide series **11** and the fluoride series **12**. The oxalate salts of the shown amine structures have been used for all assays and binding studies.

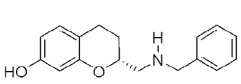

10a

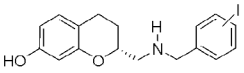

11a: para
11b: metha
11c: ortho

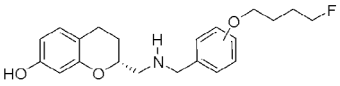

12a: para
12b: ortho

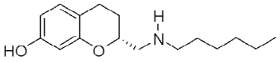

10b

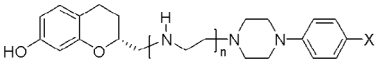

11d: n = 0, X = I
11e: n = 1, X = I

12c: n = 0, X = OCH_2CH_2F
12d: n = 1, X = OCH_2CH_2F

RESULTS

Chemical Synthesis

Scheme 1 outlines the synthetic routes to the prepared 'cold' AMCs, i.e. the unlabeled regular ^{19}F and ^{127}I compounds. Details on specific transformations can be found in the Experimental section. Even though racemates can be used for initial screening receptor binding studies, we have chosen to prepare the enantiomerically pure (*R*)-AMC-compounds, as it is already known that these enantiomers are the actively binding species [26]. Accordingly, the test compounds **10a-b**, **11a-e** and **12a-d** reported in this work are all (*R*)-enantiomers, and they all have been prepared from the same parent compound **1**, i.e. (*R*)-7-hydroxychroman-2-carboxylic acid ethyl ester. The racemate of compound **1** has been prepared from 2,4-dihydroxyacetophenone in two steps, according to Walenzyk [34] and Cohen [35], and thereafter this racemic mixture has been resolved to **1** (the *R*-enantiomer) using the lipase kinetic resolution procedure as reported by Kalaritis [36]. GC-analysis on a chiral capillary column shows for the racemate of **1** two peaks of equal intensity, whereas resolved **1** only shows one peak (e.e. 99%).

Three routes to the AMC target molecule series 10, 11 and 12 have been employed. Route A is via the unprotected tosylate 3, by reaction of 3 with the appropriate amine building blocks. This conveniently short route has been used by Mewshaw [26] also, and we have prepared molecules 10a, 11b and 11d via this Route A. However, we have experienced that yields remain low when using tosylate 3, presumably because 3 can react with itself under basic conditions, as opposed to reacting with the presented amine reactants. Furthermore, the synthesis of 3 in pyridine suffers from side-product formation; where particularly, ditosylate side product has been observed. As an alternative, we have used Route B that proceeds via tosylate 6 that is MOM-protected at the 7 OH-position of the chroman group. Route B is longer, as it requires extra (de)protection steps, but the syntheses have shown to be more reliable. Preparation of 10b, 11a, 11e, 12a, 12c and 12d has been achieved via Route B. The MOM protective group was selected over the methoxy or the benzyloxy group that had been applied by Mewshaw, as the methoxy group requires more harsh deprotection conditions and the benzyloxy group is or may be incompatibile with the (iodo)benzyl target structures. Route B still gave rise to side-product formation, as in the cases where primary amines were reacted with tosylate 6, tertiary amine side-products were formed next to the desired secondary amine main products. We have

therefore also employed Route C, which is the longest route that proceeds via primary amine 8. In this case, a reductive amination coupling step with aldehyde building blocks can be performed, so that side product formation is largely avoided. Molecules 11a, 11c and 12b have been prepared according to Route C. Provided the aldehyde counterpart for preparing the desired AMC target molecule is easily accessible; this Route C is recommended by us. It may even be possible to use the unprotected amine (i.e. amine 8 without the MOM-group) to prepare AMCs, but we have not tested this option. The synthesis of the amine or aldehyde building blocks that are required for coupling to tosylate 3 (Route A), tosylate 6 (Route B) or amine 8 (Route C) are described in the Experimental section, unless these building blocks are simply commercially available. All the test compounds 10, 11 and 12 have been converted to their oxalate salts, and these salt end products have been used in all assays and studies that are described in this paper.

Scheme 1. Synthesis of the unlabeled AMC compounds[a].

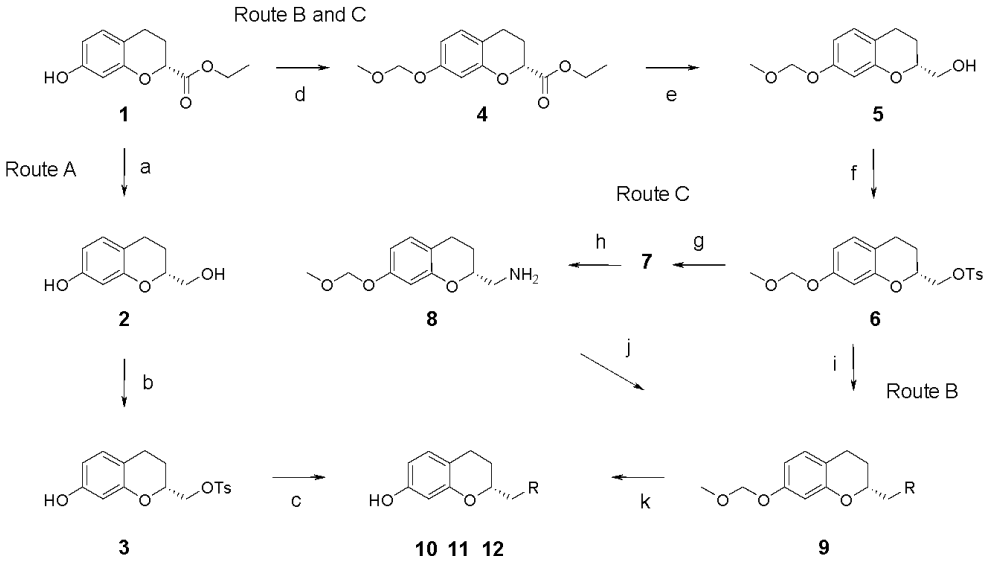

a reagents and solvents: (a) and (e) $LiBH_4$, THF; (b) and (f) TsCl, pyridine; (c) and (i) amine building block, DIPEA, DMSO; (d) MOMCl, DIPEA, CH_2Cl_2; (g) potassium phthalimide, DMF; (h) H_2NNH_2 hydrate, EtOH; (j) i. aldehyde building block, MeOH and ii. $NaBH_4$, MeOH; (k) 4M HCl, dioxane/isopropanol. The R-group in the series of compounds 10, 11 and 12 denotes a secondary or tertiary amine residue; see Chart 1 for details on the specific R-groups that have been used.

Scheme 2 shows the synthetic route to the phenols 13a and 13b, which molecules are the precursors to the radiolabeled compounds [^{18}F]12a and [^{18}F]12d, respectively. The MOM-protected amine 8 has been coupled by reductive amination to 4-hydroxy benzaldehyde to prepare 13a. Commercially available 1-(4-hydroxyphenyl)piperazine has been converted in five steps to the primary amine reactant 18 that can be coupled to tosylate 6 to provide 19. Subsequent debenzylation of 19 affords 13b. Both precursors 13a and 13b require protection at the 7-OH-chroman position, as a selective coupling of the respective [^{18}F]fluoroalkyltosylates to the other phenol moiety is desired. Protection of the NH-groups in the precursors is not needed, as coupling under basic conditions with the [^{18}F]fluoroalkyltosylates is favoured at the phenol position over that at the NH-position. For details on the preparation of [^{18}F]12a and [^{18}F]12d, the reader is referred to the Radiolabeling section.

Scheme 2. Synthesis of the phenol precursors to the ^{18}F-labeled AMCs[a].

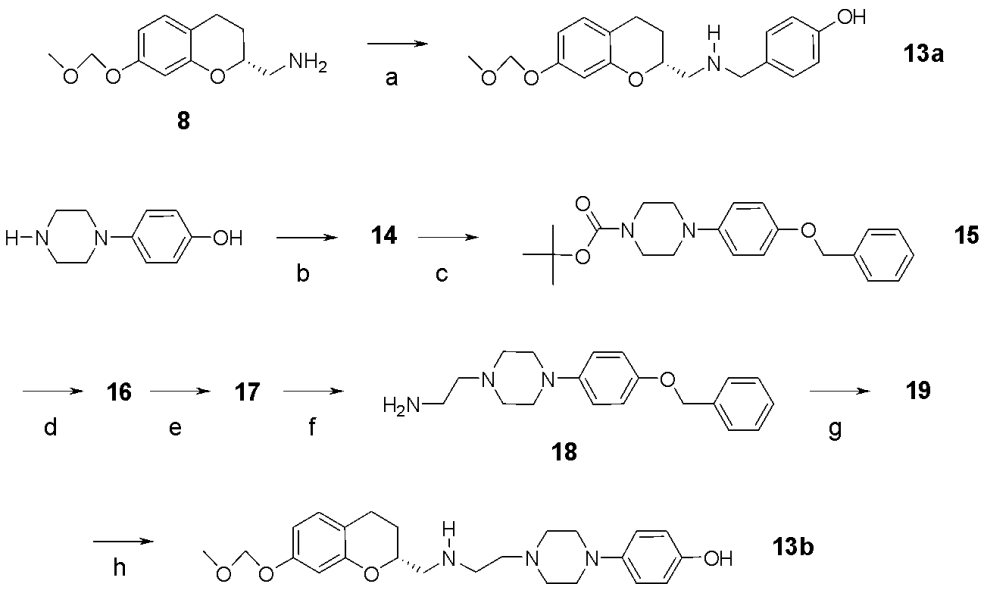

a reagents and solvents: (a) i. 4-hydroxybenzaldehyde, AcOH, CH_2Cl_2 ii $NaB(OAc)_3H$; (b) BOC-anhydride, DMF; (c) BnBr, DMF, K_2CO_3; (d) 4M HCl, dioxane; (e) tert butyl N-(2-bromoethyl) carbamate, DIPEA, DMF; (f) TFA, CH_2Cl_2; (g) tosylate 6, DIPEA, DMSO/dioxane; (h) Pd/C, H_2, EtOH.

Pharmacology

Affinity of the compounds to the dopamine receptors determined by radioligand binding

All novel AMC compounds (Chart 1) as well as the reference ligands dopamine, PHNO and NPA were tested for their ability to compete with [^{3}H]spiperone or [^{3}H]SCH23390 for binding to various receptors of the dopamine receptor family. In Table 1 the results of these binding studies are compiled. For almost all compounds, the binding experiments on the D_2L (D_{2long}) receptor produced competition curves which were significantly better explained by biphasic models (using GraphPrism). This finding indicates agonism for these ligands [37]. See Figure 1 for a typical biphasic binding curve as recorded for dopamine.

Among the AMC compounds tested, **11c** had the highest affinity for the D_2L_{high} receptor (Ki 0.68 ± 0.83 nM; mean±SD). The compounds **10a**, **10b**, **11a**, **11b**, **12a** and **12d** showed high affinities with Ki values in the low nanomolar range. The only two tertiary amine compounds, AMCs **11d** and **12c**, did not show a meaningful affinity for the D_2L receptor. For **11e** and **12b** no biphasic curves were observed and measured affinities were (well) above 10 nM (Ki 81 ± 54 nM for **11e** and 156 ± 78 nM for **12b**). All compounds showed affinities for D_2S that were comparable to those recorded for D_2L, and all tested compounds showed affinities for the dopamine D_4 receptor in the same range as that measured for the D_2L receptor, except for tertiary amines **11d** and **12c** which had a high affinity for D_4 but no meaningful binding to D_2L. These two compounds did also show an evident affinity for D_3 with Ki values of 24 ± 2.5 nM for **11d** and 40 ±15 nM for **12c**. Finally, all the tested compounds lacked reasonable affinity for the dopamine D_1-like receptors (D_1 and D_5) (Table 1).

Table 1. Affinity of reference and newly synthesized compounds for the different subtypes of dopamine receptors (data are shown as means and SD of K_i values (in nM unless stated otherwise) with the number of experiments given in parentheses).

	D_1 [a]	D_2L_{High} [a]	D_2L_{Low} [a]	D_2S_{Low} [b]	D_3 [b]	D_4 [a]	D_5 [a]
Dopamine	Not determined	231 ± 281 (6)	11.6 ± 12 µM (6)	920 ± 360 (4)	25 ± 28 (5)	34 ± 29 (4)	1.16 ± 0.8 µM (3)
PHNO	Not determined	0.45 ± 0.26 (5)	21 ± 4 (4)	19 ± 9 (3)	1.9 ± 1 (3)	Not determined	Not determined
NPA	Not determined	0.07 ± 0.01 (2)	1.7 ± 1 (5)	11 ± 18 (6)	1.9 ± 1 (3)	Not determined	Not determined
10a	7.2 ± 5 µM (3)	3.0 ± 4.7 (4)	70 ± 87 (5)	736 ± 1193 (3)	3.2 ± 0.4 (4)	12 ± 2.7 (3)	3.8 ± 1 µM (3)
10b	11 ± 4 µM (3)	8.2 ± 5.3 (4)	6.82 ± 0.22 (5)	168 ± 86 (3)	547 ± 936 (3)	5.7 ± 3.7 (3)	2.8 ± 0.6 µM (3)
11a	8.7 ± 4.3 µM (3)	3.8 ± 4.4 (4)	52 ± 55 (6)	140 ± 172 (3)	14 ± 19 (4)	1.6 ± 0.5 (3)	3.8 ± 1.6 µM (3)
11b	4.3 ± 2 µM (3)	2.1 ± 2.7 (4)	73 ± 110 (6)	31 ± 15 (3)	14 ± 19 (4)	1.0 ± 0.2 (3)	4.6 ± 1.2 µM (3)
11c	436 ± 137 (3)	0.7 ± 1.2 (4)	51 ± 68 (4)	166 ± 211 (3)	1.8 ± 0.9 (4)	Not determined	Not determined
11d	>10 µM (3)	No meaningful affinity	No meaningful affinity	No meaningful affinity	24 ± 2.5 (3)	14 ± 0.8 (3)	>10 µM (3)
11e	4.0 ± 1.0 µM (3)	Not detected	81 ± 54 (5)	131 ± 129 (3)	23 ± 8.9 (3)	9.7 ± 2.6 (3)	3.5 ± 7.2 µM (3)
12a	7.0 ± 2.8 µM (3)	5.6 ± 1.6 (2)	80 ± 64 (5)	93 ± 21 (3)	12 ± 4.0 (3)	32 ± 7 (3)	2.9 ± 2.0 µM (3)
12b	1.2 ± 0.1 µM (3)	Not detected	156 ± 78 (4)	452 ± 396 (3)	33 ± 7.5 (3)	Not determined	Not determined

(continued on the next page)

Table 1 (continuation). Affinity of reference and newly synthesized compounds for the different subtypes of dopamine receptors (data are shown as means and SD of K_i values (in nM unless stated otherwise) with the number of experiments given in parentheses).

	D_1 [a]	D_2L_{High} [a]	D_2L_{Low} [a]	D_2S_{Low} [b]	D_3 [b]	D_4 [a]	D_5 [a]
12c	No meaningful affinity	No meaningful affinity	No meaningful affinity	No meaningful affinity	39 ± 15 (4)	131 ± 129 (3)	>10 μM (3)
12d	No meaningful affinity	6.7 ± 4.7 (3)	235 ± 108 (5)	252 ± 112 (3)	10 ± 6.8 (3)	28 ± 17 (3)	9.7 ± 276 μM (3)

a data on experiments using membranes made from HEK293 cells stably transfected with the concerning dopamine receptor subtypes.
b data on experiments using membranes purchased from PerkinElmer.

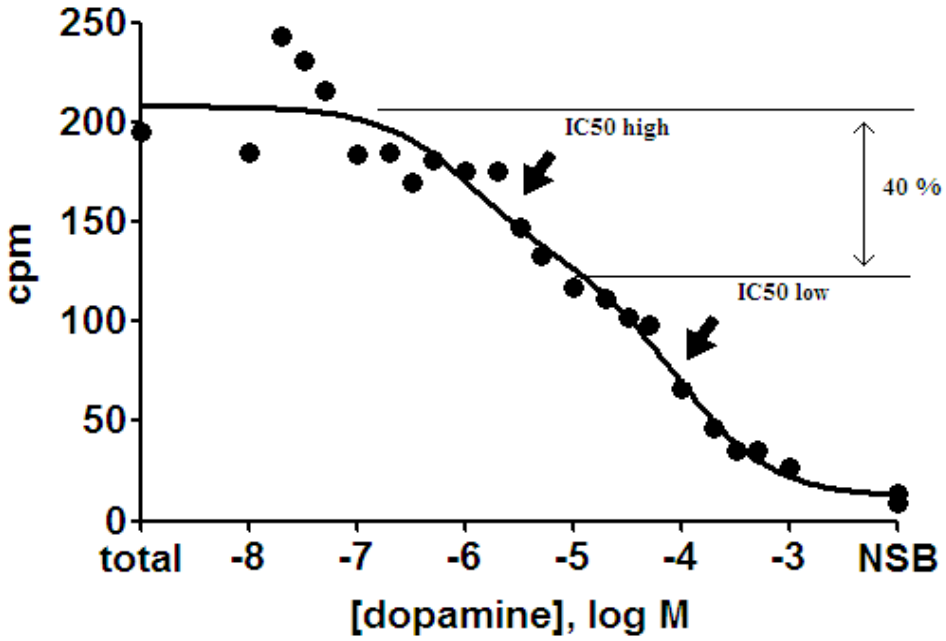

Figure 1. Representative biphasic competition binding curve, where in this case dopamine binding to the D_2L receptor is assessed.

The shown data are from one experiment, where the bound fraction of [^{3}H]spiperone in counts per minute (cpm) is plotted against the log of the concentration (mol/L) of dopamine. According to the points of inflection (arrows) this example shows an IC_{50} for the D_2 high-affinity state at 10^{-6} M dopamine and an IC_{50} for the D_2 low-affinity state at 10^{-4} M (these IC_{50}-values need to be transformed to Ki values using the Cheng Prusoff equation [38]). The fraction of the receptors in the high-affinity state is 40 ± 7%.

Ligand-induced inhibition of forskolin-induced cAMP accumulation

In HEK293 cells expressing the dopamine D_2L receptor, dopamine inhibits the forskolin-induced cAMP accumulation, where this inhibition becomes apparent as of a certain dopamine concentration. In the cAMP assay (Table 2), the AMC test compounds were compared to dopamine with respect to their inhibition potency, and it was found that **11e** appeared to be less potent than the endogenous agonist dopamine, **11a** and **12a** were similarly potent and all the other test compounds were somewhat more potent than dopamine with **11b** appearing to be the most potent of the tested ha-

logenated compounds. All compounds had efficacies comparable to that of dopamine (Table 2).

Radiolabeling

The two fluorinated compounds **12a** and **12d** were selected for ^{18}F-labeling. The labeling was accomplished via a three-step two-pot procedure, starting with the synthesis of a [^{18}F]fluoroalkyl synthon from [^{18}F]fluoride and the appropriate ditosylate precursor, followed by [^{18}F]fluoroalkylation of phenol precursors **13a** or **13b** (see Scheme 2 for their synthesis) and in situ removal of the MOM-protecting group applying acidic conditions (Scheme 3). The ^{18}F-labeled products [^{18}F]**12a** and [^{18}F]**12d** were purified by reversed phase HPLC. A typical synthesis run lasted for 150 min and started from 5 GBq of [^{18}F]fluoride, from which 20–200 MBq of formulated [^{18}F]**12a** or [^{18}F]**12d** were obtained.

Table 2. Potency and efficacy maximal response (E_{max}) expressed as % of dopamine response for various ligands at the human D_2L receptor determined in cAMP assay. All data are expressed as mean±SEM.

Ligand	pEC_{50}	E_{max} (% of dopamine)	*n*
Dopamine	9.2 ± 0.4	100	4
10a	10.7 ± 0.3	78 ± 5	4
10b	10.3 ± 0.4	82 ± 6	4
11a	9.2 ± 0.4	86 ± 5	4
11b	10.5 ± 0.4	86 ± 6	4
11e	8.8 ± 0.4	86 ± 5	4
12a	9.4 ± 0.3	96 ± 5	3
12d	9.8 ± 0.2	94 ± 3	3

Lipophilicity

Data regarding lipophilicity are shown in Table 3. Compounds **10a**, **10b**, **11a**, **11b**, **11e**, **12a**, **12b** and **12d** showed a clog D (clog$P_{7.4}$) in the range between 1 and 3 [39].

Table 3. Lipophilicity of the AMC compound series **10**, **11** and **12**, as assessed with BiologP (New ClogP) calculator program from the University of Massachusetts.

Compound	cLogP	cLogD ($cLogP_{7.4}$)
10a	3.42	1.41
10b	3.90	1.46
11a	4.35	2.43
11b	4.35	2.46
11c	4.35	3.30
11d	4.74	4.15
11e	4.38	2.42
12a	4.04	2.12
12b	4.04	2.57
12c	3.86	3.27
12d	3.49	1.54

Scheme 3. Labelling schemes of [^{18}F]**12a** and [^{18}F]**12d**.

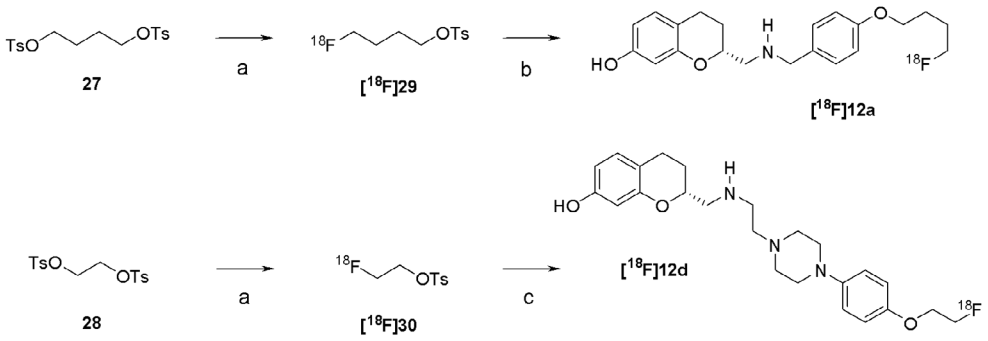

Reagents and solvents: (a) K^{18}F-Kryptofix-K_2CO_3, MeCN; (b) i. **13a**, NaH, DMF, ii. 0.4M HCl; (c) i. **13b**, NaH, DMF, ii. 0.4M HCl.

Radiochemical yields, purities and molar radioactivities of [^{18}F]**12a** and [^{18}F]**12d** are listed in Table 4.

Table 4. Radiochemical yields (RCY), radiochemical purities (RCP) and molar radioactivities (MR) of [^{18}F]**12a** and [^{18}F]**12d**. Data are expressed as means±SD and range in brackets.

Tracer	RCY, %	RCP, % (formulated tracer)	MR (GBq/μmol, at end of synthesis)
[^{18}F]**12a** *n*=10	HPLC[a]: 25±11 (3–47) formulated[b]: 7±8 (1–22)	94±4 (85–98)	92±96 (1.4–312)
[^{18}F]**12d** *n*=6	HPLC: 14±5 (6–20) formulated: 5±3 (1.4–11)	92±5 (85–98)	29±12 (8–40)

a HPLC fraction containing the tracer vs ^{18}F-fluoride taken for synthesis.
b Formulated tracer vs ^{18}F-fluoride taken for synthesis.

In vitro autoradiography

Results of in vitro autoradiography of [^{18}F]**12a** and [^{18}F]**12d** are presented in Figure 2 and Table 5.

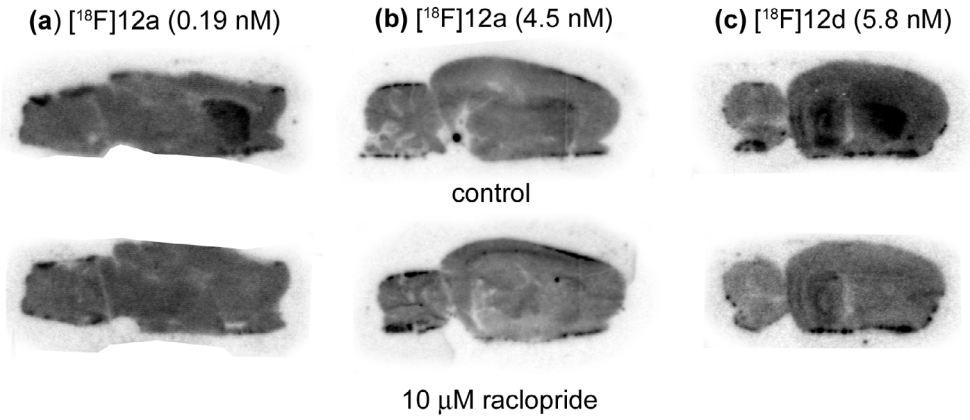

Figure 2. In vitro autoradiography with [^{18}F]**12a** at 0.19 nM (a), [^{18}F]**12a** at 4.5 nM (b) and [^{18}F]**12d** (c).

Note the specific binding in the striatum for [^{18}F]**12a** (only at lower concentration) and for [^{18}F]**12d**.

At nanomolar concentration, [^{18}F]**12a** showed rather homogeneous uptake in sagittal rat brain slices with only slightly higher binding in the striatum. Striatum-to-cerebellum and striatum-to-cortex ratios were on average 1.19 and 1.16, respectively. In the presence of 10 μM of the dopamine $D_{2/3}$ antagonist raclopride the striatum-to-cerebellum ratio was reduced by 14% and the striatum-to-cortex ratio by 11%. At sub-nanomolar concentration, however, [^{18}F]**12a** did demonstrate moderate but clearly visible specific uptake in the striatum. At 0.19 nM striatum-to-cerebellum ratios were on average 1.85 and were reduced by 40% in the presence of 10 μM raclopride and by 35% in the presence of 100 μM GTP. Striatum-to-cortex ratios were on average 1.68, and co-incubation with 10 μM raclopride or 100 μM GTP resulted in 39% and 33% decreases, respectively.

At nanomolar concentrations [^{18}F]**12d** demonstrated preferential binding in the striatum and hippocampus. In control animals, the mean striatum-to-cerebellum ratio was 2.64. In the presence of 10 μM raclopride or 100 μM guanosine triphosphate (GTP), striatum-to-cerebellum ratios were significantly reduced by 37%. Striatum-to-cortex ratios were on average 1.90 in control slices and were reduced by 37% by raclopride and by 22% by 100 μM GTP.

Table 5. In vitro autoradiography results. Values are means±SD from the total number of slides assayed in *n* independent experiments. The number of slides per condition in each experiment varied from 4 to 12.

Tracer	logD	Conditions	Striatum-to-cerebellum ratio	Striatum-to-cortex ratio
[^{18}F]**12a** upper row: 0.19 nM *lower row: 4.5±3.6 nM*	2.45±0.10	control (*n*=3)	1.85±0.23 *1.19±0.18*	1.68±0.11 *1.16±0.16*
		raclopride (*n*=1)	1.10±0.19 *1.04±0.22*	1.03±0.08 *1.05±0.11*
		GTP (*n*=1)	1.20±0.16	1.13±0.09
[^{18}F]**12d** 5.8±1.6 nM	1.48±0.01	control (*n*=4)	2.64±1.04	1.90±0.47
		raclopride (*n*=4)	1.65±0.37	1.20±0.20
		GTP (*n*=1)	1.67±0.28	1.48±0.17

DISCUSSION

Our present effort is directed at developing new agonist radiotracers that can be used in centers without an on-site cyclotron with the aim to enable visualization of dopamine $D_{2/3}$ receptors in the agonist high-affinity state. Accordingly, we have synthesized a novel group of iodinated and fluorinated compounds based on the AMC-scaffold that is known for its agonistic properties on $D_{2/3}$ dopamine receptors and for its good selectivity of binding for these receptor subtypes [26].

The primary binding site of the D_2 receptor is formed by transmembrane domains (TMs) 3, 5 and 6 of the receptor [40]. D_2 ligands contain the aromatic core which engages in interactions with the hydrophobic residues in TM3 and TM6. To this core an amino group and a hydrogen bond donating group are attached to form an ionic bond with the conserved aspartate residue in TM3 and one or more hydrogen bonds with conserved serine residues in TM5, respectively (Figure 3).

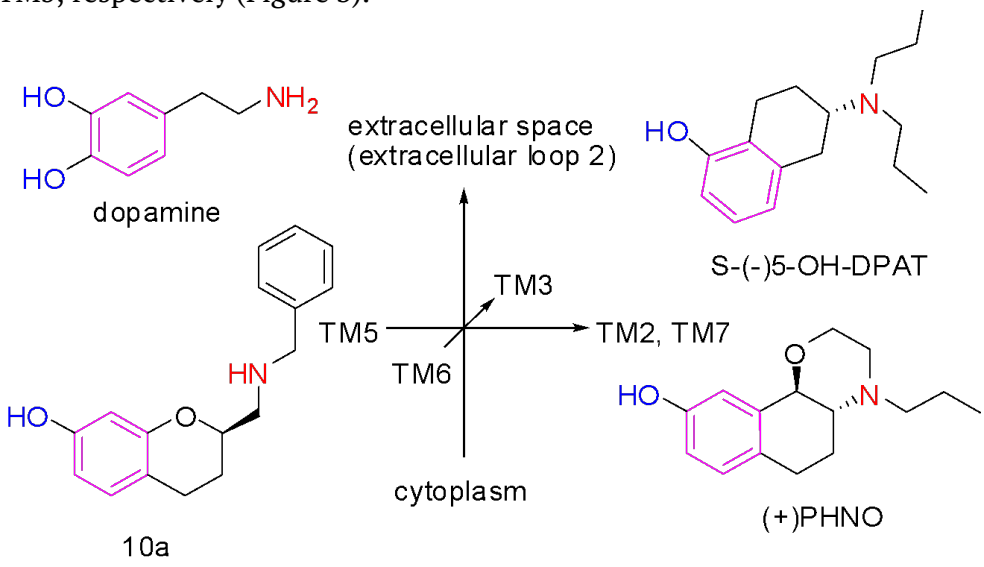

Figure 3. Comparison of the molecular structures of some D_2-agonist ligands, where their aryl cores are colored purple, basic nitrogens are red and H-bond donating hydroxyls are blue.

Orientation of the functional groups is chosen to roughly resemble the putative receptor-bound conformations of the ligands. Note that for conformationally constrained (+)PHNO the lone electron pair of the nitrogen is directed roughly normally to the aryl ring and away from us, towards the conserved aspartate in TM3. In the 3D representation, the TM6-TM3 axis is directed away from the viewer, that is, TM6 is closer to the viewer than TM5, while TM3 is farther.

Optimal distances between these groups and their optimal mutual orientation have been a subject of numerous studies which produced more or less general pharmacophore models, from the McDermed criteria developed in the late 1970s [41] to the more recent models [42, 43]. Notably it was found that the nitrogen atom can accommodate a bulky substituent extending into the ancillary binding pocket of the receptor formed by TM2 and TM7. The passage between the primary and ancillary binding pockets is narrower in D_1-like receptors than in D_2-like receptors, so the presence of such bulky substituents imparts D_2-over-D_1 selectivity [44] The second substituent at the nitrogen, however, cannot be greater than n-propyl [45].

Mewshaw et al. [26] proposed AMCs as a new series of compounds that meet the criteria for agonists with a high D_2 affinity and an appropriate D_2-over-D_1 selectivity. The AMC scaffold offers convenient possibilities to accommodate the ^{123}I or ^{18}F label on the N-substituent, and the same substituent can also be used to adjust the lipophilicity of the compound. Based on the benzylated secondary amine compound **10a**, that was developed by Mewshaw and that was found to have a high affinity (sub-nanomolar) for the D_2^{high} receptor, we designed three iodobenzyl and two fluoroalkyloxybenzyl candidate ligands. From the conformational and comparative molecular field analysis carried out for the AMC derivatives by the group of Mewshaw [46] and the modelling data for the D_2 receptor [47, 48] we concluded that the benzyl group of **10a** is likely to interact with the extracellular loop 2 of the receptor and not with the ancillary pocket of D_2 formed by TM2 and TM7. To probe the spatial requirements of such alignment we synthesized para- (**11a**), meta- (**11b**) and ortho-iodobenzyl (**11c**) and para- (**12a**) and ortho-(4-fluoro)butyloxybenzyl (**12b**) derivatives of **10a**. The butyl spacer in **12a** and **12b** was selected to bring the expected lipophilicity of the compounds within the log D range of 2 to 3 (Table 3), so as to ensure passage of the blood-brain-barrier [49].

The arylpiperazine motif is known to act as a pharmacophoric core in a number of high-affinity D_2-agonists [31] and apparently it can fit into the primary binding pocket of the D_2-like receptor [48]. Interestingly, Dutta and co-workers synthesized and evaluated a number of “hybrid” ligands based on an aminotetralin or a pramipexol scaffold to which an arylpiperazine moiety was attached via a spacer [32, 33]. In these hybrid ligands the arylpiperazine moiety is most probably bound in the ancillary binding pocket of the receptor and not in the primary binding site [50]. Inspired by these results, we designed four hybrid AMC derivatives with arylpiperazine side

chains attached to the AMC core, either directly (**11d** and **12c**) or through an ethylene spacer (**11e** and **12d**). Note accordingly that compounds **11d** and **12c** are the only tertiary amines in the series of developed compounds, where all the other compounds are secondary amine AMCs.

In the Mewshaw study that evaluated agonist ligands for the dopamine $D_{2/3}$ receptor, the affinity was measured in rat striatal membranes using the agonist [^{3}H]quinpirole and it was claimed that this approach specifically assessed the binding to the D_2L_{high} receptor, because [^{3}H]quinpirole should predominantly bind to D_2L_{high}. Measuring affinities for the D_2L_{low} was also done in rat striatal membranes, but in the presence of GTP to convert D_2L_{high} to D_2L_{low}, and with the antagonist [^{3}H]spiperone as radioligand. In addition, ketanserin was administered to preclude binding of spiperone to serotonin receptors [26]. Finally, a selection of compounds were evaluated in binding assays using membranes from cells transfected with human D_2S, D_3 and D_4 receptors. We have also used membranes from cloned human dopamine receptors expressed in cell lines, but included D_1, D_2L, and D_5 as well. We also used [^{3}H]spiperone as radioligand resulting in biphasic binding curves from which the affinities of the compounds for D_2L_{high} and D_2L_{low} could be derived (Figure 1).

Several of the prepared compounds indeed showed high affinity and selectivity for the $D_{2/3}$ receptors, and agonistic action on the D_2 receptor. Dopamine and most of the AMC compounds showed consistently biphasic competition curves for the D_2L receptor which is typical for agonists. The inflection points in these curves reflect the agonist high- (D_2L_{high}) and low-affinity (D_2L_{low}) state (Figure 1). In line with this finding, the cAMP experiments also showed agonistic properties for the tested compounds.

Nevertheless, when we compare the affinity of our reference compounds **10a** and **10b** to the values of Mewshaw et al., our findings show affinities which are 1 log scale lower (0.2 vs. 3.0 nM for **10a** and 0.7 vs. 8.2 nM for **10b**). This difference can be caused either by inter-species difference (Mewshaw used predominantly rat receptors, we only used human receptors) or by differences in techniques. The latter is more likely in our opinion, as discrepancy in the techniques is a well known cause of discrepancy in affinity measurements. For instance, for the D_2L_{high} receptor we found a dopamine dissociation constant of 230 nM, whereas literature reports values of 2 nM using [^{3}H]raclopride [51], 4.7 nM using [^{3}H]spiperone [52] and 56 nM using [^{125}I]iodosulpiride [53].

Reported affinities of dopamine for the D_2S receptor range between 4.5–229 nM using [^{3}H]spiperone as radioligand [54–56], while 22 nM was found using [^{125}I]iodosulpiride [57]. Although we did not find a high-affinity state of dopamine for the D_2S receptor in our experiments, a comparison between findings for the D_2S_{high} and the D_2L_{high} is still warranted because these receptors are structurally almost equal.

In our experiments PHNO showed an affinity for D_2L_{high} of 0.45 nM, and this is in line with literature findings of 0.6 nM [58] and 1.5 nM [59] for D_2L_{high}. NPA exhibited a Ki of 0.07 nM for D_2L_{high}, which is reasonably comparable to literature data that report Ki's of 0.38 nM [60] and 0.11 nM [61].

All AMC derivatives designed by us had at least 100-fold lower affinities towards D_1-like receptors than to D_2-like receptors. This is in agreement with the established notion that bulky substituents at the nitrogen impart D_2-selectivity.

Comparing the affinity towards D_2L_{high} of the para (**11a**), meta (**11b**) and ortho (**11c**) iodobenzyl compounds shows that **11a** and **11b** have about equal affinity (3.8 nM and 2.1 nM, respectively) with **11c** displaying a ten-fold stronger affinity (0.68 nM). This finding is in accordance with our expectation that the large iodine atom at the para-position of **11a** may be accommodated less easily within the binding pocket (possibly clashing somewhat with the receptor extracellular loop) as compared to the placement of the meta and ortho substituted iodines in **11b** and **11c**. Nevertheless, **11a** still shows a high affinity. Compound **12a** with the 4-fluorobutyloxy group at the para-position of the benzyl ring had a D_2L_{high} affinity of 5.6 nM, comparable to that of **11a**, while its ortho-isomer **12b**, surprisingly, did not appear to recognize D_2L_{high} and had about 3-fold lower affinities for D_2L_{low} and D_3 than **12a**. Apart from steric interactions, intramolecular hydrogen bonding interactions between the secondary NH and the O-atom of the fluorobutoxy-chain may also play a role here, where these interactions can only be conceived for **12b** (forming an ideal 6-ring) and not for **12a**. Similarly such interactions may exist with the I-atom in **11c**, but not with those in **11b** or **11a**. Note that these intramolecular hydrogen bonding interactions are also reflected in the increased lipophilicities of compounds **11c** and **12b** relative to those of their para- or meta-substituted counterparts (Table 3). However, it remains difficult to be conclusive about the binding mode of **12a** and particularly **12b**.

In comparison to the benzylamino-AMCs, **10a**, **11a-c** and **12a-b**, the hybrid AMCs, **11d-e** and **12c-d** generally showed lower affinities towards all dopaminergic receptor subtypes, both D_1-like and D_2-like. This fall in affinity was, however, not homogeneous, and the greatest decrease was observed for the D_2 subtype receptors, as the tertiary amine hybrids **11d** and **12c** did not show a meaningful affinity towards these receptors at all, while the ethylene-spaced secondary amine hybrid **11e** only recognized the low-affinity state of D_2L and D_2S. This observation is in agreement with the SAR studies on D_3-over-D_2 selectivity which suggest that the ancillary binding pocket of D_3 is more spacious than that of D_2, so compounds with bulkier groups attached to the nitrogen atom tend to prefer binding to D_3 [62, 63]. An interesting exception to this trend is the ethylene-spaced secondary amine hybrid **12d** that has a D_2L_{high} affinity comparable to that of the fluorobutyloxybenzyl derivative **12a**, and that has a D_2L_{high}-over-D_2L_{low} preference that is even higher than that of **12a**. It is impossible to determine on how exactly the arylpiperazine moiety interacts with the receptor in these hybrid ligands, but at least in the case of **12d** the arylpiperazine must be bound in the ancillary pocket, because arylpiperazines that interact with the primary binding pocket of the receptors have very low D_2-affinities when a bulky group, such as a fluoroalkoxy group, is placed at the para-position of the aryl ring [31, 55].

We successfully labeled two of our compounds, i.e. **12a** and **12d**, with fluorine-18. We made the selection for these two compounds based on the results of the in vitro experiments described above: **12a** and **12d** show a high affinity for dopamine $D_{2/3}$ receptors, a low affinity for dopamine D_1-like receptors, show agonism in the cAMP experiment and have an appropriate lipophilicity. Scheme 3 shows our approach to prepare [^{18}F]**12a** and [^{18}F]**12d**, where particularly we chose to use [^{18}F]fluoroalkylation onto a phenol precursor (either **13a** or **13b**) to arrive at the targeted tracers. The applied ^{18}F-labeling approach is versatile as we can quickly adapt the procedure for the preparation of homologous [^{18}F]fluoroalkyl derivatives of [^{18}F]**12a** or [^{18}F]**12d** in case adjusting of the hydrophobicity of the ligand is deemed necessary. In contrast, an approach where one would label compounds by direct ^{18}F-fluorination of tosyloxyalkyloxy or bromoalkyloxy precursors would require the preparation of every individual precursor (though fewer reaction steps involving ^{18}F-containing intermediates would be an advantage).

As can be seen from Table 4, only 25–30% of the HPLC-purified [^{18}F]**12a** or [^{18}F]**12d** ended up in the formulated tracer solution. The reason for this

was that only 30–50% of the radioactivity could be eluted from the Oasis HLB SPE cartridge using the designated portions (1–2 mL) of pure ethanol, with the remainder of the [^{18}F]**12a** and [^{18}F]**12d** amines sticking to the cartridge. Elution efficiency rose to 80–90% when the ethanol was acidified with 1 v/v% ortho-phosphoric or acetic acid, but it was decided to simply use ethanol as eluent. The tracers [^{18}F]**12a** and [^{18}F]**12d** were obtained in reasonable yields and satisfactory molar radioactivities. Radiochemical purities were also satisfactory; all radioactive impurities present in formulated [^{18}F]**12a** were much more polar than the tracer itself (not detectable on QC radio-HPLC, producing a spot with R_f = 0 on radio-TLC), and formulated [^{18}F]**12d** contained radioactive impurities both more and less hydrophobic than the tracer, but the former never amounted to more than 5% of the total radioactivity.

We evaluated the labeled compounds [^{18}F]**12a** and [^{18}F]**12d** by in vitro autoradiography in rat brain slices. Both ligands exhibited preferential uptake in the striatum region, where for [^{18}F]**12a** this was only visible at sub-nanomolar free ligand concentrations and for [^{18}F]**12d** it was found at low nanomolar levels (Figure 2). Given that the two compounds had comparable D_2L_{high} affinities, the lack of discernible $D_{2/3}$-specific binding of [^{18}F]**12a** at low nanomolar concentrations may be due to its higher lipophilicity (Table 3) which may have lead to the $D_{2/3}$-specific signal being "buried" under the non-specific signal resulting from [^{18}F]**12a** binding to membrane phospholipides.

For both compounds, binding in the striatum could be blocked with the dopamine $D_{2/3}$ receptor antagonist raclopride, and could be decreased to a similar extent in the presence of GTP, which suggests that the studied compounds indeed bind to the $D_{2/3}$-receptors in the striatum, showing a strong preference for the high-affinity state. This promising finding stimulates to perform future in vivo PET-studies of [^{18}F]**12d** in rodents, especially since the lipophilicity of this compound is in the requested range for the development of accurate PET tracers [64].

Most of our novel AMC compounds showed comparable affinities for both the dopamine D_2 and D_3 receptor. This is in line with presently available agonist dopamine receptor PET tracers such as [^{11}C]NPA, [^{11}C]MNPA. In contrast, [^{11}C]PHNO, which is D_3-preferring in vivo [24], is currently being actively used to investigate the regional distribution of D_3 receptors in the brain [65, 66] and the latest clinical research data suggest that D_3-selective tracers might be advantageous over tracers with mixed $D_{2/3}$-affinity in some applications [67, 68].

Three of our four hybrid compounds (**11d-e** and **12c**) seem selective for the D_3 receptor over the D_2 subtype. Though their D_3-affinities are too low to consider them as candidate tracers, they confirm that high-affinity D_3-selective AMCs can be made if more studies into structure-activity relationship for this compound class are undertaken. In addition, several of our novel compounds display a non-negligible affinity for the D_4R (Table 1). For instance, **11a** and **11b**, which are attractive candidates for ^{123}I-labeling, have low nanomolar K_i values on D_4 receptors. However, in the human striatum, the D_4 receptor density is 16-fold lower than that of $D_{2/3}$ receptors [69, 70]. In addition, in the striatum of rats, the D_4 receptor density is 7- and 5-fold lower than that of D_2 and D_3 receptors, respectively [71]. Consequently, we believe that striatal binding of our tracers will predominantly reflect binding to $D_{2/3}$ receptors.

Finally, our novel series of compounds may also offer the opportunity to develop ^{123}I-labeled SPECT tracers: compound **11a** may be an attractive candidate to label with iodine-123, since it has appropriate affinity, selectivity, lipophilicity and labeling seems feasible. Future studies will focus on this possibility.

CONCLUSION

We have identified a new series of agonist radiopharmaceuticals based on an AMC scaffold that bind with high affinity and selectivity to dopamine $D_{2/3}$ receptors in vitro. In cAMP assays they all show nearly full agonism. In addition, two of these compounds were labeled successfully with [^{18}F], and evaluated by in vitro autoradiography, where both of them showed specific binding in rat striatum, one at sub-nanomolar ([^{18}F]**12a**) and another at low nanomolar ([^{18}F]**12d**) concentrations. These findings stimulate further in vivo evaluations, e.g. animal PET and/or SPECT studies.

EXPERIMENTAL SECTION

Materials (chemical synthesis)

Reagents, chemicals, materials and solvents were obtained from commercial sources, and were used as received: Biosolve, Merck for solvents, Cambridge Isotope Laboratories for deuterated solvents, and Aldrich, Acros, ABCR, Merck and Fluka for chemicals, materials and reagents. All solvents were of AR quality. Moisture or oxygen-sensitive reactions were performed under an atmosphere of dry N_2 or argon.

Methods for chemical synthesis and molecular characterization

^{1}H-NMR and ^{13}C-NMR spectra were recorded on a Varian Mercury (400 MHz for ^{1}H-NMR, 100 MHz for ^{13}C-NMR) spectrometers at 298 K. Chemical shifts are reported in ppm downfield from tetramethylsilane (TMS) for ^{1}H NMR, and applying deuterated chloroform ($CDCl_3$) or other deuterated solvents as internal reference for ^{13}C NMR. Abbreviations used for splitting patterns are s = singlet, t = triplet, q = quartet, m = multiplet, dd = double doublet.

Melting points were measured on a Büchi melting point B-540 apparatus.

LC-PDA/MS analyses were performed on a Shimadzu LC-10 AD VP series LC coupled to a photo diode array (PDA) detector (Finnigan Surveyor PDA Plus detector, Thermo Electron corporation) and an ion-trap detector (LCQ Fleet, Thermo Scientific). Analyses were executed at 298 K using an Alltech Alltima HP C18 3μ column using an injection volume of 1–4 μL, a flow rate of 0.2 mL min^{-1} and typically a MeCN in H_2O gradient (from 5% to 100% MeCN, where both MeCN and H_2O contain 0.1% formic acid).

Elemental and UPLC-HRMS analyses were performed on the aminomethylchroman-7-ol (AMC) test compound series **10**, **11** and **12** in their isolated oxalate forms. Elemental analyses were done to assess the number of oxalate groups that were attached to the AMC-amines, and were performed on a PerkinElmer Series II CHNS/O Analyser 2400. UPLC-HRMS was used to assess the purity and the exact molecular weight of the AMCs. Purities were typically ca. 95%, mostly higher, and have been mentioned for every AMC-compound. Mass deviations from the theoretical mass were typically between 0 and 2 ppm. UPLC was performed on a Waters Acquity UPLC, that was equipped with a Sample Manager (an autosampler) and a Binary Solvent

Manager. An Acquity UPLC BEH C18 1.7 micrometer column was used, using H_2O and MeCN both with 0.1% formic acid as the two eluents, and applying an 8 minute gradient program where the amount of MeCN was increased from 5% to 60% in 5 minutes time. A sample solution (10% MeCN in H_2O; 0.1% formic acid) with a concentration of ca. 0.1 mg/mL was prepared and an injection volume of 0.1 microliter was used. For HRMS detection, a Xevo G2 Qtof detector using Zspray lockspray ionisation was applied.

GC-FID measurements to establish the e.e. of compound **1** were performed on a Shimadzu GC-2000, applying the Varian WCOT fused silica column (25 m, ID 0.25 mm), that is coated with CP chirasil-dex cb df 0.25 micrometer particles. An isothermal program was used (200 °C), applying a carrier gas helium flow of 30 cm/sec.

GC-MS measurements were executed on a Shimadzu GC-17A gas chromatograph coupled to a Shimadzu GCMS-QP5000 detector, using a Phenomenex Zebron ZB-35 capillary column (30 m length, ID 0.25 mm, 0.25 micrometer film thickness) that was operated using helium as the carrier gas and typically applying a temperature gradient from 80 °C to 300 °C.

Matrix-assisted laser desorption ionization time-of-flight mass spectrometry (MALDI-TOF MS) was performed on a PerSeptive Biosystems Voyager-DE PRO spectrometer using an α-cyano-4-hydroxycinnamic acid matrix.

Analytical thin layer chromatography (TLC) was performed on Kieselgel F-254 precoated silica plates. Normal phase column chromatography was carried out on flash silica gel (40–63 μm mesh) or regular silica gel (60–200 μm), both acquired from Screening Devices B.V., or on standardized aluminium oxide 90 from Merck. Reversed phase (RP) chromatography was performed on the Biotage Isolera One applying a SNAP KP-C18-HS cartridge.

The applied centrifuge was a Thermo Electron corporation Heraeus Megafuge 1.0.

The synthesis of the AMC-derivative series 10, 11 and 12

A series of 9 potential agonist compounds for the dopamine $D_{2/3}$ receptor, incorporating iodine or fluorine atoms in their structures was synthesized. Iodinated compounds were termed **11a**, **11b**, **11c**, **11d** and **11e**. Fluoridated compounds were numbered **12a**, **12b**, **12c** and **12d**. For internal standardization also 2 reference compounds without iodine or fluorine atoms in their

structure were also synthesized (namely **10a** and **10b**). Structural formulas are shown in Chart 1. All the test compound series **10**, **11** and **12** reported in this work are (*R*)-enantiomers, and they all originate from starting compound **1**, i.e. (*R*)-7-hydroxychroman-2-carboxylic acid ethyl ester.

*(R) 7-Hydroxychroman-2-carboxylic acid ethyl ester (**1**)*

The racemate of **1** [34, 35] has been resolved to **1** (the *R*-enantiomer), using the lipase kinetic resolution procedure as reported by Kalaritis [36]. Accordingly, the racemate of **1** (10 g, 45.5 mmol) was dissolved in THF (34 mL), and thereafter demi-water (270 mL) and a 0.05M phosphate buffer (68 mL) were added. Finally, amano lipase from Pseudomonas fluorescens (1.82 g) was added. The reaction mixture was treated with a 1M NaOH solution (25 mL) by dropwise addition in ten hours time. After NaOH-addition, the reaction mixture was stirred for another 8 hours. The mixture was evaporated to remove the THF, and the remaining aqueous mixture was extracted with ethyl acetate. Washing of the collected organic layers with saturated $NaHCO_3$, drying with Na_2SO_4 and concentration gave an oil that slowly crystallized. Yield: typically ca. 45%.

Note that the reaction conversion, i.e. the hydrolysis of the S-enantiomer to the acid and the e.e. of the remaining desired R-enantiomer ester **1**, was monitored using a chiral GC-FID method (see Methods section). Using this method, the racemate of **1** gives two peaks of equal intensity, while isolated **1** (i.e. the R-enantiomer after resolution) gives one peak with no or very little sign of the S-enantiomer (e.e. 99%). The S-enantiomer eluted first, the desired R-enantiomer second. Analytical data of isolated **1** are according to those from the above mentioned literature sources, particularly $[\alpha]_D^{rt} = -20.1$ ($CHCl_3$, c = 1).

*(R) (7-Hydroxychroman-2-yl)methanol (**2**)*

Ethyl ester **1** (3.18 g, 14.4 mmol) was dissolved in THF (200 mL) and cooled to 0 °C. A 2M $LiBH_4$ in THF solution (18.2 mL, 36.4 mmol, 2.5 moleqs) was added. The reaction mixture was stirred at rt for 3 hours, during which time the mixture became a milky suspension, and then it was poured into 1/1 water/brine (200 mL) that was brought to pH=2 using a 2N HCl solution. After stirring for 5 hours, the mixture was extracted with diethyl ether and dried with Na_2SO_4. The fraction of starting compound (ca. 15%) that was still present, was removed by silica column chromatography (1/1 hexane/ethyl acetate). Yield: 2.1 g (80%). Analytical data are according to those from lit-

erature [26] ^{1}H NMR ($CDCl_3$): δ = 6.9 (m, 1H), 6.35 (m, 2H), 5.35 (bs, 1H), 4.05 (m, 1H), 3.85 (m, 1H), 3.75 (m, 1H), 2.85–2.6 (multiple signals, 2H), 2.2 (bs, 1H), 1.95–1.75 (multiple signals, 2H). LC-MS: *m/z* = 181.1 $[M+H]^+$ (calcd 180.20 for $C_{10}H_{12}O_3$).

*Toluene-4-sulfonic acid, (R) (7-hydroxychroman-2-yl)-methyl ester (**3**)*

A solution of the alcohol **2** (0.5 g, 2.8 mmol) in pyridine (25 mL) was stirred at 0 °C. 4-Toluenesulfonyl chloride (0.56 g, 2.9 mmol, 1.05 moleqs) was added in small portions, and the reaction mixture was stirred for 6 hours at 4 °C. The mixture was then poured in ice water, and aqueous 2N HCl was added to acidify to pH<2. Extraction with CH_2Cl_2, drying of the collected organic layers with $MgSO_4$ and evaporation of the solvents gave a yellowish oil that was purified with silica column chromatography (2% MeOH/$CHCl_3$). Yield 0.56 g (60%). Analytical data are according to those from literature [26] ^{1}H NMR ($CDCl_3$): δ = 7.8 (m, 2H), 7.35 (m, 2H), 6.82 (m, 1H), 6.35 (m, 1H), 6.20 (m, 1H), 5.55 (bs, 1H), 4.15 (multiple signals, 3H), 2.75–2.6 (multiple signals, 2H), 2.45 (s, 3H), 1.95 (m, 1H), 1.75 (m, 1H). LC-MS: *m/z* = 335.1 $[M+H]^+$ (calcd 334.39 for $C_{17}H_{18}O_5S$).

*(R) 7-(Methoxymethoxy)chroman-2-carboxylic acid ethyl ester (**4**)*

At rt, methoxylmethyl chloride (MOMCl; 0.188 mL, 2.07 mmol, 0.92 moleqs) was added to a solution of ester **1** (0.50 g; 2.25 mmol) and DIPEA (1.2 mL; ca. 3 moleqs) in CH_2Cl_2 (25 mL). Monitoring of the progress of the reaction using ^{1}H NMR and LC-MS showed that extra MOMCl was required to complete the reaction, so another portion of MOMCl (0.188 mL; 0.92 moleqs) was added. Finally, the reaction mixture was washed with water, was concentrated and the remaining product was purified by silica column chromatography (2% MeOH/$CHCl_3$). Yield: 73%.

^{1}H NMR ($CDCl_3$): δ = 6.92 (m, 1H), 6.66 (s, 1H), 6.56 (m, 1H), 5.11 (m, 2H), 4.65 (m, 1H), 4.25 (m, 2H), 3.45 (s, 3H), 2.85–2.6 (multiple signals, 2H), 2.3–2.2 (m, 1H), 2.2–2.1 (m, 1H), 1.29 (t, 3H). ^{13}C NMR ($CDCl_3$): δ = 170.8, 156.6, 154.0, 129.8, 114.7, 109.4, 104.6, 94.5, 73.7, 61.3, 55.8, 24.7, 22.7, 14.1. LC-MS: *m/z* = 267.3 $[M+H]^+$ and 235.4 $[M-CH_3O]^+$ (calcd 266.29 for $C_{14}H_{18}O_5$).

*(R) (7-(Methoxymethoxy)chroman-2-yl)methanol (**5**)*

Ethyl ester **4** (0.551 g; 2.07 mmol) was dissolved in THF (30 mL), after which $LiBH_4$ (2.39 mL of a 2M solution in THF; 4.8 mmol) was added to this solu-

tion that was cooled using an ice bath. The reaction mixture was allowed to heat up to rt in about two hours time. After verification that the reaction was completed by monitoring with LC-MS and ^{1}H NMR, the reaction mixture was poured in water and extracted multiple times with ethyl acetate. The organic layer was dried using Na_2SO_4 and concentrated to give a colourless oil. This crude product was purified using silica column chromatography (2% MeOH/$CHCl_3$). Yield: 90% (oil).

^{1}H NMR ($CDCl_3$): δ = 6.92 (m, 1H), 6.54 (multiple signals, 2H), 5.08 (s, 2H), 4.05 (m, 1H), 3.85–3.75 (m, 1H), 3.75–3.65 (m, 1H), 3.43 (s, 3H), 2.85–2.6 (multiple signals, 2H), 2.4–2.3 (bs, 1H), 1.95–1.85 (m, 1H), 1.85–1.7 (m, 1H). ^{13}C NMR ($CDCl_3$): δ = 156.4, 155.0, 129.9, 115.4, 109.0, 104.3, 94.4, 76.4, 65.4, 55.8, 23.8, 23.7. LC-MS: *m/z* = 225.0 $[M+H]^+$ and 193.1 $[M-CH_3O]^+$ (calcd 224.26 for $C_{12}H_{16}O_4$). GC-FID analysis gave a single peak when using the chiral capillary column (see Methods section for details, see also GC-FID analysis of molecule **1**).

*Toluene-4-sulfonic acid, (R) (7-(methoxymethoxy)chroman-2-yl)-methyl ester (**6**)*

Alcohol **5** (0.56 g, 2.50 mmol) was dissolved in pyridine (7.5 mL) and the solution was cooled to 0 °C. p-Toluenesulfonylchloride (1.05 g, 5.5 mmol, 2.2 moleqs) in pyridine was added slowly, and the reaction mixture was thereafter stirred overnight at 4 °C. A small amount of ice was added to destroy the excess of p-toluenesulfonylchloride, the pH of the ice-cooled mixture was brought to pH=1 using a concentrated hydrochloric acid solution, and the product was extracted with CH_2Cl_2. The organic layer was washed with $NaHCO_3$, with a solution of $CuSO_4$ to remove traces of pyridine and finally with NaCl (aq.). Drying with Na_2SO_4 and concentration gave a slightly pinkish colored oil. Yield: 89%.

^{1}H NMR ($CDCl_3$): δ = 7.83 (m, 2H), 7.38 (m, 2H), 6.95 (m, 1H), 6.55 (multiple signals, 2H), 6.41 (s, 1H), 5.08 (s, 2H), 4.20 (multiple signals, 3H), 3.45 (s, 3H), 2.85–2.6 (multiple signals, 2H), 2.45 (s, 3H), 2.05–1.95 (m, 1H), 1.85–1.7 (m, 1H). ^{13}C NMR ($CDCl_3$): δ = 156.5, 154.4, 144.9, 132.7, 129.9, 129.6, 128.0, 114.7, 110.0, 104.4, 94.4, 72.9, 71.1, 55.9, 23.8, 23.3, 21.6. LC-MS: *m/z* = 401.3 $[M+Na]^+$, 347.4 $[M-CH_3O]^+$, (calcd 378.44 for $C_{19}H_{22}SO_6$).

*(R) N-(7-(Methoxymethoxy)chroman-2-yl)-methyl phthalimide (**7**)*

Tosylate **6** (300 mg, 0.79 mmol) and potassium phthalimide (367 mg,

1.98 mmol, 2.5 moleqs) were suspended in DMF (10 mL). The mixture was stirred for 16 hours at 80 °C, and was then allowed to cool down to rt. Diethyl ether was added and the mixture was washed twice with a saturated aqueous NH_4Cl solution, twice with water and one more time with a saturated NaCl solution in water. The organic layer was dried with Na_2SO_4. After removal of the volatiles the obtained white solid was purified with silica column chromatography (2% MeOH/ $CHCl_3$). Yield: 78%.

^{1}H NMR ($CDCl_3$): δ = 7.80 (m, 2H), 7.30 (m, 2H), 6.90 (d, 1H), 6.51 (m, 1H), 6.45 (s, 1H), 5.08 (m, 2H), 4.33 (m, 1H), 4.03 (dd, 1H), 3.84 (dd, 1H), 3.45 (s, 3H), 2.74 (m, 2H), 2.03 (m, 1H), 1.78 (m, 1H). ^{13}C NMR ($CDCl_3$): δ = 168.2, 156.4, 154.8, 134.0, 132.0, 129.8, 123.4, 115.0, 109.2, 104.5, 94.4, 73.0, 55.9, 41.9, 25.4, 23.5. LC-MS: m/z = 322.2 $[M\text{-}CH_3O]^+$, 354.3 $[M+H]^+$, 376.4 $[M+Na]^+$, 643.3 $[2M\text{-}H\text{-}2CH_3O]^+$, (calcd 353.37 for $C_{20}H_{19}NO_5$).

*(R) (7-(Methoxymethoxy)chroman-2-yl)-methyl amine (**8**)*

Phthalimide protected amine **7** (200 mg, 0.566 mmol) was stirred in EtOH (3 mL) together with hydrazine monohydrate (0.029 mL, 0.58 mmol). The mixture was heated at an oil bath temperature of 80 °C for 16 hours, during which time the reaction mixture changed from a suspension to a clear solution and back to a suspension. The mixture was allowed to cool to rt and was filtered; the filtrate was evaporated and redissolved in $CHCl_3$. The organic layer was washed once with a 0.1 M NaOH(aq) solution and once with water. The organic layer was dried with Na_2SO_4 and concentrated to give a colorless oil. Yield: 101 mg (80%).

^{1}H NMR ($CDCl_3$): δ = 6.90 (m, 1H), 6.51 (multiple signals, 2H), 5.08 (s, 2H), 3.90 (m, 1H), 3.45 (s, 3H), 2.90 (d, 2H), 2.8–2.7 (m, 1H), 2.7–2.6 (m, 1H), 1.85 (m, 1H), 1.75 (m, 1H), 1.4 (bs, 2H). ^{13}C NMR ($CDCl_3$): δ = 156.4, 155.3, 129.8, 115.4, 108.8, 104.3, 94.4, 77.6, 55.8, 46.6, 25.0, 24.0. LC-MS: m/z = 224.1 $[M+H]^+$, (calcd 223.27 for $C_{12}H_{17}NO_3$).

Route A: Coupling of tosylate 3 to the appropriate amines

*(R)-2-[(Benzylamino)methyl]chroman-7-ol (**10a**)*

Free amine. This reference compound 10a was prepared using a similar method to that described by Mewshaw [26]. Benzylamine (0.266 g; 2.48 mmol; 3 moleqs) was added to a solution of the tosylate 3 (0.285 g; 0.83 mmol) in DMSO (8 mL). The reaction mixture was stirred for 16 hours at

100 °C at which point it was poured in water (35 mL). The obtained suspension was extracted two times with ethylacetate, the collected organic layers were washed with water to remove DMSO, and the ethyl acetate solution was dried with Na_2SO_4. The crude free amine product was purified with silica column chromatography (5% MeOH/$CHCl_3$). Yield: 90 mg (40%).

^{1}H NMR ($CDCl_3$): δ = 7.45–7.15 (multiple signals, 5H), 6.8 (m, 1H), 6.35 (multiple signals, 2H), 4.05 (m, 1H), 3.95 (d, 1H), 3.85 (d, 1H), 2.85 (m, 1H), 2.75 (m, 1H), 2.7–2.6 (multiple signals, 2H), 1.85 (m, 1H), 1.65 (m, 1H). ^{13}C NMR ($CDCl_3$): δ = 156.2, 154.5, 138.3, 130.0, 128.6, 128.6, 127.4, 112.6, 109.0, 103.3, 74.3, 54.0, 53.6, 26.2, 23.7. LC-MS: *m/z* = 270.3 $[M+H]^+$, (calcd 269.34 for $C_{17}H_{19}NO_2$). MALDI-TOF-MS, *m/z* = 270.18 $[M+H]^+$.

Oxalate salt. To a solution of the free amine 10a (90 mg, 0.334 mmol) in THF (2 mL) was added a solution of oxalic acid dihydrate (84 mg, 0.67 mmol, 2 moleqs) in THF (0.5 mL). Immediately after addition a solid precipitated. The mixture was stirred for 3 hours, a small amount of ether was added to improve the precipitation, the mixture was filtrated and the white solid residue was washed with diethylether. Yield: 82 mg (68%).

^{1}H NMR (DMSO-d_6): δ = 8.0–6.0 (broad signal acidic protons), 7.55 (m, 2H), 7.4 (m, 3H), 6.8 (m, 1H), 6.28 (m, 1H), 6.23 (s, 1H), 4.27 (m, 1H), 4.23 (s, 2H), 3.2–3.0 (multiple signals, 2H), 2.75–2.5 (multiple signals, 2H), 1.95 (m, 1H), 1.65 (m, 1H). ^{13}C NMR (DMSO-d_6): δ = 164.4, 156.5, 153.9, 132.5, 130.0, 129.9, 128.8, 128.6, 111.9, 108.5, 102.9, 71.5, 50.6, 49.9, 24.7, 22.7. M.p. = 212 °C (dec). LC-MS: *m/z* = 270.2 $[M+H]^+$, (calcd 269.34 for $C_{17}H_{19}NO_2$). UPLC-HRMS $[M+H]^+$: Calcd 270.1494, Found 270.1491 (1.1 ppm). UPLC: 99% purity. Elemental analysis C,H,N: Found 63.4, 5.3, 3.7, Calcd. 63.5, 5.9, 3.9 for $C_{17}H_{19}NO_2$ + 1 $C_2H_2O_4$ (FW=359.4).

*(R)-2-[(3-Iodobenzylamino)methyl]chroman-7-ol (**11b**)*

Free amine. Tosylate 3 (0.38 g; 1.1 mmol) was mixed with commercially available 3-iodo-benzylamine (0.78 g; 3.3 mmol; 2.9 moleqs) and DIPEA (0.6 mL, 3 moleqs) in DMSO (10 mL), and this solution was stirred overnight at an oil bath temperature of 100 °C. According to LC-MS no tosylate starting material was present anymore and the mixture was poured in water, followed by extraction of the water layer with ethyl acetate (two times). The ethyl acetate layers were collected, dried with Na_2SO_4 and concentrated. Finally, the crude product was purified with silica column chromatography (2% MeOH/$CHCl_3$) giving 169 mg of an oily product (39%).

^{1}H NMR ($CDCl_3$): δ = 7.7 (s, 1H), 7.6 (m, 1H), 7.35 (m, 1H), 7.05 (m, 1H), 6.8 (m, 1H), 6.35 (multiple signals, 2H), 4.05 (m, 1H), 3.85 (d, 1H), 3.80 (d, 1H), 2.85 (m, 1H), 2.75 (m, 1H), 2.7–2.55 (multiple signals, 2H), 1.85 (m, 1H), 1.65 (m, 1H).

Oxalate salt. The free amine 11b (169 mg, 0.43 mmol) was dissolved in THF (2 mL) and oxalic acid dihydrate (118 mg, 0.94 mmol, 2.2 moleqs) was added. A precipitation formed, and after some stirring the suspension was filtrated to give a white solid product. Yield: 152 mg (73%).

^{1}H NMR (DMSO-d_6): δ = 8.0–6.0 (broad signal acidic protons), 7.9 (s, 1H), 7.75 (m, 1H), 7.55 (m, 1H), 7.25 (m, 1H), 6.85 (m, 1H), 6.28 (m, 1H), 6.25 (s, 1H), 4.25 (m, 1H), 4.15 (s, 2H), 3.2–3.0 (multiple signals, 2H), 2.75–2.5 (multiple signals, 2H), 1.95 (m, 1H), 1.65 (m, 1H). ^{13}C NMR (DMSO-d_6): δ = 164.0, 156.5, 154.0, 138.4, 137.3, 135.5, 130.7, 129.9, 129.4, 111.9, 108.5, 102.9, 94.9, 71.7, 50.2, 49.9, 24.7, 22.8. M.p. = 214 °C (dec). LC-MS: *m/z* = 396.2 $[M+H]^+$, (calcd 395.24 for $C_{17}H_{18}NO_2I$). UPLC-HRMS $[M+H]^+$: Calcd 396.0460, Found 396.0455 (1.3 ppm). UPLC: 94% purity. Elemental analysis C,H,N: Found 47.2, 4.3, 2.4, Calcd. 47.0, 4.2, 2.9 for $C_{17}H_{18}NO_2I$ + 1 $C_2H_2O_4$ (FW=485.3).

*(R) 1-(4-Iodophenyl)-4-((7-hydroxychroman-2-yl)methyl)piperazine (**11d**)*

Free amine. Tosylate 3 (289 mg, 0.865 mmol) was dissolved in DMSO (10 mL), and to the solution DIPEA (0.334 g, 2.59 mmol, 2.9 moleqs) and 1-(4-iodophenyl)-piperazine (500 mg, 1.74 mmol, 2.0 moleqs) were added. 1-(4-Iodophenyl)-piperazine had been synthesized from 1-phenyl-piperazine according to Hanson et al. [72] The reaction mixture was stirred overnight at 100 °C under an argon atmosphere. According to LC-MS all the tosylate reactant was converted. The reaction mixture was cooled down to rt and was poured into water. Extraction with ethyl acetate was followed by drying of the collected organic layers with Na_2SO_4. Evaporation of the solvent yielded crude product (844 mg) that was purified with silica column chromatography (2% MeOH/$CHCl_3$). A beige solid was obtained. Yield: 120 mg (31%).

^{1}H NMR ($CDCl_3$ with a drop of CD_3OD): δ = 7.55 (m, 2H), 6.85 (m, 1H), 6.70 (m, 2H), 6.35 (m, 1H), 6.30 (s, 1H), 4.2 (m, 1H), 3.2 (m, 4H), 2.85–2.6 (multiple signals, 7H), 2.55 (m, 1H), 2.0 (m, 1H), 1.75 (m, 1H). LC-MS: *m/z* = 451.3 $[M+H]^+$, (calcd 450.32 for $C_{20}H_{23}N_2O_2I$).

Oxalate salt. To a solution of the free amine 11d (120 mg, 0.267 mmol) in THF (4 mL) was added a solution of oxalic acid dihydrate (74 mg, 0.59 mmol, 2.2 moleqs) in THF (1 mL). Immediately a white solid precipitated. After 3 hours of stirring the reaction mixture centrifuged. The solvent was decanted and the residue was washed with a mixture of THF and ether (1/1). After drying, a white solid residue was isolated (120 mg, 83%).

^{1}H NMR (DMSO-d_6): δ = 7.5 (m, 2H), 6.8 (multiple signals, 3H), 6.25 (m, 1H), 6.20 (s, 1H), 4.3 (m, 1H), 3.25 (m, 4H), 3.1–2.9 (multiple signals, 6H), 2.8–2.6 (multiple signals, 2H), 2.0 (m, 1H), 1.65 (m, 1H). ^{13}C NMR (DMSO-d_6): δ = 162.6, 156.5, 154.3, 150.0, 137.4, 129.9, 118.0, 112.1, 108.2, 102.9, 81.3, 71.8, 60.4, 52.3, 46.4, 25.5, 22.9. M.p. = 177 °C (dec). LC-MS: *m/z* = 451.2 $[M+H]^+$, (calcd 450.32 for $C_{20}H_{23}N_2O_2I$). UPLC-HRMS $[M+H]^+$: Calcd 451.0882, Found, 451.0882 (0 ppm). UPLC: 96% purity. Elemental analysis C,H,N: Found 48.9, 4.1, 4.8, Calcd. 48.9, 4.7, 5.2 for $C_{20}H_{23}N_2O_2I$ + 1 $C_2H_2O_4$ (FW=540.4).

Route B: General procedure for coupling of the MOM-protected tosylate 6 to the appropriate amines

The tosylate **6** is added to a solution of the amine (typically in a molar excess relative to the tosylate) in DMSO. DIPEA is also present (in molar excess relative to the tosylate). The reaction mixture is heated to 80–100 °C under an inert atmosphere of argon, and during 1 or 2 days the progress of the reaction is followed with LC-MS. In cases where primary amine starting compounds are used, LC-MS analysis of the reaction mixture shows the excess of the primary amine starting compound and the secondary amine desired product, but also tertiary amine by-product. After reaction, the mixture is poured into cold water and the product is extracted using ethyl acetate. Evaporation yields an oily product that requires column chromatographic purification. The obtained secondary amine products can severely stick to silica, so alumina is sometimes used as the stationary phase. The applied eluent is a mixture of $CHCl_3$ with a small percentage of MeOH (typically 1 to 2 v/v%), or a gradient with gently increasing MeOH-contents starting from pure $CHCl_3$.

*(R) N-[7-(Methoxymethoxy)chroman-2-yl]methyl 1-hexyl amine (**9a**)*

n-Hexylamine (0.321 g, 3.18 mmol) was dissolved in DMSO (5 mL) with 5 moleqs of DIPEA (0.9 mL). Tosylate **6** (397 mg, 1.05 mmol) was added and

the reaction mixture was heated overnight at 95 °C under an argon atmosphere. The mixture was cooled and poured into water followed by extraction of the aqueous layer ethyl acetate. Concentration of the organic layer gave a slightly colored oil (378 mg), that gave 193 mg of pure product after silica column chromatography (2% MeOH/$CHCl_3$). Yield 60%.

^{1}H NMR ($CDCl_3$): δ = 6.92 (m, 1H), 6.53 (multiple signals, 2H), 5.10 (s, 2H), 4.11 (m, 1H), 3.44 (s, 3H), 2.90–2.55 (multiple signals, 5H), 2.0–1.9 (m, 1H), 1.8–1.6 (multiple signals, 3H), 1.50 (m, 2H), 1.4–1.2 (multiple signals, 6H), 0.88 (t, 3H). ^{13}C NMR ($CDCl_3$): δ = 156.4, 155.2, 129.9, 115.5, 108.8, 104.3, 94.4, 75.2, 55.8, 54.3, 50.1, 31.7, 30.0, 27.0, 25.7, 24.0, 22.6, 14.0. LC-MS: *m/z* = 308.3 $[M+H]^+$, (calcd 307.43 for $C_{18}H_{29}NO_3$).

*(R) N-[7-(Methoxymethoxy)chroman-2-yl]methyl 4-iodobenzyl amine (**9b**)*

The tosylate **6** (327 mg, 0.865 mmol) was added to a solution of commercially available para-iodobenzylamine (0.4 g; 1.83 mmol) in DMSO (5 mL) and DIPEA (0.8 mL). The mixture was heated to 85 °C, was kept under argon and was stirred overnight. After cooling down to rt, the reaction mixture was poured into water. Extraction with ethyl acetate, and evaporation of the volatiles yielded a slightly colored oil. This crude material was purified with silica column chromatography (2% MeOH/$CHCl_3$), yielding 283 mg product (75%).

^{1}H NMR ($CDCl_3$): δ = 7.64 (m, 2H), 7.12 (m, 2H), 6.95 (m, 1H), 6.53 (multiple signals, 2H), 5.11 (s, 2H), 4.15 (m, 1H), 3.80 (s, 2H), 3.45 (s, 3H), 2.9–2.6 (multiple signals, 4H), 2.0–1.9 (multiple signals, 2H), 1.75 (m, 1H). ^{13}C NMR ($CDCl_3$): δ = 156.4, 155.1, 139.9, 137.3, 130.0, 129.8, 115.4, 108.9, 104.3, 94.4, 92.1, 75.2, 55.8, 53.4, 53.1, 25.6, 23.9. LC-MS: *m/z* = 440.2 $[M+H]^+$, (calcd 439.29 for $C_{19}H_{22}NO_3I$).

*(R) 1-(4-Iodophenyl)-4-(4-(7-(methoxymethoxy)chroman-2-yl)-3-azabutyl)-piperazine (**9d**)*

Primary amine **24** (0.585 g, 1.77 mmol, 1.5 moleqs) was dissolved in DMSO (5 mL) with 4 moleqs of DIPEA (0.8 mL). Tosylate **6** (442 mg, 1.17 mmol) was added and the reaction mixture was heated to 85 °C, and was kept overnight under a gentle flow of argon. The reaction mixture was then cooled and poured into water. Extraction with ethyl acetate and evaporation of the solvent yielded a slightly colored oil that was purified with alumina column chromatography (2% MeOH/$CHCl_3$). Yield: 250 mg (40%).

^{1}H NMR ($CDCl_3$): δ = 7.50 (m, 2H), 6.95 (m, 1H), 6.67 (m, 2H), 6.53 (multiple signals, 2H), 5.08 (s, 2H), 4.15 (m, 1H), 3.44 (s, 3H), 3.17 (m, 4H), 2.95–2.65 (multiple signals, 6H), 2.65–2.55 (multiple signals, 6H), 2.0–1.9 (multiple signals, 2H), 1.75 (m, 1H). ^{13}C NMR ($CDCl_3$): δ = 156.4, 155.2, 150.9, 137.7, 129.9, 117.9, 115.5, 108.9, 104.3, 94.4, 81.2, 75.0, 57.8, 55.8, 54.2, 53.0, 48.7, 46.4, 25.7, 24.0. LC-MS: *m/z* = 538.3 $[M+H]^+$, (calcd 537.44 for $C_{24}H_{32}N_3O_3I$).

*(R) N-[7-(Methoxymethoxy)chroman-2-yl]methyl 4-(4-fluorobutoxy)benzyl amine (**9e**)*

Amine **21** (0.198 g, 1.00 mmol, 1.2 moleqs) was dissolved in DMSO (5 mL) with 5 moleqs of DIPEA (0.75 mL). The tosylate **6** (318 mg, 0.84 mmol) was added, the mixture was heated to 95 °C and was left to react for 2 days while being kept under an argon atmosphere. The reaction was cooled down and poured in water. Extraction with ethyl acetate yielded a slightly colored oil that was purified using silica column chromatography (2% MeOH/$CHCl_3$), and subsequent RP C18 chromatography using an aqueous eluent gradient. Yield: 124 mg (36%).

^{1}H NMR ($CDCl_3$): δ = 7.25 (m, 2H), 6.90 (m, 1H), 6.85 (m, 2H), 6.53 (multiple signals, 2H), 5.05 (s, 2H), 4.6 (m, 1H), 4.45 (m, 1H), 4.15 (m, 1H), 3.95 (m, 2H), 3.8 (s, 2H), 3.4 (s, 3H), 2.9–2.65 (multiple signals, 4H), 2.0–1.7 (multiple signals, 7H). LC-MS: *m/z* = 404.3 $[M+H]^+$, (calcd 403.49 for $C_{23}H_{30}NO_4F$).

*(R) 1-(4-(2-Fluoroethoxy)phenyl)-4-((7-(methoxymethoxy)chroman-2-yl)-methyl)-piperazine (**9g**)*

1-(4-(2-Fluoroethoxy)-phenyl)-piperazine was prepared from commercially available 1-(4-hydroxyphenyl)-piperazine according to Tietze et al. [73], thereby using the 1-fluoro-2-tosyloxy-ethane building block that was prepared [74] from commercially available 2-fluoroethanol. 1-(4-(2-Fluoroethoxy)-phenyl)-piperazine (0.305 gram, 1.36 mmol, 1.2 moleqs) was dissolved in DMSO (5 mL) with 3 moleqs of DIPEA (0.6 mL). The tosylate **6** (428 mg, 1.13 mmol) was added and the reaction mixture was heated to 95 °C. Overnight stirring under an inert argon atmosphere was followed by cooling down of the reaction mixture and pouring it in water. Extraction with ethyl acetate and concentration yielded a slightly colored crude oil that was purified using silica column chromatography (2% MeOH/$CHCl_3$). Yield: 320 mg (66%).

^{1}H NMR ($CDCl_3$): δ = 7.0–6.8 (multiple signals, 5H), 6.56 (multiple signals, 2H), 5.12 (s, 2H), 4.79 (m, 1H), 4.67 (m, 1H), 4.20 (m, 2H), 4.15 (m, 1H), 3.46 (s, 3H), 3.13 (m, 4H), 2.9–2.55 (multiple signals, 8H), 2.1–2.0 (m, 1H), 1.85–1.7 (m, 1H). LC-MS: *m/z* = 431.4 $[M+H]^+$, (calcd 430.52 for $C_{24}H_{31}N_2O_4F$).

*(R) 1-(4-(2-Fluoroethoxy)phenyl)-4-(4-(7-(methoxymethoxy)chroman-2-yl)-3-azabutyl)-piperazine (**9h**)*

Primary amine **26** (0.364 g, 1.36 mmol, 1.2 moleqs) was dissolved in DMSO (5 mL) with 3 moleqs of DIPEA (0.6 mL). The tosylate **6** (428 mg, 1.13 mmol) was added and the reaction mixture was heated overnight at 100 °C and was kept under a gentle flow of argon. The reaction mixture was cooled down and poured into water. Extraction with ethyl acetate, and concentration gave a slightly colored oil (0.36 g). Finally, purification with alumina column chromatography (2% MeOH/$CHCl_3$) gave a yield of 47% of pure product (250 mg).

^{1}H NMR ($CDCl_3$): δ = 7.0–6.8 (multiple signals, 5H), 6.54 (multiple signals, 2H), 5.10 (s, 2H), 4.79 (m, 1H), 4.67 (m, 1H), 4.20 (m, 1H), 4.13 (m, 2H), 3.44 (s, 3H), 3.12 (m, 4H), 3.0–2.5 (multiple signals, 12H), 2.05–1.9 (multiple signals, 2H), 1.75 (m, 1H). LC-MS: *m/z* = 474.4 $[M+H]^+$, (calcd 473.59 for $C_{26}H_{36}N_3O_4F$).

Route C: General procedure for coupling the MOM-protected amine 8 to the appropriate aldehydes

The MOM-protected primary amine **8** and the appropriate aldehyde (1 mol moleq) are mixed in MeOH and stirred overnight at rt. During this step the imine is formed. The conversion is followed with ^{1}H NMR by inspecting the aldehyde signal (due to reversibility of the reaction in the presence of water, monitoring by LC-MS is not possible). After completion of imine formation, 1.1 mol moleqs of $NaBH_4$ is added and the reaction mixture is stirred at rt for 1 up to 3 hours. ^{1}H NMR can be used to monitor imine conversion. The reaction mixture is poured in water, the aqueous solution is stirred for 1 hour and is then extracted with CH_2Cl_2, or alternatively with $CHCl_3$. Due to the presence of boron salts it may be necessary to first adjust the pH of the water layer to acidic (pH=1), then back to slightly basic (pH=8) and do the extraction at this higher pH. Drying of combined organic layers with Na_2SO_4 is followed by removal of the solvents to yield the product.

*(R) N-[7-(Methoxymethoxy)chroman-2-yl]methyl 4-iodobenzyl amine (**9b**)*

4-Iodobenzaldehyde was prepared from commercially available p-iodo benzoic acid using a two-step procedure [75] via the p-iodo benzyl alcohol. Amine **8** (418 mg, 1.87 mmol) and freshly prepared 4-iodobenzaldehyde (433 mg, 1.87 mmol) were stirred in MeOH (10 mL). $NaBH_4$ (77.7 mg, 2.06 mmol) was added. Extraction with $CHCl_3$ and thereafter with CH_2Cl_2. An oily product was obtained (766 mg, 93%). The analytical data are identical to those reported for the same **9b** product as prepared and isolated via Route B (*vide supra*).

*(R) N-[7-(Methoxymethoxy)chroman-2-yl]methyl 2-iodobenzyl amine (**9c**)*

2-Iodobenzaldehyde was prepared from its commercially available benzyl alcohol precursor [76]. Amine **8** (192 mg, 0.86 mmol) was stirred with 2-iodobenzaldehyde (200 mg, 0.86 mmol) in MeOH (5 mL). According to the ^{1}H NMR, still ca. 4% of aldehyde was present, but nevertheless $NaBH_4$ (42 mg, 1.11 mmol, 1.3 moleqs) was added. After extraction, the crude yellow oil (331 mg) was purified by silica column chromatography (ethyl acetate/hexane 1/1) to yield 209 mg (56%) of product.

^{1}H NMR ($CDCl_3$): δ = 7.80 (m, 1H), 7.40 (m, 1H), 7.28 (m, 1H), 6.95 (multiple signals, 2H), 6.53 (multiple signals, 2H), 5.08 (s, 2H), 4.15 (m, 1H), 3.87 (s, 2H), 3.45 (s, 3H), 2.9–2.6 (multiple signals, 4H), 2.05–1.85 (multiple signals, 2H), 1.85–1.75 (m, 1H). ^{13}C NMR ($CDCl_3$): δ = 156.4, 155.2, 142.0, 139.3, 129.8, 129.4, 128.7, 128.2, 115.5, 108.9, 104.4, 99.5, 94.4, 75.2, 58.0, 55.8, 53.2, 25.6, 23.9. LC-MS: *m/z* = 440.2 $[M+H]^+$, (calcd 439.29 for $C_{19}H_{22}NO_3I$).

*(R) N-[7-(Methoxymethoxy)chroman-2-yl]methyl 2-(4-fluorobutoxy)benzyl amine (**9f**)*

Amine **8** (205 mg, 0.92 mmol) was stirred with 2-(4-fluorobutoxy) benzaldehyde **22** (179 mg, 0.92 mmol) in MeOH (5 mL). According to ^{1}H NMR some 10% of aldehyde was still present, but nevertheless $NaBH_4$ (45 mg, 1.19 mmol, 1.3 moleqs) was added. The crude yellowish oil (340 mg) was purified with silica column chromatography (ethyl acetate/hexane 1/1) to yield 221 mg of product (60%).

^{1}H NMR ($CDCl_3$): δ = 7.26 (m, 1H), 7.23 (m, 1H), 6.85 (multiple signals, 2H), 6.80 (m, 1H), 6.53 (multiple signals, 2H), 5.10 (s, 2H), 4.56 (bs, 1H), 4.45 (t, 1H), 4.15 (m, 1H), 4.06 (t, 2H), 3.85 (dd, 2H), 3.44 (s, 3H), 2.90–2.6 (mul-

tiple signals, 4H), 2.05 (bs, 1H), 2.0–1.85 (multiple signals, 5H), 1.8–1.7 (m, 1H). ^{13}C NMR ($CDCl_3$): δ = 156.9, 156.4, 155.3, 129.9, 129.8, 128.3, 128.1, 120.4, 115.5, 111.0, 108.8, 104.3, 94.5, 84.5, 82.8, 75.6, 67.1, 55.8, 53.6, 49.4, 27.4, 27.2, 25.7, 25.4, 25.3, 24.0. LC-MS: *m/z* = 404.3 $[M+H]^+$, (calcd 403.49 for $C_{23}H_{30}NO_4F$).

Route B and C: General procedure for deprotection of the MOM-group

The appropriate MOM-protected compound **9** (100 to 300 mg) was dissolved in an 4M HCl solution in dioxane (2 to 5 mL; HCl in high molar excess) and isopropanol (2 to 5 mL). The reaction mixture was stirred for about 3 hours at rt, while a N_2 flow was maintained over the reaction mixture. From time to time, N_2 was bubbled through the solution in order to remove volatile reaction products from the mixture. The reaction mixture may turn hazy due to precipitation of the ammonium salt. After completion of the reaction (the reaction was monitored by LC-MS), the mixture was added to water and the pH was brought to slightly basic by addition of a NaOH-solution. The product was isolated from the water layer by several extractions using $CHCl_3$ or CH_2Cl_2 with some added THF, followed by drying of the collected organic layers with Na_2SO_4 and evaporation of the solvent.

General procedure for preparation of the oxalate salt. The isolated free amine compound was dissolved in THF and a solution of oxalic acid dihydrate in THF was added. The reaction mixture turned hazy due to precipitation of the oxalate ammonium salt. After about 3–5 hours of stirring the reaction mixture was centrifuged and the solvent was pipetted or decanted off. The residue was stirred in a fresh 1:1 mixture of diethyl ether and THF and was centrifuged again. The solvent was removed and the precipitate was dried to yield a white, off-white or slightly brownish powder product.

*(R)-2-[(Hexylamino)methyl]chroman-7-ol (**10b**)*

Free amine. This reference compounds **10b** has already been reported by Mewshaw [26], albeit that the racemic mixture was prepared and not the (*R*)-enantiomer. Furthermore, we have prepared **10b** via its MOM-protected precursor, while Mewshaw had prepared the racemate via its benzyl-protected precursor. Compound **9a** (121 mg, 0.39 mmol) was dissolved in a solution of 4M HCl in dioxane (2 mL) and isopropanol (3 mL). Yield after work up: 100 mg (96%).

^{1}H NMR ($CDCl_3$): δ = 6.78 (m, 1H), 6.45 (m, 1H), 6.32 (m, 1H), 4.07 (m, 1H), 2.90 (t, 1H), 2.8–2.5 (multiple signals, 5H), 1.85 (m, 1H), 1.75–1.5 (multiple signals, 3H), 1.4–1.2 (multiple signals, 6H), 0.88 (t, 3H). ^{13}C NMR ($CDCl_3$): δ = 156.7, 154.5, 130.0, 112.2, 109.4, 103.0, 74.2, 54.2, 50.0, 31.6, 29.2, 26.9, 26.3, 23.7, 22.5, 14.0. LC-MS: *m/z* = 264.3 $[M+H]^+$, (calcd 263.38 for $C_{16}H_{25}NO_2$).

Oxalate salt. The free amine **10b** (120 mg, 0.456 mmol) was dissolved in THF (2 mL), and oxalic acid dihydrate (86 mg, 0.68 mmol, 1.5 moleqs) in THF (1 mL) was added. A white solid precipitate was isolated (115 mg; 71%).

^{1}H NMR (DMSO-d_6): δ = 9.0–6.0 (broad signal, acidic protons), 6.85 (m, 1H), 6.28 (m, 1H), 6.23 (s, 1H), 4.25 (m, 1H), 3.25–3.05 (multiple signals, 2H), 2.9 (m, 2H), 2.75–2.5 (multiple signals, 2H), 1.95 (m, 1H), 1.65 (multiple signals, 3H), 1.25 (m, 6H), 0.9 (t, 3H). ^{13}C NMR (DMSO-d_6): δ = 164.6, 156.6, 153.9, 129.9, 111.9, 108.5, 102.9, 71.3, 50.1, 47.3, 30.7, 25.7, 25.2, 24.7, 22.7, 21.9, 13.9. M.p. = 152 °C (dec). LC-MS: *m/z* = 264.3 $[M+H]^+$, (calcd 263.38 for $C_{16}H_{25}NO_2$). UPLC-HRMS $[M+H]^+$: Calcd 264.1964, Found 264.1966 (0.8 ppm). UPLC: 92% purity. Elemental analysis C,H,N: Found 60.6, 7.7, 3.6, Calcd. 61.2, 7.7, 4.0 for $C_{16}H_{25}NO_2$ + 1 $C_2H_2O_4$ (FW=353.4).

*(R)-2-[(4-Iodobenzylamino)methyl]chroman-7-ol (**11a**)*

Free amine. Compound **9b** (171 mg, 0.389 mmol) was deprotected in 4M HCl in dioxane (3.5 mL) and isopropanol (3.5 mL). After work-up, an oil was obtained in 80% yield (123 mg).

^{1}H NMR (CD_3OD): δ = 7.65 (m, 2H), 7.15 (m, 2H), 6.80 (m, 1H), 6.27 (m, 1H), 6.23 (m, 1H), 4.05 (m, 1H), 3.80 (bs, 2H), 2.9–2.5 (multiple signals, 4H), 1.93 (m, 1H), 1.65 (m, 1H). ^{13}C NMR ($CDCl_3$): δ = 156.0, 154.4, 137.8, 137.7, 130.6, 130.1, 112.7, 109.1, 103.2, 93.1, 74.2, 53.6, 53.5, 26.2, 23.6. LC-MS: *m/z* = 396.2 $[M+H]^+$, (calcd 395.24 for $C_{17}H_{18}NO_2I$). MALDI-TOF-MS, *m/z* = 396.0 $[M+H]^+$.

Oxalate salt. The free amine **11a** (118 mg, 0.299 mmol) was dissolved in THF (4 mL), and oxalic acid dihydrate (49 mg, 0.389 mmol) in THF (1 mL) was added. A white solid was isolated (90 mg, 62%).

^{1}H NMR (DMSO-d_6): δ = 8.0–6.0 (broad signal acidic protons), 7.75 (m, 2H), 7.30 (m, 2H), 6.80 (m, 1H), 6.28 (m, 1H), 6.25 (s, 1H), 4.25 (m, 1H), 4.15 (s, 2H), 3.2–3.0 (multiple signals, 2H), 2.75–2.5 (multiple signals, 2H), 1.95 (m, 1H), 1.65 (m, 1H). ^{13}C NMR (DMSO-d_6): δ = 164.2, 156.5, 154.0, 137.4,

132.6, 132.2, 129.9, 111.9, 108.5, 102.9, 95.3, 71.7, 50.1, 50.0, 24.7, 22.8. M.p. = 211 °C (dec). LC-MS: *m/z* = 396.1 $[M+H]^+$, (calcd 395.24 for $C_{17}H_{18}NO_2I$). UPLC-HRMS $[M+H]^+$: Calcd 396.0460, Found 396.0466 (1.5 ppm). UPLC: 95% purity. Elemental analysis C,H,N: Found 48.4, 4.5, 2.3, Calcd. 47.0, 4.2, 2.9 for $C_{17}H_{18}NO_2I$ + 1 $C_2H_2O_4$ (FW=485.3).

*(R)-2-[(2-Iodobenzylamino)methyl]chroman-7-ol (**11c**)*

Free amine. Compound **9c** (209 mg, 0.48 mmol) was dissolved in a mixture of 4M HCl dioxane (2.4 mL) and isopropanol (2.4 mL). After 1 hour, extra amounts of 4M HCl in dioxane (1 mL) and isopropanol (l mL) were added. After work-up, a glassy product was obtained in a quantitative yield (188 mg).

^{1}H NMR ($CDCl_3$): δ = 7.82 (m, 1H), 7.40 (m, 1H), 7.35 (m, 1H), 6.95 (m, 1H), 6.76 (m, 1H), 6.35 (m, 1H), 6.30 (m, 1H), 4.10 (m, 1H), 4.05 (d, 1H), 3.90 (d, 1H), 2.9–2.75 (multiple signals, 2H), 2.75–2.5 (multiple signals, 2H), 1.8 (m, 1H), 1.65 (m, 1H). ^{13}C NMR ($CDCl_3$): δ = 155.9, 154.7, 140.6, 139.7, 130.2, 130.0, 129.3, 128.5, 112.8, 108.8, 103.4, 99.7, 74.4, 57.8, 53.0, 26.1, 23.7. LC-MS: *m/z* = 396.2 $[M+H]^+$, (calcd 395.24 for $C_{17}H_{18}NO_2I$).

Oxalate salt. The free amine **11c** (188 mg, 0.48 mmol) was dissolved in THF (2 mL) and oxalic acid dihydrate (132 mg, 1.05 mmol, 2.2 moleqs) in THF (1 mL) was added. A white solid residue was isolated (219 mg, 94%).

^{1}H NMR (DMSO-d_6): δ = 8.0–6.0 (broad signal acidic protons), 7.95 (m, 1H), 7.60 (m, 1H), 7.45 (m, 1H), 7.13 (m, 1H), 6.80 (m, 1H), 6.30–6.25 (multiple signals, 2H), 4.3–4.1 (multiple signals, 3H), 3.1 (m, 2H), 2.7–2.6 (multiple signals, 2H), 2.05 (m, 1H), 1.65 (m, 1H). ^{13}C NMR (DMSO-d_6): δ = 163.6, 156.5, 154.1, 139.4, 136.8, 130.3, 130.2, 129.9, 128.6, 112.0, 108.4, 103.0, 100.9, 72.3, 55.5, 50.9, 24.9, 22.8. M.p. = 209 °C (dec). LC-MS: *m/z* = 396.2 $[M+H]^+$, (calcd 395.24 for $C_{17}H_{18}NO_2I$). UPLC-HRMS $[M+H]^+$: Calcd 396.0460, Found 396.0466 (1.5 ppm). UPLC: 97% purity. Elemental analysis C,H,N: Found 46.8, 4.0, 2.6, Calcd. 47.0, 4.2, 2.9 for $C_{17}H_{18}NO_2I$ + 1 $C_2H_2O_4$ (FW=485.3).

*(R) 1-(4-Iodophenyl)-4-(4-(7-hydroxychroman-2-yl)-3-azabutyl)-piperazine (**11e**)*

Free amine. Compound **9d** (115 mg, 0.214 mmol) was dissolved in 4M HCl in dioxane (3.5 mL) and isopropanol (4 mL). The reaction was not complete after 3 hours, so the reaction mixture was evaporated to yield an oily product. A fresh solution of 4M HCl in dioxane was added, and after a further

90 minutes of stirring under N_2, the reaction was complete. A quantitative yield of an oil was obtained after work-up.

^{1}H NMR ($CDCl_3$): δ = 7.50 (m, 2H), 6.77 (m, 1H), 6.64 (m, 2H), 6.49 (s, 1H), 6.28 (m, 1H), 4.08 (m, 1H), 3.10 (m, 2H), 3.05 (m, 2H), 2.9–2.3 (multiple signals, 14H), 1.83 (m, 1H), 1.65 (m, 1H). ^{13}C NMR ($CDCl_3$): δ = 156.4, 154.5, 150.9, 137.7, 129.9, 117.7, 112.2, 109.2, 103.4, 81.0, 74.5, 56.4, 54.0, 52.6, 48.7, 46.0, 26.3, 23.7. LC-MS: *m/z* = 494.2 $[M+H]^+$, (calcd 493.39 for $C_{22}H_{28}N_3O_2I$). MALDI-TOF-MS, *m/z* = 494.0 $[M+H]^+$.

Oxalate salt. The free amine **11e** (105 mg, 0.214 mmol) was dissolved in THF (4 mL), and oxalic acid dihydrate (63 mg, 0.50 mmol, 2.3 moleqs) in THF (1 mL) was added. A white solid was isolated (93 mg, 57%).

^{1}H NMR (DMSO-d_6): δ = 8.0–6.0 (broad signal acidic protons), 7.5 (m, 2H), 6.85 (m, 1H), 6.8 (m, 2H), 6.28 (m, 1H), 6.23 (s, 1H), 4.3 (m, 1H), 3.35–3.1 (multiple signals, 8H), 2.8–2.6 (multiple signals, 8H), 2.0 (m, 1H), 1.65 (m, 1H). ^{13}C NMR (DMSO-d_6): δ = 162.9, 156.5, 153.8, 150.4, 137.3, 130.0, 117.8, 111.9, 108.6, 102.9, 80.7, 71.2, 52.9, 52.2, 50.2, 47.4, 43.7, 24.7, 22.7. M.p. = 201 °C. LC-MS: *m/z* = 494.2 $[M+H]^+$, (calcd 493.39 for $C_{22}H_{28}N_3O_2I$). UPLC-HRMS $[M+H]^+$: Calcd 494.1304, Found 494.1294 (2.0 ppm). UPLC: 99% purity. Elemental analysis C,H,N: Found 43.4, 4.8, 5.4, Calcd. 44.1, 4.5, 5.5 for $C_{22}H_{28}N_3O_2I$ + 3 $C_2H_2O_4$ (FW=763.5).

*(R)-2-[(4-(4-Fluorobutoxy)benzylamino)methyl]chroman-7-ol (**12a**)*

Free amine. Compound **9e** (124 mg, 0.308 mmol) was dissolved in a solution of 4M HCl in dioxane (2 mL) and isopropanol (2 mL). No starting compound was present according to LC-MS analysis, but there were some impurities present. After aqueous work-up, the crude product was purified by silica column chromatography (eluent: heptane/THF =1/1). Yield: 45 mg (41%) of a solid.

^{1}H NMR ($CDCl_3$): δ = 7.35 (d, 2H), 6.90 (d, 2H), 6.78 (m, 1H), 6.38 (multiple signals, 2H), 4.60 (m, 1H), 4.45 (m, 1H), 4.08 (m, 1H), 4.00 (t, 2H), 3.90 (dd, 2H), 2.9–2.5 (multiple signals, 4H), 2.0–1.75 (multiple signals, 5H), 1.7 (m, 1H). ^{13}C NMR ($CDCl_3$): δ = 158.3, 156.3, 154.5, 130.2, 130.1, 130.0, 114.6, 112.4, 109.2, 103.3, 84.6, 82.9, 74.2, 67.2, 53.6, 53.5, 27.3, 27.1, 26.3, 25.2, 23.7. LC-MS: *m/z* = 360.0 $[M+H]^+$, (calcd 359.44 for $C_{21}H_{26}NO_3F$). MALDI-TOF-MS, *m/z* = 360.1 $[M+H]^+$.

Oxalate salt. The free amine **12a** (87 mg, 0.242 mmol) was dissolved in THF (2 mL), and oxalic acid dihydrate (46 mg, 0.365 mmol, 1.5 moleqs) in THF (1 mL) was added. The residue was a white solid (68 mg, 68%).

^{1}H NMR (DMSO-d_6): δ = 7.5–5.0 (broad signal acidic protons), 7.45 (d, 2H), 6.95 (d, 2H), 6.8 (m, 1H), 6.3 (m, 1H), 6.25 (s, 1H), 4.55 (m, 1H), 4.45 (m, 1H), 4.25 (m, 1H), 4.1 (s, 2H), 4.0 (m, 2H), 3.2–3.0 (multiple signals, 2H), 2.75–2.6 (multiple signals, 2H), 1.95 (m, 1H), 1.85–1.7 (multiple signals, 4H), 1.65 (m, 1H). ^{13}C NMR (DMSO-d_6): δ = 164.4, 158.9, 156.5, 153.9, 131.6, 129.9, 124.0, 114.5, 111.9, 108.5, 102.9, 84.4, 82.8, 71.5, 67.1, 50.0, 49.5, 26.7, 26.5, 24.7, 22.7. M.p. = 177 °C. LC-MS: *m/z* = 360.1 $[M+H]^+$, (calcd 359.44 for $C_{21}H_{26}NO_3F$). UPLC-HRMS $[M+H]^+$: Calcd 360.1975, Found 360.1970 (1.4 ppm). UPLC: 95% purity. Elemental analysis C,H,N: Found 60.4, 6.0, 2.8, Calcd. 61.5, 6.3, 3.1 for $C_{21}H_{26}NO_3F + C_2H_2O_4$ (FW=449.5).

*(R)-2-[(2-(4-Fluorobutoxy)benzylamino)methyl]chroman-7-ol (**12b**)*

Free amine. Compound **9f** (227 mg, 0.563 mmol) was dissolved in a mixture of 4M HCl dioxane (2.4 mL) and isopropanol (2.4 mL). After 1 hour, an extra amount of 4M HCl in dioxane (1.5 mL) was added. After work-up, an oily product was obtained (202 mg, 100%).

^{1}H NMR ($CDCl_3$): δ = 7.25 (multiple signals, 2H), 6.95 (m, 1H), 6.90 (m, 1H), 6.75 (m, 1H), 6.40 (m, 1H), 6.27 (m, 1H), 4.45 (m, 1H), 4.36 (m, 1H), 4.1–4.0 (multiple signals, 4H), 3.80 (d, 1H), 2.85–2.5 (multiple signals, 4H), 2.0–1.75 (multiple signals, 5H), 1.65 (m, 1H). ^{13}C NMR ($CDCl_3$): δ = 157.0, 156.5, 154.6, 130.3, 129.9, 128.8, 126.5, 120.6, 112.4, 111.1, 109.1, 103.3, 84.5, 82.8, 74.4, 67.2, 53.2, 49.1, 27.4, 27.2, 26.3, 25.4, 25.3, 23.7. LC-MS: *m/z* = 360.3 $[M+H]^+$, (calcd 359.44 for $C_{21}H_{26}NO_3F$).

Oxalate salt. The free amine **12b** (202 mg, 0.563 mmol) was dissolved in THF (2 mL) and oxalic acid dihydrate (156 mg, 1.24 mmol, 2.2 moleqs) in THF (1 mL) was added. In this case, no precipitate was formed after addition, nor after 3 hours of stirring at rt, so diethylether was added to induce precipitation. Centrifugation, washing and drying gave a white solid residue (159 mg, 63%).

^{1}H NMR (DMSO-d_6): δ = 8.0–6.0 (broad signal acidic protons), 7.45 (m, 1H), 7.4 (m, 1H), 7.05 (m, 1H), 7.0 (m, 1H), 6.85 (m, 1H), 6.28 (m, 1H), 6.23 (s, 1H), 4.5 (m, 1H), 4.4 (m, 1H), 4.3 (m, 1H), 4.2 (q, 2H), 4.1 (m, 2H), 3.2–3.1 (multiple signals, 2H), 2.75–2.6 (multiple signals, 2H), 1.95 (m, 1H), 1.85–1.7

(multiple signals, 4H), 1.65 (m, 1H). ^{13}C NMR (DMSO-d_6): δ = 164.2, 156.9, 156.5, 153.9, 131.3, 130.6, 129.9, 125.1, 120.4, 111.9, 111.8, 108.5, 102.9, 84.4, 82.8, 71.5, 67.4, 50.2, 45.6, 26.7, 26.5, 24.7, 22.7. M.p. = 54 °C. LC-MS: *m/z* = 360.3 $[M+H]^+$, (calcd 359.44 for $C_{21}H_{26}NO_3F$). UPLC-HRMS $[M+H]^+$: Calcd 360.1975, Found 360.1978 (0.8 ppm). UPLC: 99% purity. Elemental analysis C,H,N: Found 61.3, 6.1, 2.8, Calcd. 61.5, 6.3, 3.1 for $C_{21}H_{26}NO_3F$ + $C_2H_2O_4$ (FW=449.5).

*(R) 1-(4-(2-Fluoroethoxy)phenyl)-4-((7-hydroxychroman-2-yl)-methyl)-piperazine (**12c**)*

Free amine. Compound **9g** (120 mg, 0.279 mmol) was dissolved in a solution of 4M HCl in dioxane (2.5 mL) and isopropanol (4 mL). A slightly colored solid was obtained.

^{1}H NMR (THF-d_8): δ = 7.75 (bs, 1H), 6.8–6.6 (multiple signals, 5H), 6.08 (m, 1H), 6.03 (m, 1H), 4.58 (m, 1H), 4.45 (m, 1H), 4.1–3.9 (multiple signals, 3H), 2.95 (bs, 4H), 2.7–2.4 (multiple signals, 8H), 1.98 (m, 1H), 1.6 (m, 1H). ^{13}C NMR (THF-d_8): δ = 157.7, 156.5, 153.4, 147.2, 130.2, 118.3, 115.7, 113.2, 108.5, 103.8, 83.5, 81.9, 74.6, 68.5, 68.3, 63.1, 55.0, 51.1, 27.1, 24.5. LC-MS: *m/z* = 387.3 $[M+H]^+$, (calcd 386.47 for $C_{22}H_{27}N_2O_3F$).

Oxalate salt. The free amine **12c** (108 mg, 0.279 mmol) was dissolved in THF (4 mL), and oxalic acid dihydrate (155 mg, 1.23 mmol, ca. 4.5 moleqs) in THF (1 mL) was added. A white solid residue was obtained (119 mg, 90%).

^{1}H NMR (DMSO-d_8): δ = 8.0–6.0 (broad signal acidic protons), 6.95–6.8 (multiple signals, 5H), 6.28 (m, 1H), 6.2 (s, 1H), 4.75 (m, 1H), 4.65 (m, 1H), 4.35 (m, 1H), 4.15 (m, 1H), 4.1 (m, 1H), 3.25–3.0 (multiple signals, 10H), 2.75–2.6 (multiple signals, 2H), 1.98 (m, 1H), 1.6 (m, 1H). ^{13}C NMR (DMSO-d_6): δ = 163.0, 156.5, 154.2, 152.1, 144.8, 129.9, 117.6, 115.1, 112.1, 108.3, 102.9, 83.1, 81.4, 71.5, 67.4, 67.2, 60.2, 52.5, 47.8, 25.4, 22.8. M.p. = 105 °C. LC-MS: *m/z* = 387.3 $[M+H]^+$, (calcd 386.47 for $C_{22}H_{27}N_2O_3F$). UPLC-HRMS $[M+H]^+$: Calcd 387.2084, Found 387.2078 (1.5 ppm). UPLC: 95% purity. Elemental analysis C,H,N: Found 60.3, 5.7, 5.5, Calcd. 60.5, 6.1, 5.9 for $C_{22}H_{27}N_2O_3F$ + $C_2H_2O_4$ (FW=476.5).

*(R) 1-(4-(2-Fluoroethoxy)phenyl)-4-(4-(7-hydroxychroman-2-yl)-3-azabutyl)-piperazine (**12d**)*

Free amine. Compound **9h** (200 mg, 0.422 mmol) was dissolved in a 4M HCl solution in dioxane (2 mL) and isopropanol (2 mL). The reaction was not

complete after 3 hours, so an extra portion of 4M HCl solution in dioxane was added (2 mL), and the mixture was stirred overnight at rt under N_2. A slightly colored oil was obtained after work-up. Yield: 160 mg (88%).

^{1}H NMR ($CDCl_3$): δ = 6.85 (m, 4H), 6.8 (m, 1H), 6.5 (m, 1H), 6.3 (m, 1H), 4.8 (m, 1H), 4.7 (m, 1H), 4.2 (m, 1H), 4.15 (multiple signals, 2H), 3.1–2.4 (multiple signals, 16H), 1.8 (m, 1H), 1.65 (m, 1H). LC-MS: *m/z* = 430.3 $[M+H]^+$, (calcd 429.54 for $C_{24}H_{32}N_3O_3F$).

Oxalate salt. The free amine **12d** (160 mg, 0.373 mmol) was dissolved in THF (4 mL), and oxalic acid dihydrate (300 mg, 2.38 mmol, ca. 6 moleqs) in THF (1 mL) was added. The isolated residue was a white solid (225 mg, 86%).

^{1}H NMR (DMSO-d_6): δ = 8.0–6.0 (broad signal acidic protons), 6.9–6.8 (multiple signals, 5H), 6.28 (m, 1H), 6.24 (s, 1H), 4.75 (m, 1H), 4.64 (m, 1H), 4.30 (m, 1H), 4.20 (m, 1H), 4.12 (m, 1H), 3.3–3.1 (multiple signals, 4H), 3.1 (m, 4H), 2.8–2.5 (multiple signals, 8H), 1.95 (m, 1H), 1.65 (m, 1H). ^{13}C NMR (DMSO-d_6): δ = 162.4, 156.5, 153.8, 151.8, 145.4, 130.0, 117.3, 115.1, 111.9, 108.6, 102.9, 83.1, 81.5, 71.2, 67.5, 67.3, 52.9, 52.4, 50.3, 49.0, 43.6, 24.7, 22.7. M.p. = 198 °C (dec). LC-MS: *m/z* = 430.3 $[M+H]^+$, (calcd 429.54 for $C_{24}H_{32}N_3O_3F$). UPLC-HRMS $[M+H]^+$: Calcd 430.2506, Found 430.2499 (1.6 ppm). UPLC: 99% purity. Elemental analysis C,H,N: Found 52.6, 5.4, 5.5, Calcd. 51.5, 5.5, 6.0 for $C_{24}H_{32}N_3O_3F$ + 3 $C_2H_2O_4$ (FW=699.6).

The synthesis of the precursors to [^{18}F]12a and [^{18}F]12d: phenols 13a and 13b

Precursor to [^{18}F]12a: (*R*) N-[7-(Methoxymethoxy)chroman-2-yl] methyl 4-hydroxybenzyl amine (13a).

The primary amine 8 (146 mg, 0.65 mmol), commercially available 4-hydroxybenzaldehyde (80 mg, 0.65 mmol) and acetic acid (43 mg, 0.72 mmol, 1.1 moleqs) were stirred in CH_2Cl_2 (4 mL) for 2.5 hours and at rt. According to ^{1}H NMR, the reaction was complete, so sodium triacetoxyborohydride (305 mg, 1.44 mmol, 2.2 moleqs) was added and the reaction mixture was left to stir for 18 hours at rt. Monitoring with LC-MS showed that conversion to the desired product was ca. 80%. The mixture was brought to a pH of 7 with a 0.1M NaOH aqueous solution, and was then extracted with CH_2Cl_2. Drying of the organic layer with Na_2SO_4, evaporation of the solvent and purification with silica column chromatography (hexane/ethyl acetate 1/1) gave the product in a yield of 76% (164 mg).

^{1}H NMR ($CDCl_3$): δ = 7.12 (m, 2H), 6.9 (m, 1H), 6.65 (m, 2H), 6.55 (multiple signals, 2H), 5.1 (s, 2H), 5.05 (bs, 2H), 4.2 (m, 1H), 3.75 (m, 2H), 3.4 (s, 3H), 2.9–2.6 (multiple signals, 4H), 1.9 (m, 1H), 1.7 (m, 1H). ^{13}C NMR ($CDCl_3$): δ = 156.4, 156.0, 155.0, 130.0, 129.9, 129.8, 115.8, 115.5, 109.0, 104.3, 94.5, 74.5, 55.9, 53.3, 53.2, 25.7, 23.9. LC-MS: *m/z* = 330.1 $[M+H]^+$, (calcd 329.40 for $C_{19}H_{23}NO_4$).

Precursor to [^{18}F]12d: the multistep synthesis to phenol 13b.

Compounds 15 and 16 were prepared according to a patent procedure [77].

*4-(4-Benzyloxy-phenyl)-piperazine-1-carboxylic acid tert butyl ester (**15**)*

4-(4-Hydroxyphenyl)-piperazin-1-carboxylic acid tert butyl ester (14) was prepared according to Tietze [73]. Compound 14 (2 g, 7.19 mmol), benzyl bromide (1.23 g, 7.19 mmol) and K_2CO_3 (0.99 g, 7.19 mmol) were mixed in DMF (2 mL). The reaction mixture was stirred at 50 °C under argon for 16 hours, and was then poured in water. The suspension was filtrated and the residue was purified with silica column chromatography (2% MeOH/$CHCl_3$). Yield: 1.94 g (73%). Analytical data were according to those reported in a patent [77]. ^{1}H NMR ($CDCl_3$): δ = 7.5–7.3 (multiple signals, 5H), 6.9 (multiple signals, 4H), 5.02 (s, 2H), 3.56 (t, 4H), 3.0 (t, 4H), 1.48 (s, 9H). LC-MS: *m/z* = 369.2 $[M+H]^+$, (calcd 368.48 for $C_{22}H_{28}N_2O_3$).

*1-(4-Benzyloxyphenyl)piperazine (**16**)*

Compound 15 (1.75 g, 4.75 mmol) was mixed with a 4N HCl dioxane solution (30 mL) and was stirred for 1 hour at rt. The reaction mixture was filtrated and washed with ethyl acetate to afford the HCl-salt, a white solid residue. Extraction using chloroform and a basic aqueous solution gave the amine product. Yield: 1.3 g (100%). Analytical data were according to those reported in a patent [77]. ^{1}H NMR ($CDCl_3$): δ = 7.5–7.3 (multiple signals, 5H), 6.9 (multiple signals, 4H), 5.0 (s, 2H), 3.0 (bs, 8H), 1.5 (bs, 1H). LC-MS: *m/z* = 269.3 $[M+H]^+$, (calcd 268.36 for $C_{17}H_{20}N_2O$).

*1-(4-Benzyloxyphenyl)-4-(2-N-(tertbutyl-carbamate)-ethyl)-piperazine (**17**)*

tert-Butyl N-(2-bromoethyl)carbamate was prepared according to a literature procedure [78]. Secondary amine 16 (0.4 g; 1.49 mmol) was mixed with DMF (5 mL), DIPEA (2.6 mL; 14.9 mmol; 10 moleqs) and tert-butyl N-(2-bromoethyl)carbamate (0.33 g: 1.49 mmol) yielding a suspension. The

mixture was stirred at 40 °C for 72 hours, and turned into a clear brown solution. Pouring into water gave a suspension that was extracted with diisopropyl ether. The organic layer was dried with Na_2SO_4 and evaporated till dryness; the crude product residue was purified using silica column chromatography (2/1 pentane/THF). Yield: 369 mg (60%).

^{1}H NMR ($CDCl_3$): δ = 7.5–7.3 (multiple signals, 5H), 6.9 (multiple signals, 4H), 5.0 (s, 2H), 4.95 (bs, 1H), 3.25 (m, 2H), 3.05 (m, 4H), 2.6 (m, 4H), 2.5 (t, 2H), 1.45 (s, 9H). ^{13}C NMR ($CDCl_3$): δ = 152.9, 145.9, 137.3, 128.5, 127.8, 127.4, 125.5, 118.0, 115.5, 79.2, 70.5, 57.2, 53.0, 50.5, 37.1, 28.4. LC-MS: *m/z* = 412.3 $[M+H]^+$, (calcd 411.55 for $C_{24}H_{33}N_3O_3$).

*1-(4-Benzyloxyphenyl)-4-(2-aminoethyl)-piperazine (**18**)*

BOC protected amine 17 (0.74 g; 1.79 mmol) was dissolved in CH_2Cl_2 (8 mL) and TFA (2 mL), and the solution was stirred for 1 hour at rt. Evaporation of the solvents and redissolution into (8 mL) and TFA (2 mL) was followed by further stirring at rt until ^{1}H NMR and TLC analyses showed that the BOC group had been deprotected. Dilution with $CHCl_3$ and washing of the organic layer with a 0.1 M NaOH (pH=10) to which NaCl was added to enhance the phase separation, was followed by drying of the organic layer with Na_2SO_4 and evaporation of the volatiles to yield a beige solid (528 mg, 95%).

^{1}H NMR ($CDCl_3$): δ = 7.5–7.3 (multiple signals, 5H), 6.9 (multiple signals, 4H), 5.0 (s, 2H), 3.15 (m, 4H), 2.8 (m, 2H), 2.6 (m, 4H), 2.5 (t, 2H), 1.65 (bs, 2H). LC-MS: *m/z* = 312.3 $[M+H]^+$, (calcd 311.43 for $C_{19}H_{28}N_3O$).

*(R) 1-(4-Benzyloxyphenyl)-4-(4-(7-(methoxymethoxy)chroman-2-yl)-3-azabutyl)-piperazine (**19**)*

A solution of tosylate 6 (300 mg, 0.793 mmol) in 1/1 dioxane /DMSO (1 mL) was added to a mixture of DIPEA (1.4 mL, 7.93 mmol, 10 moleqs) and amine 18 (306 mg, 0.952 mmol, 1.2 moleqs) in 1/1 dioxane /DMF (1 mL). This mixture was stirred overnight at 90 °C. According to LC-MS there was still some tosylate present so DIPEA (0.5 mL) was added and the reaction mixture was stirred at 90 °C for another 24 hours. The mixture was then poured into water (pH became ca. 9–10), and the aqueous layer was extracted with $CHCl_3$. The organic layer was washed with NaCl (aq), dried with Na_2SO_4 and concentrated to the crude product that was purified with alumina column chromatography (1/1 ethyl acetate/pentane). Yield: 156 mg (32%).

^{1}H NMR ($CDCl_3$): δ = 7.45–7.3 (multiple signals, 5H), 6.9 (multiple signals, 5H), 6.55 (multiple signals, 2H), 5.1 (s, 2H), 5.0 (s, 2H), 4.15 (m, 1H), 3.4 (s, 3H), 3.1 (m, 4H), 2.9–2.7 (multiple signals, 6H), 2.6 (multiple signals, 6H), 1.95 (multiple signals, 2H), 1.75 (m, 1H). ^{13}C NMR ($CDCl_3$): δ = 156.5, 155.2, 152.9, 146.0, 137.4, 129.9, 128.5, 127.8, 127.4, 118.0, 115.5, 114.9, 108.9, 104.4, 94.5, 75.1, 70.5, 57.8, 55.9, 54.3, 53.4, 50.6, 46.5, 25.8, 24.0. LC-MS: *m/z* = 540.4 $[M+Na]^+$, 518.5 $[M+H]^+$ and 259.8 $[M+2H]^{2+}$ (calcd 517.67 for $C_{31}H_{39}N_3O_4$).

*(R) 1-(4-Hydroxyphenyl)-4-(4-(7-(methoxymethoxy)chroman-2-yl)-3-azabutyl)-piperazine (**13b**)*

The benzylated molecule 19 (156 mg, 0.30 mmol) was dissolved in EtOH and Pd/C catalyst (Degussa type) was added. The mixture was shaken under hydrogen at 70 psi, and the conversion was monitored by ^{1}H NMR. Filtration over two paper filters and one using a syringe filter (45 μm regenerated cellulose) gave a yield of 121 mg product (94%).

^{1}H NMR ($CDCl_3$): δ = 6.9 (m, 1H), 6.8 (m, 2H), 6.75 (m, 2H), 6.5 (multiple signals, 2H),5.1 (s, 2H), 4.2 (m, 1H), 3.4 (s, 3H), 3.1 (m, 4H), 2.9–2.7 (multiple signals, 6H), 2.6 (multiple signals, 6H), 1.95 (m, 1H), 1.75 (m, 1H). ^{13}C NMR ($CDCl_3$): δ = 156.5, 155.1, 150.3, 145.4, 130.0, 118.5, 116.0, 115.5, 109.0, 104.4, 94.5, 74.7, 57.4, 55.9, 54.1, 53.3, 50.8, 46.1, 25.8, 24.0. LC-MS: *m/z* = 428.4 $[M+H]^+$ and 214.7 $[M+2H]^{2+}$, (calcd 427.55 for $C_{24}H_{33}N_3O_4$).

The preparation of amine and aldehyde building blocks for coupling to tosylate 3 (Route A), tosylate 6 (Route B) or amine 8 (Route C)

*tert-Butyl (4-(4-fluorobutoxy)-benzyl)-carbamate (**20**)*

tert-Butyl (4-hydroxybenzyl)-carbamate, as prepared [79] from the HBr salt of 4-hydroxy-benzylamine (3.17 g, 14.2 mmol), was mixed with commercially available 1-bromo-4-fluoro-butane (2.62 g, 17 mmol, 1.2 moleqs) and K_2CO_3 (2.36 g, 17 mmol, 1.2 moleqs) in MeCN (75 mL). The reaction mixture was stirred overnight at 80 °C under an inert argon atmosphere, was cooled down to rt and was filtered to remove salts. The filtrate was concentrated and the crude product was purified with silica column chromatography (2% MeOH/$CHCl_3$). Drying under vacuum removed traces of 1-bromo-4-fluorobutane. Yield: 2.9 g (68%).

^{1}H NMR ($CDCl_3$): δ = 7.2 (m, 2H), 6.85 (m, 2H), 4.8 (bs, 1H), 4.55 (m, 1H), 4.45 (t, 1H), 4.2 (m, 2H), 3.95 (t, 2H), 1.95–1.8 (multiple signals, 4H), 1.45 (s, 9H). ^{13}C NMR ($CDCl_3$): δ = 158.2, 155.8, 131.0, 128.8, 114.5, 84.5, 82.9, 79.1, 67.2, 44.1, 28.3, 27.2, 27.0, 25.2, 25.1. LC-MS: *m/z* = 242.0 $[M\text{-}C_4H_8]^+$, (calcd 297.37 for $C_{16}H_{24}NO_3F$).

*4-(4-Fluorobutoxy)-benzyl amine (**21**)*

BOC-protected amine 20 (0.56 g, 1.87 mmol) was stirred at rt for 10 minutes in 4M HCl in dioxane (0.6 mL). The reaction mixture developed into a hazy suspension. The mixture was evaporated to dryness and the residue was dissolved in water that was adjusted to a basic pH using a NaOH solution. The product was extracted using CH_2Cl_2. the organic layer was dried using Na_2SO_4 and was evaporated to yield the desired amine product. Yield: 261 mg (71%).

^{1}H NMR ($CDCl_3$): δ = 7.2 (m, 2H), 6.85 (m, 2H), 4.55 (m, 1H), 4.45 (t, 1H), 4.0 (t, 2H), 3.8 (s, 2H), 1.9 (multiple signals, 4H), 1.4 (bs, 2H). ^{13}C NMR ($CDCl_3$): δ = 157.8, 135.6, 128.2, 114.5, 84.5, 82.9, 67.2, 45.9, 27.3, 27.1, 25.3, 25.2. LC-MS: *m/z* = 198.1 $[M+H]^+$, 181.3 $[M\text{-}NH_2]^+$, (calcd 197.25 for $C_{11}H_{16}NOF$).

*2-(4-Fluorobutoxy)-benzaldehyde (**22**)*

2-Hydroxybenzalhyde (1 g, 8.18 mmol) and 1-bromo-4-fluorobutane (1.52 g, 9.8 mmol, 1.2 moleqs), both commercially available, were mixed with K_2CO_3 (2.26 g, 16.3 mmol, 2 moleqs) in DMF (40 mL). The suspension was stirred overnight under argon at an oil bath temperature of 50 °C. The next day the reaction mixture was filtrated and diluted with water, so that the product could be extracted from the water layer using diethyl ether (twice). The ether layer was washed twice with water and once with a saturated NaCl solution and was then dried with Na_2SO_4. Starting bromide was still present in the product, but it could be removed by co-evaporation with diisopropylether. Yield: 1.43 g (89%).

^{1}H NMR ($CDCl_3$): δ = 10.5 (s, 1H), 7.8, (m, 1H), 7.55 (m, 1H), 7.0 (m, 2H), 4.60 (m, 1H), 4.46 (m, 1H), 4.13 (t, 2H), 2.05–1.8 (multiple signals, 4H). ^{13}C NMR ($CDCl_3$): δ = 189.6, 161.2, 135.9, 128.3, 124.8, 120.6, 112.4, 84.3, 82.7, 67.8, 27.2, 27.0, 25.2, 25.1. GC-MS: *m/z* = 121 $[M\text{-}C_4H_8F]^+$, (calcd 196.22 for $C_{11}H_{13}O_2F$).

*1-(2-N-(tert-Butyl carbamate)ethyl)-4-(4-iodophenyl)-piperazine (**23**)*

1-(4-Iodophenyl)-piperazine [72] (4.6 g, 15.1 mmol), tert-butyl N-(2-bromoethyl)carbamate [78] 3.7 g, 16.6 mmol, 1.1 moleqs.) and DIPEA (5.3 mL, 30.4 mmol, 2 moleqs.) were dissolved in MeCN (30 mL). The mixture was stirred overnight at 50 °C and was kept under argon. The reaction mixture was evaporated till dryness and was redissolved in $CHCl_3$. The solution was washed two times with water and once with a NaCl solution, and was then dried over Na_2SO_4. After concentration, the crude product was purified with silica column chromatography (1% MeOH /$CHCl_3$). Yield 80%.

^{1}H NMR ($CDCl_3$): δ = 7.50 (m, 2H), 6.65 (m, 2H), 4.95 (bs, 1H), 3.25 (m, 2H), 3.15 (m, 4H), 2.6 (m, 4H), 2.5 (t, 2H), 1.45 (s, 9H). LC-MS: *m/z* = 432.1 $[M+H]^+$, (calcd 431.32 for $C_{17}H_{26}N_3O_2I$).

*1-(2-Aminoethyl)-4-(4-iodophenyl)-piperazine (**24**)*

The BOC protected amine 23 (1.58 g, 3.65 mmol) was added slowly to a concentrated 10M HCl solution in water (2 mL). The reaction was stirred for 15 minutes at rt, was diluted with water (50 mL) and was adjusted to a pH of 9 to 10 using a NaOH solution in water. The product was isolated by extraction of the water layer with ethyl acetate (twice), drying of the organic layer over Na_2SO_4 and evaporation of the volatiles. Yield: 0.78 g (65%).

^{1}H NMR ($CDCl_3$): δ = 7.45 (m, 2H), 6.75 (m, 2H), 3.1 (m, 4H), 3.0 (bs, 2H), 2.65 (t, 2H), 2.5 (m, 4H), 2.35 (m, 2H). ^{13}C NMR ($CDCl_3$): δ = 150.9, 137.7, 118.0, 81.2, 61.1, 53.0, 48.7, 38.8. LC-MS: *m/z* = 332.1 $[M+H]^+$, (calcd 331.20 for $C_{12}H_{18}N_3I$).

*1-(2-N-(tert-Butyl carbamate)ethyl)-4-(4-(4-fluoroethoxy)phenyl)-piperazine (**25**)*

1-(4-(2-Fluoroethoxy)-phenyl)-piperazine [73] (1.88 g, 8.4 mmol), tert-butyl N-(2-bromoethyl)carbamate [78] (2.07 g, 9.24 mmol, 1.1 moleqs) and DIPEA (mL) were mixed in MeCN (20 mL). The mixture was stirred overnight under argon at an oil bath temperature of 50 °C. The reaction mixture was concentrated and redissolved in CH_2Cl_2 to enable washing with water (twice) and with a saturated NaCl solution (once). The organic layer was dried with Na_2SO_4 and was concentrated to afford crude product that was purified using silica column chromatography (elution gradient starting with $CHCl_3$ and finally using 3% MeOH/ $CHCl_3$). After evaporation of the solvent a yellowish solid was obtained. Yield: 2.42 g (78%).

^{1}H NMR ($CDCl_3$): δ = 6.85 (multiple signals, 4H), 4.95 (bs, 1H), 4.75 (m, 1H), 4.65 (m, 1H), 4.2 (m, 1H), 4.15 (m, 1H), 3.25 (m, 2H), 3.05 (m, 4H), 2.6 (m, 4H), 2.5 (t, 2H), 1.45 (s, 9H). ^{13}C NMR ($CDCl_3$): δ = 155.9, 152.5, 146.2, 118.0, 115.5, 82.9, 81.2, 79.0, 67.8, 67.6, 57.2, 53.0, 50.4, 37.1, 28.4.

*1-(2-Aminoethyl)-4-(4-(4-fluoroethoxy)phenyl)-piperazine (**26**)*

The BOC protected amine 25 (2.42 g, 6.58 mmol) was stirred in concentrated 10M HCl solution in water (20 mL). A thick white foam formed, and after 20 minutes water (75 mL) was added as well as solid NaOH to adjust the pH to about 10. The product was extracted from the water layer using CH_2Cl_2 (2 times). Drying of the collected organic layers (Na_2SO_4) and after evaporation of the solvent gave a white solid. Yield: 1.47 g (84%).

^{1}H NMR ($CDCl_3$): δ = 6.85 (multiple signals, 4H), 4.75 (m, 1H), 4.65 (m, 1H), 4.2 (m, 1H), 4.15 (m, 1H), 3.05 (m, 4H), 2.8 (t, 2H), 2.6 (m, 4H), 2.45 (t, 2H), 1.4 (bs, 2H). ^{13}C NMR ($CDCl_3$): δ = 152.4, 146.2, 117.9, 115.4, 82.8, 81.1, 67.7, 67.5, 61.1, 53.3, 50.4, 38.7. LC-MS: *m/z* = 268.3 $[M+H]^+$, (calcd 267.35 for $C_{14}H_{22}N_3OF$).

The preparation of [^{18}F]fluoroalkylation precursors and reference compounds: tosylates 27–30

*1,4-Butanediol ditosylate (**27**)*

p-Toluenesulfonyl chloride (3.17 g, 16.6 mmol) was dissolved in 10 mL of dry CH_2Cl_2. To this solution 3.0 mL (2.29 g, 22.7 mmol) of dry triethylamine was added. The mixture was cooled to 0 °C in an ice bath and 610 μL (616 mg, 7.6 mmol) of dry 1,4-butanediol was added. After 30 min of stirring, another 60 μL of 1,4-butanediol was added. The mixture was left to stir overnight, with the reaction mixture temperature coming up to rt. On the next day, the mixture was diluted with an extra portion of CH_2Cl_2 (15 mL), cooled to 0 °C and acidified by slowly adding 50 mL 0.8M HCl. The organic layer was separated and washed with 0.3M HCl (3×50 mL). The CH_2Cl_2 solution of the crude product was then concentrated in vacuo and the product was purified on a silica column eluted with hexane/ CH_2Cl_2/ethyl acetate (6/6/1) to yield 1.93 g of final product as white crystals. Yield: 58%.

^{1}H-NMR (300 MHz, $CDCl_3$) δ: 7.76 (d, J = 8.4 Hz, 4H), 7.35 (d, J = 8.4 Hz, 4H), 3.95–4.03 (m, 4H), 2.45 (s, 6H), 1.65–1.74 (m, 4H).

*1,2-Ethanediol ditosylate (**28**)*

This compound was prepared and isolated in as similar fashion as its butane-spaced counterpart 27. Analytical data were according to expectations.

*4-Fluorobutyl tosylate (**29**)*

Tetrabutylammonium fluoride trihydrate (66 mg, 0.25 mmol) was dried by co-evaporation in vacuo with three 3 mL portions of acetonitrile (the temperature in the flask was not allowed to rise above 30 °C to prevent decomposition of the tetrabutyl ammonium fluoride). Then the dried tetrabutyl ammonium fluoride was redissolved in a small quantity of dry acetonitrile and this solution was added to a solution of 1,4-butanediol ditosylate (100 mg, 0.25 mmol). The reaction was conducted in refluxing acetonitrile for 24 h, and the conversion was monitored by TLC on silica plates (hexane/ethyl acetate 2/1, Rf = 0.75). After the reaction ended, acetonitrile was evaporated in vacuo, the residue redissolved in hexane/ethyl acetate (2/1 v/v) and the product was purified on a silica column eluted with hexane/ethyl acetate (2/1 v/v) to yield 30 mg of final product as brownish crystals. Yield: 48%.

^{1}H-NMR (300 MHz, $CDCl_3$) δ: 7.79 (d, J = 8.1 Hz, 2H), 7.35 (d, J = 8.1 Hz, 2H), 4.44 (dt, J_1 = 47.0 Hz, J_2 = 5.6 Hz, 2H), 4.08 (t, J = 4.08 Hz, 2H), 2.46 (s, 3H), 1.67–1.84 (m, 4H).

*2-Fluoroethyl tosylate (**30**)*

2-Fluoroethyl tosylate was synthesized according to the same protocol as 1,4-butanediol ditosylate. Instead of 1,4-butanediol, 2-fluoroethanol (240 μL, 268 mg, 4.2 mmol) was reacted with p-toluenesulfonyl chloride (755 mg, 4.0 mmol). Yield: 760 mg of final product was obtained (86%) as a colorless slightly yellowish oil.

^{1}H-NMR (200 MHz, $CDCl_3$) δ: 7.82 (d, J = 7.6 Hz, 2H), 7.37 (d, J = 6.8 Hz, 2H), 4.58 (dt, J_1 = 47.0 Hz, J_2 = 4.2 Hz, 2H), 4.27 (dt, J_1 = 27.6 Hz, J_2 = 4.0 Hz, 2H), 2.48 (s, 3H).

Cell culturing and preparation of membranes

Human embryonic kidney 293 cells (HEK293) stably expressing the human dopamine receptor subtypes were cultured in RPMI 1640 medium with 2 mM L-glutamine in the additional presence of 100 U/ml penicillin, 100 U/ml streptomycin. To maintain selection pressure, 50 μg/ml neomycin and

5 μg/ml puromycin was also added to the medium of cells expressing dopamine D_2L, D_2S, D_3 and D_4 receptors, and D_1 and D_5 receptors, respectively. Cells were harvested by scraping the culture dishes, washed by centrifugation at 200 g and afterwards lysed in ice-cold buffer containing 5 mM TRIS and 5 mM $MgCl_2$ at pH 7.4. The suspension was homogenized with 8 up and down strokes in a glass/teflon homogenizer and centrifuged twice for 1 h at 30,000 g at 4 °C. Pellets were resuspended in buffer (50 mM TRIS pH 7.4) and rehomogenized with 4 up and down strokes in the glass/teflon homogenizer, aliquots were frozen in liquid nitrogen and stored at −80 °C. Protein content was measured by using the method of Bradford [80]. For experiments on dopamine D_2S and D_3 receptors, membrane preparations were obtained from PerkinElmer (Waltham USA).

Receptor binding assays

For the radioligand experiments the samples were thawed and re-homogenized in Mg-containing buffer (50 mM TRIS, 5 mM KCl, 2 mM $CaCl_2$ and 2 mM $MgCl_2$ pH 7.4) to allow formation of the agonist high-affinity state. Re-homogenization was done with a short burst (10 sec) of an ultra turrax at full speed. Binding experiments were performed with 40–60 μg protein per assay, an assay volume of 1000 μl, a radioligand concentration of 0.15 nM for the [^{3}H]spiperone (D_2L, D_2S, D_3 and D_4 receptors) assays and 1.5 nM for [^{3}H]SCH23390 (D_1 and D_5 receptor) assay with an incubation time of 2 h at 25 °C and a pre-incubation of 15 minutes at 25 °C. Non-specific binding was defined using 1 μM (+)-butaclamol (antagonist for dopamine receptors). To avoid oxidation of the compounds 0.05% ascorbic acid was added to all solutions. All experiments were performed in duplicate in 96 well platform, reactions were terminated by rapid vacuum filtration over Whatman GF/C filter plate with ice-cold buffer (50 mM TRIS). For the D_3 receptor binding experiments plates were pre-coated with 0.1 % PEI. Filter radioactivity was measured in a PerkinElmer Topcount with Microscint-O cocktail as scintillant. The competition experiments were analysed using the Prism programme (version 5.01, Graphpad Software, San Diego, Calif. USA) fitting sigmoidal curves to the data. Resulting IC_{50} values were converted to K_i values based upon the Cheng-Prusoff equation [38].

cAMP accumulation

To determine concentrations of cAMP formed in the assay the LANCE™ cAMP 384 kit of PerkinElmer was used according to the manufacturer's pro-

tocol. Transfected HEK 293 cells stably expressing the dopamine D_2L were cultured as mentioned before. They were detached from the surface of the culture dish with 2 ml dissociation solution and washed with HBSS and after that resuspended in a standard buffer (SB) containing HBSS 0.05% BSA (and 5 mM HEPES. The stimulation solutions contained SB with 1.0 mM 3-isobutyl-1-methylxanthine (IBMX), 63.2 μM forskolin and the different concentrations of the dopamine agonists. After the stimulation solutions were added to the well plate the cell suspensions (diluted to 6000 cells/well) were added in a 1:1 ratio so the final concentrations of IBMX and forskolin in the assay were 0.5 mM and 31.6 μM, respectively. The plate was incubated for 30 min at room temperature for the stimulation and subsequently different detection reagents and antibody solutions were added to a total volume of 20 μl/well. Measurements were carried out on a Victor 2 plate reader (Wallac, PerkinElmer, Zaventum, Belgium) 3 hours after adding the detection mixtures.

Lipophilicity

Lipophilicity (clog*P* and clog*D*) of the unlabeled compounds was calculated using the BiologP (New ClogP) calculator program from the University of Massachusetts, Boston:

http://intro.bio.umb.edu/111-112/OLLM/111F98/newclogp.html

LogD of the ^{18}F-labeled compounds was determined using radioactivity remaining on the HLB cartridge after its elution with ethanol during the formulation procedure (*vide infra*). The cartridge was dried for 5 min in strong N_2 flow and eluted with at least 1.5 ml n-octanol. Then 500 μl of octanol eluate was mixed with 500 μl 1 M phosphate buffer pH 7.4 and vigorously vortexed for 5 min. After that, the mixture was centrifuged at 17 000 g for 10 min and 3×100 μl aliquots of organic and aqueous phase were loaded into a gamma-counter for radioactivity measurement. To correct for possible presence of radioactive impurities in the tracer, aliquots of organic and aqueous phases were later analyzed by radio-TLC and the counts obtained from the gamma-counter were corrected according to the percentage of impurities found in aqueous and organic phases. LogD was calculated with the formula:

$$\mathrm{LogD} = \lg\left(\frac{\mathrm{CPM}_{\mathrm{org}} \times \mathrm{X}_{\mathrm{org}}^{\mathrm{tracer}}}{\mathrm{CPM}_{\mathrm{aq}} \times \mathrm{X}_{\mathrm{aq}}^{\mathrm{tracer}}}\right),$$

where $\mathrm{CPM}_{\mathrm{org}}$ is the mean cpm in the organic aliquots, $\mathrm{X}_{\mathrm{org}}^{\mathrm{tracer}}$ is the mean

percentage of radioactivity accounting for intact tracer in organic aliquots (as determined from radio-TLC) and CPM_{org} and X_{org}^{tracer} are the corresponding values for the aqueous phase.

For each tracer batch used for logD determination, the experiment was conducted in duplicate. LogD values are means calculated from at least two independent experiments.

Materials (in vitro experiments)

The transfected dopamine receptor cell lines were a generous gift of Prof. Gross (Abbott). Human D_2S and D_3 membranes were obtained from Perkin-Elmer (Waltham USA). [^{3}H]spiperone (molar radioactivity 16.2 Ci/mmol) and [^{3}H]SCH23390 (molar radioactivity 73.1 Ci/mmol) were obtained from PerkinElmer (Boston USA). (+)butaclamol, R(−)-propylnorapomorphine HCl and dopamine HCl were obtained from Sigma-Aldrich (Zwijndrecht, The Netherlands). (+)-PHNO HCl was obtained from Axon Medchem (Groningen, The Netherlands).

Radiochemistry

*Preparation of [^{18}F]**12a***

^{18}F-fluoride in enriched $H_2{}^{18}O$ water was adsorbed on an anion-exchange column (QMA) and later eluted into a reaction vial with 1–1.5 ml of 1.5 mg/ml K_2CO_3, 5 mg/ml Kryptofix solution in 9:1 v/v mixture of acetonitrile and water. After the elution of QMA, acetonitrile and water were evaporated at 130 °C under nitrogen flow. For further water removal, 1 ml anhydrous acetonitrile was added into the reaction vial and evaporated. Then 5 mg of 1,4-butanediol ditosylate (27) in 1 ml anhydrous acetonitrile was added into the vial, the vial was sealed, and the reaction was carried out for 4 min at 130 °C followed by cooling for 5 min . One ml of water was added to the cooled reaction mixture and the resulting mixture was loaded into the HPLC loop. 4-[^{18}F]fluorobutyltosylate was purified by reverse-phase HPLC using Alltima C18 5µ 250×10 mm column eluted with acetonitrile/10 mM H_3PO_4 (65/35 v/v) at 5 ml/min (retention time 7.0 min, k' = 3.9; as confirmed using the reference compound 4-fluorobutyltosylate 29). The collected radioactive fraction was diluted 2–3 fold with water and 4-[^{18}F]fluorobutyltosylate was adsorbed on a tC18 light Seppak cartridge. The cartridge was rinsed with 5 ml pure water and dried for 5 min in strong nitrogen flow. Afterwards 4-[^{18}F]fluorobutyltosylate was eluted from the cartridge with 0.7 ml

dry DMF into a v-vial containing 0.6 mg the precursor 13a, 30 μl dry DMF and 2–3 mg NaH. The reaction vial was sealed and the alkylation reaction was conducted for 10 min at 120 °C, then 1 ml 0.4 M HCl was added into the vial with a syringe. Then the MOM-group was deprotected which lasted 10 min at 120 °C. [^{18}F]**12a** was purified by reverse-phase HPLC using Alltima C18 5μ 250×10 mm column eluted with acetonitrile/10 mM H_3PO_4 (40/60 v/v) at 5 ml/min (retention time 9.8 min, k' = 5.4 (see Scheme 3).

The collected HPLC fraction was diluted with 2–3 volumes of water and [^{18}F]**12a** was adsorbed on a Oasis HLB SPE cartridge. The cartridge was rinsed with 5 ml pure water and [^{18}F]**12a** was then eluted with 1–2 ml absolute ethanol (typically 20–40% recovery). After the partial or complete evaporation of ethanol in nitrogen flow (with or without application of vacuum) the tracer was formulated in physiological saline (ethanol content in the formulated tracer was kept below 10%). The identity of [^{18}F]**12a** was confirmed by co-elution with the unlabeled **12a** on reverse-phase HPLC and radio-TLC. From the same data radiochemical purity was assessed. Reverse-phase HPLC was carried out on Platinum EPS 5μ 250×4.6 column eluted with acetonitrile/physiological saline/formic acid (70/30/0.1 v/v) at 2 ml/min (retention time 6.4 min, k' = 4.5). For quality control radio-TLC was carried out on silica plates eluted with dichloromethane/methanol/ammonia (100/5/1, R_f = 0.25) and ethyl acetate/methanol/triethylamine (100/5/1, R_f = 0.5).

*Preparation of [^{18}F]**12d***

The procedure described above for [^{18}F]**12a** was also used for the preparation of [^{18}F]**12d**, with the following modifications: Ethylene glycol ditosylate (28) and precursor 13b were used instead of 1,4-butanediol ditosylate (27) and precursor 13a, respectively. 2-[^{18}F]fluoroethyl tosylate purification conditions were: Alltima C18 5μ 250×10 mm column eluted with acetonitrile/10 mM sodium acetate buffer pH 4.0 (60/40 v/v) at 5 ml/min (tR = 6.8 min, k'= 3.8; as confirmed using the reference tosylate 30). At the end of the deprotection step, the reaction mixture was diluted with 10 ml water, titrated with 1 M NaOH to pH of 4–7 and then put through the Oasis HLB SPE cartridge. Adsorbed radioactivity was then eluted from the cartridge with 1 ml acetonitrile/DMF mixture (1/1 v/v). The eluate was further diluted with water to a total volume of 1.5–2 ml and injected onto the Alltima C18 5μ 250×10 mm HPLC column for purification of [^{18}F]**12d**, (see Scheme 3).

[^{18}F]**12d** purification conditions were: Alltima C18 5μ 250×10 mm column eluted with a gradient of acetonitrile in 10 mM sodium acetate buffer: iso-

cratic 45% acetonitrile during the first 2 minutes, then a linear decrease from 45% at 2 minutes to 30% acetonitrile at 15 minutes (retention time of [^{18}F]12d, 10.6 min, k' = 5.9.

HPLC conditions for the identity confirmation and RCP assessment were: Platinum EPS 5μ 250×4.6 column eluted with acetonitrile/10 mM phosphate buffer pH 7 (65/35 v/v) at 2 ml/min (t_R = 11.0 min, k' = 7.3).

Quality control TLC conditions were: dichloromethane:methanol:ammonia 100:5:1 (R_f = 0.25) and ethyl acetate:methanol:ammonia:triethylamine 100:5:5:1 (R_f = 0.3). Before putting radioactive samples onto the TLC plates, drops of 12d oxalate standard solution containing 2 μg of compound were put onto the start positions of each lane to exclude on-plate decomposition of no-carrier-added ^{18}F-labeled compound.

Autoradiography

Frozen brains of young (10–12 weeks of age; 300–350 g body-weight) male Sprague-Dawley rats (Harlan, Netherlands) were cut into two halves along the sagittal symmetry plane. Each half was mounted, lateral side up, on a paper slide pre-treated by Tissue-Tek fixing cocktail (Sakura, the Netherlands) and fixed by placing it onto a Petri dish floating on liquid nitrogen. After fixing, brains were cut at −12 °C into sagittal slices 20 μm thick using a Leica microtome, and the slices were thaw-mounted on Superfrost (70×22 mm, Fischer) adhesive slides. Only slices containing both striatal and cerebellar regions (representing non-specific binding) were used. Slides were organized in pairs and in each pair new slices were mounted alternately on the first or the second slide of the pair, so that slices in corresponding positions on the two slides forming a pair would represent adjacent tissue layers. The slices were allowed to dry, then put into storage boxes with dessicator (silicagel) bags and kept at −80 °C till they were used (no longer than 1 week).

On the day of the experiment the slides with mounted slices were taken out of storage and allowed to come to room temperature for 5–10 minutes. After that, incubation buffer (50 mM Tris-HCl, 5 mM KCl, 2 mM $CaCl_2$, 2 mM $MgCl_2$, 120 mM NaCl, pH 7.4 25 °C) was applied to the slides using an automatic pipette (1–1.2 ml/slide) and the slides were pre-incubated for 15 min at room temperature. The pre-incubation buffer was then removed and the slides were placed into staining jars containing incubation buffer and radioligand ([^{18}F]**12a** or [^{18}F]**12d**) at the concentration of about 5 nM (4.5±3.6 nM for [^{18}F]**12a**; 5.8±1.6 nM for [^{18}F]**12d**; (*n*=4)). Four condi-

tions were tested: radioligand only, radioligand in NaCl-free buffer, radioligand and 10 μM raclopride (non-specific binding only) and radioligand and 100 μM GTP (low-affinity state only). The slides were incubated for 35 min at 37 °C, then washed once with ice-cold incubated buffer (3.5 min) and dipped for 30 sec into ice-cold sterile water to remove buffer salts.

After drying the slides in a stream of room-temperature air, they were exposed on phosphor storage screens for 6–10 hours. Afterwards the storage screens were read by Cyclone Storage Phosphor System (Packard Instruments Co). Quantification of plate readings was done with Optiquant software (version 3.00, Packard Instruments Co), drawing regions of interest manually on the striatum and cerebellum.

The animal experiments were performed by licensed investigators in compliance with the Law on Animal Experiments of The Netherlands. The protocol was approved by the Committee on Animal Ethics of the University of Groningen. The rats were maintained at a 12-h light/12-h dark regime and were fed standard laboratory chow ad libitum.

Acknowledgements

J.A.J.M. (Jef) Vekemans, Eindhoven University of Technology, (TU/e), is thanked for his advice on synthetic design; J.L.J. (Joost) van Dongen and R.A.A. (Ralf) Bovee (both TU/e) are thanked for their expertise on and execution of the HRMS measurements and the elemental analyses, respectively. Prof. E.W. (Bert) Meijer (TU/e and ICMS Eindhoven), is thanked for enabling the execution of the synthetic part of the presented research. Jan Keijser (Center for behavior and neurosciences, University of Groningen) is thanked for his advice on the design and execution of in vitro autoradiography experiments. Jan Koerts (laboratory of pathology and medical biology, UMCG) is thanked for providing access to the equipment needed for the preparation of brain slices. This work has been supported by a grant from the Dutch Technology Foundation STW (grant 10127).

Conflict of interest

AGMJ is an employee of GE Healthcare, a company marketing the DA $D_{2/3}$ receptor antagonist radiopharmaceutical [^{123}I]IBZM. MCM is an employee of Boehringer Ingelheim, a company marketing the DA D_2 agonist pramipexole. JB is consultant at GE Healthcare. The other authors declare that they have no conflict of interest.

REFERENCES

1. Booij, J.; Tissingh, G.; Winogrodzka, A.; van Royen, E. A. Imaging of the dopaminergic neurotransmission system using single-photon emission tomography and positron emission tomography in patients with parkinsonism. Eur. J. Nucl. Med. 1999, 26, 171–182.

2. McKeith, I.; O'Brien, J.; Walker, Z.; Tatsch, K.; Booij, J.; Darcourt, J.; Padovani, A.; Giubbini, R.; Bonuccelli, U.; Volterrani, D.; Holmes, C.; Kemp, P.; Tabet, N.; Meyer, I.; Reininger, C. Sensitivity and specificity of dopamine transporter imaging with [^{123}I]-FP-CIT SPECT in dementia with Lewy bodies: a phase III, multicentre study. Lancet Neurology 2007, 6, 305–313.

3. Kapur, S.; Mamo, D. Half a century of antipsychotics and still a central role for dopamine D_2 receptors. Progr. Neuropsychopharmacol. Biol. Psychiatry 2003, 27, 1081–1090.

4. Volkow, N. D.; Fowler, J. S.; Wang, G. J.; Swanson, J. M. Dopamine in drug abuse and addiction: results from imaging studies and treatment implications. Mol. Psychiatry 2004, 9, 557–569.

5. von Campenhausen, S.; Bornschein, B.; Wick, R.; Bötzel, K.; Sampaio, C.; Poewe, W.; Oertel, W.; Siebert, U.; Berger, K.; Dodel, R. Prevalence and incidence of Parkinson's disease in Europe. Eur. Neuropsychopharmacol. 2005, 15, 473–490.

6. Kirkbride, J. B.; Errazuriz, A.; Croudace, T. J.; Morgan, C.; Jackson, D.; Boydell, J.; Murray, R. M.; Jones, P. B. Incidence of schizophrenia and other psychoses in England, 1950–2009: A systematic review and meta analyses. Plos One 2012, 7, e 31660

7. Goldstein, R. B.; Dawson, D. A.; Chou, P.; Grant, B. F. Sex differences in prevalence and comorbidity of alcohol and drug use disorders: Results from wave 2 of the national epidemiologic survey on alcohol and related conditions. J. Stud. Alcohol. Drugs. 2012, 73, 938–950.

8. James, B. D.; Bennett, D. A.; Boyle, P. A.; Leurgans, S.; Schneider, J. A. Dementia from alzheimer disease and mixed pathologies in the oldest old. JAMA 2012, 307, 1798–1800.

9. Stoof, J. C.; Kebabian, J. W. Opposing roles for D_1 and D_2 dopamine receptors in efflux of cyclic AMP from rat neostriatum. Nature 1981, 294, 366–368.

10. Strange, P. G. New insights into dopamine receptors in the central nervous system. Neurochem. Int. 1993, 22, 223–236.

11. Sibley, D. R.; De Lean, A.; Creese, I. Anterior pituitary dopamine receptors. Demonstration of interconvertible high and low affinity states of the D_2 dopamine receptor. J. Biol. Chem. 1982, 257, 6351–6361.

12. Chio, C. L.; Lajiness, M. E.; Huff, R. M. Activation of heterologously expressed D_3 dopamine receptors: Comparison with D_2 dopamine-receptors. Mol. Pharmacol. 1994, 45, 51–60.

13. Seeman, P.; Weinshenker, D.; Quirion, R.; Srivastava, I. A. K.; Bhardwaj, S. K.; Grandy, D. K.; Premont, R. T.; Sotnikova, T. D.; Boksa, P.; El-Ghundi, M.; O'Dowd, B. F.; George, S. R.; Perreault, M. L.; Mannisto, P. T.; Robinson, S.; Palmiter, R. D.; Tallerico, T. Dopamine supersensitivity correlates with D_2High states, implying many paths to psychosis. Proc. Natl. Acad. Sci USA 2005, 102, 3513–3518.

14. Zahniser, N. R.; Molinoff, P. B. Effect of guanine nucleotides on striatal dopamine receptors. Nature 1978, 275, 453–455.

15. van Wieringen, J.-P.; Booij, J.; Shalgunov, V.; Elsinga, P.; Michel, M. Agonist high- and low-affinity states of dopamine D_2 receptors: methods of detection and clinical implications. Naunyn-Schmiedeberg's Arch Pharmacol 2013, 386, 135–154.

16. George, S. R.; Watanabe, M.; Seeman, P. Dopamine D_2-receptors in the anterior-pituitary - A single population without reciprocal antagonist agonist states. J. Neurochem. 1985, 44, 1168–1177.

17. Seeman, P.; Schwarz, J.; Chen, J. F.; Szechtman, H.; Perreault, M.; McKnight, G. S.; Roder, J. C. Psychosis pathways converge via D_2high dopamine receptors. Synapse 2006, 60, 319–346.

18. Finnema, S. J.; Bang-Andersen, B.; Wikstrom, H. V.; Halldin, C. Current state of agonist radioligands for imaging of brain dopamine D_2/D_3 receptors in vivo with positron emission tomography. Curr. Top. Med. Chem. 2010, 10, 1477–1498.

19. Narendran, R.; Frankle, W. G.; Mason, N. S.; Laymon, C. M.; Lopresti, B. J.; Price, J. C.; Kendro, S.; Vora, S.; Litschge, M.; Mountz, J. M.; Mathis, C. A. Positron emission tomography imaging of $D_{2/3}$ agonist binding in healthy human subjects with the radiotracer [^{11}C]-N-propyl-norapomorphine: Preliminary evaluation and reproducibility studies. Synapse 2009, 63, 574–584.

20. Ginovart, N.; Willeit, M.; Rusjan, P.; Graff, A.; Bloomfield, P. M.; Houle, S.; Kapur, S.; Wilson, A. A. Positron emission tomography quantification of

[^{11}C]-(+)-PHNO binding in the human brain. J. Cerebr. Blood Flow Metabol. 2007, 27, 857–871.

21. Ginovart, N.; Galineau, L.; Willeit, M.; Mizrahi, R.; Bloomfield, P. M.; Seeman, P.; Houle, S.; Kapur, S.; Wilson, A. A. Binding characteristics and sensitivity to endogenous dopamine of [^{11}C]-(+)-PHNO, a new agonist radiotracer for imaging the high-affinity state of D_2 receptors in vivo using positron emission tomography. J. Neurochem. 2006, 97, 1089–1103.

22. Narendran, R.; Mason, N. S.; Laymon, C. M.; Lopresti, B. J.; Velasquez, N. D.; May, M. A.; Kendro, S.; Martinez, D.; Mathis, C. A.; Frankle, W. G. A comparative evaluation of the dopamine $D_{2/3}$ agonist radiotracer [^{11}C](–)-N-propyl-norapomorphine and antagonist [^{11}C]raclopride to measure amphetamine-induced dopamine release in the human striatum. J. Pharmacol. Exp. Ther. 2010, 333, 533–539.

23. Narendran, R.; Hwang, D. R.; Slifstein, M.; Talbot, P. S.; Erritzoe, D.; Huang, Y.; Cooper, T. B.; Martinez, D.; Kegeles, L. S.; Abi-Dargham, A.; Laruelle, M. In vivo vulnerability to competition by endogenous dopamine: Comparison of the D_2 receptor agonist radiotracer (–)-N-[^{11}C]propyl-norapomorphine ([^{11}C]NPA) with the D_2 receptor antagonist radiotracer [^{11}C]-raclopride. Synapse 2004, 52, 188–208.

24. Shotbolt, P.; Tziortzi, A. C.; Searle, G. E.; Colasanti, A.; van der Aart, J.; Abanades, S.; Plisson, C.; Miller, S. R.; Huiban, M.; Beaver, J. D.; Gunn, R. N.; Laruelle, M.; Rabiner, E. A. Within-subject comparison of [^{11}C]-(+)-PHNO and [^{11}C]raclopride sensitivity to acute amphetamine challenge in healthy humans. J. Cerebr. Blood Flow Metabol. 2012, 32, 127–136.

25. Skinbjerg, M.; Sibley, D. R.; Javitch, J. A.; Abi-Dargham, A. Imaging the high-affinity state of the dopamine D_2 receptor in vivo: Fact or fiction? Biochem. Pharmacol. 2012, 83, 193–198.

26. Mewshaw, R. E.; Kavanagh, J.; Stack, G.; Marquis, K. L.; Shi, X. J.; Kagan, M. Z.; Webb, M. B.; Katz, A. H.; Park, A.; Kang, Y. H.; Abou-Gharbia, M.; Scerni, R.; Wasik, T.; Cortes-Burgos, L.; Spangler, T.; Brennan, J. A.; Piesla, M.; Mazandarani, H.; Cockett, M. I.; Ochalski, R.; Coupet, J.; Andree, T. H. New generation dopaminergic agents. 1. Discovery of a novel scaffold which embraces the D_2 agonist pharmacophore. Structure-activity relationships of a series of 2-(aminomethyl) chromans. J. Med. Chem. 1997, 40, 4235–4256.

27. Mewshaw, R. E.; Shi, X. J.; Mazandarani, H.; Coupet, J.; McGaughey, G. B.; Andree, T. H. New generation dopaminergic agents. 3. Accessing the D_2 pharmacophore via the 7-hydroxy-2-aminomethyl benzoxazine moiety. Medicinal Chemistry Research 1997, 7, 429–435.

28. Mewshaw, R. E.; Verwijs, A.; Shi, X. J.; McGaughey, G. B.; Nelson, J. A.; Mazandarani, H.; Brennan, J. A.; Marquis, K. L.; Coupet, J.; Andree, T. H. New generation dopaminergic agents. 5. Heterocyclic bioisosteres that exploit the 3-OH-N-1-phenylpiperazine dopaminergic template. Bioorganic & Medicinal Chemistry Letters 1998, 8, 2675–2680.

29. Mewshaw, R. E.; Marquis, K. L.; Shi, X. J.; McGaughey, G.; Stack, G.; Webb, M. B.; Abou-Gharbia, M.; Wasik, T.; Scerni, R.; Spangler, T.; Brennan, J. A.; Mazandarani, H.; Coupet, J.; Andree, T. H. New generation dopaminergic agents. 4. Exploiting the 2-methyl chroman scaffold. Synthesis and evaluation of two novel series of 2-(aminomethyl)-3,4,7,9-tetrahydro-2H-pyrano[2,3-e]indole and indol-8-one derivatives. Tetrahedron 1998, 54, 7081–7108.

30. Mewshaw, R. E.; Webb, M. B.; Marquis, K. L.; McGaughey, G. B.; Shi, X. J.; Wasik, T.; Scerni, R.; Brennan, J. A.; Andree, T. H. New generation dopaminergic agents. 6. Structure-activity relationship studies of a series of 4-(aminoethoxy)indole and 4-(aminoethoxy)indolone derivatives based on the newly discovered 3-hydroxyphenoxyethylamine D_2 template. J. Med. Chem. 1999, 42, 2007–2020.

31. Mewshaw, R. E.; Husbands, M.; Gildersleeve, E. S.; Webb, M. B.; Xiaojie, S.; Mazandarani, H.; Cockett, M. I.; Ochalski, R.; Brennan, J. A.; Abou-Gharbia, M.; Marquis, K.; McGaughey, G. B.; Coupet, J.; Andree, T. H. New generation dopaminergic agents. 2. Discovery of 3-OH-phenoxyethylamine and 3-OH-N1-phenylpiperazine dopaminergic templates. Bioorganic & Medicinal Chemistry Letters 1998, 8, 295–300.

32. Biswas, S.; Hazeldine, S.; Ghosh, B.; Parrington, I.; Kuzhikandathil, E.; Reith, M. E. A.; Dutta, A. K. Bioisosteric heterocyclic versions of 7-{[2-(4-phenylpiperazin-1-yl)ethyl]propylamino}-5,6,7,8-tetrahydronaph thalen-2-ol: Identification of highly potent and selective agonists for dopamine D_3 receptor with potent in vivo activity. J. Med. Chem. 2008, 51, 3005–3019.

33. Biswas, S.; Zhang, S. H.; Fernandez, F.; Ghosh, B.; Zhen, J.; Kuzhikandathil, E.; Reith, M. E. A.; Dutta, A. K. Further structure-activity relationships study of hybrid 7-{[2-(4-phenylpiperazin-1-yl)ethyl]propylamino}-5,6,7,8-tetrahydronapht halen-2-ol analogues: Identification of a high-affinity D_3 preferring agonist

with potent in vivo activity with long duration of action. J. Med. Chem. 2008, 51, 101–117.

34. Walenzyk, T.; Carola, C.; Buchholz, H.; Konig, B. Chromone derivatives which bind to human hair. Tetrahedron 2005, 61, 7366–7377.

35. Cohen, N.; Weber, G.; Banner, B. L.; Lopresti, R. J.; Schaer, B.; Focella, A.; Zenchoff, G. B.; Chiu, A. M.; Todaro, L.; Odonnell, M.; Welton, A. F.; Brown, D.; Garippa, R.; Crowley, H.; Morgan, D. W. 3,4-dihydro-2H-1-benzopyran-2-carboxylic acids and related-compounds as leukotriene antagonists. J. Med. Chem. 1989, 32, 1842–1860.

36. Kalaritis, P.; Regenye, R. W.; Partridge, J. J.; Coffen, D. L. Kinetic resolution of 2-substituted esters catalyzed by a lipase ex pseudomonas-fluorescens. Journal of Organic Chemistry 1990, 55, 812–815.

37. Hamblin, M. W.; Leff, S. E.; Creese, I. Interactions of agonists with D_2 dopamine receptors: Evidence for a single receptor population existing in multiple agonist affinity-states in rat striatal membranes. Biochem. Pharmacol. 1984, 33, 877–887.

38. Cheng, Y.-C.; Prusoff, W. H. Relationship between the inhibition constant (K_I) and the concentration of inhibitor which causes 50 per cent inhibition (I_{50}) of an enzymatic reaction. Biochem. Pharmacol. 1973, 22, 3099–3108.

39. Wong, D. F.; Pomper, M. G. Predicting the success of a radiopharmaceutical for in vivo imaging of central nervous system neuroreceptor systems. Mol. Imaging Biol. 2003, 5, 350–362.

40. Floresca, C. Z.; Schetz, J. A. Dopamine receptor microdomains Involved in molecular recognition and the regulation of drug affinity and function. J. Recept. Signal Transduc. Res. 2004, 24, 207–239.

41. Mcdermed, J. D.; Mckenzie, G. M.; Phillips, A. P. Synthesis and pharmacology of some 2-aminotetralins - Dopamine receptor agonists. J. Med. Chem. 1975, 18, 362–367.

42. Malo, M.; Brive, L.; Luthman, K.; Svensson, P. Selective pharmacophore models of dopamine D_1 and D_2 full agonists based on extended pharmacophore features. ChemMedChem 2010, 5, 232–246.

43. Malo, M.; Brive, L.; Luthman, K.; Svensson, P. Investigation of D_2 receptor–agonist interactions using a combination of pharmacophore and receptor homology modeling. ChemMedChem 2012, 7, 471–482.

44. Lan, H.; DuRand, C. J.; Teeter, M. M.; Neve, K. A. Structural determinants of pharmacological specificity between D_1 and D_2 dopamine receptors. Mol. Pharmacol. 2006, 69, 185–194.

45. Seiler, M. P.; Stoll, A. P.; Closse, A.; Frick, W.; Jaton, A.; Vigouret, J. M. Structure-activity relationships of dopaminergic 5-hydroxy-2-aminotetralin derivatives with functionalized N-alkyl substituents. J. Med. Chem. 1986, 29, 912–917.

46. McGaughey, G. B.; Mewshaw, R. E. Application of comparative molecular field analysis to dopamine D_2 partial agonists. Bioorg. Med. Chem. 1999, 7, 2453–2456.

47. McRobb, F. M.; Capuano, B.; Crosby, I. T.; Chalmers, D. K.; Yuriev, E. Homology modeling and docking evaluation of aminergic G protein-coupled receptors. J. Chem. Inf. Model. 2010, 50, 626–637.

48. Ehrlich, K.; Gotz, A.; Bollinger, S.; Tschammer, N.; Bettinetti, L.; Harterich, S.; Hubner, H.; Lanig, H.; Gmeiner, P. Dopamine D_2, D_3, and D_4 selective phenylpiperazines as molecular probes to explore the origins of subtype specific receptor binding. J. Med. Chem. 2009, 52, 4923–4935.

49. Waterhouse, R. N. Determination of lipophilicity and its use as a predictor of blood–brain barrier penetration of molecular imaging agents. Molecular Imaging & Biology 2003, 5, 376–389.

50. Kortagere, S.; Cheng, S. Y.; Antonio, T.; Zhen, J.; Reith, M. E. A.; Dutta, A. K. Interaction of novel hybrid compounds with the D_3 dopamine receptor: Site-directed mutagenesis and homology modeling studies. Biochem. Pharmacol. 2011, 81, 157–163.

51. Malmberg, A.; Mikaels, A.; Mohell, N. Agonist and inverse agonist activity at the dopamine D_3 receptor measured by guanosine 5 '-[γ-thio]triphosphate-[^{35}S] binding. J. Pharmacol. Exp. Ther. 1998, 285, 119–126.

52. Chio, C. L.; Lajiness, M. E.; Huff, R. M. Activation of heterologously expressed D_3 dopamine receptors: Comparison with D_2 dopamine receptors. Mol. Pharmacol. 1994, 45, 51–60.

53. Perachon, S.; Schwartz, J. C.; Sokoloff, P. Functional potencies of new anti-parkinsonian drugs at recombinant human dopamine D_1, D_2 and D_3 receptors. Eur. J. Pharmacol. 1999, 366, 293–300.

54. Wiens, B. L.; Nelson, C. S.; Neve, K. A. Contribution of serine residues to constitutive and agonist induced signaling via the D_{2S} dopamine receptor: Evidence

for multiple, agonist-specific active conformations. Mol. Phamacol. 1998, 54, 435–444.

55. Payne, S. L.; Johansson, A. M.; Strange, P. G. Mechanisms of ligand binding and efficacy at the human $D_{2(short)}$ dopamine receptor. J. Neurochem. 2002, 82, 1106–1117.

56. Grunewald, S.; Reilander, H.; Michel, H. In vivo reconstitution of dopamine D_{2S} receptor-mediated G protein activation in baculovirus-infected insect cells: Preferred coupling to G_{i1} versus G_{i2}. Biochemistry 1996, 35, 15162–15173.

57. Sokoloff, P.; Andrieux, M.; Besancon, R.; Pilon, C.; Martres, M. P.; Giros, B.; Schwartz, J. C. Pharmacology of human dopamine D_3 receptor expressed in a mammalian-cell line: Comparison with D_2 Receptor. Eur. J. Pharmacol. 1992, 225, 331–337.

58. Seeman, P. Dopamine agonist radioligand binds to both D_2High and D_2Low receptors, explaining why alterations in D_2High are not detected in human brain scans. Synapse 2012, 66, 88–93.

59. Seeman, P.; Van Tol, H. H. M. Dopamine receptor pharmacology. Trends Pharmacol. Sci. 1994, 15, 264–270.

60. Gardner, B.; Strange, P. G. Agonist action at D_2(long) dopamine receptors: ligand binding and functional assays. Br. J. Pharmacol. 1998, 124, 978–984.

61. Kara, E.; Lin, H.; Strange, P. G. Co-operativity in agonist binding at the D_2 dopamine receptor: evidence from agonist dissociation kinetics. J. Neurochem. 2010, 112, 1442–1453.

62. Salama, I.; Hocke, C.; Utz, W.; Prante, O.; Boeckler, F.; Hübner, H.; Kuwert, T.; Gmeiner, P. Structure–selectivity investigations of D_2-like receptor ligands by CoMFA and CoMSIA guiding the discovery of D_3 selective PET radioligands. J. Med. Chem. 2007, 50, 489–500.

63. Wang, Q.; Mach, R. H.; Luedtke, R. R.; Reichert, D. E. Subtype selectivity of dopamine receptor ligands: Insights from structure and ligand-based methods. J. Chem. Inf. Model. 2010, 50, 1970–1985.

64. Laruelle, M.; Slifstein, M.; Huang, Y. Relationships between radiotracer properties and image quality in molecular imaging of the brain with positron emission tomography. Mol. Imaging Biol. 2003, 5, 363–375.

65. Rabiner, E. A.; Laruelle, M. Imaging the D_3 receptor in humans in vivo using [^{11}C](+)-PHNO positron emission tomography (PET). Int. J. Neuropsychopharmacol. 2010, 13, 289–290.

66. Tziortzi, A. C.; Searle, G. E.; Tzimopoulou, S.; Salinas, C.; Beaver, J. D.; Jenkinson, M.; Laruelle, M.; Rabiner, E. A.; Gunn, R. N. Imaging dopamine receptors in humans with [^{11}C]-(+)-PHNO: Dissection of D_3 signal and anatomy. NeuroImage 2011, 54, 264–277.

67. Boileau, I.; Payer, D.; Houle, S.; Behzadi, A.; Rusjan, P. M.; Tong, J. C.; Wilkins, D.; Selby, P.; George, T. P.; Zack, M.; Furukawa, Y.; McCluskey, T.; Wilson, A. A.; Kish, S. J. Higher binding of the dopamine D_3 receptor-preferring ligand [^{11}C] -(+)-propyl-hexahydro-naphtho-oxazin in methamphetamine polydrug users: A positron emission tomography study. J. Neurosci. 2012, 32, 1353–1359.

68. Caravaggio, F.; Raitsin, S.; Gerretsen, P.; Nakajima, S.; Wilson, A.; Graff-Guerrero, A. Ventral striatum binding of a dopamine $D_{2/3}$ receptor agonist but not antagonist predicts normal body mass index. Biol. Psychiatry 2013.

69. Cumming, P. Absolute abundances and affinity states of dopamine receptors in mammalian brain: A review. Synapse 2011, 65, 892–909.

70. Lahti, R. A.; Roberts, R. C.; Cochrane, E. V.; Primus, R. J.; Gallager, D. W.; Conley, R. R.; Tamminga, C. A. Direct determination of dopamine D_4 receptors in normal and schizophrenic postmortem brain tissue: a [^{3}H]NGD-94-1 study. Mol. Psychiatry 1998, 3, 528–533.

71. Primus, R. J.; Thurkauf, A.; Xu, J.; Yevich, E.; McInerney, S.; Shaw, K.; Tallman, J. F.; Gallager, D. W. Localization and characterization of dopamine D_4 binding sites in rat and human brain by use of the novel, D_4 receptor-selective ligand [^{3}H]NGD 94-1 .2. J. Pharmacol. Exp. Ther. 1997, 282, 1020–1027.

72. Hanson, R. N.; Hariharan, S.; Astik, R. Synthesis of 4-(4-Iodophenyl)piperazine and the 1-carboxamidino derivative. J. Heterocyclic Chem. 1985, 22, 47–48.

73. Tietze, R.; Hocke, C.; Lober, S.; Hubner, H.; Kuwert, T.; Gmeiner, P.; Prante, O. Syntheses and radiofluorination of two derivatives of 5-cyano-indole as selective ligands for the dopamine subtype-4 receptor. J. Labelled Comp. Radiopharm. 2006, 49, 55–70.

74. Parenty, A. D. C.; Smith, L. V.; Pickering, A. L.; Long, D. L.; Cronin, L. General one-pot, three-step methodology leading to an extended class of N-heterocy-

clic cations: Spontaneous nucleophilic addition, cyclization, and hydride loss. J. Org. Chem. 2004, 69, 5934–5946.

75. Fesser, P.; Iacovita, C.; Wackerlin, C.; Vijayaraghavan, S.; Ballav, N.; Howes, K.; Gisselbrecht, J. P.; Crobu, M.; Boudon, C.; Stohr, M.; Jung, T. A.; Diederich, F. Visualizing the product of a formal cycloaddition of 7,7,8,8-tetracyano-p-quinodimethane (TCNQ) to an acetylene-appended porphyrin by scanning tunneling microscopy on Au(111). Chem. Eur. J. 2011, 17, 5246–5250.

76. Tummatorn, J.; Dudley, G. B. Generation of medium-ring cycloalkynes by ring expansion of vinylogous acyl triflates. Org. Lett. 2011, 13, 1572–1575.

77. Sandanayaka, V. Preparation of phenylpiperazine derivatives as LTA4H (leukotriene A4 hydrolase) inhibitors for treating inflammation. 20070149544. 28-6-2007.

Ref Type: Patent

78. Shoji, A.; Kuwahara, M.; Ozaki, H.; Sawai, H. Modified DNA aptamer that binds the (R)-isomer of a thalidomide derivative with high enantioselectivity. J. Am. Chem. Soc. 2007, 129, 1456–1464.

79. Chichak, K. S.; Peters, A. J.; Cantrill, S. J.; Stoddart, J. F. Nanoscale borromeates. J. Org. Chem. 2005, 70, 7956–7962.

80. Bradford, M. M. A rapid and sensitive method for the quantitation of microgram quantities protein utilizing the principle of protein-dye binding. Anal. Biochem. 1976, 72, 248–254.

Chapter 4

Synthesis and Evaluation in Rats of the Dopamine $D_{2/3}$ Receptor Agonist [^{18}F]AMC20 as Potential Radioligand for PET

Vladimir Shalgunov[1], Jan-Peter van Wieringen[2], Henk M. Janssen[3], P. Michel Fransen[3], Rudi A.J.O. Dierckx[1], Martin C. Michel[4], Jan Booij[2], Philip H. Elsinga[1]

1 Department of Nuclear Medicine and Molecular Imaging, University Medical Center Groningen, University of Groningen, Groningen, The Netherlands

2 Department of Nuclear Medicine, Academic Medical Center, University of Amsterdam, Amsterdam, The Netherlands

3 SyMO-Chem BV, Eindhoven, The Netherlands

4 Department of Pharmacology, Johannes Gutenberg University, Mainz, Germany

(Journal of Nuclear Medicine 2015;56:133–9)

LIST OF ABBREVIATIONS

1TCM – one-tissue compartment model

2TCM – two-tissue compartment model

BP_{ND} – Binding Potential Non-Displaceable (equilibrium concentration ratio of specifically bound radioligand to non-displaceable radioligand in tissue)

DMF – N,N'-dimethylformamide

DMSO – dimethylsulphoxide

GPCR – G-protein coupled receptor

GTP – guanosine triphospate

HPLC – high-pressure liquid chromatography

HRMS – high-resolution mass-spectrometry

MOMCl – methoxymethyl chloride

PET – positron emission tomography

ROI – region of interest

SRTM – simplified reference-tissue model

SUV – standardized uptake value (regional uptake relative to mean uptake across the body)

TAC – time-activity curve

THF – tetrahydrofurane

TLC – thin-layer chromatography

TsCl – p-toluenesulfonyl chloride

UPLC – ultra-productive liquid chromatography

V_T – total distribution volume of a radioligand in the tissue (i.e. the sum of distribution volumes of free, non-specifically and specifically bound radioligand)

ABSTRACT

Dopamine $D_{2/3}$ receptor ($D_{2/3}R$) agonist positron emission tomography (PET) tracers are better suited for the imaging of synaptic dopaminergic neurotransmission than $D_{2/3}R$ antagonists, and may also offer the opportunity to study in vivo the high-affinity state of $D_{2/3}R$ ($D_{2/3}RHigh$). Aiming to develop ^{18}F-labeled $D_{2/3}R$ agonists suitable for widespread clinical application, we report here on the synthesis, in vitro and in vivo evaluation of a $D_{2/3}R$-agonist ligand from the aminomethyl chromane (AMC) class – (*R*)-2-[(4-[^{18}F]fluorobenzylamino)methyl]chroman-7-ol ([^{18}F]AMC20).

Methods: In vitro affinities of AMC20 towards dopaminergic receptor subtypes were measured in membrane homogenates prepared from HEK293 cells expressing human dopamine receptors. Agonism of AMC20 was assessed in the arrestin recruitment assay in CHO-K1 cells expressing D_2RLong receptors. $D_{2/3}R$-specific binding of [^{18}F]AMC20 was evaluated in brain slices of Sprague-Dawley rats by in vitro autoradiography and in living rats by in vivo small-animal PET imaging and *ex vivo* autoradiography. PET data were analyzed with one and two-tissue compartmental models (1TCM/2TCM), simplified reference tissue model (SRTM) and Logan graphical analysis. Specificity of binding was tested by blocking $D_{2/3}R$ with raclopride (co-incubation with 10 μM in vitro, administration of 1.0 mg/kg in vivo).

Results: In membrane homogenates AMC20 demonstrated picomolar affinity at D_2RHigh (mean K_i = 85 pM) and excellent selectivity against D_2RLow (mean K_i = 84 nM, 988-fold selectivity) and D_1-like receptors (mean K_i = 5062 nM at D_1R). The efficacy of AMC20 was 90% of that of dopamine in the arrestine recruitment assay. Up to 70% of total binding of [^{18}F]AMC20 in the $D_{2/3}R$-rich striatum in rat brain slices was $D_{2/3}R$-specific, in living rats the uptake ratio between the striatum and the $D_{2/3}R$-poor cerebellum reached 2.0–2.5, depending on the measurement method. Radiometabolites of [^{18}F]AMC20 did not enter the brain. Striatal binding potential (BP_{ND}) of [^{18}F]AMC20 varied between 0.49 and 0.59 depending on the estimation method. Pre-treatment with 1 mg/kg raclopride reduced the apparent specific binding of [^{18}F]AMC20 in the striatum.

Conclusion: [^{18}F]AMC20 shows specific binding to $D_{2/3}R$ in the striatum of living rats. Further optimization of the chemical structure of [^{18}F]AMC20 can lead to ^{18}F-labeled $D_{2/3}$ agonist PET tracers more suitable for in vivo clinical application.

INTRODUCTION

Imaging of dopamine D_2 and D_3 receptors ($D_{2/3}R$) by PET is a topic of particular interest, as deregulation of $D_{2/3}$-signaling is implied in many neuropsychiatric disorders [1–4].

Most PET tracers currently used for $D_{2/3}R$ imaging are antagonists [5]. Throughout the recent two decades, development of agonist tracers for G-protein-coupled neurotransmitter receptors has gained popularity, spurred by the consistent observations by several authors [6–8] that in vitro agonists bound to receptor-G-protein complexes with higher affinity than to free receptors, while antagonists bound to all receptors with equal affinity.

Preference for this subset of receptors (called the "high affinity state") makes agonists potentially better suited than antagonists for the imaging of synaptic neurotransmission, as the neurotransmitters themselves are agonists and exhibit the same preference. Indeed, ^{11}C-labeled $D_{2/3}R$-agonists demonstrated greater sensitivity to amphetamine-induced dopamine release in humans compared to the antagonist [^{11}C]raclopride [9,10].

Moreover, dysregulated relative abundance of the high-affinity state of $D_{2/3}R$ might underlie the state of dopamine supersensitivity, which is associated with psychosis, Parkinson's disease and addiction [11]. Agonist tracers might provide new insights for the research into and (early) diagnosis of such disorders.

Of many candidate compounds of various classes tested as potential $D_{2/3}R$ agonist PET tracers [12] only three were eventually used in humans, namely the apomorphines (–)-N-propyl-norapomorphine ([^{11}C](–)NPA), (*R*)-2-$^{11}CH_3O$-*N*-*n*-propylnorapomorphine ([^{11}C]MNPA) and the naphtoxazine (+)-4-propyl-3,4,4a,5,6,10b-hexahydro-2H-naphtho[1,2-b][1,4]oxazin-9-ol ([^{11}C](+)PHNO). The scope of use of [^{11}C]tracers is limited by the short half-life of carbon-11 (20.4 min), while tracers labeled with longer-living radioisotopes like fluorine-18 (half-life of 109.8 min) have a much greater potential. (*R*)-(–)-2-[^{18}F]fluoroethoxy-N-n-propylnorapomorphine ([^{18}F]MCL-524), an ^{18}F-labeled apomorphine derivative, showed very promising results in monkeys [13], but has not yet been reported to be used in humans.

We aimed to develop ^{18}F-labeled $D_{2/3}R$-agonist radioligands for PET. We have based our research on the aminomethyl chromanes (AMCs), a class of

$D_{2/3}$-agonists first described as such by Mewshaw and co-workers [14]. AMCs were not used for the PET tracer development before.

Elaborating on the molecules described by Mewshaw, in particular (*R*)-2-(benzylaminomethyl)chroman-7-ol (AMC1, denoted as **10a** in Chapter 3), we have recently prepared a series of fluorinated AMCs and evaluated them as potential PET tracers [15]. By attaching a fluoroalkoxy moiety to the benzyl ring of AMC1 and systematically varying the length of the fluoroalkoxy group we obtained FBu-AMC13 and FEt-AMC13 (Figure 1; denoted as, respectively, **12a** and **12d** in Chapter 3). [^{18}F]FEt-AMC13 demonstrated specific binding to striatal $D_{2/3}$R in rat brain slices as well as in living rats, with a strong preference towards $D_{2/3}$RHigh (high-affinity state of $D_{2/3}$R) [16].

The [^{18}F]fluorine label can also be attached directly to the benzyl ring of AMC1. This would minimize the alteration of the AMC1 structure caused by the introduction of the label and provide greater potential in vivo stability compared to [^{18}F]fluoroalkyl derivatives. In fact, racemic para-fluorobenzyl derivative of AMC1 was already reported by Mewshaw to have sub-nanomolar affinity towards D_2Rhigh receptors and very good selectivity against D_2RLow [1]. Here we report the preparation of the R-enantiomer of this derivative, AMC20 and its in vitro and in vivo evaluation.

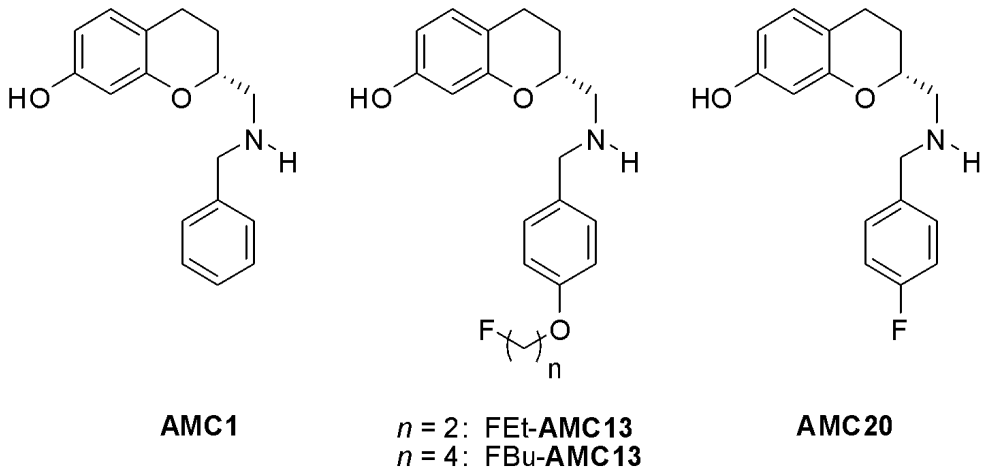

Figure 1. Structures of AMC1, FBu-AMC13, FEt-AMC13 and AMC20.

MATERIALS AND METHODS

Chemistry, Radiochemistry and Pharmacology

The preparation and characterization of [^{18}F]AMC20, of its ^{19}F-reference and precursors are described in the Appendix (see also Figure S1 there).

In vitro binding experiments in HEK293 cell membrane homogenates were performed as described earlier [15]. β-Arrestin recruitment assay was performed as described in the Appendix.

In vitro autoradiography in rat brain slices is described in detail in the Appendix. Briefly, sagittal slices from male Sprague-Dawley rats containing both striatum and cerebellum were incubated in a Tris-based buffer (pH 7.4) in the presence of varying concentrations of [^{18}F]AMC20 (~2…80 nM) with or without 10 μM raclopride ($D_{2/3}$-antagonist) or 100 μM guanosine-5'-triphosphate sodium salt (GTP, stimulator of G-protein uncoupling from the receptors). Then the slices were washed, dried and exposed against phosphor storage screens. On the resulting images, striatal and cerebellar regions of interest were manually drawn and mean exposure per region was quantified.

Animals

Animal experiments were performed by licensed investigators in compliance with the Law on Animal Experiments of The Netherlands. The protocol was approved by the Committee on Animal Ethics of the University of Groningen. Young male (10–12 weeks of age, 300–350 g body weight) Sprague-Dawley rats (Harlan, the Netherlands) were used for all experiments. The rats were maintained at a 12-h light/12-h dark regime and were fed standard laboratory chow *ad libitum*.

Small-animal PET

Distribution of [^{18}F]AMC20 was studied in rats pre-treated with physiological saline (controls, n=4) or 1 mg/kg $D_{2/3}$R-antagonist raclopride (as tartrate salt, n=4). Saline and raclopride (in random order) were injected intravenously about 30 min before tracer injection. An extra group of rats (n=4) were pre-treated with saline and injected with [^{11}C]raclopride to serve as positive controls for $D_{2/3}$-specific brain uptake.

Before all manipulations the animals were anesthetized with a mixture of isoflurane/air (inhalation anesthesia, 5% ratio during induction, 2% at

maintenance). Cannulae were inserted into their left femoral arteries and veins; the operation took 45–50 min. Then they were positioned supine inside the camera (Focus 220 microPET, Siemens-Concorde), two rats at a time, one above the other with their heads in the camera's field of view. A 515 sec transmission scan with a Co-57 point source was carried out. Tracer ([^{18}F]AMC20 or [^{11}C]raclopride, Table 1) in 1 ml saline was injected through the venous cannula as a 60-second long using an infusion pump. The second (upper) animal was injected 16 min after the first (lower).

PET data were acquired using a list-mode protocol (106-minute long for [^{18}F]AMC20, 76-minute long for [^{11}C]raclopride). Acquisition began at the moment of the injection of radioactivity in the first rat.

In each rat, arterial blood samples of 0.10–0.15 ml were withdrawn through the arterial cannula at 10, 20, 30, 40, 50, 60, 90, 120, 180, 300, 450, 600, 900, 1800, 3600 and 5400 (for [^{18}F]AMC20) seconds after tracer injection.

After withdrawing aliquots of intact blood, samples were centrifuged to obtain plasma. Radioactivity of plasma and intact blood aliquots was measured with a gamma-counter. Radiometabolite content in the deproteinated plasma was assessed by thin layer chromatography (radio-TLC). Detailed procedures of arterial blood and plasma workup are described in the Appendix.

After the end of the PET scans (98±8 min post-injection for [^{18}F]AMC20) anesthetized animals were sacrificed by heart extirpation and dissected. Samples of brain and peripheral tissues were taken. All samples were weighed and their radioactivity was measured in a gamma-counter.

Table 1. Injected doses and pre-treatment timing.

Tracer	Injected radioactivity, MBq/rat	Injected dose, nmol/kg	Pre-treatment time interval, min
[^{18}F]AMC20	6.3±1.7	1.58±1.00	32±16
[^{11}C]raclopride	16.9±5.3	1.26±0.16	36±3

MicroPET Data Analysis

List-mode data from the 106-minute-long and 76-minute-long scans were reframed into, respectively, 90-minute-long and 60-minute-long dynamic sequences of 6×10, 4×30, 2×60, 1×120, 1×180, 4×300, 3×600 and (for 90-min-

ute-long scans) 2×900 sec frames. The data were reconstructed per time frame using an iterative reconstruction algorithm (attenuation-weighted 2-dimensional ordered-subset expectation maximization, provided by Siemens; 4 iterations, 16 subsets; zoom factor, 2). Datasets were fully corrected for random coincidences, scatter, and attenuation. Data from the transmission scan were used for attenuation correction. The final datasets consisted of 95 slices, with a slice thickness of 0.8 mm and an in-plane image matrix of 128×128 pixels of size 0.47×0.47 mm.

PET data were analyzed with Inveon 3.0 software package (Siemens Medical Solutions, USA, Inc). Regions of interest (ROIs) were drawn manually on a T2 MRI template of rat brain around the striatum, brainstem, cortex, hippocampus, hypothalamus, thalamus, olfactory bulbs and cerebellum, around the whole brain and around the pituitary gland. The MRI template was co-registered with the PET scan by image fusion. The time-activity curves (TAC) per ROI were determined in Bq/cm^3 and used in this form for kinetic analysis, but converted into standardized uptake values (SUVs) for presentation purposes.

Kinetic analysis is described using the nomenclature proposed by Innis et al [17]. ROI TACs were analyzed with one-tissue (1TCM) and two-tissue (2TCM) compartmental models of reversible binding and with Logan graphical analysis, using metabolite-corrected plasma-derived arterial input function and whole blood time-activity curve. Fractional cerebral blood volume was defined as 3.6%. ROI TACs were also analyzed with simplified reference tissue model (SRTM), using cerebellum as reference region.

Distribution volumes (V_T) per ROI were determined from 1TCM and 2TCM-derived rate constants and by Logan analysis.

Binding potentials (BP_{ND}) per ROI relative to cerebellum were calculated from the obtained V_T values as V_T (target) / V_T (cerebellum) – 1, or estimated directly with STRM.

Ex Vivo Autoradiography and Brain Radiometabolite Analysis

Anesthetized rats, pre-treated with saline (*n*=3) or raclopride (*n*=3) were injected (30±5 min after pre-treatment) with a short bolus of [^{18}F]AMC20 (3.8±1.0 MBq, 0.75±0.19 nmol/kg) into the penile vein. Rats were sacrificed by heart extirpation 35 min post-injection. Brains were quickly extracted

and separated into two halves along the sagittal symmetry plane or along the coronal plane spanning the thalamus.

One brain half was sliced on the microtome and the slices containing the striatum were exposed against the phosphor storage screens. From the other half, radioactivity was extracted by homogenization in acetonitrile (>90% efficiency) and analyzed by radio-TLC. Detailed protocols for both procedures are presented in the Appendix.

Outcome Measures of $D_{2/3}$R-specific Binding

$D_{2/3}$R-specific binding of [^{18}F]AMC20 was quantified using BP_{ND} values (as described above) and specific binding ratios (SBR), the latter calculated as: target region radioactivity / cerebellar radioactivity – 1. Both were estimated under control conditions as well as under raclopride challenge conditions.

Statistics

All data are presented as means ± standard deviations. Where a comparison of means was done, 2-sided unpaired Welch t-test was used. P-values below 0.05 were considered significant. In case of multiple comparisons, no correction of α-levels was performed.

RESULTS

Pharmacology

Competition curves of [^{3}H]spiperone displacement from the Long isoform of D_2R by AMC20 were significantly better fitted by the two-site binding model (K_iHigh = 85 pM, K_iLow = 84 nM, 988-fold difference) than by one-site binding model. Such bi-phasic binding is a hallmark of an agonist, and the difference in the agonist affinities for the two recognized binding sites is known to correlate with the intrinsic activity [18]. This also accounted for D_2RShort and D_3R (Table 2). No second high-affinity binding component was detected for D_1R. The D_1R affinity of AMC20 was an order of magnitude lower than the lowest affinity at a D_2-like receptor (Table 2).

Arrestin recruitment assay showed AMC20 to be an almost full agonist (E_{max} of 90.3±5.4% compared to dopamine) with a pEC_{50} of 8.86±0.05.

Table 2. In vitro affinity of AMC20 towards dopamine receptor subtypes.

Ligand	D_1	D_2Long			D_2Short		D_3	
		high	low	$K_i$low/ $K_i$high	high	low	high	low
AMC20	5062	0.085	84	988	25	399	0.6	219
FBu-AMC13[a]	6912	5.6	80.5	14.4	1.3	92.7	n.d.[b]	12.1
AMC1[a]	7253	2.98	70	23.5	40	736	n.d.	3.2
(–)NPA[a]	–[c]	0.075	1.73	23.1	0.1	10.6	n.d.	1.91
(+)PHNO[a]	–	0.45	21.4	47.6	n.d.	19	n.d.	1.08
dopamine[a]	–	231	11581	50	n.d.	920	n.d.	24.8

All values are mean K_i values (⩾3 independent experiments) in nM.
a data from [15].
b no high-affinity component detected.
c not determined.

Radiochemistry

[^{18}F]AMC20 was synthesized within 150 min (including purification and quality control) using the three-step two-pot reductive amination procedure (Figure 2) in 24±7% radiochemical yield and >95% radiochemical purity (both values referring to the formulated product). The molar radioactivity was 39±23 GBq/μmol at end-of-synthesis

The logD distribution coefficient (octanol/phosphate buffer pH 7.4) of [^{18}F]AMC20 was found to be 2.33±0.03.

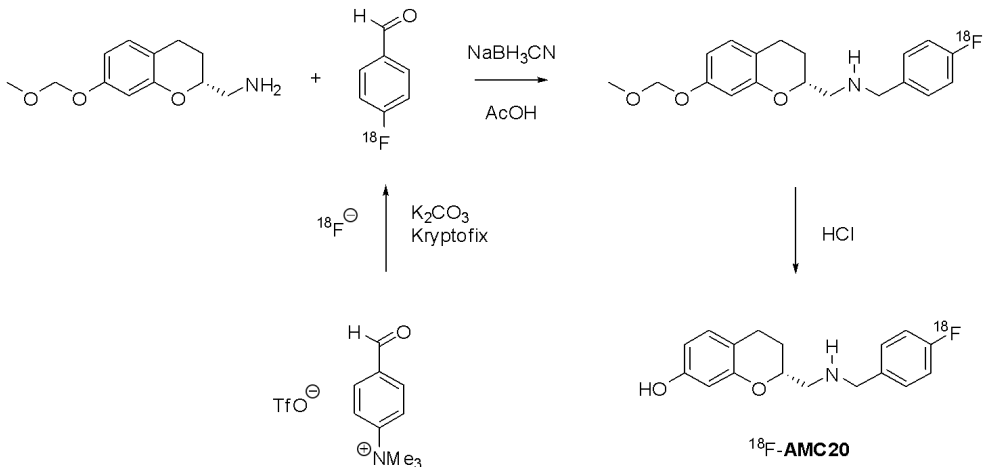

Figure 2. The radiosynthesis of [^{18}F]AMC20.

In Vitro Autoradiography

In rat brain slices, [^{18}F]AMC20 showed preferential uptake in the $D_{2/3}$R-rich striatum (Figure 3A). At the lowest radioligand concentration tried (1.7 nM), striatal SBR of [^{18}F]AMC20 was 5.27±1.49 at baseline and 0.89±0.29 (by 83%) in the presence of 10 μM raclopride, so 70% of the [^{18}F]AMC20 binding in the striatum was $D_{2/3}$R-specific. In the concentration range of 1.7–7.8 nM, 10 μM raclopride decreased striatal SBR values by 74–89% compared to control conditions, while 100 μM GTP decreased the SBR by 62–78%, implying that most of the $D_{2/3}$R-specific striatal binding of [^{18}F]AMC20 was to the high-affinity subset of the receptors (Figure 3B).

Uptake in Living Rat Brain under Control Conditions

[^{18}F]AMC20 showed excellent blood-brain barrier (BBB) penetration (Figure 4): 3.5 min post-injection 1.7% injected dose (ID) accumulated in the brain.

The tracer primarily accumulated in the striatum, while the cerebellum showed the lowest uptake (Figure 5A). PET-derived striatum-to-cerebellum uptake ratio of [^{18}F]AMC20 peaked 35 min post-injection at 1.97±0.13 (Figure 5B). The same ratio for [^{11}C]raclopride 35 min post-injection was 6.43±0.89. Ex vivo autoradiography-derived striatum-to-cerebellum ratio of [^{18}F]AMC20 at the same time post-injection was 2.48±0.34.

Ex vivo measurements of the [^{18}F]AMC20 uptake in the brain and peripheral tissues performed after the PET scan are given in Table S1 (figures and tables with the letter S are found in the Appendix).

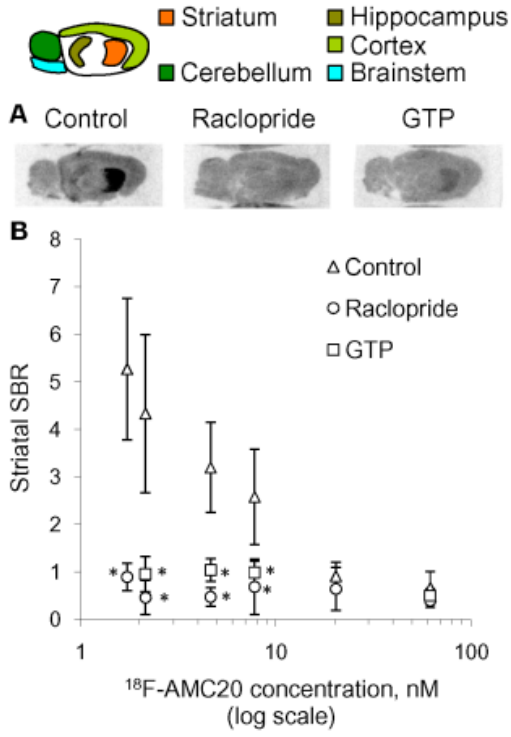

Figure 3. In vitro autoradiography assay results of [^{18}F]AMC20.

Representative images (A) and the influence of radioligand concentration on the mean±SD striatal SBR of [^{18}F]AMC20 (B) in control slices and in slices co-incubated with raclopride (10 μM) or GTP (100 μM). * $P < 0.05$ relative to control values, 2-sided Welch test.

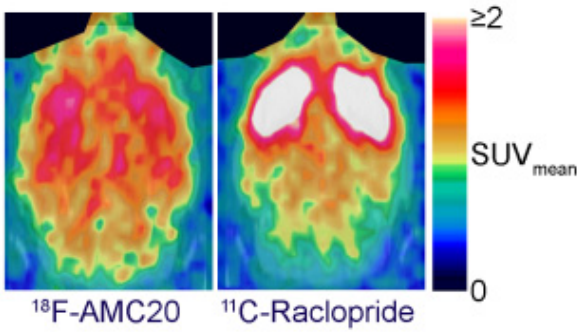

Figure 4. Representative in vivo PET images of [^{18}F]AMC20 and [^{11}C]raclopride.
Images are summed from 5 min post-injection till the end of scan. Harderian glands (on top) are masked.

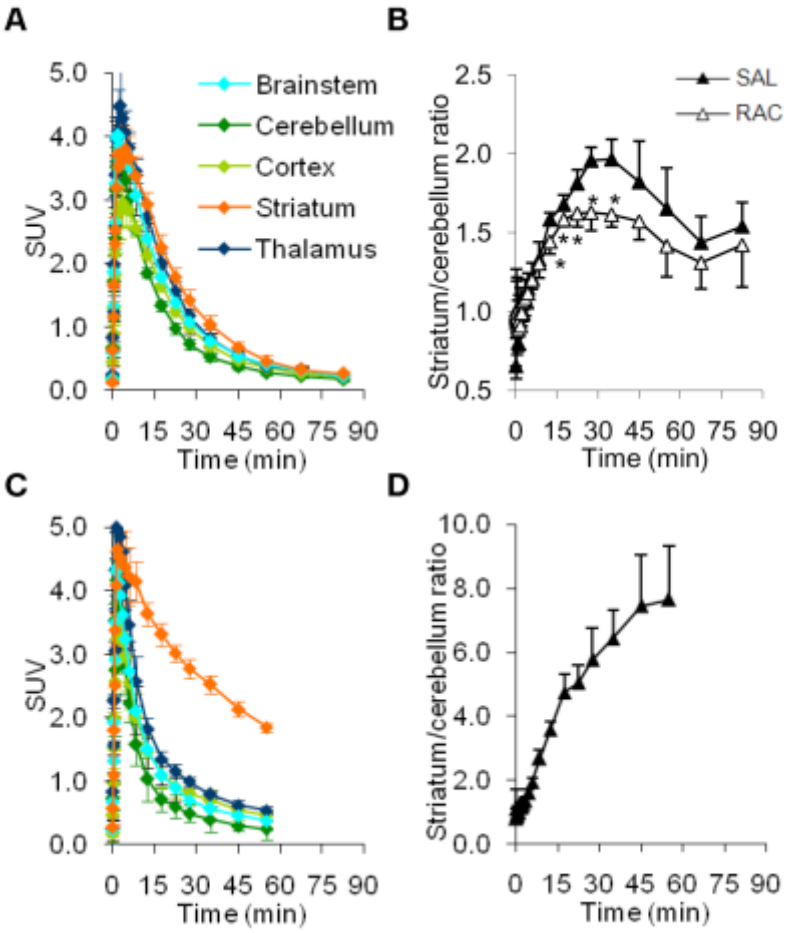

Figure 5 (previous page). Uptake of [^{18}F]AMC20 (A, B) and [^{11}C]raclopride (C, D) in the rat brain.

A, C – ROI TACs of control rats. B, D – striatum-to-cerebellum ratios in saline (SAL) and raclopride-pre-treated (RAC) rats.

Points represent group means, error bars show standard deviations. * P < 0.05 relative to control group, 2-tailed Welch t-test.

Tracer Metabolism

[^{18}F]AMC20 was quickly metabolized and excreted from the plasma (Figure 6A,B). Plasma elimination half-life was 3.9 min. Radiometabolites found in the plasma and in the radioactivity extracted from the brain 35 min post-injection showed R_f values of 0 in the radio-TLC analysis, compared to R_f of 0.65 for [^{18}F]AMC20. Intact [^{18}F]AMC20 constituted 95% of radioactivity from the abovementioned brain tissue extract (Figure S2), suggesting that radiometabolites of [^{18}F]AMC20 were hydrophilic and did not penetrate the BBB.

In vivo defluorination was also low, as follows from the much lower tracer uptake in the parietal bone compared to the brain tissue (Table S1).

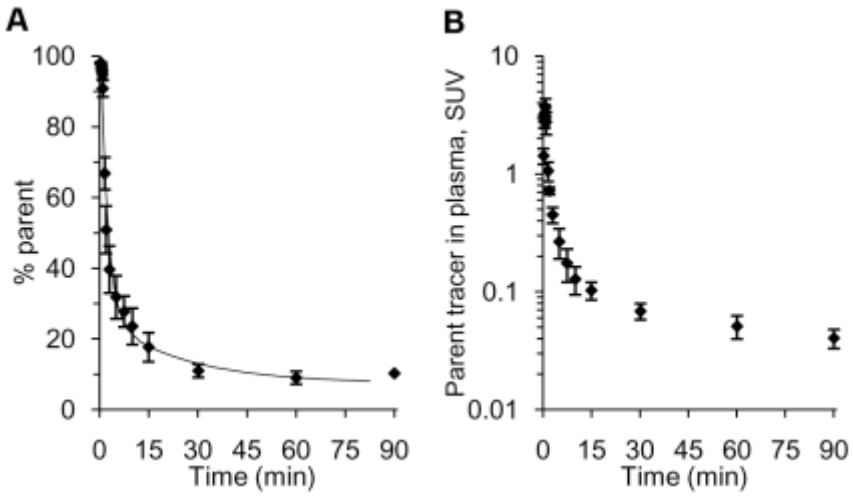

Figure 6. Metabolism and pharmacokinetics of [^{18}F]AMC20 in the plasma of living rats.

A – percentage of parent in plasma radioactivity; B – intact [^{18}F]AMC20 concentration in plasma.

Points represent group means, error bars show standard deviations. Horizontal axes show time after tracer injection.

Kinetic Analysis

ROI TACs of control rats were consistently better approximated by 2TCM and SRTM than by 1TCM (Figure S3), as assessed by Akaike information criterion. However, no consistent estimates of individual rate constants could be obtained from 2TCM fits (Table S2).

Logan graphical analysis produced the most robust ROI V_T estimates (Table S3). 2TCM-derived V_T values correlated better with Logan V_T values ($r = 0.98$) than did 1TCM V_T values ($r = 0.95$; Figure S4). The 2TCM rate constant ratios k_3/k_4 did not provide robust BP_{ND} estimates (data not shown), but V_T-based 2TCM BP_{ND} were robust and correlated better with Logan BP_{ND} values ($r = 0.99$) than did 1TCM BP_{ND} values ($r = 0.93$).

SRTM BP_{ND} values correlated best with Logan BP_{ND} ($r = 0.95$), somewhat less well with 2TCM BP_{ND} ($r=0.92$) and still less well with 1TCM BP_{ND} ($r=0.88$; Figure S5).

The highest BP_{ND} values in saline-pre-treated rats, 0.49–0.59 depending on the estimation method, were found in the striatum (Table 3, Table S4).

Raclopride Challenge

Raclopride pre-treatment resulted in 35% decrease of peak PET-derived striatal SBR of [^{18}F]AMC20 relative to controls (0.63±0.12 vs 0.97±0.13, $p<0.01$). Blockade of $D_{2/3}R$-specific signal in striatum was clearly seen on the ex vivo autoradiography images (Figure S6), autoradiography-based SBR fell by 41% (0.88±0.21 vs 1.48±0.34, $p<0.01$).

Depending on the model used for kinetic analysis, striatal BP_{ND} fell by 21–29% ($p<0.05$ for SRTM; $p<0.07$ for Logan and 1TCM; $p=0.09$ for 2TCM; Table 3, Table S4).

The occupancy of $D_{2/3}R$ by raclopride estimated from ROI V_T values with modified Lassen plot analysis [19] was found to be 34–37% ($p<0.05$ for 1TCM, 2TCM and Logan). Comparison of the actual ROI V_T values with the estimated non-displaceable volume of distribution (V_{ND}) implied that 39–48% of striatal V_T and 5–22% of cerebellar V_T were potentially displaceable (Figure S5).

Table 3. Logan and SRTM-derived BP_{ND} values for [^{18}F]AMC20.

Region of interest	Logan BP_{ND}		SRTM BP_{ND}	
	control	raclopride	control	raclopride
Striatum	0.49±0.09	0.36±0.07 (−26%)[a]	0.49±0.08	0.35±0.07 (−29%)*
Hippocampus	0.35±0.06	0.35±0.08 (0%)	0.37±0.05	0.34±0.09 (−6%)
Thalamus	0.39±0.05	0.36±0.09 (−10%)	0.39±0.05	0.32±0.07 (−19%)
Hypothalamus	0.20±0.08	0.13±0.05 (−35%)	0.14±0.09	0.12±0.05 (−14%)
Cortex	0.09±0.03	0.11±0.07 (22%)	0.08±0.01	0.10±0.06 (+18%)
Brainstem	0.29±0.08	0.16±0.04 (−43%)*	0.29±0.08	0.14±0.03 (−53%)*
Olfactory Bulbs	0.06±0.05	0.07±0.10 (25%)	0.07±0.05	0.07±0.12 (+2%)
Pituitary	0.09±0.11	0.06±0.09 (−36%)	0.15±0.13	0.07±0.10 (−55%)

Data are presented as means±SD (n=4 per treatment group). Change in BP_{ND} value after raclopride challenge relative to the control group is shown in parentheses. *a* P < 0.07, * P < 0.05, 2-sided Welch test. 1TCM and 2TCM-derived BP_{ND} values are presented in Table S4.

DISCUSSION

This study is a continuation of our work on the development of $D_{2/3}R$ agonist PET tracers based on the AMC scaffold [15,16]. Here we evaluated in vitro and in vivo a new candidate tracer, AMC20.

AMC20 was confirmed to be a potent D_2R-agonist by arrestine recruitment assay and demonstrated the highest D_2RHigh affinity (85 pM) and D_2RHigh/D_2RLow selectivity (988-fold) of all AMCs so far evaluated by us (Table 2). Likewise, in rat brain slices [^{18}F]AMC20 exhibited high striatal SBRs and was as highly sensitive to the $D_{2/3}R$High-eliminating GTP as to the $D_{2/3}R$-blocker raclopride.

In living rats, [^{18}F]AMC20 penetrated the BBB well and preferentially accumulated in the striatum. The 2TCM model approximated the time-activity curves of [^{18}F]AMC20 generally better than the 1TCM model, but there was no consistency in the estimates of individual rate constants of 2TCM. It may be that the data (i.e. PET counts and input curves) were not of sufficiently high quality to precisely estimate these constants. Still, the V_T values derived from the 2TCM rate constants, as well as V_T-based BP_{ND} values, were robust and consistent, so these outcome measures were used for the evaluation of [^{18}F]AMC20. Interestingly, both V_T and BP_{ND} obtained from 2TCM correlated better than V_T and BP_{ND} obtained from 1TCM with the corresponding measures obtained by Logan analysis, which does not assume any particular number of kinetic compartments.

Changes of striatal BP_{ND} and SBR induced by 1 mg/kg raclopride were generally consistent with the estimates of $D_{2/3}R$ occupancy by raclopride, but disagreed with the literature data for ^{11}C-labeled $D_{2/3}R$ agonists: as little as 0.2 mg/kg displaced over 80% of apparent $D_{2/3}R$-specific [^{11}C](+)PHNO uptake [20], while 1–2 mg/kg raclopride displaced >90% specific striatal uptake of [^{11}C]MNPA and [^{11}C]PHNO in Sprague-Dawley rats [20–22].

Crude estimation of the $D_{2/3}R$ occupancy by [^{18}F]AMC20 in our experiments, assuming the equality of non-$D_{2/3}R$-specific binding in striatum and cerebellum and using the approach described by Skinbjerg et al. [23], produced values ranging from 2% to 15% (7% on average). This means our injected tracer doses could have been high enough to cause a “mass effect” distorting our measurements. However, baseline SBRs and binding potentials of [^{18}F]AMC20 in control rats did not tend to decrease with the injected dose (Figure S6), so we do not consider the violation of tracer conditions likely.

Imprecise estimation of the specific portion of total tracer binding, resulting from high non-specific binding, may have led to the underestimation of the degree of specific binding blockade by raclopride. Low apparent displacement of $D_{2/3}$R-specific striatal binding may also suggest that in the brain [^{18}F]AMC20 specifically binds to sites other than $D_{2/3}$R, which have comparatively high density in the striatum. Binding to D_1 has been ruled out in this study, while racemic AMC20 was shown to be selective for D_2R against 5-HT_{1A} and α_1 receptors [14], but selectivity against other non-dopaminergic receptors has yet to be tested.

Compared to the earlier evaluated [^{18}F]FEt-AMC13 [16], [^{18}F]AMC20 showed greater decrease of striatal SBRs and BP_{ND} in response to raclopride treatment in living rats (Table S5). However, [^{18}F]AMC20 is inferior to existing ^{11}C-labeled $D_{2/3}$ agonists [13,21,22] in terms of baseline striatal BP_{ND} (0.49–0.59 vs >0.8) and, apparently, also in terms of sensitivity to raclopride treatment.

The higher non-specific binding of [^{18}F]AMC20, resulting from its considerably higher lipophilicity (LogD 2.33±0.03) relative to [^{18}F]FEt-AMC13 (LogD 1.67±0.07), seems to have prevented [^{18}F]AMC20 from attaining a high signal-to-noise ratio despite its high $D_{2/3}$Rhigh affinity.

[^{18}F]AMC20 and [^{18}F]FEt-AMC13, both based on the AMC1 structure, have, therefore, two common problems. One is the low signal-to-noise ratio, proportional to the association and dissociation rates of tracer binding to the receptors at equilibrium. Signal-to-noise ratio may be limited by the non-specific binding of the tracer in the tissue, which leaves less free tracer available for specific binding, or by the quick release of specifically bound agonist tracer from the receptors due to the receptor's relaxation into the low-affinity state after G-protein activation by agonist – a known potential issue for agonist tracers of G-protein-coupled receptors [11].

Another problem is the suspected lack of pharmacological selectivity of [^{18}F]AMC20 and [^{18}F]FEt-AMC13 towards $D_{2/3}$R.

Screening of the AMC20 and FEt-AMC13 against non-dopaminergic receptors and more thorough studies of their binding kinetics in a more controlled environment (in vitro) are necessary to find out which factors limit the signal-to-noise ratio of these compounds as $D_{2/3}$R-imaging agents and to produce and evaluate new optimized AMC derivatives.

CONCLUSION

We have evaluated a novel aminomethyl chromane-derived $D_{2/3}R$ agonist radiopharmaceutical. The agonist, AMC20, demonstrated very high affinity towards the high-affinity state of human $D_{2/3}R$Long in cell membrane homogenates. [^{18}F]AMC20 showed specific binding to the striatal $D_{2/3}R$ in rat brain slices in vitro as well as in living rat brain. The signal-to-noise ratio of [^{18}F]AMC20 was on a par with that of the structurally related tracer [^{18}F]FEt-AMC13 evaluated by us earlier. Further investigations of the structure-activity relationships of [^{18}F]AMC20 and related compounds can lead to a radioligand suitable for $D_{2/3}R$ imaging in vivo.

Acknowledgements

J.A.J.M. (Jef) Vekemans, Eindhoven University of Technology, (TU/e), is thanked for his advice on synthetic design; J.L.J. (Joost) van Dongen and R.A.A. (Ralf) Bovee (both TU/e) are thanked for their expertise on and execution of the HRMS measurements and the elemental analyses, respectively. Prof. E.W. (Bert) Meijer (TU/e and ICMS Eindhoven), is thanked for enabling the execution of the synthetic part of the presented research.

Aren van Waarde, Antoon Willemsen, Janine Doorduin, Jurgen Sijbesma and Mohammed Khayum (all – department of Nuclear Medicine and Molecular Imaging, University Medical Center Groningen, University of Groningen) are thanked for their advice on the design and help with the execution of the microPET study.

This work was supported by a grant from the Dutch Technology Foundation STW (grant 10127).

APPENDIX

Chemistry

Materials and methods

Reagents, chemicals, materials and solvents were obtained from commercial sources, and were used as received: Biosolve, Merck for solvents, Cambridge Isotope Laboratories for deuterated solvents, and Aldrich, Acros, ABCR, Merck and Fluka for chemicals, materials and reagents. All solvents were of AR quality.

^{1}H-NMR and ^{13}C-NMR spectra were recorded on Varian MR (300 or 400 MHz for ^{1}H-NMR, 100 MHz for ^{13}C-NMR) spectrometers at ambient temperature. Chemical shifts are reported in ppm, applying deuterated chloroform ($CDCl_3$) or other deuterated solvents as internal reference. Abbreviations used for splitting patterns are s = singlet, t = triplet, q = quartet, m = multiplet, dd = double doublet.

LC-PDA/MS analyses were performed on a Shimadzu LC-10 AD VP series LC coupled to a photo diode array (PDA) detector (Finnigan Surveyor PDA Plus detector, Thermo Electron corporation) and an ion-trap detector (LCQ Fleet, Thermo Scientific). Analyses were executed at 298 K using an Alltech Alltima HP C18 3μ column using an injection volume of 1–4 μL, a flow rate of 0.2 mL min-1 and typically a MeCN in H_2O gradient (from 5% to 100% MeCN, where both MeCN and H_2O contain 0.1% formic acid).

Elemental analyses and UPLC-HRMS analyses were performed on AMC20 in its isolated oxalate form. Elemental analyses were done to assess the number of oxalate groups attached to AMC20 and were performed on a Perkin-Elmer Series II CHNS/O Analyser 2400. UPLC-HRMS was used to determine the purity and the exact molecular weight of AMC20. UPLC was performed on a Waters Acquity UPLC equipped with a sample manager (an autosampler) and a binary solvent manager. An Acquity UPLC BEH C18 1.7 micrometer column was used applying H_2O and MeCN, both containing 0.1% formic acid, as the two eluents and applying an 8 minute gradient program where the content of MeCN was increased from 5 to 60% in 5 minutes time. A sample solution (10% MeCN in H_2O with 0.1% formic acid) with a concentration of ca. 0.1 mg/mL was prepared and an injection volume of 0.1 microliter was used. For HRMS detection, a Xevo G2 Qtof detector using Zspray lockspray ionisation was applied.

Analytical thin layer chromatography (TLC) was performed on Kieselgel F-254 precoated silica plates. Normal phase column chromatography was carried out on flash silica gel (40–63 μm mesh) or regular silica gel (60–200 μm), both acquired from Screening Devices B.V., or on standardized aluminium oxide 90 from Merck.

Synthesis of AMC20 reference and precursors

The synthetic routes to the [^{19}F]AMC20 and the [^{18}F]AMC20 precursor amine **5** are outlined in Figure S1. The synthesis of all AMC derivatives shown in this figure has been already described in detail elsewhere [15], except the preparation of AMC20 itself and of its precursor **4**, which is described here. Briefly, all compounds were prepared starting from 2,4-dihydroxyacetophenone (**1**) that was converted in two steps [24,25] and a third lipase kinetic resolution step [26] to the key AMC-intermediate (*R*)-ethyl 7-hydroxychroman-2-carboxylate (**2**). The 7-hydroxyl group of the chromane moiety of **2** was protected by the methoxymethyl (MOM) group, the ethyl ester group was reduced to the primary alcohol, and this alcohol was tosylated to arrive at molecule **3**. 'Cold' AMC20 was obtained by coupling of **3** with *p*-fluorobenzylamine to give molecule **4** and then removing the MOM protecting group. Secondary amineAMC20 was converted to its oxalate salt, and this salt was used in the assays that are described in this manuscript. Finally, tosylate **3** was used in a standard two-step Gabriel synthesis to prepare primary amine **5**.

*(R) N-[7-(Methoxymethoxy)chroman-2-yl]methyl 4-fluorobenzyl amine (**4**)*

Tosylate **3** (250 mg, 0.66 mmol), commercially available 4-fluorobenzylamine (124 mg, 0.99 mmol, 1.5 moleqs) and DIPEA (341 mg, 2.64 mmol, 4 moleqs) were dissolved in DMSO (5 mL). The reaction mixture was stirred for 24 hours at 85 °C, and was then poured into ice water. The aqueous layer was extracted with ethyl acetate to yield crude product that was purified by alumina column chromatography (2% MeOH/$CHCl_3$). Yield: 124 mg (57%).

^{1}H NMR ($CDCl_3$): δ = 7.30 (m, 2H), 7.00 (m, 2H), 6.93 (m, 1H), 6.53 (multiple signals, 2H), 5.08 (s, 2H), 4.15 (m, 1H), 3.85 (s, 2H), 3.45 (s, 3H), 2.9–2.6 (multiple signals, 4H), 1.93 (m, 1H), 1.8 (multiple signals, 2H). LC-MS: m/z = 332.4 $[M+H]^+$, (calcd 331.39 for $C_{19}H_{22}NO_3F$).

(R)-2-[(4-Fluorobenzylamino)methyl]chroman-7-ol (AMC20)

The MOM-protected secondary amine **4** (125 mg, 0.378 mmol) was dissolved in an 4M HCl solution in dioxane (2 mL) and isopropanol (2 mL). The reaction mixture was stirred for about 3 hours at rt, while a N_2 flow was maintained over the reaction mixture. From time to time, N_2 was bubbled through the solution in order to remove volatile reaction products from the mixture. The reaction mixture may turn hazy due to precipitation of the ammonium salt. After completion of the reaction (the reaction was monitored by LC-MS), the mixture was added to water and the pH was brought to slightly basic by addition of a NaOH-solution. The free amine oil product was isolated from the water layer by several extractions using $CHCl_3$ or CH_2Cl_2 with some added THF, followed by drying of the collected organic layers with Na_2SO_4 and evaporation of the solvent.

Yield 63 mg (58%).

^{1}H NMR ($CDCl_3$): δ = 7.35 (m, 2H), 7.0 (m, 2H), 6.77 (m, 1H), 6.30 (multiple signals, 2H), 4.05 (m, 1H), 3.90 (d, 1H), 3.85 (d, 1H), 2.85–2.75 (multiple signals, 2H), 2.7–2.5 (multiple signals, 2H), 1.8 (m, 1H), 1.7 (m, 1H). ^{13}C NMR ($CDCl_3$): δ = 163.5, 161.0, 156.1, 154.4, 133.5, 130.5, 130.4, 130.1, 115.6, 115.4, 112.6, 109.2, 103.2, 74.1, 53.4, 53.2, 26.2, 23.6. LC-MS: *m/z* = 288.4 $[M+H]^+$, (calcd 287.33 for $C_{17}H_{18}NO_2F$).

Preparation of the oxalate salt of AMC20: the free amine of AMC20 (63 mg, 0.219 mmol) was dissolved in THF (3 mL) and oxalic acid dihydrate (61 mg, 0.484 mmol, 2.2 moleqs) in THF (1 mL) was added. The reaction mixture turned hazy due to precipitation of the oxalate ammonium salt. After about 3–5 hours of stirring the reaction mixture was centrifuged and the solvent was pipetted or decanted off. The residue was stirred in a fresh 1:1 mixture of diethyl ether and THF, and was centrifuged again. The solvent was removed and the precipitate was dried to yield a white solid residue (41 mg, 50%).

^{1}H NMR (DMSO-d_6): δ = 6.0–3.5 (broad signal acidic protons), 7.55 (m, 2H), 7.25 (m, 2H), 6.8 (m, 1H), 6.3 (m, 1H), 6.25 (s, 1H), 4.25 (m, 1H), 4.2 (m, 1H), 3.2–3.0 (m, 2H), 2.75–2.6 (multiple signals, 2H), 2.0 (m, 1H), 1.65 (m, 1H). ^{13}C NMR (DMSO-d_6): δ = 164.0, 163.4, 161.3, 156.5, 153.9, 132.4, 132.3, 129.9, 128.9, 115.6, 115.4, 111.9, 108.5, 102.9, 71.6, 49.9 (2Cs), 24.7,

22.8. LC-MS: *m/z* = 288.4 $[M+H]^+$, (calcd 287.33 for $C_{17}H_{18}NO_2F$). HRMS $[M+H]^+$: Calcd 288.1400, Found 288.1403 (1.0 ppm). Anal. $C_{17}H_{18}NO_3F$ + $C_2H_2O_4$ (FW=377.37).

Radiochemistry

Materials

[^{18}F]fluoride was produced in the Scanditronix MC-17F cyclotron (Scanditronix, Uppsala, Sweden) and delivered from the target into the hotcell with helium overpressure. Synthetic procedures were performed manually. Radiochemical conversions and purities were determined by radio-HPLC using beta-sensitive detectors and dose-calibrators (Veenstra Instruments) and by radio-TLC using Cyclone phosphor storage screens (multisensitive, Packard) and OptiQuant software.

[^{18}F]fluoride production and drying

[^{18}F]fluoride in enriched [^{18}O]water was adsorbed on an anion-exchange column (QMA) (pre-activated with $NaHCO_3$ solution) and then eluted from it into the drying vial with 1–1.5 ml of K_2CO_3-Kryptofix solution in 9:1 v/v mixture of acetonitrile and water, respectively. After the elution of QMA, acetonitrile and water were evaporated at 130 °C under nitrogen flow. For further water removal, 1 ml anhydrous acetonitrile was added into the reaction vial and evaporated. The operation was repeated three times. In total, [^{18}F]fluoride drying process took about 15 min.

Preparation of [^{18}F]AMC20

Trimethylammonium benzaldehyde triflate (2 mg) in 1 mL anhydrous DMSO were added into the vial with dried [^{18}F]fluoride (prepared as described above) complexed with K_2CO_3 (1.5–2.2 mg) and 5–7.5 mg/ml Kryptofix. The vial was sealed and the reaction was carried out for 2.5 min at 130 °C followed by cooling for 5 min. Then 1 mL of water was added to the cooled reaction mixture. [^{18}F]FBA was purified by reverse-phase HPLC using Platinum C18 EPS 5μ 250×10 mm column eluted with acetonitrile/10 mM H_3PO_4 (40/60 v/v) at 4 ml/min (retention time 9.7 min, k' = 3.0). Collected radioactive fraction was diluted 2–3 fold with water and 4-[^{18}F]fluorobenzaldehyde was adsorbed on Oasis HLB SPE cartridge. The cartridge was rinsed with 5 mL of pure water and dried for 5 min in strong nitrogen flow. Afterwards 4-[^{18}F]fluoroben-

zaldehyde was eluted from the cartridge with 0.9 mL methanol (cartridge was eluted in reverse position; about one third of ethanol got absorbed by the resin) into a v-vial containing primary amine **5** (0.6 mg) and $NaBH_3CN$ (2 mg) in 100 μl methanol. 5 μl glacial acetic acid was added into the vial, the vial was sealed and reductive amination was conducted for 10 min at 120 °C. The vial was allowed to cool down for 2–3 min, then 1 mL 0.4N HCl was added into it to allow for deprotection of the MOM-group that lasted 10 min at 120 °C. [^{18}F]AMC20 was purified by reverse-phase HPLC using Platinum C18 EPS 5μ 250×10 mm column eluted with acetonitrile/10 mM H_3PO_4 (50/50 v/v) at 5 mL/min (retention time 10.1 min, k' = 4.1).

The collected HPLC fraction was diluted with 10 volumes of water and [^{18}F]AMC20 was adsorbed on an Oasis HLB SPE cartridge. The cartridge was rinsed with 5 mL pure water and [^{18}F]AMC20 was then eluted with 1–2 mL absolute ethanol (typically giving a 50% recovery). After partial or complete evaporation of ethanol in nitrogen flow (with or without application of vacuum) the tracer was formulated in physiological saline (ethanol content in the formulated tracer was kept below 10%). The identity of [^{18}F]AMC20 was confirmed and the radiochemical purity was assessed by reverse-phase HPLC and radio-TLC, respectively. Reverse-phase HPLC was carried out on Platinum EPS 5μ 250×4.6 column eluted with acetonitrile/water/formic acid (60/40/0.1 v/v) at 2 mL/min (retention time 14.7 min, k' = 13.6). Radio-TLC was carried out on silica plates eluted with ethylacetate/methanol/triethylamine (100/5/1, R_f = 0.61) and hexane/ethylacetate/triethylamine (50/50/1, R_f = 0.28).

Pharmacology

Arrestin recruitment assay

Agonism of AMC20 at D_2 receptors was determined with the PathHunter™ eXpress DRD2L CHO-K1 β-Arrestin GPCR Assay (catalog number 93-0446CP2M) from DiscoveRx (Fremont, CA), used according to the supplied protocol. At first 8000 cells/well were seeded in a 96-well plate and incubated 48 hours at 5% CO_2 and 37 °C. Then dilutions of AMC20 were added and the plates were incubated for 90 minutes at 5% CO_2 and 37 °C. After that the detection mixture was prepared and added to the assay. Subsequently the plates were incubated for 60 minutes at room temperature after which chemiluminescence was measured on a multiplate reader (Victor 2, Wallac, PerkinElmer).

In vitro autoradiography assay

Frozen brains of young (10–12 weeks of age; 300–350 g body-weight) male Sprague-Dawley rats (Harlan, Netherlands) were cut into two halves along the sagittal symmetry plane. Each half was mounted, lateral side up, on a paper slide pre-treated by Tissue-Tek fixing cocktail (Sakura, the Netherlands) and fixed by placing it onto a Petri dish floating on liquid nitrogen. After fixing, brains were cut at −12 °C into sagittal slices 20 μm thick using a Leica microtome, and the slices were thaw-mounted on Superfrost (70×22 mm, Fischer) adhesive slides. Only slices containing both striatal and cerebellar regions (representing non-specific binding) were used. Slides were organized in pairs and in each pair new slices were mounted alternately on the first or the second slide of the pair, so that slices in corresponding positions on the two slides forming a pair would represent adjacent tissue layers. The slices were allowed to dry, then put into storage boxes with dessicator (silicagel) bags and kept at −80 °C till they were used (no longer than 1 week).

On the day of the experiment the slides with mounted slices were taken out of storage and allowed to come to room temperature for 5–10 minutes. After that, incubation buffer (50 mM Tris-HCl, 5 mM KCl, 2 mM $CaCl_2$, 2 mM $MgCl_2$, 120 mM NaCl, pH 7.4 25 °C) was applied to the slides using an automatic pipette (1–1.2 ml/slide) and the slides were pre-incubated for 15 min at room temperature. The pre-incubation buffer was then removed and the slides were placed into staining jars containing incubation buffer and radioligand ([^{18}F]AMC20) with or without 10 μM raclopride ($D_{2/3}$-antagonist) or 100 μM guanosine-5'-triphosphate sodium salt (GTP, stimulator of G-protein uncoupling from the receptors). The slides were incubated for 35 min at 37 °C, then washed once with ice-cold incubated buffer (3.5 min) and dipped for 30 sec into ice-cold sterile water to remove buffer salts.

After drying the slides in a stream of room-temperature air, they were exposed on phosphor storage screens for 6–10 hours. Afterwards the storage screens were read by Cyclone Storage Phosphor System (Packard Instruments Co). Quantification of plate readings was done with Optiquant software (version 3.00, Packard Instruments Co), drawing regions of interest manually on the striatum and cerebellum.

Animal tissues workup

Measuring the whole blood time-activity curve and metabolite-corrected plasma input curve

25 μl aliquots of whole blood were withdrawn from each arterial blood sample taken from each rat. The rest was centrifuged at 3500 g for 5 min, 25 μl supernatant (plasma) aliquots were withdrawn and deproteinated with 75 μl of ice-cold acetonitrile. From the resulting 100 μl, 2–8 μl portions (i.e. 2–8% of volume) were taken for thin layer chromatography analysis (radio-TLC), to assess radiometabolite content. Radio-TLC was performed on silica plates. Samples of the formulated tracers (diluted) were run along with deproteinated plasma samples to confirm the identity of the parent compound in plasma. Eluent system was ethylacetate/methanol/triethylamine 100/5/1, recorded R_f of [^{18}F]AMC20 was 0.65.

The radioactivity of the plasma and whole blood samples was measured using a well-type gamma-counter (LKB-1282-Compugamma, LKB Wallac).

Ex vivo autoradiography

The selected half of the brain (rostral or randomly taken left/right) was quickly frozen over liquid nitrogen and prepared for cutting on the microtome in the same manner as brains used for in vitro autoradiography (see above). 40 μm thick slices were cut, mounted on Superfrost glass slides, permitted to dry and then directly applied to the phosphor storage screens.

Brain radiometabolite analysis

The half of the brain not selected for ex vivo autoradiography was homogenized in 3 ml ice-cold acetonitrile using Heidolph IDAX600 homogenizer at maximum speed. Homogenate was centrifuged at 3500 g for 5 min and the supernatant (containing >95% total radioactivity) was analyzed by radio-TLC in the same way as described above for the plasma.

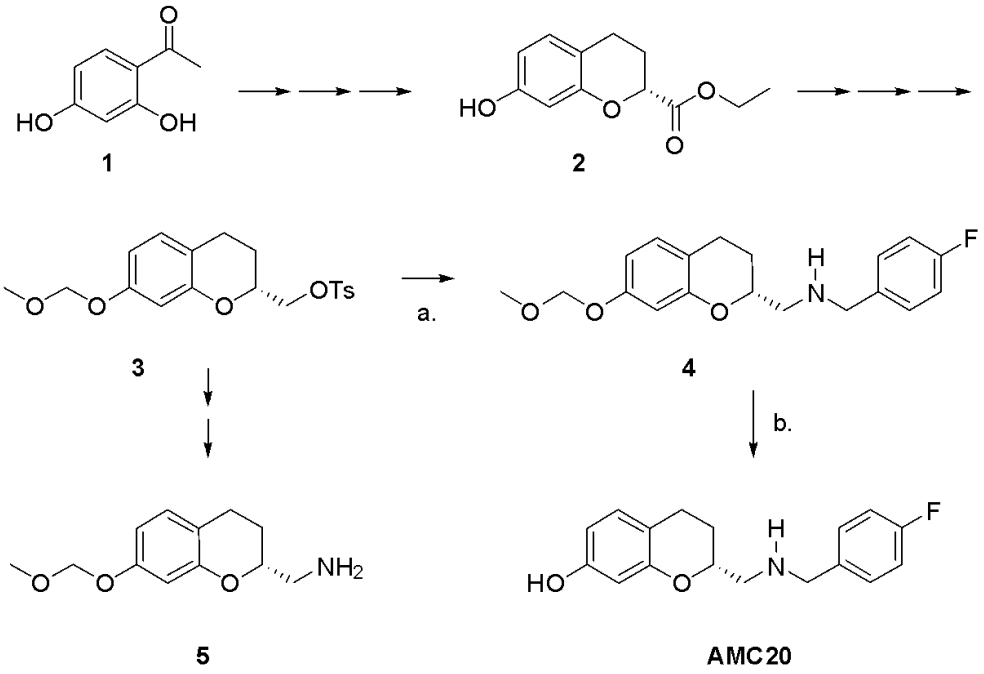

Figure S1. The scheme of synthesis of unlabeled AMC20 and of primary amine **5**, the precursor to [^{18}F]AMC20.

Reagents and solvents: (a) *p*-fluorobenzylamine, DIPEA, DMSO; (b) 4M HCl, dioxane/isopropanol.

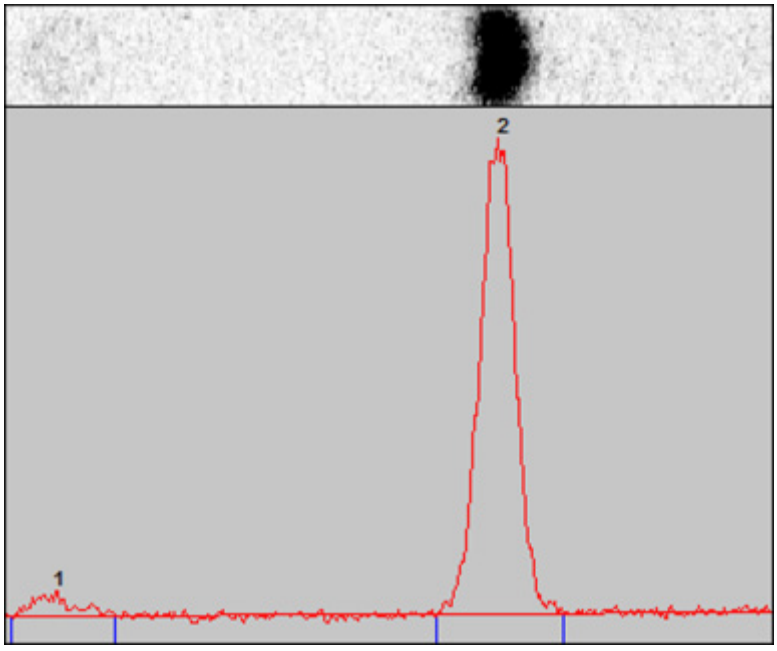

Figure S2. Radio-TLC analysis of brain tissue radiometabolites of [^{18}F]AMC20.

A representative TLC lane is shown, as an actual image (top) and as a profile graph of total exposure (bottom). Solvent system is ethylacetate/methanol/triethylamine (100/5/1). Solvent front movement is left-to-right. Peak 1 represents radiometabolites of [^{18}F]AMC20, peak 2 represents intact [^{18}F]AMC20.

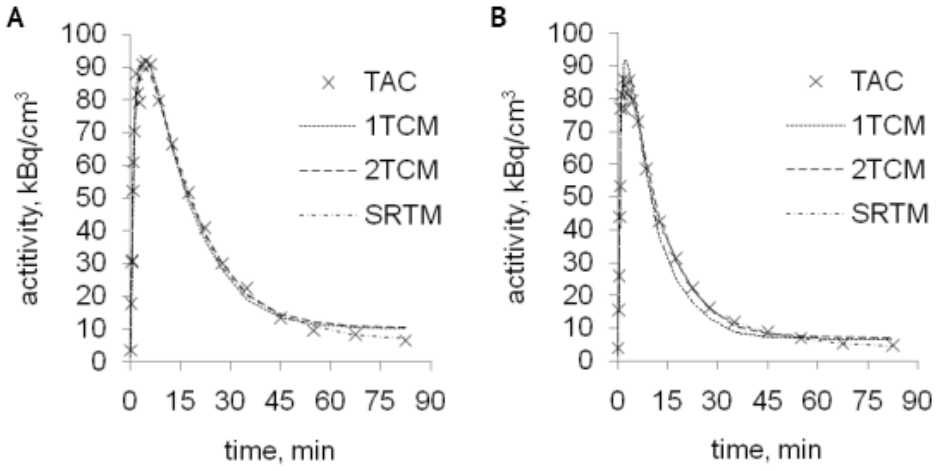

Figure S3. Representative striatal (A) and cerebellar (B) TACs of [^{18}F]AMC20 (in a control rat) and the corresponding fits with 1TCM, 2TCM and SRTM models.
2TCM fits had lower Akaike's information criterion (AIC) value than 1TCM fits in 57 out of 80 (71%) cases. SRTM fits had lower AIC value than 2TCM fits in 69 out of 80 (86%) cases.

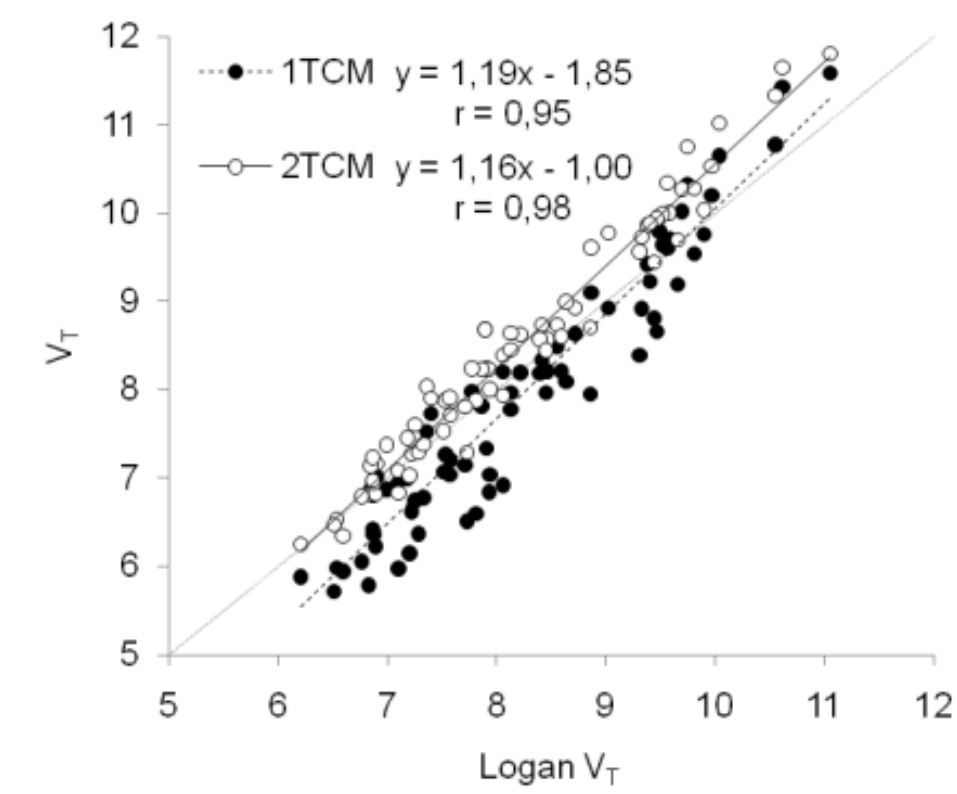

Figure S4. Correlation of region-of-interest total distribution volumes (V_T) of [^{18}F]AMC20 obtained by Logan analysis with V_T values obtained by analyses with 1TCM and 2TCM models.

Points represent fits for individual regions in individual animals (both control and raclopride-pre-treated). Data for striatum, hippocampus, thalamus, hypothalamus, cortex, brainstem, cerebellum, olfactory bulbs and pituitary are used.

Unity line (x = y) and linear regression lines for 1TCM and 2TCM data, along with their equations and r-criterion values are shown on the graphs.

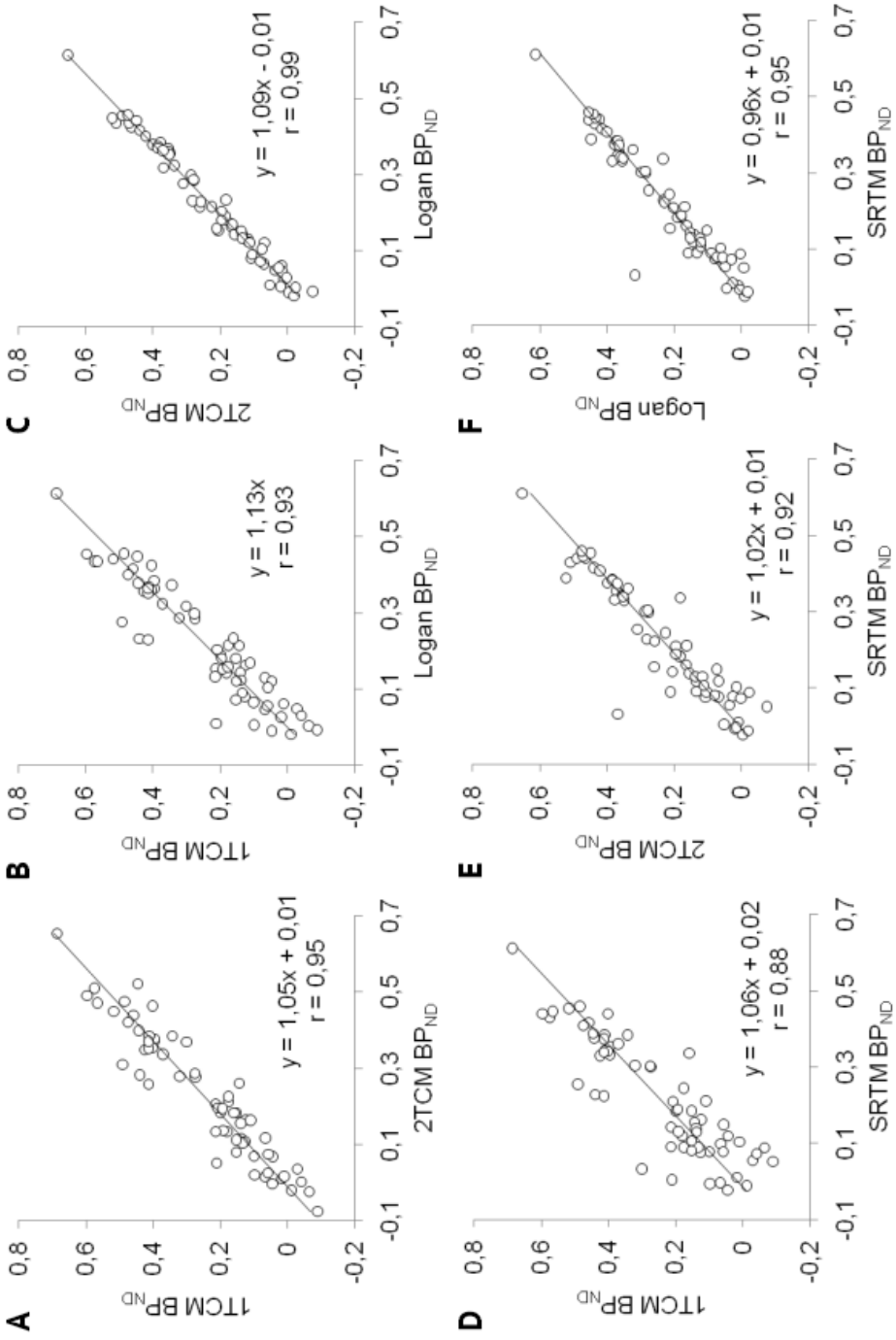
A
1TCM BP$_{ND}$
2TCM BP$_{ND}$
y = 1,05x + 0,01
r = 0,95
B
1TCM BP$_{ND}$
Logan BP$_{ND}$
y = 1,13x
r = 0,93
C
2TCM BP$_{ND}$
Logan BP$_{ND}$
y = 1,09x - 0,01
r = 0,99
D
1TCM BP$_{ND}$
SRTM BP$_{ND}$
y = 1,06x + 0,02
r = 0,88
E
2TCM BP$_{ND}$
SRTM BP$_{ND}$
y = 1,02x + 0,01
r = 0,92
F
Logan BP$_{ND}$
SRTM BP$_{ND}$
y = 0,96x + 0,01
r = 0,95

Figure S5 (previous page). Mutual correlation of region-of-interest binding potential (BP_{ND}) values of [^{18}F]AMC20 obtained from different models.

A – correlation of 1TCM and 2TCM BP_{ND} values. B, C – correlation of Logan BP_{ND} values with 1TCM, 2TCM values. D, E, F – correlation of SRTM BP_{ND} with 1TCM, 2TCM and Logan BP_{ND} values. Linear regression lines, along with their equations and r-criterion values are shown on the graphs.

Points represent fits for individual regions in individual animals, both saline and raclopride-pre-treated. Data for the striatum, hippocampus, thalamus, hypothalamus, cortex, brainstem, olfactory bulbs and pituitary are presented. BP_{ND} values are calculated using the cerebellum as a reference region, therefore the data for the cerebellum are not presented. 2TCM BP_{ND} values are calculated from V_T estimates, not from individual rate constants.

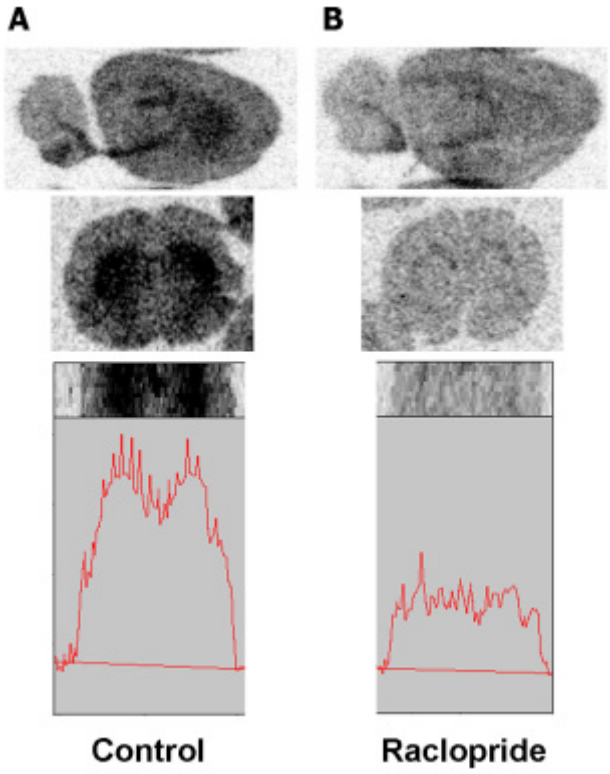

Figure S6. Ex vivo autoradiography images of [^{18}F]AMC20 uptake in control (A) and raclopride-treated (B) rats.

Representative sagittal and coronal slices are shown. Profile section through the striatum in coronal slices is presented at the bottom, showing absolute exposure values.

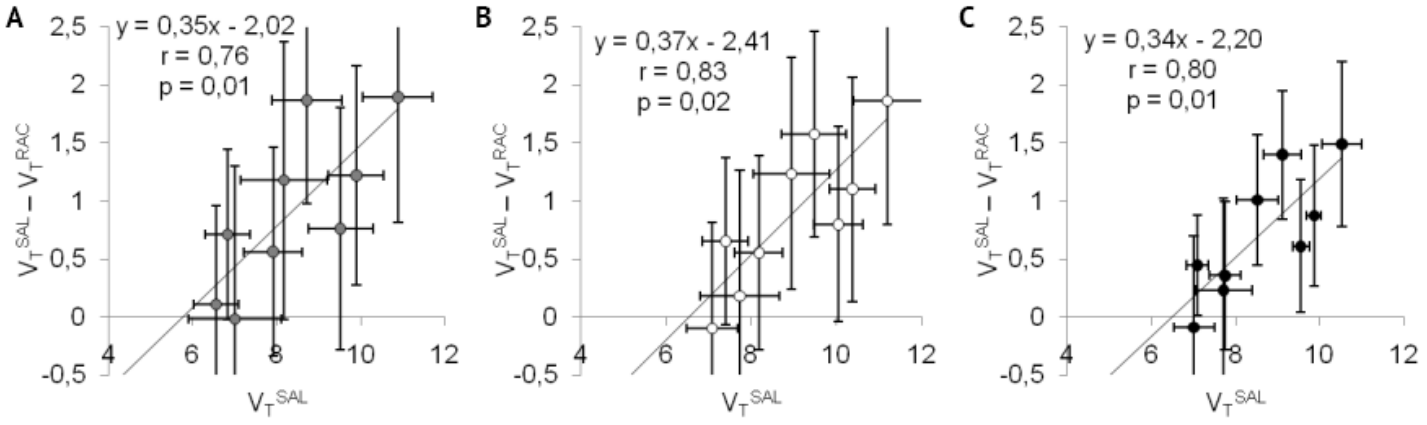

Figure S7. Modified Lassen plots [*19*] built with V_T values from 1TCM (A), 2TCM (B) and Logan (C) analysis of [^{18}F]AMC20 uptake.

Horizontal axes represent region-of-interest distribution volumes as baseline. Vertical axes represent the decrease of regional distribution volumes in raclopride-pre-treated rats relative to control rats. Assuming equal occupancy of receptors by raclopride and equal non-displaceable volume of distribution (V_{ND}) of the tracer in all ROIs, the slope and the X-intersect of the linear regression line show, respectively, the fraction of receptors occupied by raclopride and the V_{ND}.

Data forstriatum (always the rightmost topmost circle), hippocampus, thalamus, hypothalamus, cortex, brainstem, cerebellum (always the second circle from the left), pituitary and olfactory bulbs are used. Points represent means, error bars represent standard deviations. Equations of linear regression lines and r-criterion values are shown on the graphs.

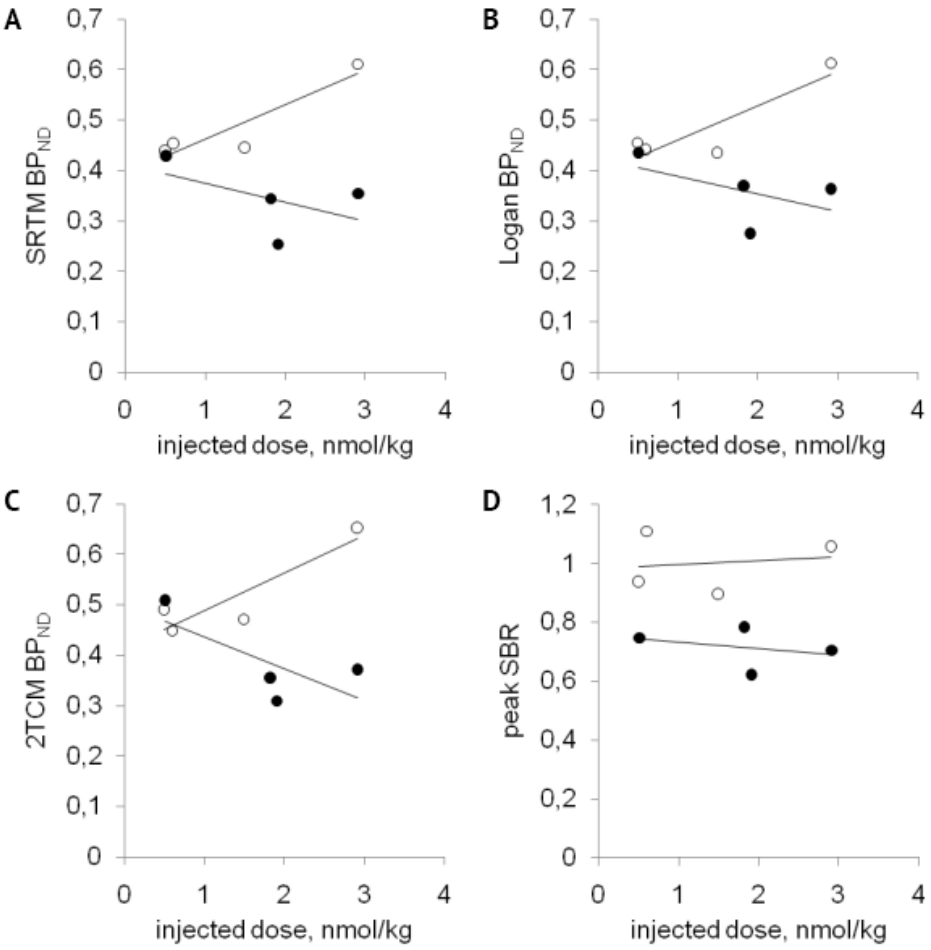

Figure S8. Relationship of injected doses of [^{18}F]AMC20 with SRTM-derived (A), Logan-derived (B) and 2TCM-derived (C) striatal binding potentials (BP_{ND}) and with PET-derived peak striatal specific binding ratios (D) in saline (open circles) and raclopride-pre-treated rats (closed circles).

Points represent measurements in individual animals. Linear trend lines are shown for each treatment group.

Table S1. Ex vivo uptake (SUV units, mean±SD) of [^{18}F]AMC20 in brain and peripheral tissues of saline (SAL) and raclopride-pre-treated (RAC) rats.

Tissue	Saline (*n*=4)	Raclopride (*n*=4)
Peripheral tissues		
Adipose tissue	0.40±0.33	0.46±0.55
Adrenal glands	1.52±0.77	1.07±0.37
Bladder	2.37±1.90	1.04±0.61
Bone	0.09±0.03	0.12±0.02
Bone marrow	0.38±0.17	0.37±0.16
Caecum	0.20±0.07	0.26±0.07
Duodenum	2.74±2.99	1.14±0.45
Heart	0.15±0.06	0.12±0.03
Kidney	1.23±0.51	0.80±0.46
Large Intestine	0.45±0.42	0.36±0.19
LI Content	0.02±0.01	0.01±0.01
Liver	1.49±0.28	1.26±0.26
Lung	1.03±0.43	0.94±0.26
Muscle	0.19±0.10	0.17±0.04
Pancreas	1.41±0.56	1.24±0.49
Prostate	0.57±0.30	1.25±0.95
Small Intestine	0.18±0.09	3.25±3.63
SI content	0.41±0.48	25.8±28.6
Spleen	0.42±0.27	0.43±0.20
Stomach	1.60±0.77	0.81±0.41

(continued on the next page)

Table S1 (continuation). Ex vivo uptake (SUV units, mean±SD) of [^{18}F]AMC20 in brain and peripheral tissues of saline (SAL) and raclopride-pre-treated (RAC) rats.

Tissue	Saline (*n*=4)	Raclopride (*n*=4)
Submandibular gland	0.74±0.33	0.68±0.21
Testes	0.44±0.14	0.48±0.08
Thymus	0.30±0.12	0.24±0.06
Brain tissues		
Cerebellum	0.16±0.07	0.13±0.03
Hippocampus	0.24±0.11	0.19±0.03
Medulla with pons	0.25±0.11	0.18±0.03
Midbrain	0.21±0.09	0.16±0.04
Olfactory bulbs	0.20±0.08	0.15±0.02
Pituitary	0.47±0.14	0.49±0.04
Rest of brain	0.23±0.10	0.18±0.04
Striatum	0.25±0.12	0.17±0.03
Thalamus + Hypothalamus	0.21±0.09	0.16±0.05
Total Brainstem	0.23±0.10	0.18±0.03
Total Cortex	0.20±0.09	0.17±0.04
Whole brain	0.21±0.09	0.17±0.04
Bodily fluids		
Whole Blood	0.21±0.06	0.14±0.06
Blood Cells	0.07±0.03	0.05±0.03
Plasma	0.34±0.10	0.20±0.08
Urine	20.0±15.3	17.1±10.6

Table S2. 1TCM and 2TCM rate constant estimates of [^{18}F]AMC20 uptake in brain regions of control rats.

ROI	Rat	1TCM			2TCM				
		K_1 (ml/g/min)	k_2 (1/min)	AIC	K_1 (ml/g/min)	k_2 (1/min)	k_3 (1/min)	k_4 (1/min)	AIC
Striatum	A	1.03±0.04	0.09±0.01	465	1.70±0.94	2.13±4.73	2.57±3.17	0.19±0.12	461
	B	1.10±0.03	0.11±0.01	470	303±37758	1769±222120	5.93±3.00	0.10±0.04	447
	C	1.18±0.07	0.11±0.01	506	400[a]	1284[a]	3.32[a]	0.09[a]	483
	D	1.05±0.04	0.09±0.01	455	1.40±0.42	0.89±1.79	1.74±2.80	0.27±0.14	454
Hippo-campus	A	1.00±0.05	0.10±0.01	475	2.07±0.72	2.44±2.39	1.64±0.89	0.14±0.03	459
	B	1.22±0.05	0.14±0.01	487	2.46±0.44	2.38±1.19	1.49±0.45	0.18±0.02	451
	C	1.21±0.08	0.14±0.02	506	1022[a]	2917[a]	2.86[a]	0.11[a]	470
	D	0.94±0.03	0.09±0.01	449	1.16±0.20	0.48±1.57	0.95±5.61	0.29±6.14	448
Thalamus	A	1.35±0.05	0.13±0.01	471	3.29±3.00	6.15±13.10	3.57±2.90	0.18±0.09	461
	B	1.40±0.06	0.15±0.01	487	3.45±1.88	5.08±0.58	2.65±4.27	0.20±11.77	468
	C	1.51±0.09	0.16±0.02	508	288[a]	872[a]	3.93[a]	0.13[a]	489
	D	1.25±0.05	0.12±0.01	459	1.36±0.14	0.22±0.18	0.22±0.61	0.32±0.36	461

(continued on the next page)

Table S2 (continuation). 1TCM and 2TCM rate constant estimates of [^{18}F]AMC20 uptake in brain regions of control rats.

ROI	Rat	1TCM			2TCM				
		K_1 (ml/g/min)	k_2 (1/min)	AIC	K_1 (ml/g/min)	k_2 (1/min)	k_3 (1/min)	k_4 (1/min)	AIC
Hypo-thalamus	A	1.20±0.05	0.13±0.01	469	1.70±0.25	0.83±0.70	0.92±2.03	0.25±2.56	457
	B	1.17±0.08	0.17±0.02	500	2.59±0.61	2.36±1.35	1.03±0.40	0.17±0.02	475
	C	1.09±0.07	0.14±0.02	504	22.7±121.3	67.7±396.6	2.79±1.06	0.12±0.03	482
	D	1.00±0.08	0.11±0.02	487	5.45±3.62	9.46±4.86	1.56±3.30	0.10±11.01	457
Cortex	A	0.75±0.02	0.09±0.01	444	0.75±0.03	0.09±0.01	1.33×10^{-12}±0.01	0.09±958.27	448
	B	0.99±0.04	0.14±0.01	471	2.08±0.18	2.79±0.64	1.72±0.22	0.19±0.01	399
	C	1.09±0.05	0.13±0.01	485	498[a]	2332[a]	4.51[a]	0.11[a]	452
	D	0.71±0.02	0.09±0.01	431	182±25437	1739±245250	6.40±3.91	0.09±0.04	413
Brainstem	A	1.47±0.06	0.15±0.01	475	2.22±0.26	1.08±0.51	0.98±0.44	0.24±0.03	450
	B	1.31±0.06	0.16±0.01	487	2.53±0.30	2.14±0.73	1.31±0.30	0.21±0.02	441
	C	1.25±0.08	0.16±0.02	503	4.85±1.46	7.83±1.43	1.97±0.48	0.15±5.40	449
	D	1.21±0.05	0.13±0.01	456	1.79±0.16	0.95±0.39	0.94±1.12	0.22±1.48	428

(continued on the next page)

Table S2 (continuation). 1TCM and 2TCM rate constant estimates of [^{18}F]AMC20 uptake in brain regions of control rats.

ROI	Rat	1TCM			2TCM				
		K_1 (ml/g/min)	k_2 (1/min)	AIC	K_1 (ml/g/min)	k_2 (1/min)	k_3 (1/min)	k_4 (1/min)	AIC
Cerebellum	A	1.30±0.05	0.17±0.01	462	2.05±0.34	1.52±0.75	1.45±2.35	0.29±3.28	441
	B	1.30±0.05	0.21±0.02	478	2.40±0.31	2.27±0.87	1.47±0.40	0.27±0.02	435
	C	1.42±0.09	0.21±0.03	503	461.76[a]	1282[a]	3.13[a]	0.16[a]	454
	D	1.03±0.03	0.15±0.01	438	204±23305	1568±178070	7.31±177210	0.14±181530	419
Olfactory bulbs	A	0.86±0.03	0.11±0.01	452	398[a]	2671[a]	5.30[a]	0.10[a]	433
	B	0.89±0.05	0.14±0.01	482	1.73±0.20	1.63±0.55	0.91±0.24	0.16±0.01	443
	C	0.93±0.05	0.13±0.01	483	2.84±1.11	6.08±0.89	2.27±1.40	0.15±7.44	449
	D	0.74±0.04	0.11±0.01	451	1.39±0.23	1.72±0.88	1.14±0.42	0.15±0.02	424
Pituitary	A	0.86±0.05	0.11±0.01	472	1.56±0.25	1.32±0.69	0.89±0.37	0.14±0.02	449
	B	0.94±0.06	0.16±0.02	491	1.93±0.42	1.96±1.12	0.95±0.40	0.16±0.02	468
	C	0.99±0.07	0.16±0.02	500	362±21029	1178±68329	2.55±68174	0.12±68981	467
	D	0.74±0.03	0.09±0.01	443	0.82±0.07	0.17±0.09	0.13±0.21	0.16±0.13	443

Data are presented as means±SD.
a Standard deviation could not be estimated.

Table S3. Region-of-interest V_T measurements of [^{18}F]AMC20.

Region of interest	Logan V_T		1TCM V_T		2TCM V_T	
	control	raclopride	control	raclopride	control	raclopride
Striatum	10.53±0.48 (5)	9.04±0.53 (6)	10.89±0.83 (8)	8.99±0.69 (8)	11.21±0.80 (7)	9.34±0.70 (7)
Hippocampus	9.55±0.20 (2)	8.94±0.53 (6)	9.52±0.77 (8)	8.75±0.70 (8)	10.05±0.58 (6)	9.25±0.61 (7)
Thalamus	9.87±0.17 (2)	8.99±0.58 (6)	9.90±0.65 (7)	8.67±0.68 (8)	10.38±0.55 (5)	9.28±0.79 (9)
Hypothalamus	8.52±0.49 (6)	7.51±0.27 (4)	8.18±1.02 (13)	7.00±0.61 (9)	8.94±0.89 (10)	7.71±0.45 (6)
Cortex	7.76±0.37 (5)	7.40±0.52 (7)	7.92±0.69 (9)	7.36±0.58 (8)	8.19±0.56 (7)	7.63±0.62 (8)
Brainstem	9.11±0.44 (5)	7.72±0.34 (4)	8.72±0.82 (9)	6.85±0.34 (5)	9.48±0.76 (8)	7.91±0.45 (6)
Cerebellum	7.09±0.26 (4)	6.64±0.35 (5)	6.84±0.53 (8)	6.13±0.50 (8)	7.40±0.53 (7)	6.74±0.48 (7)
Olfactory Bulbs	7.01±0.48 (7)	7.10±0.63 (9)	6.56±0.52 (8)	6.45±0.67 (10)	7.09±0.61 (9)	7.18±0.69 (10)
Pituitary	7.72±0.67 (9)	7.49±0.42 (6)	7.02±1.10 (16)	7.03±0.72 (10)	7.74±0.94 (12)	7.55±0.55 (7)

Data are presented as means±SD (*n*=4 per treatment group). Coefficients of variation (in %) are shown in parentheses.

Table S4. BP_{ND} of [^{18}F]AMC20 per brain region in control and raclopride-treated rats.

Region of interest	1TCM BP_{ND}		2TCM BP_{ND}		Logan BP_{ND}		SRTM BPND	
	control	raclopride	control	raclopride	control	raclopride	control	raclopride
Striatum	0.59±0.07	0.47±0.08 (−21%)[a]	0.52±0.09	0.39±0.09 (−25%)	0.49±0.09	0.36±0.07 (−26%)[a]	0.49±0.08	0.35±0.07 (−29%)*
Hippocampus	0.39±0.06	0.43±0.02 (+9%)	0.36±0.07	0.37±0.08 (+4%)	0.35±0.06	0.35±0.08 (0%)	0.37±0.05	0.34±0.09 (−6%)
Thalamus	0.45±0.04	0.42±0.02 (−7%)	0.40±0.06	0.38±0.11 (−7%)	0.39±0.05	0.36±0.09 (−10%)	0.39±0.05	0.32±0.07 (−19%)
Hypothalamus	0.19±0.08	0.14±0.03 (−26%)	0.21±0.11	0.14±0.06 (−31%)	0.20±0.08	0.13±0.05 (−35%)	0.14±0.09	0.12±0.05 (−14%)
Cortex	0.16±0.04	0.20±0.02 (+27%)	0.11±0.02	0.13±0.06 (24%)	0.09±0.03	0.11±0.07 (22%)	0.08±0.01	0.10±0.06 (+18%)
Brainstem	0.27±0.06	0.12±0.04 (−56%)**	0.28±0.08	0.17±0.06 (−38%)	0.29±0.08	0.16±0.04 (−43%)*	0.29±0.08	0.14±0.03 (−53%)*
Olfactory Bulbs	0.03±0.06	0.05±0.09 (+97%)	0.02±0.04	0.07±0.11 (215%)	0.06±0.05	0.07±0.10 (25%)	0.07±0.05	0.07±0.12 (+2%)
Pituitary	0.02±0.11	0.07±0.09 (+227%)	0.05±0.11	0.05±0.10 (15%)	0.09±0.11	0.06±0.09 (−36%)	0.15±0.13	0.07±0.10 (−55%)

Data are presented as means±SD (n=4 per treatment group). Next to the BP_{ND} values of the raclopride-treated group, percentage of change relative to the control group is shown. *a* P < 0.07,* P < 0.05, ** P < 0.01, 2-sided Welch test.

Table S5. Comparison of [^{18}F]AMC20 and [^{18}F]FEt-AMC13.

Parameter		[^{18}F]AMC20		[^{18}F]FEt-AMC13[a]	
		mean baseline value	decrease after raclopride blockade[b]	mean baseline value	decrease after raclopride blockade[b]
In vitro striatal SBR[c]		5.27±1.49	83%	3.56±0.86	72%
Peak striatal SBR (PET)		0.97±0.13	35%	1.08±0.25	17%
Striatal SBR (ex vivo autoradiography)[d]		1.48±0.34	41%	1.81±0.29	39%
PET striatal BP_{ND} (by model)[e]	1TCM:	0.59±0.07	21%	0.63±0.08	25%
	2TCM:	0.52±0.09	25%	0.56±0.05	23%
	Logan:	0.49±0.09	26%	0.52±0.02	23%
	SRTM	0.49±0.08	29%	0.51±0.02	26%
V_T-based striatal $D_{2/3}R$ occupancy by raclopride (by model)[f]	1TCM:	35%		20%	
	2TCM:	37%		25%	
	Logan:	34%		21%	
Average baseline PET SUV of the whole brain: maximum/end-of-scan		3.38±0.18/0.18±0.04		1.94±0.26/0.22±0.02	

a data from [16] and [27].
b 1 mg/kg approximately 30 min before tracer injection.
c radioligand concentration – 1.7 nM.
d 35 min post-injection.
e cerebellum as reference region.
f estimated from the modified Lassen plot.

REFERENCES

1. Howes OD, Kapur S. The dopamine hypothesis of schizophrenia: version III – the final common pathway. Schizophr Bull. 2009;35:549–562.

2. Booij J, Tissingh G, Winogrodzka A, van Royen EA. Imaging of the dopaminergic neurotransmission system using single-photon emission tomography and positron emission tomography in patients with parkinsonism. Eur J Nucl Med. 1999;26:171–182.

3. Volkow ND, Fowler JS, Wang G-J, Swanson JM. Dopamine in drug abuse and addiction: results from imaging studies and treatment implications. Mol Psychiatry. 2004;9:557–569.

4. Volkow ND, Fowler JS, Wang GJ, Baler R, Telang F. Imaging dopamine's role in drug abuse and addiction. Neuropharmacology. 2009;56:3–8.

5. Elsinga PH, Hatano K, Ishiwata K. PET tracers for imaging of the dopaminergic system. Curr Med Chem. 2006;13:2139–2153.

6. Chio CL, Lajiness ME, Huff RM. Activation of heterologously expressed D_3 dopamine receptors: comparison with D_2 dopamine receptors. Mol Pharmacol. 1994;45:51–60.

7. Sibley DR, De Lean A, Creese I. Anterior pituitary dopamine receptors. Demonstration of interconvertible high and low affinity states of the D_2 dopamine receptor. J Biol Chem. 1982;257:6351–6361.

8. Liu IS, George SR, Seeman P. The human dopamine D_2(Longer) receptor has a high-affinity state and inhibits adenylyl cyclase. Brain Res Mol Brain Res. 2000;77:281–284.

9. Narendran R, Mason NS, Laymon CM, et al. A comparative evaluation of the dopamine $D_{2/3}$ agonist radiotracer [^{11}C](–)-N-propyl-norapomorphine and antagonist [^{11}C]raclopride to measure amphetamine-induced dopamine release in the human striatum. J Pharmacol Exp Ther. 2010;333:533–539.

10. Shotbolt P, Tziortzi AC, Searle GE, et al. Within-subject comparison of [^{11}C](+)-PHNO and [^{11}C]raclopride sensitivity to acute amphetamine challenge in healthy humans. J Cereb Blood Flow Metab. 2012;32:127–136.

11. Van Wieringen J-P, Booij J, Shalgunov V, Elsinga P, Michel MC. Agonist high- and low-affinity states of dopamine D_2 receptors: methods of detection and clinical implications. Naunyn Schmiedebergs Arch Pharmacol. 2013;386:135–154.

12. Finnema SJ, Bang-Andersen B, Wikström H V, Halldin C. Current state of agonist radioligands for imaging of brain dopamine D_2/D_3 receptors in vivo with positron emission tomography. Curr Top Med Chem. 2010;10:1477–1498.

13. Finnema SJ, Stepanov V, Nakao R et al. [^{18}F]MCL-524, an ^{18}F-labeled dopamine D_2 and D_3 receptor agonist sensitive to dopamine: a preliminary PET study. J Nucl Med. 2014;55:1–7.

14. Mewshaw RE, Kavanagh J, Stack G, et al. New generation dopaminergic agents. 1. Discovery of a novel scaffold which embraces the D_2 agonist pharmacophore. Structure-activity relationships of a series of 2-(aminomethyl)chromans. J Med Chem. 1997;40:4235–4256.

15. Van Wieringen J-P, Shalgunov V, Janssen HM, et al. Synthesis and characterization of a novel series of agonist compounds as potential radiopharmaceuticals for imaging dopamine $D_{2/3}$ receptors in their high-affinity state. J Med Chem. 2014;57:391–410.

16. Shalgunov V, van Wieringen J, Sijbesma J, et al. Evaluation of [^{18}F]AMC-15, [^{18}F]FPr-AMC-13 and [^{18}F]FEt-AMC-13 as candidate dopamine $D_{2/3}$-agonist radioligands for PET [Abstract]. J Nucl Med. 2013,54:1108.

17. Innis RB, Cunningham VJ, Delforge J, et al. Consensus nomenclature for in vivo imaging of reversibly binding radioligands. J Cereb Blood Flow Metab. 2007;27:1533–1539.

18. Lahti RA, Figur LM, Piercey MF, Ruppel PL, Evans DL. Intrinsic activity determinations at the dopamine D_2 guanine nucleotide-binding protein-coupled receptor: utilization of receptor state binding affinities. Mol Pharmacol. 1992;42:432–438.

19. Cunningham VJ, Rabiner EA, Slifstein M, Laruelle M, Gunn RN. Measuring drug occupancy in the absence of a reference region: the Lassen plot re-visited. J Cereb Blood Flow & Metab. 2009;30:46–50.

20. Wilson AA, McCormick P, Kapur S, et al. Radiosynthesis and evaluation of [^{11}C](+)-4-propyl-3,4,4a,5,6,10b-hexahydro-2H-naphtho[1,2-b][1,4]oxazin-9-ol as a potential radiotracer for in vivo imaging of the dopamine D_2 high-affinity state with positron emission tomography. J Med Chem. 2005;48:4153–4160.

21. Seneca N, Zoghbi SS, Skinbjerg M, et al. Occupancy of dopamine $D_{2/3}$ receptors in rat brain by endogenous dopamine measured with the agonist positron emission tomography radioligand [^{11}C]MNPA. Synapse. 2008;62:756–763.

22. Egerton A, Hirani E, Ahmad R, et al. Further evaluation of the carbon-11-labeled $D_{2/3}$ agonist PET radiotracer PHNO: reproducibility in tracer characteristics and characterization of extrastriatal binding. Synapse. 2010;64:301–312.

23. Skinbjerg M, Seneca N, Liow J-S, et al. Dopamine beta-hydroxylase-deficient mice have normal densities of D_2 dopamine receptors in the high-affinity state based on in vivo PET imaging and in vitro radioligand binding. Synapse. 2010;64:699–703.

24. Walenzyk T, Carola C, Buchholz H, Konig B. Chromone derivatives which bind to human hair. Tetrahedron. 2005;61:7366–7377.

25. Cohen N, Weber G, Banner BL, et al. 3,4-dihydro-2H-1-benzopyran-2-carboxylic acids and related-compounds as leukotriene antagonists. J Med Chem. 1989;32:1842–1860.

26. Kalaritis P, Regenye RW, Partridge JJ, Coffen DL. Kinetic resolution of 2-substituted esters catalyzed by a lipase ex pseudomonas-fluorescens. J Org Chem. 1990;55:812–815.

27. Shalgunov V., van Wieringen J.P., Janssen H.M. et al. Synthesis and evaluation in rats of homologous series of ^{18}F-labeled dopamine $D_{2/3}$ receptor agonists based on the 2-aminomethylchroman scaffold as potential PET tracers. EJNMMI Res., 2015, 5(41), DOI 10.1186/s13550-015-0119-x.

Chapter 5

Synthesis and evaluation in rats of homologous series of ^{18}F-labeled dopamine $D_{2/3}$ receptor agonists based on the 2-aminomethylchroman scaffold as potential PET tracers

Vladimir Shalgunov[1], Jan-Peter van Wieringen[2], Henk M. Janssen[3], P. Michel Fransen[3], Rudi A.J.O. Dierckx[1], Martin C. Michel[4], Jan Booij[2], Philip H. Elsinga[1]

1 Department of Nuclear Medicine and Molecular Imaging, University Medical Center Groningen, University of Groningen, Groningen, The Netherlands.

2 Department of Nuclear Medicine, Academic Medical Center, University of Amsterdam, Amsterdam, The Netherlands.

3 SyMO-Chem BV, Eindhoven, The Netherlands.

4 Department of Pharmacology, Johannes Gutenberg University, Mainz, Germany.

(EJNMMI Research 2015;5:41)

LIST OF ABBREVIATIONS

1TCM – one-tissue compartment model

2TCM – two-tissue compartment model

BP_{ND} – binding potential non-displaceable (equilibrium concentration ratio of specifically bound radioligand to non-displaceable radioligand in tissue)

DMF – N,N'-dimethylformamide

ESI-MS – electron-spray ionization mass-spectrometry

GPCR – G-protein coupled receptor

GTP – guanosinetriphospate

HPLC – high-pressure liquid chromatography

LC – liquid chromatography

MS/MS – tandem mass spectrometry

PET – positron emission tomography

ROI – region of interest

SPECT – single photon emission computed tomography

SRTM – simplified reference-tissue model

SUV – standardized uptake value (regional uptake relative to mean uptake across the body)

TAC – time-activity curve

TLC – thin-layer chromatography

UV-VIS – ultraviolet/visible

V_T – total distribution volume of a radioligand in the tissue (i.e. the sum of distribution volumes of free, non-specifically and specifically bound radioligand)

ABSTRACT

Background: Agonist positron emission tomography (PET) tracers for dopamine $D_{2/3}$ receptors ($D_{2/3}$Rs) offer greater sensitivity to changes in endogenous dopamine levels than $D_{2/3}$R antagonist tracers. $D_{2/3}$R agonist tracers currently available for clinical research are labeled with the short-lived isotope carbon-11, which limits their use. We aimed to develop high-affinity D_2R agonists amenable for labeling with the longer-living fluorine-18. Here we report the evaluation as potential PET tracers of two homologous series of [^{18}F]fluorinated tracers based on the 2-aminomethylchroman (AMC) scaffold: (*R*)-2-((4-(2-fluoroalkoxy)benzylamino)methyl)chroman-7-ols (AMC13 homologues) and (*R*)-2-((2-(4-(4-(fluoroalkoxy)phenyl)piperazin-1-yl)ethylamino)methyl)chroman-7-ols (AMC15 homologues). We varied the length of the ^{18}F-fluoroalkyl chain in these structures to balance brain penetration and non-specific binding of the radioligands by adjusting their lipophilicity.

Methods: The tracers were evaluated in brain slices of Sprague-Dawley rats by in vitro autoradiography and in living rats by microPET imaging and ex vivo autoradiography. PET data were analyzed with one and two-tissue compartmental models (1TCM/2TCM), simplified reference tissue model (SRTM) and Logan graphical analysis. Specificity of binding was tested by blocking $D_{2/3}$R with raclopride.

Results: Homologues with shorter fluoroalkyl chain consistently showed greater $D_{2/3}$R-specific-to-total binding ratios in the striatum than those with longer chains. The fluoroethoxy homologue of AMC13 ([^{18}F]FEt-AMC13) demonstrated the highest degree of $D_{2/3}$R-specific binding among the evaluated tracers: mean striatum-to-cerebellum uptake ratio reached 4.4 in vitro and 2.1/2.8 in vivo/ex vivo (PET/autoradiography). Striatal binding potential (BP_{ND}) relative to cerebellum was 0.51–0.63 depending on the estimation method. Radiometabolites of [^{18}F]FEt-AMC13 did not enter the brain. In vitro, application of 10 μmol/L raclopride reduced $D_{2/3}$R-specific binding of [^{18}F]FEt-AMC13 in the striatum by 81%. In vivo, pre-treatment with 1 mg/kg (2.9 μmol/kg) raclopride led to 17–39% decrease in $D_{2/3}$R-specific binding in the striatum.

Conclusions: Varying the length of the [^{18}F]fluoroalkyl chain helped improve the characteristics of the original candidate tracers. Further modifications of the current lead [^{18}F]FEt-AMC13 can provide an agonist radiopharmaceutical suitable for $D_{2/3}$R imaging by PET.

INTRODUCTION

Disregulation of dopamine signaling through dopamine D_2 and D_3 receptors ($D_{2/3}$Rs) is implicated in many neuropsychiatric disorders [1–4], making imaging of $D_{2/3}$Rs by positron emission tomography (PET) highly relevant.

The majority of PET tracers developed for $D_{2/3}$R imaging are antagonists [5], but in the last two decades, agonists have attracted attention as potential PET ligands for G-protein coupled neurotransmitter receptors (GPCRs). In in vitro competition studies, agonists consistently show higher affinity for receptor molecules bound to G-proteins ("high-affinity state") than for free receptors ("low-affinity state") [6–8]. Agonists are therefore expected to selectively recognize the "high-affinity" subset of receptor population in the imaging experiments, while antagonists bind to all receptors disregarding "affinity states" [9].

Though the existence of a separate "high-affinity state" subpopulation of $D_{2/3}$R in the brain is still not conclusively demonstrated in vivo [10], radiolabeled $D_{2/3}$R agonists indeed turned out to be more sensitive than the antagonist [^{11}C]raclopride to amphetamine-induced release of dopamine (itself also an agonist) in rodents, cats, non-human primates and humans [11–17]. Alteration of the relative abundance of "high-affinity state" $D_{2/3}$Rs ($D_{2/3}$R-high), detected by in vitro methods, is implied in dopamine supersensitivity, a state relevant to psychosis, Parkinsonism and drug addiction [18]. Changes in this in vitro-based parameter are likely to be translated into effects observable in vivo, so agonist tracers might provide new insights for the research into, and (early) diagnosis of, these common neuropsychiatric disorders.

Numerous scaffolds have been investigated in the development of $D_{2/3}$R agonist PET tracers [19], but representatives of only two classes, namely the apomorphines [^{11}C](−)NPA and [^{11}C]MNPA and the naphtoxazine [^{11}C](+)PHNO, have hitherto been used in human PET studies. These tracers can only be used in hospitals with an on-site cyclotron due to the short half-life of carbon-11. Fluorine-18-labeled tracers (half-life of 109.8 min) have greater potential of widespread application in the clinic and are also more suitable for long-duration experiments in the research set-up. [^{18}F]5-OH-FPPAT, an aminotetraline tracer, showed promising results in rats and monkeys [20], but no evaluation in humans has been published so far. A [^{18}F]fluorinated analog of [^{11}C](+)PHNO failed to demonstrate $D_{2/3}$R specific binding in rats [21], while the recently described [^{18}F]MCL-524, struc-

turally related to [^{11}C]MNPA, showed very promising results in non-human primates [22].

We aimed to increase the availability of fluorine-18-labeled $D_{2/3}R$ agonist tracers for PET. For this purpose we selected the 2-aminomethylchroman-7-ol (AMC) scaffold. Structure-activity relationships of this class of high-affinity D_2R-agonists were previously investigated by Mewshaw and co-workers [23].

Recently, we have described the preparation of two ^{18}F-labeled AMCs (Figure 1): (*R*)-2-[(4-(4-[^{18}F]fluorobutoxy)benzylamino)methyl]chroman-7-ol ([^{18}F]FBu-AMC13, denoted as **12a** in Chapter 3) and (*R*) 1-(4-(2-[^{18}F] fluoroethoxy)phenyl)-4-(4-(7-hydroxychroman-2-yl)-3-azabutyl)-piperazine ([^{18}F]FEt-AMC15, denoted as **12d** in Chapter 3). Both compounds, when tested in their non-radioactive ^{19}F-form, showed nearly full agonism at the long isoform of human D_2R and low-nanomolar affinities towards the high-affinity state of these receptors: on average 5.6 nM and 6.7 nM for FBu-AMC13 and FEt-AMC15, respectively. The affinities of these two compounds towards human D_2R and D_3R were comparable to each other, with no detectable preference for any of the two receptor subtypes [24]. Both [^{18}F]FBu-AMC13 and [^{18}F]FEt-AMC15 also demonstrated specific binding to the $D_{2/3}R$-high in rat striata. We wanted to further evaluate these radioligands in vivo and optimize their brain penetration and non-specific binding by adjusting their lipophilicity. We reasoned that the latter goal could be achieved by varying the length of the [^{18}F]fluoroalkyl chain in the structures of the tracers, because these chains are situated outside the main pharmacophore of the AMCs [24], so shortening or elongating them will likely have no influence on the affinity of the resulting ligands towards $D_{2/3}R$.

This study reports on the synthesis of ^{18}F-labeled AMC13 and AMC15 homologues with varied alkyl chain lengths and on the in vitro and in vivo evaluation of these compounds.

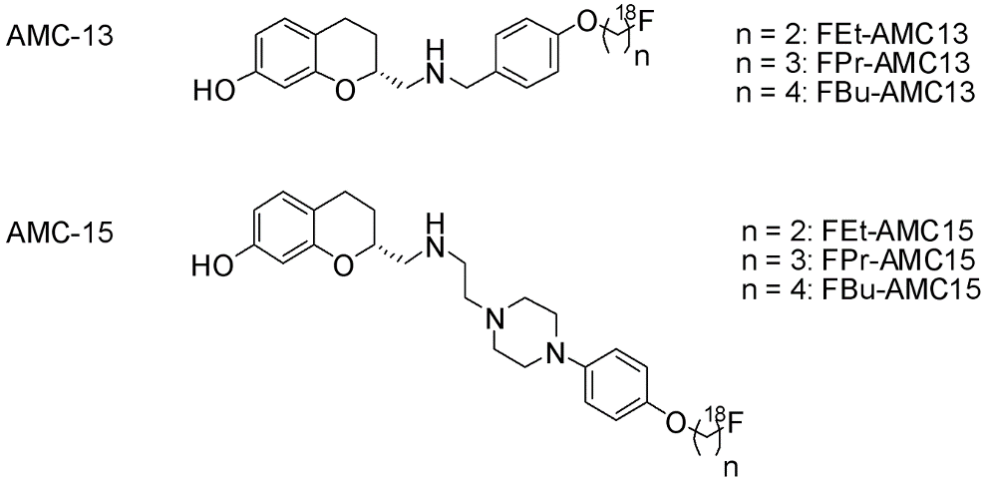

Figure 1. Structures of the evaluated homologues of AMC13 and AMC15.

METHODS

Chemistry

Reagents, chemicals, materials and solvents were obtained from commercial sources, and were used as received: Biosolve, Merck for solvents, Cambridge Isotope Laboratories for deuterated solvents, and Aldrich, Acros, ABCR, Merck and Fluka for chemicals, materials and reagents. All solvents were of analytical grade quality.

^{1}H-NMR and ^{13}C-NMR spectra were recorded on Varian MR (300 or 400 MHz for ^{1}H-NMR, 100 MHz for ^{13}C-NMR) spectrometers at ambient temperature. Chemical shifts are reported in ppm, applying deuterated chloroform ($CDCl_3$) or other deuterated solvents as internal reference. Abbreviations used for splitting patterns are s = singlet, t = triplet, q = quartet, m = multiplet, dd = double doublet.

LC/ESI-MS/MS analyses were performed on a Shimadzu LC-20AD series LC coupled to an API3000 mass-spectrometer (Applied Biosystems/MDS-SCIEX, Toronto, Canada), a triple quadrupole mass spectrometer supplied with an atmospheric pressure ionization source, and an ion-spray interface. Analyses were executed at 298 K using an Alltech Alltima C18 5μ 150×2.1 mm column using an injection volume of 10 μL, a flow rate of 0.4 mL/min and a gradient of MeCN/propan-2-ol in H_2O (from 5% to 95% organic component, where both MeCN/propan-2-ol and H_2O contain 0.1% formic acid). MS/MS analysis was performed in the Multiple Reaction Monitoring mode.

Analytical thin layer chromatography (TLC) was performed on Kieselgel F-254 precoated silica plates. Normal phase column chromatography was carried out on regular silica gel 60 (0.040–0.063, Merck).

1,2-Ethanediol ditosylate, 1,3-propanediol ditosylate, 1,4-butanediol ditosylate, 2-fluoroethyl tosylate, 3-fluoropropyl tosylate and 4-fluorobutyl tosylate were prepared according to procedures described in the literature [24, 25]. Analytical data (^{1}H-NMR, ^{13}C-NMR) were according to expectations.

The preparation and characterization of phenol precursors for ^{18}F-fluoroalkylation, (*R*) N-[7-(methoxymethoxy)chroman-2-yl]methyl 4-hydroxybenzyl amine and (*R*) 1-(4-hydroxyphenyl)-4-(4-(7-hydroxychroman-2-yl)-3-azabutyl)-piperazine were described earlier in van Wieringen et al. [24].

^{19}F-references for FBu-AMC13 and FEt-AMC15 were prepared and char-

acterized as described previously in van Wieringen et al. [24]. Of the new homologous ligands, ^{19}F-reference was only prepared for FEt-AMC13, the homologue that showed the most promising results *in vivo*. Given the use of the very similar radiolabeling methods for all ligands, and the close structural relatedness of the new homologues to the originally developed FBu-AMC13 and FEt-AMC15, we decided not to prepare ^{19}F-references for other homologues.

(R)-2-[(4-(4-Fluoroethoxy)benzylamino)methyl]chroman-7-ol (^{19}F-reference of FEt-AMC13)

A solution of (*R*) N-[7-(methoxymethoxy)chroman-2-yl]methyl 4-hydroxybenzyl amine (28.4 mg, 0.11 mmol) in 1.5 ml dry DMF and 5 mg NaH were stirred in an oil bath at 80 °C. To this mixture 2-fluoroethyl tosylate (22.8 mg, 0.11 mmol) dissolved in 1.2 ml dry DMF was added in three portions of 0.4 ml over the period of 1 hour. The mixture was stirred at 80 °C for 24 h. After that, the reaction mixture was cooled down and N_2 was bubbled through the solution to create inert atmosphere. Then 2 ml of 4M HCl solution in dioxane were added to the mixture, and it was stirred for 5 h at room temperature in the atmosphere of N_2. N_2 was further bubbled through the solution to remove volatile reaction products from the mixture. Thereafter the reaction mixture was diluted with 50 ml water and the pH was brought to 8–8.5 by addition of a Na_2CO_3-solution. The mixture was extracted by CH_2Cl_2 (3×10 ml), organic extract was washed with water (3×10 ml), dried with Na_2SO_4 and evaporated *in vacuo*. The residue was purified using silica column chromatography (ethyl acetate/methanol/triethylamine 100/5/1). Yield: 8.5 mg (24%), as a slightly yellowish solid.

^{1}H NMR ($CD_3OD/CDCl_3$): δ = 7.37 (d, 2H), 6.98 (d, 2H), 6.87 (d, 1H), 6.39 (dd, 1H), 6.21 (d, 1H), 4.83 (t, 1H), 4.71 (t, 1H), 4.29 (t, 1H), 4.22 (t, 1H), 4.12 (m, 1H), 4.01 (bs 2H), 3.01 (m, 2H), 2.9–2.5 (multiple signals, 2H), 2.05–1.65 (multiple signals, 2H). ^{13}C NMR ($CD_3OD/CDCl_3$): δ = 162.7, 160.0, 158.2, 134.5, 133.9, 133.0, 118.8, 116.6, 112.5, 107.0, 86.6, 84.8, 76.6, 71.3, 71.1, 55.6, 55.2, 35.7, 33.4, 29.5, 27.3.

Radiochemistry

[^{18}F]Fluoride was produced in the Scanditronix MC-17F cyclotron (Scanditronix, Uppsala, Sweden) and delivered from the target into the hotcell with helium overpressure. Figure 2 gives an overview of the applied radio-

chemistry.

Synthetic procedures were performed manually. Radiochemical conversions and purities were determined by radio-HPLC using beta-sensitive detectors and dose-calibrators (Veenstra Instruments) and by radio-TLC using Cyclone phosphor storage screens (multisensitive, Packard) and OptiQuant software.

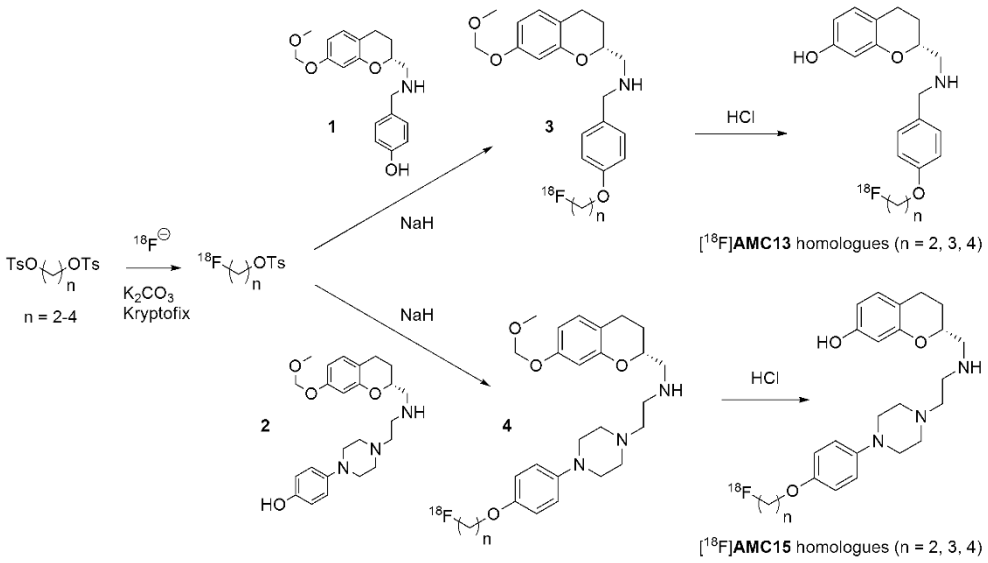

Figure 2. Labelling routes for the homologous series of [^{18}F]AMC13 and [^{18}F]AMC15.

Preparation of [^{18}F]fluoroalkyl tosylates

[^{18}F]Fluoride in enriched $H_2{}^{18}O$ water was adsorbed on an activated anion-exchange column (QMA) and later eluted into the reaction vial with 1–1.5 ml of 1.5 mg/ml K_2CO_3, 5 mg/ml Kryptofix solution in 9:1 v/v mixture of acetonitrile and water, respectively. After the elution of QMA, acetonitrile and water were evaporated at 130 °C under nitrogen flow. For further water removal, 1 ml anhydrous acetonitrile was added into the reaction vial and evaporated. Then 5 mg of alkyl ditosylate precursor (ethyl, propyl or butyl) in 1 ml anhydrous acetonitrile was added into the vial, the vial was

sealed and reaction was carried out for 4 min at 130 °C followed by cooling for 5 min. 1 ml of water was added to the cooled reaction mixture and the resulting mixture was loaded into the HPLC loop. [^{18}F]fluoroalkyl tosylates were purified by reverse-phase HPLC using Alltima C18 5μ 250×10 mm column eluted with acetonitrile/water at 5 ml/min. Acetonitrile content in the mobile phase was 65% for [^{18}F]fluorobutyl tosylate and 50% for [^{18}F]fluoropropyl and [^{18}F]fluoroethyl tosylate. Under these conditions, retention times of all thee [^{18}F]fluoroalkyl tosylates were in the range of 6–8 min. Collected radioactive fraction was diluted 2–3 fold with water and 4-[^{18}F]fluoroalkyl tosylate was adsorbed on tC18 light Seppak cartridge. The cartridge was rinsed with 5 ml pure water and dried for 5 min in strong nitrogen flow.

Preparation of [^{18}F]FEt-AMC13, [^{18}F]FPr-AMC13 and [^{18}F]FBu-AMC13

(*R*) N-[7-(Methoxymethoxy)chroman-2-yl]methyl 4-hydroxybenzyl amine (**1**, 0.6 mg) in 30 μl dry DMF and 2–3 mg NaH were put into a V-vial. Thereafter, the corresponding [^{18}F]fluoroalkyltosylate was eluted into the vial from the tC18 light Seppak cartridge with 0.6–0.7 ml dry DMF. The reaction vial was sealed and the alkylation reaction to acquire compounds **3** were conducted for 10 min at 120 °C. Then 1 ml 0.4N HCl was added into the vial with a syringe and deprotection of the MOM-group followed that also lasted 10 min at 120 °C. The product was purified by reverse-phase HPLC using Alltima C18 5μ 250×10 mm column eluted with acetonitrile/10 mM H_3PO_4 at 5 ml/min. Acetonitrile content in the mobile phase was 30% for [^{18}F]FEt-AMC13 and 35% for [^{18}F]FPr-AMC13 and [^{18}F]FBu-AMC13. Retention times were 10.6 min for [^{18}F]FEt-AMC13, 9.2 min for [^{18}F]FPr-AMC13 and 10.8 min for [^{18}F]FBu-AMC13. Collected HPLC fraction was diluted with 2–3 volumes of water and the radioactivity was adsorbed on Oasis HLB SPE cartridge. The cartridge was rinsed with 5 ml pure water and radioactivity was then eluted with 1–2 ml absolute ethanol. Typical recovery was 20–40% for pure ethanol and 80–90% for 100/1 v/v mixture of ethanol with acetic or ortho-phosphoric acid; in synthesis runs for in vivo experiments only pure ethanol was used. After partial or complete evaporation of ethanol in nitrogen flow (with or without application of vacuum) the tracer was formulated in physiological saline (ethanol content in the formulated tracer was kept below 10%).

Preparation of [^{18}F]FEt-AMC15, [^{18}F]FPr-AMC15 and [^{18}F]FBu-AMC15

The procedure described above for [^{18}F]AMC13 homologues was also used for the preparation of [^{18}F]AMC15 homologues, with the following modifications:

Instead of (*R*) N-[7-(methoxymethoxy)chroman-2-yl]methyl 4-hydroxybenzyl amine (**1**), (*R*) 1-(4-hydroxyphenyl)-4-(4-(7-hydroxychroman-2-yl)-3-azabutyl)-piperazine (**2**) was used as the precursor. MOM-protected molecules **4** were the intermediates for the [^{18}F]AMC15 homologues (Figure 2). At the end of the deprotection step the reaction mixture was diluted with 10 ml water, titrated with 1 M NaOH to pH of 4–7 and then put through the Oasis HLB SPE cartridge. Adsorbed radioactivity was then eluted from the cartridge with 1 ml acetonitrile/DMF mixture (1/1 v/v). Eluate was further diluted with water to a total volume of 1.5–2 ml and the crude product was purified by HPLC using Alltima C18 5μ 250×10 mm column. For [^{18}F]FEt-AMC15 purification the column was eluted with a gradient of acetonitrile in 10 mM acetate buffer with pH 4.0 at 5 ml/min (45% acetonitrile during the first 2 min, then a linear decrease from 45% at 2 min to 30% acetonitrile at 15 min). Retention time of [^{18}F]FEt-AMC15 was 8.4 min. [^{18}F]FPr-AMC15 and [^{18}F]FBu-AMC15 purification the column was eluted with 25% acetonitrile in 10 mM H_3PO_4at 5 ml/min. Retention times were 9.2 min for [^{18}F]FPr-AMC15 and 11.0 min for [^{18}F]FBu-AMC15.

Non-carrier-added [^{18}F]FEt-AMC15 was found to decompose on the silica plate, so before TLC runs with [^{18}F]FEt-AMC15 and its longer-chain homologues (including the analysis of plasma and tissue extracts), the start positions of the lanes on the TLC plate were pre-treated with AMC15 oxalate standard aqueous solution (2 μg in 2 μl) to hamper the on-plate decomposition.

Characterization and identity confirmation of tracers

All tracers were characterized by analytical radio-HPLC and radio-TLC. Conditions and results of the characterization are presented in Table S1 (for tables and figures with the letter S see Appendix).

The presence of the corresponding “carrier” (i.e. tracer molecules that contain a ^{19}F-atom) in the formulated tracer solutions was confirmed by high

performance liquid chromatography – electron spray tandem mass-spectrometry (LC-ESI-MS/MS) analysis with the monitoring of fragmentation reactions of the tracer molecules. For all radioligands, ion current peaks with expected M/z ratios giving expected fragmentation products were observed (Table S2). Identity of [^{18}F]FEt-AMC13, [^{18}F]FBu-AMC15 and [^{18}F]FEt-AMC15 was also confirmed by co-elution with reference products.

LogD measurement

LogD of the tracers was measured using the radioactivity remaining on the HLB SPE cartridges after their elution with ethanol during the tracer formulation procedure (see above). The cartridge was dried with nitrogen for 5 min and eluted with at least 1.5 ml n-octanol. 500 µl of octanol eluate was mixed with 500 µl of 1 M phosphate buffer (pH 7.4) and vigorously vortexed for 5 min. The mixture was then centrifuged at 17 000 g for 10 min and 3×100 µl aliquots of organic and aqueous phase were loaded into a gamma-counter for radioactivity measurement. To correct for possible presence of radioactive impurities in the tracer, aliquots of organic and aqueous phases were later analyzed by radio-TLC and the counts obtained from the gamma-counter were corrected according to the percentage of impurities found in aqueous and organic phases. LogD was calculated with the formula:

$$\mathrm{LogD} = \lg\left(\frac{\mathrm{CPM}_{org} \times \mathrm{X}_{org}^{tracer}}{\mathrm{CPM}_{aq} \times \mathrm{X}_{aq}^{tracer}}\right),$$

where CPM_{org} is the mean radioactivity of the organic aliquots, $\mathrm{X}_{org}^{tracer}$ is the mean percentage of radioactivity accounting for intact tracer in organic aliquots (as determined from radio-TLC) and CPM_{org} and $\mathrm{X}_{org}^{tracer}$ are the corresponding values for the aqueous phase.

For each tracer batch used for logD determination, the experiment was performed in duplicate. LogD values are means calculated from at least two independent experiments.

In vitro autoradiography

In vitro autoradiography assay was performed as previously described [24]. Frozen brains of young (10–12 weeks of age; 300–350 g body-weight) male Sprague-Dawley rats (Harlan, Netherlands) were cut at −12 °C into sagit-

tal slices 20 μm thick using a Leica microtome, and the slices were thaw-mounted on Superfrost (70×22 mm, Fischer) adhesive slides. Only slices containing both striatal and cerebellar regions were used. The slides with slices mounted them were allowed to dry, then put into storage boxes with silicagel bags and stored at −80 °C.

On the day of the experiment (within one week from the preparation of the slices) the slides were taken out of storage and allowed to come to room temperature for 5–10 minutes. Then 1–1.2 ml of incubation buffer (50 mM Tris-HCl, 5 mM KCl, 2 mM $CaCl_2$, 2 mM $MgCl_2$, 120 mM NaCl, pH 7.4 25 °C) was applied per slide and the slides were pre-incubated for 15 minutes at room temperature. The buffer was then removed and the slides were placed into staining jars containing radioligand solution (concentration range of 0.1–10 nM) in the incubation buffer with or without 10 μM raclopride ($D_{2/3}$ antagonist) or 100 μM guanosine-5'-triphosphate sodium salt (GTP, stimulator of G-protein uncoupling from the receptors). After 35 minutes of incubation at 37 °C, slides were washed once with ice-cold incubation buffer (3.5 min) and dipped for 30 sec into ice-cold distilled water to remove buffer salts.

After drying the slides in a stream of room-temperature air, they were exposed on phosphor storage screens for 6–10 hours. The storage screens were read by Cyclone Storage Phosphor System (Packard Instruments Co). Quantification of plate readings was done with Optiquant software (version 3.00, Packard Instruments Co).

MicroPET study in rats

Three radioligands were evaluated in vivo: the originally developed [^{18}F]FBu-AMC13 and [^{18}F]FEt-AMC15, and [^{18}F]FEt-AMC13, the homologue that showed the best results in the in vitro autoradiography experiments (see Results section).

Animal experiments were performed by licensed investigators in compliance with the Law on Animal Experiments of The Netherlands. The protocol was approved by the Committee on Animal Ethics of the University of Groningen. Young male (10–12 weeks of age, 300–350 g body weight) Sprague-Dawley rats (Harlan, the Netherlands) were used for all experiments. The rats were maintained at a 12-h light/12-h dark regime and were fed standard laboratory chow *ad libitum*.

Distribution of the radiotracers was studied in rats pre-treated, at random, with physiological saline (controls) or raclopride tartrate (1 mg/kg calculated per raclopride base, equivalent to 2.9 μmol/kg). Saline and raclopride were administered intravenously (1 ml/kg injected volume).

An additional group of saline pre-treated rats, injected with [^{11}C]raclopride, served as positive controls for $D_{2/3}R$ specific brain uptake.

Two rats were scanned simultaneously. Before all manipulations, animals were anesthetized with a mixture of isoflurane/air (inhalation anesthesia, 5% ratio during induction, 2% at maintenance). Cannulae were placed into the rats' left femoral arteries and veins; the operation took 45–50 min. The rats were positioned supine inside the camera (Focus 220 microPET, Siemens-Concorde), one above the other with their heads in the camera's field of view. A 515 sec transmission scan with a Co-57 point source was performed. Tracer was injected through the venous cannula as a slow bolus (1 ml volume, 60-second long) using an infusion pump. The second (upper) animal was injected 16 min after the first (lower). Injected radioactivities and doses are given in Table 1.

Table 1. Injection data for the PET study.

Tracer	Injected radioactivity, MBq/rat	Injected dose, nmol/kg	Rats per treatment group (saline/raclopride)	Pre-treatment time interval, min
[^{18}F]FEt-AMC13	9.4±1.2	0.55±0.14	4/4	47±27
[^{18}F]FBu-AMC13	20.8±10.6	0.45±0.26, 10.4, 11.0[a]	3/3	52±19
[^{18}F]FEt-AMC15	26.6±15.2	1.06±0.65	3/3	48±10
[^{11}C]raclopride	16.9±5.3	1.26±0.16	4 (saline only)	36±3

a One rat in the saline-treated group and one rat in the raclopride-treated group were injected with respectively 10.4 and 11.0 nmol/kg tracer. As all outcome measures (time-activity curves, uptake ratios) obtained from these animals were very close to the results from other animals in the corresponding groups, these results were not omitted or separated, but combined with the rest of the data.

PET acquisition was started during the injection of radioactivity in the first rat. A 106 minute-long (76 minute-long in case of [^{11}C]raclopride) list-mode

acquisition protocol was used for the scan.

Throughout the scan, arterial blood samples (15–19 samples; 0.10–0.15 mL each) were withdrawn from each rat through the arterial cannula. Time intervals between samples gradually increased from 5–10 sec right after injection to 30 min at the end of the scan.25 μl aliquots of whole blood were withdrawn from each sample. The rest was centrifuged at 3500 g for 5 min, 25 μl supernatant (plasma) aliquots were withdrawn and deproteinated with 75 μl of ice-cold acetonitrile. From the resulting 100 μl, 2–8 μl portions (i.e. 2–8% of volume) were taken for thin layer chromatography analysis (radio-TLC), to assess radiometabolite content.

The radioactivity of the plasma and whole blood samples was measured using a well-type gamma-counter (LKB-1282-Compugamma, LKB Wallac).

Radio-TLC was performed on silica plates. Samples of the formulated tracers (diluted) were run along with deproteinated plasma samples to confirm the identity of the parent compound in plasma. Eluent systems used and TLC R_f-values recorded are presented in Table S1.

After the end of the PET scans (i.e. 98±8 min after tracer injection) anesthetized animals were sacrificed by heart extirpation and dissected. Samples of brain and peripheral tissues were taken. All samples were weighed and their radioactivity was measured in a gamma-counter.

MicroPET image reconstruction and data analysis

List-mode data from the 106-minute-long and 76-minute-long scans were reframed into, respectively, 90-minute-long and 60-minute-long dynamic sequences of 6×10, 4×30, 2×60, 1×120, 1×180, 4×300, 3×600 and (for 90-minute-long scans) 2×900 sec frames. The data were reconstructed per time frame using an iterative reconstruction algorithm (attenuation-weighted 2-dimensional ordered-subset expectation maximization, provided by Siemens; 4 iterations, 16 subsets; zoom factor 2). Datasets were fully corrected for random coincidences, scatter, and attenuation. Data from the transmission scan were used for attenuation correction. The final datasets consisted of 95 slices, with a slice thickness of 0.8 mm and an in-plane image matrix size of 128×128 and pixel size of 0.47×0.47 mm.

Reconstructed images were analyzed with Inveon 2.0 software (Siemens Medical Solutions, USA, Inc). Regions of interest (ROIs) were drawn manu-

ally on a T_2-weighted MRI template of rat brain around the striatum, brainstem, cortex, hippocampus, hypothalamus, thalamus, olfactory bulbs and cerebellum, around the whole brain and around the pituitary gland. The MRI template was co-registered with the PET scan by image fusion. The time-activity curves (TAC) per ROI were determined in Bq/cm^3 units and converted into standardized uptake values (SUVs).

Kinetic analysis is described using the nomenclature proposed by Innis et al [26]. ROI TACs of [^{18}F]FEt-AMC13 were analyzed with one-tissue and two-tissue compartmental models of reversible binding (1TCM and 2TCM, respectively) to obtain individual rate constants. From these, the regional distribution volumes (V_T) were calculated and compared to those obtained with Logan graphical analysis. Binding potentials (BP_{ND}) were calculated from the distribution ratios as V_T (target) / V_T (cerebellum) – 1, or estimated with the simplified reference tissue model (SRTM) using the cerebellum as reference region.

Metabolite-corrected plasma-derived arterial input function and whole blood time-activity curve were used for Logan, 1TCM and 2TCM analyses. Fractional cerebral blood volume was set to 3.6% [27]. For one rat in the raclopride-treated group no input curves could be obtained, therefore its PET data were only analyzed with SRTM.

Ex vivo autoradiography study in rats

To further assess the specific binding of [^{18}F]FEt-AMC13 to the striatal $D_{2/3}R$, two groups of rats were anesthetized, pre-treated with saline (n=3) or raclopride (n=3) and 26±3 min later injected with a bolus of [^{18}F]FEt-AMC13 (4.2±1.4 MBq, 0.14±0.04 nmol/kg) into the penile vein. 35 min later rats were sacrificed by heart extirpation. Brains were quickly extracted and separated into two halves along the sagittal symmetry plane or along the coronal plane spanning the thalamus.

One half of the brain (rostral or randomly taken left/right) was quickly frozen over liquid nitrogen and prepared for cutting on the microtome in the same manner as brains used for in vitro autoradiography [24]. 40 μm thick slices were cut, mounted on Superfrost glass slides, permitted to dry and then directly applied to the phosphor storage screens.

Another half of the brain was homogenized in 3 ml ice-cold acetonitrile using Heidolph IDAX600 homogenizer at maximum speed. Homogenate

was centrifuged at 3500 g for 5 min and the supernatant (containing >95% total radioactivity) was analyzed by radio-TLC in the same way as described above for the plasma.

$D_{2/3}$R-specific binding quantification

Degree of $D_{2/3}$R-specific binding of the tracers was characterized by BP_{ND} (as given above) or the specific binding ratio (SBR) given as:

target region radioactivity / cerebellar radioactivity - 1.

Both were calculated under control conditions and in response to the raclopride challenge.

Statistics

All data are presented as means ± standard deviations. Comparison of means was done using 2-sided unpaired Welch t-test. P-values below 0.05 were considered significant. No multiple comparison corrections were performed.

RESULTS

Preparation of radioligands

The labeling scheme used for the preparation of the tracers is given in Figure 2. Radiochemical yields and purities, molar radioactivities and logD values of the prepared tracers are listed in Table 2. Radio-HPLC and radio-TLC characterization data of the prepared tracers can be found in Table S1. LC-ESI-MS/MS characterization data of the ^{19}F-compounds (remaining carrier) in the decayed samples of purified tracers are described in Table S2.

For both [^{18}F]AMC13 and [^{18}F]AMC15 homologues, reverse-phase radio HPLC retention times, normal-phase TLC retention factors and logD values increased with the length of the [^{18}F]fluoroalkyl chain.

Table 2. Synthetic and analytical data for [^{18}F]AMC13 and [^{18}F]AMC15 homologues.

Compound	Radiochemical yield, %	Radiochemical purity, %	End-of-synthesis molar radioactivity, GBq/μmol	logD
[^{18}F]FEt-AMC13	12±6	>95	102±30	1.67±0.07
[^{18}F]FPr-AMC13	7±6	>95	29±27	1.98±0.08
[^{18}F]FBu-AMC13	8±7	93±2	85±83	2.50±0.06
[^{18}F]FEt-AMC15	5±3	93±2	25±15	1.48±0.002
[^{18}F]FPr-AMC15	3±1	93±5	9±7	2.39±0.001
[^{18}F]FBu-AMC15	6±0.3	93±6	10±3	2.71±0.07

Radiochemical yields and purities refer to isolated products. Values are means±SD of ⩾3 determinations from ⩾2 independent experiments.

In vitro autoradiography

All [^{18}F]fluoroethyl and [^{18}F]fluoropropyl compounds showed preferential uptake in the $D_{2/3}$R-rich striatum (Figure 3). [^{18}F]FEt-AMC13 had the highest striatal SBR, followed by [^{18}F]FPr-AMC13 and [^{18}F]FEt-AMC15 (Table 3). [^{18}F]FBu-AMC13 only showed discernible specific binding at the lowest concentration tested.

In the presence of 10 μM of raclopride SBR values of all AMC13 homologues decreased by 79–88%, and those of all AMC15 homologues by 60–64% compared to control conditions. GTP decreased the SBR values to the same extent, implying that the striatal binding of all tracers was predominantly to the high-affinity subset of the $D_{2/3}$Rs (Table 3).

In vivo and ex vivo brain uptake of the tracers under control conditions

[^{18}F]FEt-AMC13 and [^{18}F]FBu-AMC13 showed good blood-brain barrier (BBB) penetration (Figure 4). Brain uptake peaked at 0.7% injected dose (ID) and 0.9% ID, respectively, 3 min after radiotracer injection.

For both tracers the brain region with the lowest uptake was the cerebellum. [^{18}F]FBu-AMC13 had the highest uptake in the brainstem, followed by the striatum; striatum-to-cerebellum uptake ratio peaked at 1.41±0.08 (Figure S1). [^{18}F]FEt-AMC13 and [^{11}C]raclopride had the highest uptake in the striatum (Figure 5). Striatum-to-cerebellum uptake ratio of [^{18}F]FEt-AMC13 peaked 45 min post-injection at 2.08±0.25 (Figure 5b); the same ratio measured by ex vivo autoradiography was 2.81±0.29 (35 min post-injection). The striatum-to-cerebellum ratio of [^{11}C]raclopride was 7.45±1.60 (45 min post-injection; Figure 5d).

[^{18}F]FEt-AMC15 essentially did not penetrate the BBB. Its in vivo brain uptake peaked at 0.2% ID, 3 min post-injection and fell to 0.04% ID 60 min post-injection.

Ex vivo measurements of the uptake of the tracers in the brain and peripheral tissues performed after the PET scan are given, respectively, in Table 4 and Table S3.

Table 3. Quantitative results of in vitro autoradiography.

Tracer	Tracer concentration, nM[a]	Striatal SBR[b] (% change relative to control condition)		
		control	raclopride	GTP
[^{18}F]FEt-AMC13	0.9±0.7 (*n*=3)	3.40±1.25	0.63±0.53 (−81%)*	0.66±0.52 (−81%)*
[^{18}F]FPr-AMC13	1.4±1.6 (*n*=3)	2.07±1.06	0.41±0.23 (−80%)*	0.42±0.23 (−80%)*
[^{18}F]FBu-AMC13[c]	0.2 (*n*=1)	0.85±0.23	0.10±0.19 (−88%)*	0.20±0.16 (−76%)*
	4.5±3.6 (*n*=3)	0.19±0.18	0.04±0.22 (−79%)	–
[^{18}F]FEt-AMC15[c]	5.8±1.6 (*n*=4)	1.64±1.04	0.65±0.37 (−60%)*	0.67±0.28 (−59%)*
[^{18}F]FPr-AMC15	5.0±7.2 (*n*=3)	1.01±0.46	0.39±0.22 (−61%)*	0.37±0.24 (−63%)*
[^{18}F]FBu-AMC15	2.3±1.8 (*n*=3)	0.69±0.30	0.25±0.23 (−64%)*	0.23±0.23 (−67%)*

a Concentrations are means±SD from *n* independent experiments. *b* SBR (specific binding ratio) values are means±SD from the total number of slides (3–28 per condition) assayed in all experiments. *c* Published earlier [24].* $P < 0.05$ relative to control values, 2-sided Welch test.

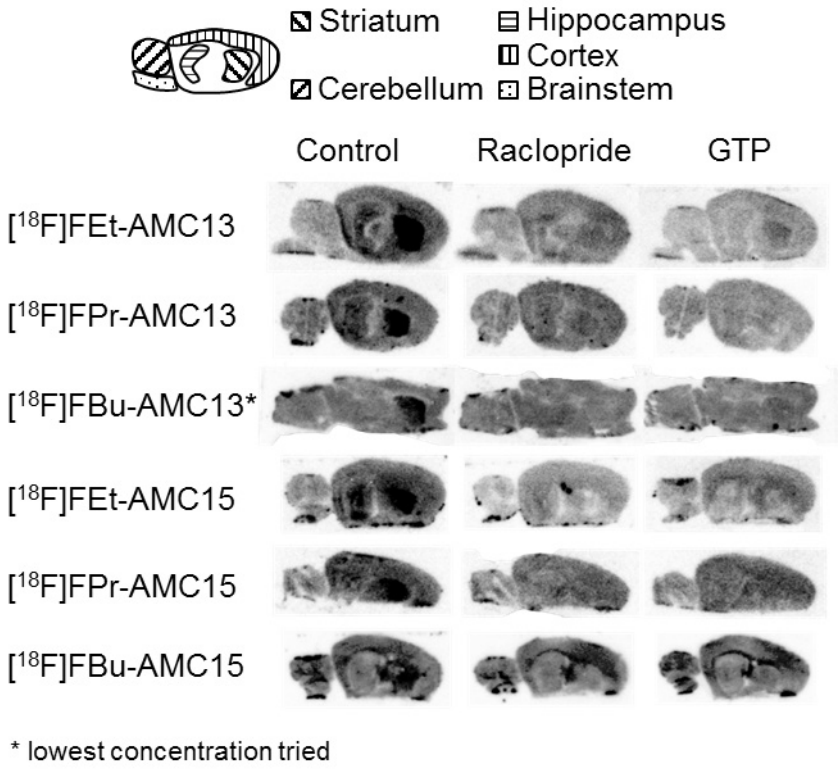

Figure 3. Representative in vitro autoradiography images of rat brain slices for the assayed radioligands.

Left column – slides incubated with radioligand only. Middle column – radioligand and 10 μM raclopride. Right column – radioligand and 100 μM GTP.

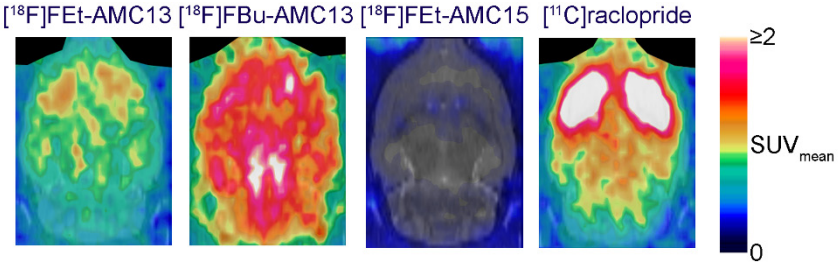

Figure 4. Representative PET images for three [^{18}F]fluoroalkyl-AMC radioligands and [^{11}C]raclopride acquired in rats.

Images are summed from 5 min post-injection till the end of scan. Harderian glands (on top) are masked.

Table 4. Ex vivo uptake of the evaluated tracers in brain regions and skull bones of rats.

Tracer	[^{18}F]FEt-AMC13		[^{18}F]FBu-AMC13		[^{18}F]FEt-AMC15	
Treatment Region	saline (*n*=4)	raclopride (*n*=4)	saline (*n*=3)	raclopride (*n*=3)	saline (*n*=3)	raclopride (*n*=3)
Striatum	0.28±0.03 (1)	0.23±0.08	1.60±0.33 (5)	1.21±0.14	0.02±0.02	0.03±0.01
Hippocampus	0.22±0.02 (2)	0.23±0.08	1.50±0.25 (6)	1.21±0.06	0.03±0.02	0.03±0.01
Thalamus+ hypothalamus	0.19±0.003 (4)	0.19±0.05	2.07±0.70 (1)	1.07±0.10	0.03±0.01	0.03±0.01
Cortex	0.18±0.01 (5)	0.16±0.04	1.50±0.32 (7)	1.01±0.11	0.03±0.003	0.03±0.01
Brainstem	0.18±0.02 (6)	0.16±0.04	1.97±0.42 (2)	1.25±0.14	0.03±0.004	0.03±0.01
Olfactory bulbs	0.17±0.01 (7)	0.15±0.04	1.85±0.64 (3)	0.86±0.09	0.03±0.001	0.03±0.02
Rest of brain	0.20±0.02 (3)	0.18±0.03	1.60±0.25 (4)	1.10±0.17	0.02±0.02	0.03±0.02
Cerebellum	0.13±0.01 (8)	0.13±0.02	1.11±0.29 (8)	0.73±0.08	0.03±0.01	0.03±0.01
Mean brain uptake	0.18±0.01	0.16±0.04	1.56±0.33	1.03±0.11	0.03±0.01	0.03±0.01
Pituitary	0.76±0.08	0.59±0.20	3.19±0.29	2.72±0.77	1.36±0.30	1.08±0.27
Parietal bone	0.10±0.01	0.10±0.01	0.61±0.17	0.70±0.18	0.09±0.03	0.08±0.03

Data are presented as means±standard deviations of standard uptake values. The ranking of the uptake magnitude (highest to lowest) among brain regions within the BBB is shown in parentheses (only for [^{18}F]AMC13 homologues).

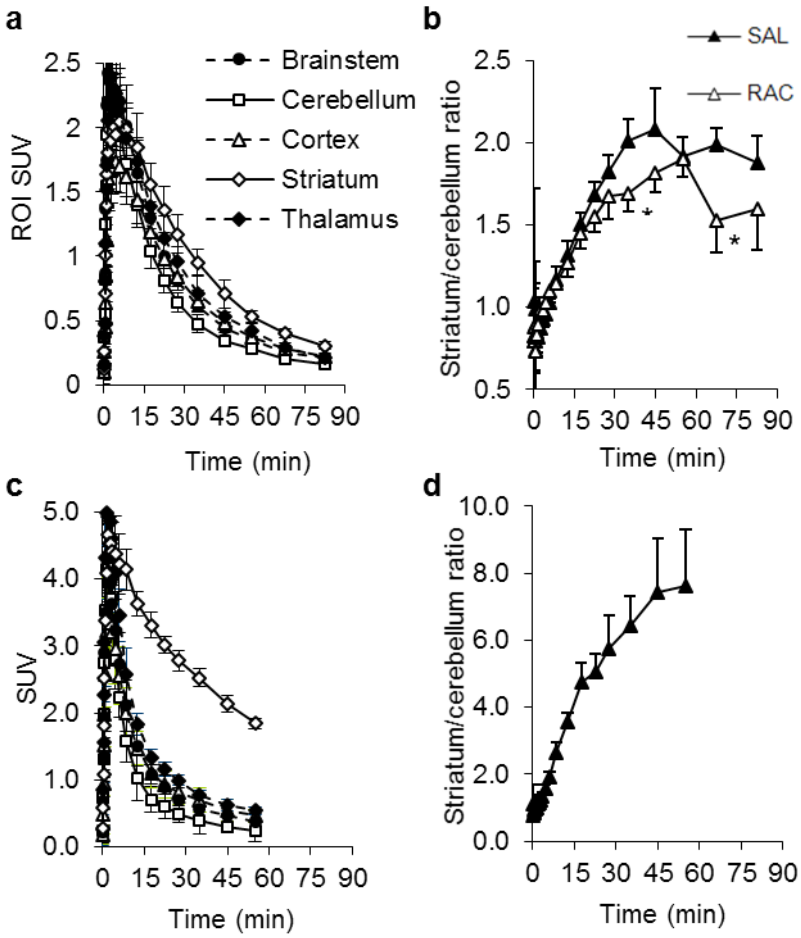

Figure 5. Uptake of [^{18}F]FEt-AMC13 (a, b) and [^{11}C]raclopride (c, d) in rat brain.
a, c – region-of-interest time-activity curves of control rats. b, d – Striatum-to-cerebellum ratios in rats pre-treated with saline (SAL) and 1 mg/kg (2.9 μmol/kg) raclopride (RAC). Points represent group means, error bars show standard deviations.

Tracer metabolism

[^{18}F]FEt-AMC13 and [^{18}F]FBu-AMC13 were quickly metabolized in the plasma, while [^{18}F]FEt-AMC15 was more stable (Figure 6). Tracers were eliminated from the plasma with half-lives of 3 to 12 min. Radiometabolites of all tracers in the plasma and in the brain tissue extract were considerably more hydrophilic than their corresponding parent compounds, as they all had TLC R_f values of 0, compared to R_f of 0.16–0.56 for the tracers themselves

(Table S1). Intact [^{18}F]FEt-AMC13 constituted 92% of radioactivity from brain tissue extract 35 min post-injection (Figure S2).

Uptake in the parietal bone was lower than in the brain tissue for all [^{18}F]AMC13 homologues (Table 4), suggesting low levels of in vivo defluorination.

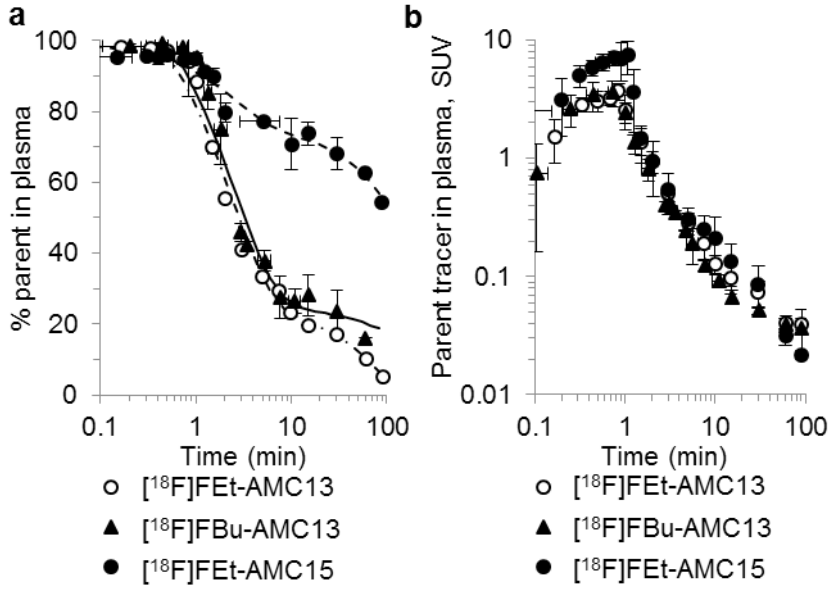

Figure 6. Metabolism and pharmacokinetics of [^{18}F]FEt-AMC13, [^{18}F]FBu-AMC13 and [^{18}F]FEt-AMC15 in the plasma of living rats.

a – percentage of intact tracer in the total plasma radioactivity. b – concentration of intact tracer in the plasma (i.e. metabolite-corrected plasma input curves). Points represent group means, error bars show standard deviations. Horizontal axes show time after tracer injection.

Kinetic modeling for [^{18}F]FEt-AMC13

2TCM and SRTM fits of ROI TACs were consistently better than 1TCM fits (Figure S3) as assessed by Akaike's information criterion, but the estimates of individual rate constants of 2TCM were highly variable and often physiologically implausible (Table S4).

The most robust ROI V_T estimates were obtained from the Logan analysis (Table S5). Logan V_T values correlated better with 2TCM V_T (r = 0.97) than with 1TCM V_T values (r = 0.89; Figure S4). No robust BP_{ND} estimates could

be obtained from the k_3/k_4 rate constant ratio of 2TCM (data not shown), but BP_{ND} estimates calculated from 1TCM, 2TCM and Logan V_T data and obtained by SRTM correlated well with each other for all regions except the pituitary and olfactory bulbs (Figure S5).

The highest BP_{ND} values in control rats were found in the striatum (1TCM: 0.63±0.08; 2TCM: 0.56±0.05, Logan: 0.52±0.01; SRTM: 0.51±0.02).

Blocking experiments

Pre-treatment with 1 mg/kg (2.9 μmol/kg) raclopride decreased peak PET-based striatal SBR of [^{18}F]FEt-AMC13 by 17% (from 1.08±0.25 to 0.90±0.11), though the SBR change was not statistically significant (p=0.25). Striatal SBR based on after-scan biodistribution measurements decreased by 31% (from 1.07±0.10 to 0.74±0.27), but was also not statistically significant (p=0.17). Ex vivo autoradiography-based SBR fell by 39% (from 1.81±0.29 to 1.06±0.17), which was statistically significant (p<0.01), and the blocking of $D_{2/3}$R specific striatal binding was clearly visible on the autoradiography images (Figure S6).

Striatal BP_{ND} fell by 18–27% (p<0.05 for 2TCM, Logan and SRTM; see Table 5 and Table S6) depending on the kinetic model used. Modified Lassen plot analysis [28] estimated the raclopride-induced $D_{2/3}$R occupancy at 20–25% (p<0.05 for 1TCM and 2TCM), while 41–55% of striatal V_T and 11–26% of cerebellar V_T were estimated to be potentially displaceable, i.e. represent $D_{2/3}$R specific binding (Figure S7).

For [^{18}F]FBu-AMC13 pre-treatment with raclopride decreased absolute uptake in all brain regions, and striatum-to-cerebellum uptake ratios were higher in raclopride-treated group than in the saline-treated group (Figure S1c).

For [^{18}F]FEt-AMC15, pre-treatment with raclopride caused no detectable alterations of radioactivity distribution in the brain (data not shown).

Table 5. 2TCM and SRTM-derived BP_{ND} of [^{18}F]FEt-AMC13 per brain region in control and raclopride-treated rats.

Region of interest	2TCM BP_{ND} (V_T-based)		SRTM BP_{ND}	
	control	raclopride	control	raclopride
Striatum	0.56±0.05	0.41±0.05 (−27%)*	0.51±0.02	0.38±0.05 (−26%)**
Hippocampus	0.30±0.07	0.26±0.06 (−13%)	0.26±0.04	0.23±0.05 (−13%)
Thalamus	0.33±0.02	0.30±0.01 (−10%)*	0.28±0.06	0.26±0.02 (−7%)
Hypothalamus	0.22±0.03	0.18±0.06 (−19%)	0.21±0.03	0.16±0.04 (−23%)
Cortex	0.13±0.04	0.10±0.02 (−27%)	0.11±0.03	0.08±0.02 (−24%)
Brainstem	0.22±0.02	0.10±0.02 (−53%)**	0.18±0.04	0.07±0.03 (−60%)**
Olfactory bulbs	0.08±0.13	0.01±0.04 (−88%)	0.10±0.13	0.11±0.05 (+10%)
Pituitary	0.36±0.07	0.13±0.04 (−23%)	0.71±0.32	0.55±0.53 (−22%)

Data are presented as means±SD, *n*=4 for the control group, *n*=3 for the raclopride-treated group (except for the SRTM BP_{ND} values, where *n*=4). Next to the BP_{ND} values of the raclopride-treated group, percentage of change relative to the control group is shown. * $P < 0.05$, ** $P < 0.01$, 2-sided Welch test.

DISCUSSION

We have previously described the design, synthesis and in vitro evaluation of a series of high-affinity $D_{2/3}$ agonists based on the AMC scaffold. Two compounds from that series, FBu-AMC13 and FEt-AMC15, were confirmed to have high-affinity towards $D_{2/3}R$ and act as agonists at D_2R [24]. They were ^{18}F-labeled and showed favorable results in the in vitro autoradiography experiments. In this study we have evaluated these compounds in vivo and further optimized their characteristics by shortening or lengthening the [^{18}F]fluoroalkyl chains in their structures. We did not directly measure the affinities and intrinsic activities of the shorter-chain homologues of FBu-AMC13 and longer-chain homologues of FEt-AMC15 towards $D_{2/3}R$, assuming that changing the fluoroalkyl chain would have negligible influence on these parameters, because this fluoroalkyl chain is situated outside the main AMC pharmacophore [24].

Both raclopride and GTP decreased striatal SBRs of all tracers significantly and to a similar extent, which was consistent across the homologous series (Table 3). This indicates that all our tracers specifically bind to striatal dopamine $D_{2/3}$ receptors in their G-protein-coupled "high-affinity state". Tracers with a shorter alkyl chain showed higher in vitro autoradiography-based striatal SBR values (Et>Pr>Bu). These findings are in agreement with our hypothesis that varying the [^{18}F]fluoroalkyl chain length would influence non-specific binding, but not the $D_{2/3}R$-affinity or agonism of the tracers.

In vivo, [^{18}F]FEt-AMC15 showed very low levels of BBB penetration, which may be the consequence of the tracer's low lipophilicity and/or may imply that it is a substrate for one of the drug efflux pump proteins such as P-glycoprotein. Meanwhile, [^{18}F]FEt-AMC13, which is the short-alkyl-chain homologue of [^{18}F]FBu-AMC13, showed greatly improved specific-to-non-specific binding ratios compared to the "original" radioligand, while retaining good brain penetration and favorable metabolic profile.

Our approach has proven to be a useful and relatively simple tactic for the adjustment of the radioligands' lipophilicity with the goal of optimizing their non-specific binding and brain penetration.

The time-activity curves of [^{18}F]FEt-AMC13 were better approximated with the 2TCM model than with 1TCM model, and 2TCM-derived V_T and BP_{ND} estimates correlated better than 1TCM-derived V_T and BP_{ND} estimates with the same data obtained from Logan analysis that makes no assumptions

regarding the number of kinetic compartments. However, the 2TCM model did not always provide reliable estimates of the individual rate constants of [^{18}F]FEt-AMC13 uptake in the brain. This may have been caused by the quality of input data: insufficient counts or imprecise estimates of the plasma input can make the optimization routine converge at a local minimum. Fortunately, the estimates of V_T and BP_{ND} were more robust and consistent, so these were used for the evaluation of [^{18}F]FEt-AMC13.

Estimation of the magnitude of the $D_{2/3}R$ blockade induced by 1 mg/kg (2.9 μmol/kg) raclopride in rats' striata in vivo performed with the use of different approaches produced consistent results: changes in striatal BP_{ND} and (PET and autoradiography-derived) SBR were similar to the modified Lassen plot-based estimate of $D_{2/3}R$ occupancy by raclopride. Depending on the estimate, raclopride pre-treatment blocked 17–39% of $D_{2/3}R$-specific signal in the striatum. Though a bolus dose injected in an in vivo experiment can't be directly compared with ligand concentration applied in an in vitro experiment, our in vivo findings are also arguably consistent with our in vitro findings, where a higher concentration of raclopride (10 μmol/L) used in the in vitro autoradiography study induced a greater decrease (81%) in striatal SBR in rat brain slices compared to control conditions.

Our in vivo findings, however, do not agree with the published studies which reported >90% displacement of apparent $D_{2/3}R$-specific striatal uptake of [^{11}C]MNPA and [^{11}C]PHNO in Sprague-Dawley rats with 1–2 mg/kg (2.9–5.8 μmol/kg) raclopride [29–31]. Even a 5-fold lower dose (0.2 mg/kg, 0.58 μmol/kg) displaced over 80% of apparent $D_{2/3}R$-specific [^{11}C](+)PHNO uptake [30]. It is not clear why the apparent displacement of [^{18}F]FEt-AMC13 from the striatum by 1 mg/kg raclopride is lower than what is reported for other $D_{2/3}R$ tracers in the literature. It's unlikely that we violated the so-called "tracer conditions", because crude estimation of the $D_{2/3}R$ occupancy by [^{18}F]FEt-AMC13 itself using the approach described by Skinbjerg et al. [32] produced the values of no more than 3% in all our experiments. It may be that the signal-to-noise ratio in our data was insufficient, which made it difficult to precisely estimate the contribution of specific binding to total tracer binding in various ROIs. The presence of specific binding of [^{18}F]FEt-AMC13 to sites other than $D_{2/3}R$, which have comparatively high density in the striatum, may also be implied. We have previously demonstrated that FBu-AMC13, a longer-chain homologue of FEt-AMC13, has low affinity towards D_1 receptors (7 μM on average) [24], while (*R*)-2-[(benzylamino)methyl]chroman-7-ol and 2-[(4-hydroxybenzylamino)-

methyl]chroman-7-ol, compounds structurally closely related to FEt-AMC13, were shown by Mewshaw and co-workers to be selective for $D_{2/3}R$ against serotonin-1A and adrenergic α_1 receptors [23]. In the in vitro autoradiography study, presence of 10 μmol/L raclopride decreased striatal SBR of [^{18}F]FEt-AMC13 by 81%, which also does not support the hypothesis of the existence of significant non-$D_{2/3}R$-specific binding of [^{18}F]FEt-AMC13 in the striatum. Still, a separate study of pharmacological selectivity of FEt-AMC13, including direct determination of the affinities of FEt-AMC13 towards high- and low-affinity states of $D_{2/3}R$, is necessary to clarify this issue.

Apart from striatum, olfactory bulbs and pituitary gland are known to contain high densities of $D_{2/3}R$ available to agonist radioligands [33]. However, no blocking effect of raclopride could be observed in these regions (Table 4, Table 5), and the relatively high tracer uptake in the pituitary is more likely to be explained by the pituitary being situated outside the BBB than by the presence of $D_{2/3}R$-specific binding of [^{18}F]FEt-AMC13 there.

Striatum-to-cerebellum ratio of 2.08 is on par with the value of 2 reported in rats for [^{18}F]5-OH-FPPAT [20] and with the value of 1.97 obtained for our other separately evaluated AMC derivative [^{18}F]AMC20 [34]. However, the striatal BP_{ND} values of 0.51–0.63 obtained for [^{18}F]FEt-AMC13 are lower than the values of at least 0.8–1.0 reported in rodents for existing ^{11}C-labeled $D_{2/3}$ agonists [19,29,31]. Non-specific binding of the tracer in the tissue can slow down the association rate of the tracer-receptor binding by leaving less free tracer in the tissue. The launch of the canonical signaling cascade induced by agonist binding eventually leads to the uncoupling of the G-protein from the receptor and the relaxation of the receptor into its low-affinity state [18, 35], which may increase the effective dissociation rate of an agonist tracer from the receptors. To find out which factors limit the signal-to-noise ratio of [^{18}F]FEt-AMC13, a more thorough study of its binding kinetics in a more controlled environment (e.g. in vitro) is necessary.

CONCLUSIONS

We have evaluated two homologous series of agonist radiopharmaceuticals based on the AMC scaffold that bind with high affinity and selectivity to $D_{2/3}R$ in vitro. Varying the length of the [^{18}F]fluoroalkyl group allowed us to significantly improve the specific-to-non-specific binding ratio of one of our original structures. The resulting ligand, [^{18}F]FEt-AMC13, demonstrated specific binding to the striatal $D_{2/3}R$ in vitro as well as in vivo. In vitro findings also confirmed the tracer's binding to the high-affinity state of $D_{2/3}R$. Further investigation of the binding characteristics of FEt-AMC13 and optimization of its molecular structure can lead to an improved ^{18}F-labeled radioligand suitable for clinical $D_{2/3}R$ imaging by PET.

Competing Interests

MCM is an employee of Boehringer Ingelheim, a company marketing the dopamine D_2R agonist pramipexole. JB is consultant at GE Healthcare a company marketing the $D_{2/3}R$ radiopharmaceutical [^{123}I]IBZM. The other authors declare that they have no competing interest.

Authors' Contributions

VS synthesized ^{18}F-labeled aminomethylchroman compounds, performed in vitro and in vivo experiments, analyzed the data and drafted the manuscript. JPvW helped with the design of in vitro experiments and with the drafting of the manuscript. HMJ and MF synthesized the "cold" aminomethylchroman compounds and precursors for radiolabeling and provided critical feedback on the manuscript. RAJOD helped with the general design of the study and provided critical feedback on the manuscript. MCM helped with the design of in vitro experiments and provided critical feedback on the manuscript. JB helped with the interpretation of the results and critically revised the manuscript. PHE helped with the design of radiosynthetic protocols and interpretation of the results and critically revised the manuscript. All authors read and approved the final manuscript.

Acknowledgements

The authors wish to thank Aren van Waarde, Antoon Willemsen, Janine Doorduin, Jurgen Sijbesma and Mohammed Khayum (department of Nuclear Medicine and Molecular Imaging, University Medical Center Gronin-

gen, University of Groningen) for their help with the microPET study, and Margot Jeronimus-Stratingh (department of Pharmacy, University Medical Center Groningen, University of Groningen) for performing the LC-MS/MS analyses.

This work was supported by a grant from the Dutch Technology Foundation STW (grant 10127).

APPENDIX

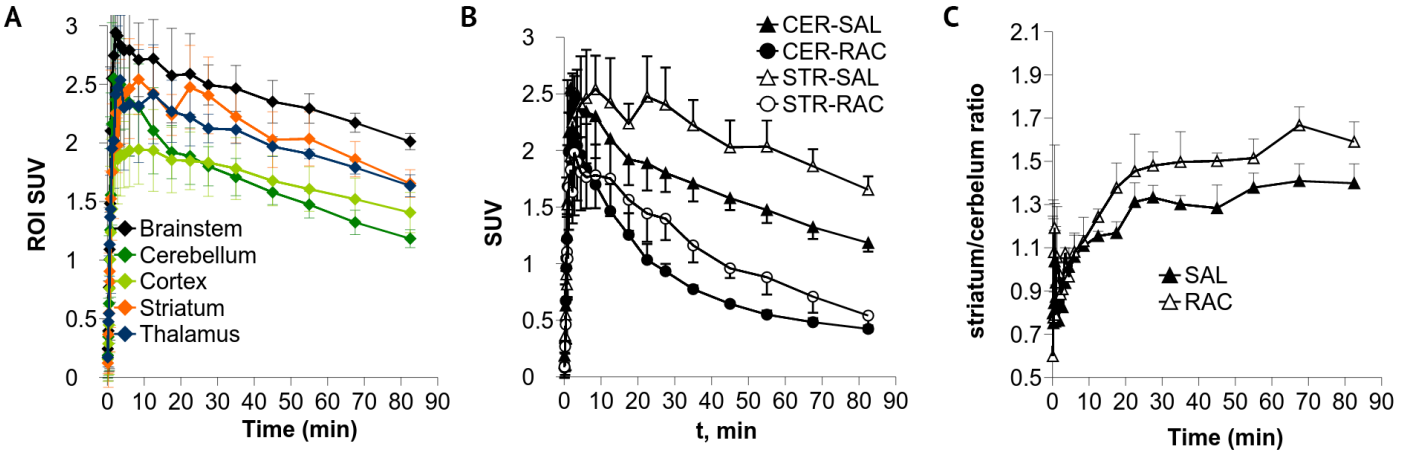

Figure S1. Brain uptake (means±SD) of [^{18}F]FBu-AMC13 in rat brain.

A – time-activity curves (TACs) per region-of-interest (ROI) in control (saline-treated) rats. B – cerebellar (CER) and striatal (STR) TACs of in saline-treated (SAL) and raclopride-treated (RAC) rats. C – striatum-to-cerebellum uptake ratios in saline-treated and raclopride-treated rats.

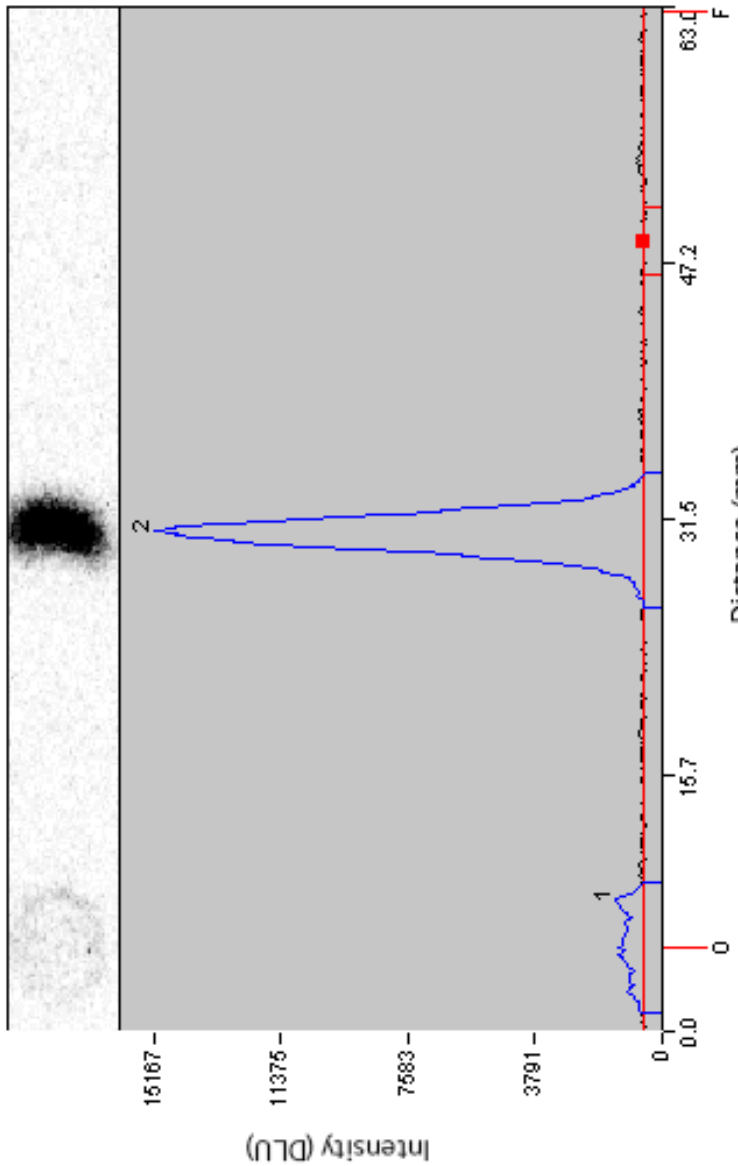

Figure S2. Representative TLC of radioactivity extracted from the brain of a rat injected with [^{18}F]FEt-AMC13.
Peak 1 corresponds to radiometabolites remaining on the start. Peak 2 corresponds to intact [^{18}F]FEt-AMC13. Eluent is ethylacetate/methanol/triethylamine 100/5/1.

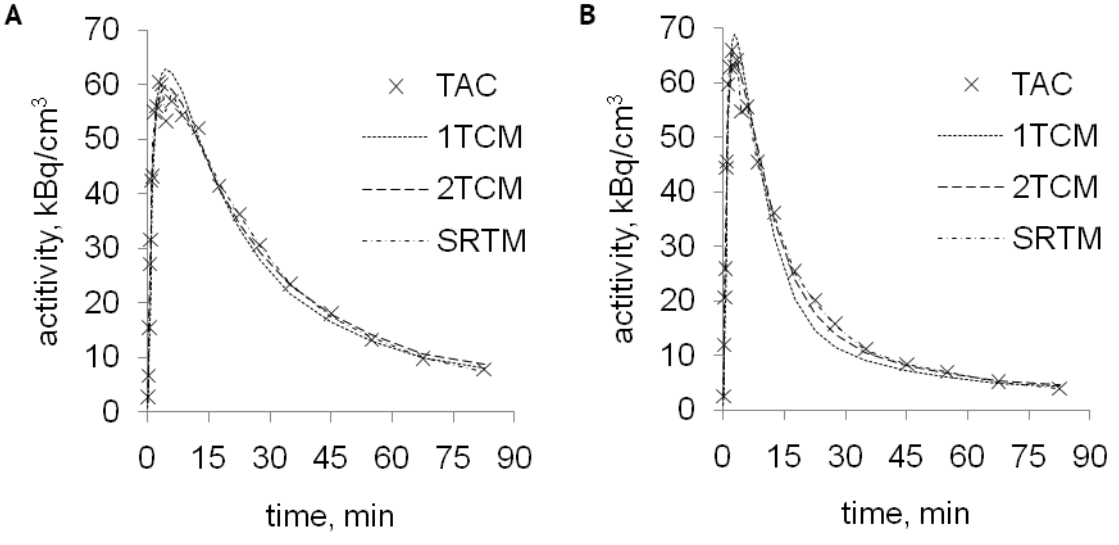

Figure S3. Representative striatal (A) and cerebellar (B) TACs of [^{18}F]FEt-AMC13 for a control rat and the corresponding fits with 1TCM, 2TCM and SRTM models.

2TCM fits were better than 1TCM fits in 69 out of 70 (99%) cases, as assessed by Akaike's information criterion (AIC). SRTM fits had lower AIC value than 2TCM fits in 44 out of 70 (63%) cases.

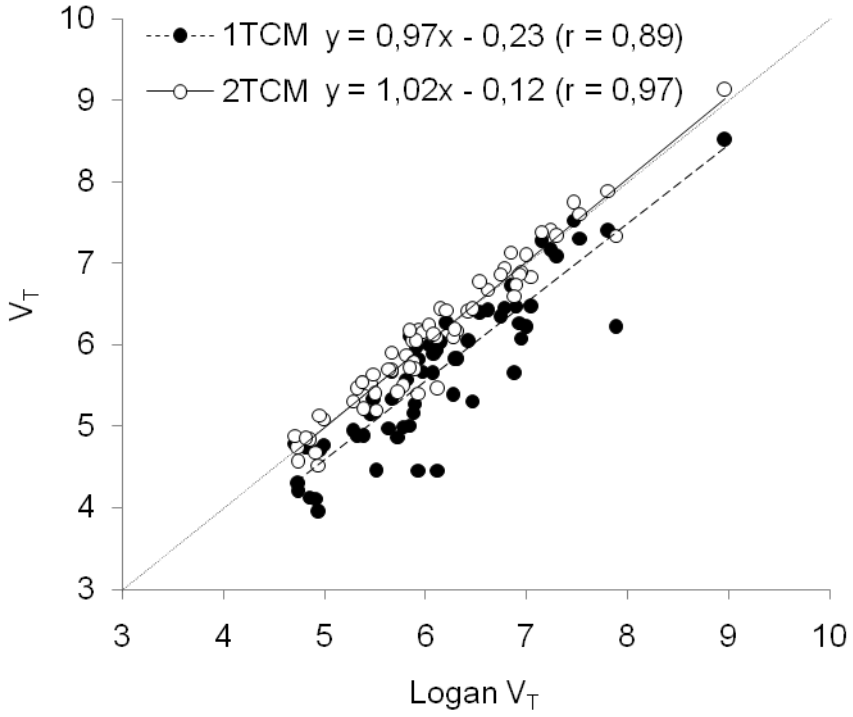

Figure S4. Correlation of region-of-interest total distribution volumes (V_T) of [^{18}F]FEt-AMC13 obtained by Logan analysis with V_T values obtained by analyses with 1TCM and 2TCM models.

Linear regression lines along with their equations and r and p values and the unity line (x=y) are shown on the graphs.

Points represent fits for individual regions in individual animals (both control and raclopride-pre-treated). Data for striatum, hippocampus, thalamus, hypothalamus, cortex, brainstem, cerebellum, olfactory bulbs and pituitary are used.

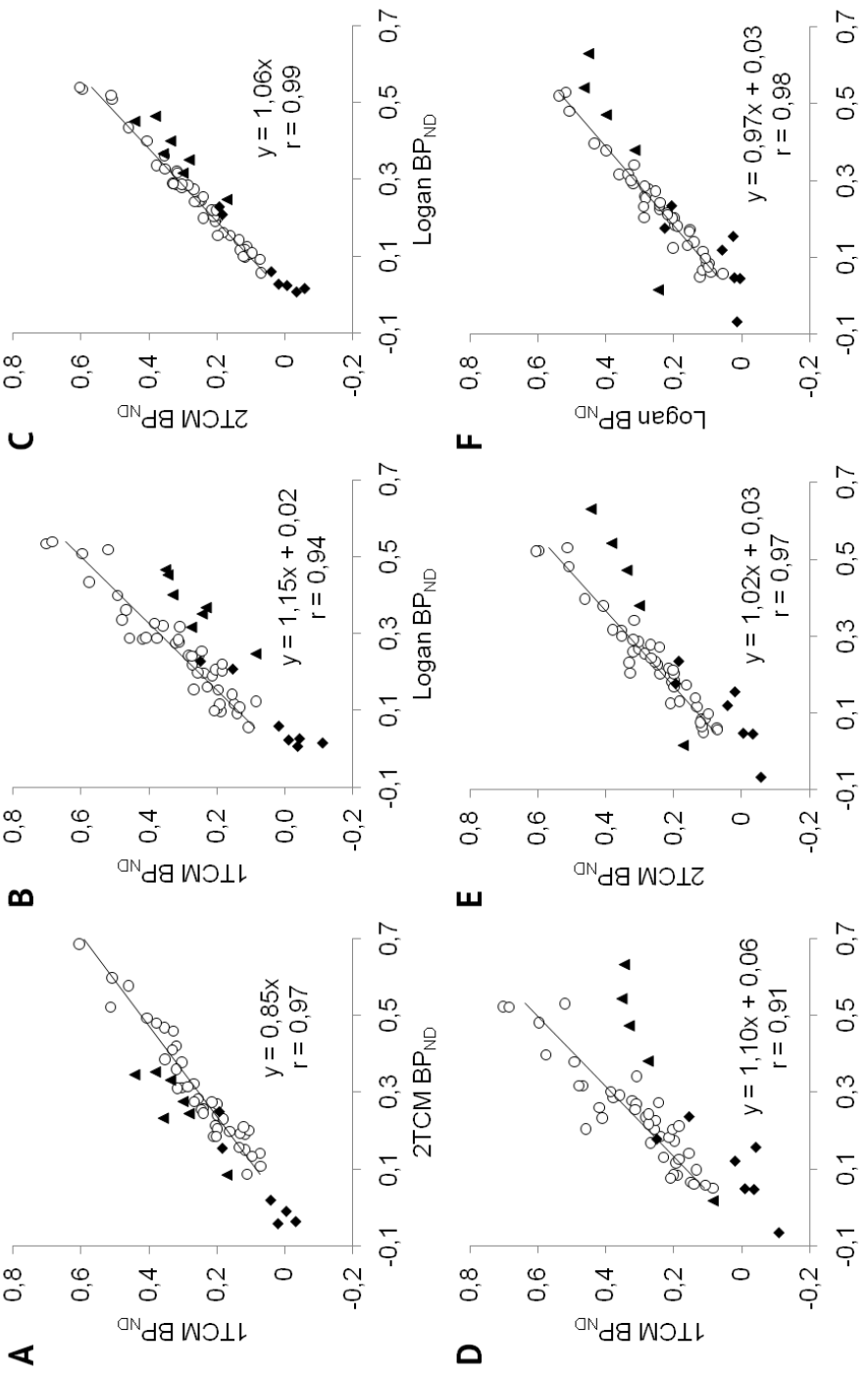
A
1TCM BPND
2TCM BPND
y = 0,85x
r = 0,97
B
1TCM BPND
Logan BPND
y = 1,15x + 0,02
r = 0,94
C
2TCM BPND
Logan BPND
y = 1,06x
r = 0,99
D
1TCM BPND
SRTM BPND
y = 1,10x + 0,06
r = 0,91
E
2TCM BPND
SRTM BPND
y = 1,02x + 0,03
r = 0,97
F
Logan BPND
SRTM BPND
y = 0,97x + 0,03
r = 0,98

Figure S5 (previous page). Mutual correlation of region-of-interest binding potential (BP_{ND}) values of [^{18}F]FEt-AMC13 obtained from different models.

A – correlation of 1TCM and 2TCM BP_{ND} values; B, C – correlation of Logan-derived values with 1TCM and 2TCM-derived data; D, E, F – correlation of SRTM-derived values 1TCM, 2TCM and Logan-derived data. Linear regression lines, along with their equations and r and p values are shown on the graphs.

Points represent fits for individual regions in individual animals (both control and raclopride-pre-treated). Data for the striatum, hippocampus, thalamus, hypothalamus, cortex and brainstem are given as white circles. Data for the olfactory bulbs and pituitary are given as black diamonds and black triangles, respectively. These data are not used for the building of the linear regression lines shown on the graphs. BP_{ND} values are calculated using the cerebellum as a reference region, therefore the data for the cerebellum are not presented. V_T-based BP_{ND} values are used in case of 2TCM.

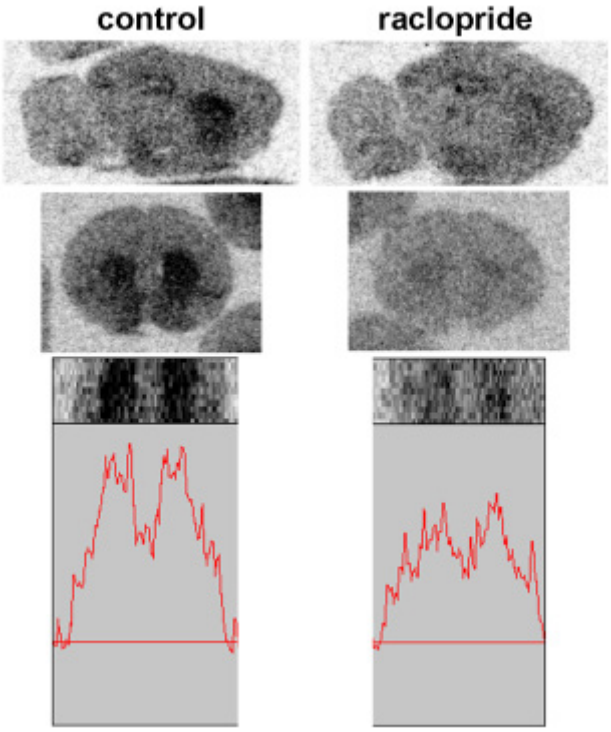

Figure S6. Ex vivo autoradiography images of [^{18}F]FEt-AMC13 from control (left) and raclopride-treated (right) rats.

Representative sagittal and coronal slices (top) and a profile section through the coronal slices showing absolute exposure values (bottom).

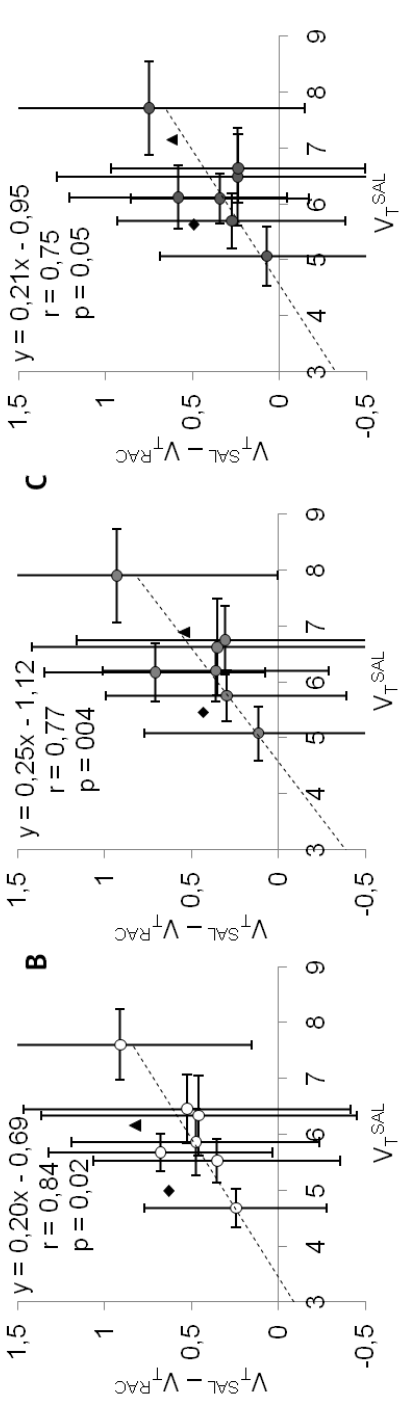

Figure S7. Modified Lassen plots [28] for [^{18}F]FEt-AMC13 built from 1TCM (A), 2TCM (B) and Logan (C) data.
V_T^{SAL} –ROI distribution volume in the control group; V_T^{RAC} –ROI distribution volume in the raclopride-treated group. Assuming equal receptor occupancy by raclopride and equal non-displaceable volume of distribution (V_{ND}) of the tracer in all ROIs, the slope of the linear regression line represents the fraction of receptors occupied by raclopride, while the X-intersect represents V_{ND}.
Points show mean values, error bars show standard deviations. Data for striatum (always the rightmost topmost circle), hippocampus, thalamus, hypothalamus, cortex, brainstem and cerebellum (always the leftmost bottommost circle) are presented. Data for the olfactory bulbs and pituitary are given without error bars as, respectively, black diamonds and black triangles, and are not used for the building of the linear regression lines. Equations and r and p values of linear regression are shown on the graphs. Fits were performed disregarding the variability of the means.

Table S1. Radio-HPLC and radio-TLC characterization data for [^{18}F]AMC13 and [^{18}F]AMC15 homologues.

Compound	QC1 k'	QC2 k'	TLC R_f
[^{18}F]FEt-AMC13	12.3[a]	2.1[c]	0.40[e]
[^{18}F]FPr-AMC13	12.9[a]	4.0[c]	0.46[e]
[^{18}F]FBu-AMC13	12.9[a]	5.9[c]	0.56[e]
[^{18}F]FEt-AMC15	9.1[b]	7.1[d]	0.16[f]
[^{18}F]FPr-AMC15	9.8[b]	9.5[d]	0.22[f]
[^{18}F]FBu-AMC15	12.2[b]	12.3[d]	0.50[f]

a Platinum C18 EPS 100A 5 µm, 250×5 mm; acetonitrile/water/formic acid 55/45/0.1; 2 ml/min.

b Platinum C18 EPS 100A 5 µm, 250×5 mm; acetonitrile/10 mM NaH_2PO_4 pH7.0 70/30; 2 ml/min.

c Gracesmart5 µm, 250×5 mm;acetonitrile/10 mM H_3PO_4 25/75, 2 ml/min.

d Gracesmart5 µm, 250×5 mm;acetonitrile/10 mM NaH_2PO_4 pH7.0 40/60, 2 ml/min.

e ethylacetate/methanol/triethylamine 100/5/1, silica plates.

f ethylacetate/methanol/ammonia/triethylamine 100/5/5/1, silica plates.

Table S2. MS/MS transitions and LC retention times of [^{18}F]AMC13 and [^{18}F]AMC15 homologues.

Compound	Precursor		Monitored transition products[a]		Retention time, min
	calcd M / formula	m/z $[M+H]^+$	calcd M / formula	m/z M^+	
FEt-AMC13	331.16 $C_{19}H_{22}FNO_3$	332.20	153.07 $C_9H_{10}FO^+$	153.10	6.27
			107.05 $C_7H_7O^+$	107.10	
FPr-AMC13	345.17 $C_{20}H_{24}FNO_3$	346.20	167.09 $C_{10}H_{12}FO^+$	167.10	7.07
			107.05 $C_7H_7O^+$	107.10	

(continued on the next page)

Table S2 (continuation). MS/MS transitions and LC retention times of [^{18}F]AMC13 and [^{18}F]AMC15 homologues.

Compound	Precursor		Monitored transition products[a]		Retention time, min
	calcd M / formula	m/z $[M+H]^+$	calcd M / formula	m/z M^+	
FBu-AMC13	359.19 $C_{21}H_{26}FNO_3$	360.20	181.10 $C_{11}H_{14}FO^+$	181.10	8.17
			107.05 $C_7H_7O^+$	107.10	
FEt-AMC15	429.24 $C_{24}H_{32}N_3O_3F$	430.30	206.12 $C_{12}H_{16}NO_2^+$	206.20	4.62
FPr-AMC15	443.26 $C_{25}H_{34}FN_3O_3$	444.30	206.12 $C_{12}H_{16}NO_2^+$	206.20	5.87
FBu-AMC15	457.27 $C_{26}H_{36}FN_3O_3$	458.30	206.12 $C_{12}H_{16}NO_2^+$	206.20	6.11

a Putative fragmentation reactions are as follows:

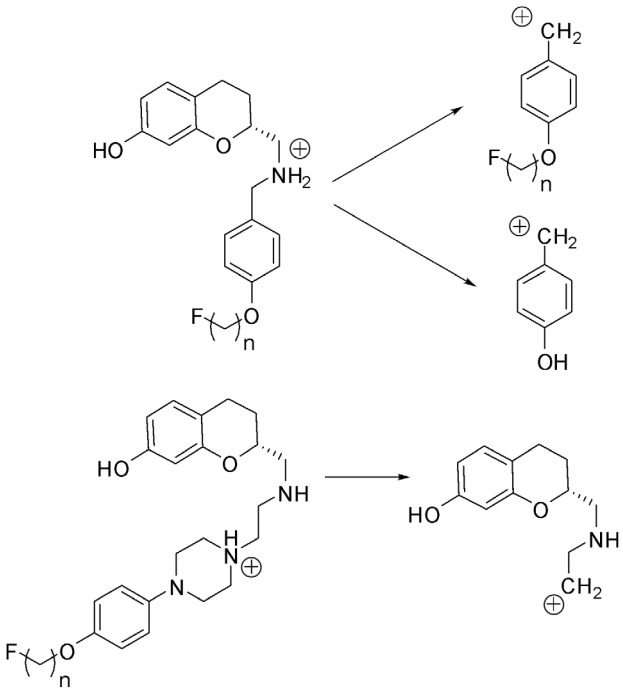

5

Table S3. *Ex vivo* uptake (SUV) of the evaluated tracers in the peripheral tissues of saline (SAL) and raclopride-pre-treated (RAC) rats.

Tracer	[^{18}F]FEt-AMC13		[^{18}F]FBu-AMC13		[^{18}F]FEt-AMC15	
Treatment Region	SAL (*n*=4)	RAC (*n*=4)	SAL (*n*=3)	RAC (*n*=3)	SAL (*n*=3)	RAC (*n*=3)
Whole blood	0.16±0.03	0.17±0.01	ND[a]	ND	0.06±0.03	0.12±0.08
Blood cells[b]	0.07±0.01	0.06±0.01	ND	ND	0.05±0.04	0.05±0.04
Plasma[b]	0.22±0.04	0.23±0.01	0.15±0.02	0.16±0.03	0.14±0.11	0.07±0.02
Adipose tissue	0.30±0.42	0.09±0.02	ND	ND	0.18±0.09	0.10±0.05
Adrenal glands	0.84±0.29	0.59±0.20	34.5±3.5	32.1±3.6	1.53±0.58	1.73±1.07
Bladder	1.00±0.52	0.83±0.64	0.43±0.16	0.59±0.26	0.23±0.05	0.69±0.30
Bone	0.24±0.21	0.17±0.05	0.73±0.47	0.77±0.46	0.14±0.03	0.12±0.08
Bone marrow	0.68±0.38	2.00±3.17	2.31±1.19	2.18±0.09	0.98±0.36	0.91±0.53
Caecum	0.46±0.29	0.63±0.84	ND	ND	0.15±0.10	0.91±1.10
Duodenum	1.15±0.25	4.01±4.63	3.24±1.2	2.70±1.37	1.92±0.35	22.8±36.6
Heart	0.15±0.04	0.16±0.02	0.50±0.25	0.36±0.03	0.11±0.04	0.15±0.10
Kidney	0.64±0.20	0.48±0.07	3.24±0.69	2.36±0.54	0.40±0.10	0.61±0.51
Large intestine	0.57±0.36	0.41±0.33	0.60±0.13	0.46±0.19	0.15±0.07	1.20±1.48

(continued on the next page)

Table S3 (continuation). *Ex vivo* uptake (SUV) of the evaluated tracers in the peripheral tissues of saline (SAL) and raclopride-pre-treated (RAC) rats.

Tracer	[^{18}F]FEt-AMC13		[^{18}F]FBu-AMC13		[^{18}F]FEt-AMC15	
Treatment Region	SAL (*n*=4)	RAC (*n*=4)	SAL (*n*=3)	RAC (*n*=3)	SAL (*n*=3)	RAC (*n*=3)
Large intestine content	0.06±0.03	0.09±0.12	ND	ND	0.02±0.01	0.06±0.04
Liver	1.51±0.14	1.43±0.30	1.49±0.15	1.99±0.86	0.86±0.23	1.47±1.56
Lung	1.67±0.41	1.38±0.20	4.85±2.15	4.26±1.02	1.18±0.16	1.19±0.40
Muscle	0.17±0.04	0.19±0.05	0.33±0.13	0.27±0.02	0.07±0.04	0.15±0.11
Pancreas	1.31±0.31	1.47±0.32	3.78±0.41	3.54±0.64	0.75±0.27	0.92±0.77
Prostate	0.62±0.18	0.40±0.26	0.95±0.17	1.27±0.40	0.38±0.15	0.42±0.10
Small intestine	3.15±2.00	2.39±1.94	4.52±5.94	3.21±3.67	0.18±0.07	11.1±18.4
Small intestine content	54.2±57.7	24.6±32.8	20.9±31.4	11.0±11.4	0.56±0.24	60.5±104
Spleen	0.46±0.05	0.52±0.10	2.48±1.27	2.14±0.20	1.52±0.68	1.62±1.15
Stomach	1.36±0.35	2.09±1.19	1.90±0.26	2.19±0.67	1.79±0.92	1.73±0.75
Submandibular gland	0.36±0.12	0.28±0.06	2.01±0.53	2.12±0.85	1.51±0.26	1.41±0.34

(continued on the next page)

Table S3 (continuation). *Ex vivo* uptake (SUV) of the evaluated tracers in the peripheral tissues of saline (SAL) and raclopride-pre-treated (RAC) rats.

Tracer	[^{18}F]FEt-AMC13		[^{18}F]FBu-AMC13		[^{18}F]FEt-AMC15	
Treatment Region	SAL (*n*=4)	RAC (*n*=4)	SAL (*n*=3)	RAC (*n*=3)	SAL (*n*=3)	RAC (*n*=3)
Testes	0.40±0.06	0.42±0.10	ND	ND	0.04±0.01	0.04±0.01
Thymus	0.32±0.06	0.30±0.06	2.04±0.27	1.54±0.12	0.49±0.09	0.43±0.15
Urine	11.0±9.5	4.40±3.88	0.63±0.53	1.51±0.95	0.69±0.33	2.32±3.35

Data are presented as means±SD *a* Not determined *b* Plasma and cell fractions were obtained from whole blood by short centrifugation (3500 g, 5 min).

Table S4. 1TCM and 2TCM rate constant estimates of [^{18}F]FEt-AMC13 uptake in brain regions of control rats.

ROI	Rat	1TCM			2TCM				
		K_1 (ml/g/min)	k_2 (1/min)	AIC	K_1 (ml/g/min)	k_2 (1/min)	k_3 (1/min)	k_4 (1/min)	AIC
Striatum	A	0.45±0.03	0.05±0.01	489	1.77±0.62	4.95±3.00	1.34±0.29	0.05±0.01	449
	B	0.49±0.02	0.06±0.01	472	0.63±0.14	0.48±0.68	0.81±1.13	0.17±0.07	471
	C	0.47±0.02	0.07±0.004	456	0.98±0.85	3.47±8.55	2.81±3.01	0.11±0.08	454
	D	0.51±0.02	0.07±0.01	465	8.06±30.34	58.0±203.8	3.54±188.40	0.07±263.98	433
Hippo-campus	A	0.41±0.02	0.06±0.01	483	2.21±1.25	8.56±3.62	1.60±2.24	0.05±8.88	443
	B	0.51±0.02	0.08±0.01	466	0.71±0.07	0.50±0.23	0.50±0.27	0.14±0.03	449
	C	0.46±0.01	0.08±0.004	441	0.60±0.12	0.57±0.77	1.17±1.34	0.24±0.09	438
	D	0.48±0.02	0.08±0.01	455	101±14615	1246±181990	5.49±4.23	0.07±0.05	441
Thalamus	A	0.44±0.02	0.06±0.01	475	14.0±117.5	104±848	3.05±820.48	0.05±961.03	452
	B	0.65±0.03	0.10±0.01	473	0.88±0.12	0.58±0.58	0.67±1.63	0.19±1.99	464
	C	0.55±0.02	0.09±0.01	460	0.71±0.13	0.48±0.97	0.76±3.17	0.23±3.61	457
	D	0.64±0.03	0.11±0.01	479	3.13±3.18	12.3±18.9	2.61±0.96	0.11±0.02	453

(continued on the next page)

Table S4 (continuation). 1TCM and 2TCM rate constant estimates of [^{18}F]FEt-AMC13 uptake in brain regions of control rats.

ROI	Rat	1TCM			2TCM				
		K_1 (ml/g/min)	k_2 (1/min)	AIC	K_1 (ml/g/min)	k_2 (1/min)	k_3 (1/min)	k_4 (1/min)	AIC
Hypothal-amus	A	0.40±0.03	0.06±0.01	493	273[a]	1355[a]	1.65[a]	0.05[a]	459
	B	0.53±0.03	0.09±0.01	478	1.17±0.88	3.45±1.30	2.22±6.73	0.13±14.19	472
	C	0.50±0.02	0.08±0.01	460	0.64±0.24	0.63±1.60	1.37±2.85	0.27±0.20	462
	D	0.59±0.04	0.12±0.02	489	680±116990	3105±534810	2.16±0.48	0.09±0.01	453
Cortex	A	0.37±0.02	0.06±0.01	468	1.68±0.46	7.83±1.43	1.84±0.62	0.06±4.47	401
	B	0.47±0.02	0.09±0.01	450	0.66±0.04	0.64±0.21	0.72±0.24	0.16±0.02	416
	C	0.41±0.01	0.07±0.002	417	0.43±0.12	0.19±1.58	1.50±19.49	1.00±1.64	421
	D	0.47±0.02	0.09±0.01	452	1.46±0.45	6.65±0.77	2.62±1.18	0.11±6.33	403
Brain-stem	A	0.63±0.04	0.10±0.02	501	2.03±0.40	3.53±1.32	1.05±0.19	0.10±0.01	451
	B	0.60±0.03	0.11±0.01	475	0.96±0.11	0.89±0.30	0.72±0.83	0.15±1.20	449
	C	0.68±0.02	0.12±0.01	467	1.11±0.22	1.19±0.59	1.10±1.86	0.21±2.66	452
	D	0.71±0.03	0.13±0.01	479	4.75±5.87	19.6±19.9	2.79±15.04	0.12±37.81	446

(continued on the next page)

Table S4 (continuation). 1TCM and 2TCM rate constant estimates of [^{18}F]FEt-AMC13 uptake in brain regions of control rats.

ROI	Rat	1TCM			2TCM				
		K_1 (ml/g/min)	k_2 (1/min)	AIC	K_1 (ml/g/min)	k_2 (1/min)	k_3 (1/min)	k_4 (1/min)	AIC
Cerebellum	A	0.57±0.04	0.11±0.02	492	2.10±0.32	4.90±1.30	1.23±0.13	0.10±0.005	420
	B	0.61±0.02	0.13±0.01	461	0.81±0.05	0.53±0.24	0.46±0.55	0.20±0.71	436
	C	0.62±0.01	0.13±0.01	439	0.86±0.21	1.13±1.45	1.84±1.78	0.34±0.12	433
	D	0.68±0.03	0.16±0.02	473	48.7±819.7	298±5152	3.55±1.05	0.13±0.03	438
Olfactory bulbs	A	0.55±0.05	0.12±0.02	500	3.58±1.65	9.75±3.75	1.20±2.96	0.09±7.03	449
	B	0.49±0.02	0.08±0.01	453	0.63±0.07	0.47±0.34	0.69±0.56	0.20±0.04	444
	C	0.44±0.01	0.09±0.005	438	0.59±0.10	0.68±0.93	1.07±3.21	0.23±3.75	431
	D	0.50±0.03	0.10±0.01	479	1.08±0.20	1.82±0.90	0.92±0.31	0.11±0.01	452
Pituitary	A	0.52±0.05	0.08±0.02	510	6.16±6.57	16.8±16.5	1.11±15.04	0.06±22.82	472
	B	0.63±0.04	0.10±0.01	490	1.23±0.31	1.62±0.42	0.99±1.42	0.12±2.70	474
	C	0.52±0.02	0.08±0.01	472	0.97±0.34	1.54±0.73	1.23±2.61	0.13±4.28	464
	D	0.67±0.05	0.12±0.02	497	1.38±0.24	1.48±0.20	0.69±0.58	0.11±1.34	473

Data are presented as means±SD. *a* Standard deviation could not be estimated.

Table S5. V_T of [^{18}F]FEt-AMC13 per brain region in control and raclopride-treated rats.

Region of interest	Logan V_T		1TCM V_T		2TCM V_T	
	control	raclopride	control	raclopride	control	raclopride
Striatum	7.72±0.84 (11)	6.97±0.32 (5)	7.60±0.64 (8)	6.69±0.41 (6)	7.90±0.84 (11)	6.97±0.39 (6)
Hippocampus	6.49±0.88 (14)	6.25±0.56 (9)	6.34±0.71 (11)	5.88±0.56 (10)	6.62±0.86 (13)	6.27±0.63 (10)
Thalamus	6.64±0.61 (9)	6.40±0.40 (6)	6.45±0.62 (10)	5.93±0.71 (12)	6.75±0.62 (9)	6.44±0.60 (9)
Hypothalamus	6.10±0.44 (7)	5.76±0.26 (5)	5.86±0.60 (10)	5.38±0.38 (7)	6.20±0.55 (9)	5.83±0.34 (6)
Cortex	5.69±0.49 (9)	5.42±0.44 (8)	5.53±0.38 (7)	5.17±0.60 (12)	5.75±0.45 (8)	5.45±0.52 (10)
Brainstem	6.12±0.57 (9)	5.53±0.26 (5)	5.67±0.33 (6)	4.99±0.56 (11)	6.17±0.52 (8)	5.46±0.36 (7)
Cerebellum	5.06±0.53 (11)	4.99±0.30 (6)	4.68±0.34 (7)	4.43±0.40 (9)	5.08±0.49 (10)	4.96±0.44 (9)
Olfactory Bulbs	5.64±0.57 (10)	5.14±0.43 (8)	4.99±0.62 (12)	4.36±0.55 (13)	5.45±0.52 (10)	5.02±0.61 (12)
Pituitary	7.15±0.49 (7)	6.53±0.44 (7)	6.16±0.35 (6)	5.33±0.88 (17)	6.89±0.32 (5)	6.34±0.82 (13)

Data are presented as means±SD, *n*=4 for the control group, *n*=3 for the raclopride-treated group. Coefficients of variation (in %) are shown in parentheses.

Table S6. BP_{ND} of [^{18}F]FEt-AMC13 per brain region in control and raclopride-treated rats.

Region of interest	1TCM BP_{ND}		2TCM BP_{ND} (V_T-based)		Logan BP_{ND}		SRTM BP_{ND}	
	control	raclopride	control	raclopride	control	raclopride	control	raclopride
Striatum	0.63±0.08	0.51±0.06 (−18%)	0.56±0.05	0.41±0.05 (−27%)*	0.52±0.01	0.40±0.04 (−24%)*	0.51±0.02	0.38±0.05 (−26%)**
Hippocampus	0.35±0.11	0.33±0.09 (−8%)	0.30±0.07	0.26±0.06 (−13%)	0.28±0.04	0.25±0.05 (−10%)	0.26±0.04	0.23±0.05 (−13%)
Thalamus	0.38±0.06	0.33±0.04 (−12%)	0.33±0.02	0.30±0.01 (−10%) *	0.31±0.02	0.28±0.005 (−10%)*	0.28±0.06	0.26±0.02 (−7%)
Hypothalamus	0.25±0.04	0.22±0.04 (−14%)	0.22±0.03	0.18±0.06 (−19%)	0.21±0.04	0.16±0.04 (−25%)	0.21±0.03	0.16±0.04 (−23%)
Cortex	0.18±0.05	0.17±0.05 (−9%)	0.13±0.04	0.10±0.02 (−27%)	0.13±0.03	0.09±0.03 (−32%)	0.11±0.03	0.08±0.02 (−24%)
Brainstem	0.21±0.03	0.13±0.03 (−41%)*	0.22±0.02	0.10±0.02 (−53%)**	0.21±0.02	0.11±0.02 (−47%)**	0.18±0.04	0.07±0.03 (−60%)**
Olfactory Bulbs	0.07±0.16	−0.02±0.03 (−127%)	0.08±0.13	0.01±0.04 (−88%)	0.12±0.12	0.03±0.03 (−74%)	0.10±0.13	0.11±0.05 (+10%)
Pituitary	0.32±0.05	0.18±0.05 (−38%)	0.36±0.07	0.13±0.04 (−23%)	0.42±0.05	0.13±0.03 (−26%)	0.71±0.32	0.55±0.53 (−22%)

Data are presented as means±SD, *n*=4 for the control group, *n*=3 for the raclopride-treated group (except for the SRTM BP_{ND} values, where *n*=4). Next to the BP_{ND} values of the raclopride-treated group, percentage of change relative to the control group is shown. * $P < 0.05$, ** $P < 0.01$, 2-sided Welch test.

REFERENCES

1. Howes OD, Kapur S. The dopamine hypothesis of schizophrenia: version III – the final common pathway. Schizophr Bull. 2009;35(3):549–62.

2. Booij J, Tissingh G, Winogrodzka A, van Royen EA. Imaging of the dopaminergic neurotransmission system using single-photon emission tomography and positron emission tomography in patients with parkinsonism. Eur J Nucl Med. 1999;26(2):171–182.

3. Volkow ND, Fowler JS, Wang G-J, Swanson JM. Dopamine in drug abuse and addiction: results from imaging studies and treatment implications. Mol Psychiatry. 2004;9(6):557–69.

4. Volkow ND, Fowler JS, Wang GJ, Baler R, Telang F. Imaging dopamine's role in drug abuse and addiction. Neuropharmacology. 2009;56 Suppl 1:3–8.

5. Elsinga PH, Hatano K, Ishiwata K. PET tracers for imaging of the dopaminergic system. Curr Med Chem. 2006;13(18):2139–53.

6. Chio CL, Lajiness ME, Huff RM. Activation of heterologously expressed D_3 dopamine receptors: comparison with D_2 dopamine receptors. Mol Pharmacol. 1994;45(1):51–60.

7. Sibley DR, De Lean A, Creese I. Anterior pituitary dopamine receptors. Demonstration of interconvertible high and low affinity states of the D_2 dopamine receptor. J Biol Chem. 1982;257(11):6351–61.

8. Liu IS, George SR, Seeman P. The human dopamine D_2(Longer) receptor has a high-affinity state and inhibits adenylyl cyclase. Brain Res Mol Brain Res. 2000;77(2):281–4.

9. George SR, Watanabe M, Seeman P. Dopamine D_2 Receptors in the Anterior Pituitary: A Single Population Without Reciprocal Antagonist/Agonist States. J Neurochem. 1985;44(4):1168–1177.

10. Skinbjerg M, Sibley DR, Javitch JA, Abi-Dargham A. Imaging the high-affinity state of the dopamine D_2 receptor in vivo: Fact or fiction? Biochem Pharmacol. 2012;83(2):193–8.

11. Cumming P, Wong DF, Gillings N, Hilton J, Scheffel U, Gjedde A. Specific binding of [^{11}C]raclopride and N-[^{3}H]propyl-norapomorphine to dopamine receptors in living mouse striatum: occupancy by endogenous dopamine and guanosine triphosphate-free G protein. J Cereb Blood Flow Metab. 2002;22:596–604.

12. McCormick PN, Ginovart N, Wilson AA. Isoflurane anaesthesia differentially affects the amphetamine sensitivity of agonist and antagonist D_2/D_3 positron emission tomography radiotracers: implications for in vivo imaging of dopamine release. Mol Imaging Biol. 2011;13:737–46.

13. Ginovart N, Galineau L, Willeit M, Mizrahi R, Bloomfield PM, Seeman P, et al. Binding characteristics and sensitivity to endogenous dopamine of [^{11}C]-(+)-PHNO, a new agonist radiotracer for imaging the high-affinity state of D_2 receptors in vivo using positron emission tomography. J Neurochem. 2006;97:1089–1103.

14. Narendran R, Hwang DR, Slifstein M, Talbot PS, Erritzoe D, Huang Y, et al. In vivo vulnerability to competition by endogenous dopamine: comparison of the D_2 receptor agonist radiotracer (–)-N-[^{11}C]propyl-norapomorphine ([^{11}C]NPA) with the D_2 receptor antagonist radiotracer [^{11}C]-raclopride. Synapse. 2004;52:188–208.

15. Seneca N, Finnema SJ, Farde L, Gulyas B, Wikstrom HV, Halldin C, Innis RB. Effect of amphetamine on dopamine D_2 receptor binding in nonhuman primate brain: a comparison of the agonist radioligand [^{11}C]MNPA and antagonist [^{11}C]raclopride. Synapse. 2006;59:260–269.

16. Narendran R, Mason NS, Laymon CM, Lopresti BJ, Velasquez ND, May MA, et al. A comparative evaluation of the dopamine $D_{2/3}$ agonist radiotracer [^{11}C](–)-N-propyl-norapomorphine and antagonist [^{11}C]raclopride to measure amphetamine-induced dopamine release in the human striatum. J Pharmacol Exp Ther. 2010;333(2):533–9.

17. Shotbolt P, Tziortzi AC, Searle GE, Colasanti A, van der Aart J, Abanades S, et al. Within-subject comparison of [^{11}C]-(+)-PHNO and [^{11}C]raclopride sensitivity to acute amphetamine challenge in healthy humans. J Cereb Blood Flow Metab. 2012;32(1):127–36.

18. Van Wieringen J-P, Booij J, Shalgunov V, Elsinga P, Michel MC. Agonist high- and low-affinity states of dopamine D_2 receptors: methods of detection and clinical implications. Naunyn Schmiedebergs Arch Pharmacol. 2013;386(2):135–54.

19. Finnema SJ, Bang-Andersen B, Wikström H V, Halldin C. Current state of agonist radioligands for imaging of brain dopamine D_2/D_3 receptors in vivo with positron emission tomography. Curr Top Med Chem. 2010;10(15):1477–98.

20. Shi B, Narayanan TK, Christian BT, Chattopadhyay S, Mukherjee J. Synthesis and biological evaluation of the binding of dopamine D_2/D_3 receptor agonist,

(R,S)-5-hydroxy-2-(N-propyl-N-(5'-[^{18}F]fluoropentyl) aminotetralin ([^{18}F]-5-OH-FPPAT) in rodents and nonhuman primates. Nucl Med Biol. 2004;31(3):303–11.

21. Vasdev N, Seeman P, Garcia A, Stableford WT, Nobrega JN, Houle S, Wilson AA. Syntheses and in vitro evaluation of fluorinated naphthoxazines as dopamine D_2/D_3 receptor agonists: radiosynthesis,ex vivo biodistribution and autoradiography of [^{18}F]F-PHNO. Nucl Med Biol. 2007;34(2):195–203.

22. Finnema SJ, Stepanov V, Nakao R, Sromek AW, Zhang T, Neumeyer JL, et al. [^{18}F]-MCL-524, an ^{18}F-Labelled Dopamine D_2 and D_3 Receptor Agonist Sensitive to Dopamine: A Preliminary PET Study. J Nucl Med. 2014;55(7):1164–70.

23. Mewshaw RE, Kavanagh J, Stack G, Marquis KL, Shi X, Kagan MZ, et al. New generation dopaminergic agents. 1. Discovery of a novel scaffold which embraces the D_2 agonist pharmacophore. Structure-activity relationships of a series of 2-(aminomethyl)chromans. J Med Chem. 1997;40(26):4235–56.

24. Van Wieringen J-P, Shalgunov V, Janssen HM, Fransen PM, Janssen AMG, Michel MC, et al. Synthesis and characterization of a novel series of agonist compounds as potential radiopharmaceuticals for imaging dopamine $D_{2/3}$ receptors in their high-affinity state. J Med Chem. 2014;57(2):391–410.

25. Kämäräinen EL, Kyllönen T, Airaksinen A, Lundkvist C, Yu M, Någren K, et al. Preparation of [^{18}F]β-CFT-FP and [^{11}C]β-CFT-FP, selective radioligands for visualisation of the dopamine transporter using positron emission tomography (PET). J Labelled Compd Radiopharm. 2000;43(12):1235–44.

26. Innis RB, Cunningham VJ, Delforge J, Fujita M, Gjedde A, Gunn RN, et al. Consensus nomenclature for in vivo imaging of reversibly binding radioligands. J Cereb Blood Flow Metab. 2007;27(9):1533–9.

27. Julien-Dolbec C, Tropres I, Montigon O, Reutenauer H, Ziegler A, Decorps M, Payen JF. Regional response of cerebral blood volume to graded hypoxic hypoxia in rat brain. Br J Anaesth. 2002;89:287–293.

28. Cunningham VJ, Rabiner EA, Slifstein M, Laruelle M, Gunn RN. Measuring drug occupancy in the absence of a reference region: the Lassen plot re-visited. J Cereb Blood Flow & Metab. 2009;30:46–50.

29. Seneca N, Zoghbi SS, Skinbjerg M, Liow JS, Hong J, Sibley DR, et al. Occupancy of dopamine $D_{2/3}$ receptors in rat brain by endogenous dopamine measured with the agonist positron emission tomography radioligand [^{11}C]MNPA. Synapse. 2008;62(10):756–63.

30. Wilson AA, McCormick P, Kapur S, Willeit M, Garcia A, Hussey D, et al. Radiosynthesis and evaluation of [^{11}C]-(+)-4-propyl-3,4,4a,5,6,10b-hexahydro-2H-naphtho[1,2-b][1,4]oxazin-9-ol as a potential radiotracer for in vivo imaging of the dopamine D_2 high-affinity state with positron emission tomography. J Med Chem. 2005;48(12):4153–60.

31. Egerton A, Hirani E, Ahmad R, Turton DR, Brickute D, Rosso L, et al. Further evaluation of the carbon-11-labeled $D_{2/3}$ agonist PET radiotracer PHNO: reproducibility in tracer characteristics and characterization of extrastriatal binding. Synapse. 2010;64(4):301–12.

32. Skinbjerg M, Seneca N, Liow J-S, Hong J, Weinshenker D, Pike VW, et al. Dopamine beta-hydroxylase-deficient mice have normal densities of D_2 dopamine receptors in the high-affinity state based on in vivo PET imaging and in vitro radioligand binding. Synapse. 2010;64(9):699–703.

33. Levant B, Grigoriadis DE, DeSouza EB. [^{3}H]Quinpirole binding to putative D_2 and D_3 dopamine receptors in rat brain and pituitary gland: a quantitative autoradiographic study. J Pharmacol Exp Ther. 1993;264:991–1001.

34. Shalgunov V, van Wieringen JP, Janssen HM, Fransen PM, Dierckx RAJO, Michel MC, et al. Synthesis and evaluation in rats of the dopamine $D_{2/3}$ receptor agonist [^{18}F]-AMC20 as a potential radioligand for PET. J Nucl Med. 2015;56(1):133–139.

35. van Wieringen JP, Michel MC, Janssen HM, Janssen AG, Elsinga PH, Booij J. Agonist signalling properties of radiotracers used for imaging of dopamine $D_{2/3}$ receptors. EJNMMI Res. 2014;doi:10.1186/s13550-014-0053-3.

Chapter 6

Automated preparation of ^{18}F-synthons on a microfluidic synthesis module with and without the use of azeotropic distillation for [^{18}F]fluoride drying

Vladimir Shalgunov, Erik F.J. de Vries,
Rudi A.J.O. Dierckx, Philip H. Elsinga

Department of Nuclear Medicine and Molecular Imaging,
University Medical Center Groningen, University of Groningen,
the Netherlands

ABSTRACT

Background: Microchannel microfluidic platforms are popular tools for the development of radiosynthetic approaches, offering rapid testing of reaction conditions and dose-on-demand production. However, radioactivity losses during [^{18}F]fluoride drying by azeotropic distillation have a particularly adverse impact on isolated product yields in microfluidic syntheses. Here, we report the development of an azeotropic distillation-free method of .[^{18}F]fluoride drying and its use in automated syntheses of ^{18}F-labeled building blocks for candidate positron emission tomography (PET) tracers.

Methods: Azeotropic distillation-free drying of [^{18}F]fluoride ("flushing-elution" procedure) was achieved by flushing the [^{18}F]fluoride-loaded anion-exchange column with dry acetonitrile or dimethyl sulfoxide (DMSO) and then eluting the [^{18}F]fluoride with tetraethyl ammonium bicarbonate (TEAB) solutions in acetonitrile/tert-butanol or DMSO/tert-butanol mixtures. [^{18}F]Fluoride dried in this fashion was used to prepare w-[^{18}F]fluoroalkyl tosylates from ditosylate precursors in acetonitrile and 4-[^{18}F]fluorobenzaldehyde from trimethylammonium precursor in DMSO on the microfluidic module Advion Nanotek LF, in reaction optimization and batch production modes.

Results: [^{18}F]Fluoride drying by flushing-elution took 5 min, while drying by azeotropic distillation took 15 min on average. At reaction temperatures of 150 °C and higher, [^{18}F]fluoride dried by flushing-elution could be converted into w-[^{18}F]fluoroalkyl tosylates and 4-[^{18}F]fluorobenzaldehyde with yields as high as observed with [^{18}F]fluoride conventionally dried by azeotropic distillation. Batch synthesis protocols with optimized labeling conditions using azeotropically dried [^{18}F]fluoride produced 2-[^{18}F]fluoroethyl tosylate in 78±16% non-isolated and 28±11% isolated yield. Protocols using the flushing-elution procedure produced 2-[^{18}F]fluoroethyl tosylate in 85±5% non-isolated and 53±9% isolated yield. 4-[^{18}F]fluorobenzaldehyde was obtained in 77±13% non-isolated and 14±6% isolated yield with azeotropic distillation and in 73±14% non-isolated and 37±7% isolated yield without.

Conclusion: [^{18}F]Fluoride dried by flushing-elution procedure was successfully used to label both aliphatic and activated aromatic substrates; optimal ^{18}F-fluorination yields were similar to those obtained with conventionally dried [^{18}F]fluoride. In automated batch syntheses of ^{18}F-labeled building blocks, replacement of azeotropic distillation by flushing-elution cut total synthesis time and improved isolated yields by decreasing losses of [^{18}F]fluoride radioactivity during the drying step.

INTRODUCTION

The use of microfluidic radiochemistry for positron emission tomography (PET) tracer production has attracted significant interest in the recent decade. Microfluidic synthesis systems provide flexibility in the choice of reaction conditions (e.g. permit to use solvents at temperatures above their "normal" boiling points) and decrease time and reagent expenses connected with the optimization of labeling conditions [1,2]. Two major categories of microfluidic reactors are "microvessel" and "microchannel" types [2]. The former are scaled-down versions of conventional batch reactors, while in the latter the labeling takes place in a microscopic channel, through which the reaction mixture is pumped.

Microchannel synthesis systems are a popular platform for the development of microfluidic synthetic approaches. For example, the commercially available Advion Nanotek LF synthesis system has been used for proof-of-concept radiolabeling studies [3–7] as well as for the production of PET tracers for pre-clinical [8] as well as clinical imaging [9,10]. Nevertheless, the value of the microchannel modules like Nanotek for radiopharmaceutical synthesis on a clinical scale is not yet fully assessed. The use of Nanotek to optimize labeling conditions for automated batch syntheses on conventional modules is limited by the peculiarities of microchannel microfluidic labeling [11], although the correspondence between conventional and microfluidic conditions may be more straightforward for simple substrates [12]. Alternatively, multi-dose batch syntheses can be performed on the microfluidic module itself: greater reaction speed and wider applicable temperature range may provide greater possibilities, compared to the conventional setup, to enhance the yield of target product over byproducts. However, the majority of published studies that involved radiolabeling on Nanotek focused on small-scale labeling runs, deliberately using no more than half (and often less than one tenth) of total ^{18}F-radioactivity loaded into the module per run. Therefore, more studies are needed to investigate the net efficiency of reagent and [^{18}F]fluoride use in batch microfluidic syntheses carried out on microchannel platforms.

Preparation of [^{18}F]fluoride for radiolabeling is a major concern in the development of both conventional and microfluidic procedures. Drying of [^{18}F]fluoride by azeotropic distillation, the classical approach, is time-consuming and leads to the loss of [^{18}F]fluoride through its adsorption on the walls of the drying vessel. The "stickiness" of dried [^{18}F]fluoride is partic-

ularly detrimental for microchannel setups, because of the high surface-to-volume ratio of the environment and the fact that drying and labeling processes take place in different locations. Elimination of azeotropic distillation is thus especially beneficial for microfluidic synthesis.

The main goal of the current work was to streamline [^{18}F]fluoride preparation for microfluidic ^{18}F-labeling by eliminating the azeotropic distillation step. To achieve this goal, we have tested the reactivity of [^{18}F]fluoride in solvent mixtures containing tert-butanol [13,14] or water (as reference protic solvent) in microfluidic labeling. Tetraethylammonium bicarbonate (TEAB) was used as phase transfer agent, because it led to fewer microreactor cloggings than potassium-Kryptofix complex [15]. Model reactions chosen were the formation of [^{18}F]fluoroalkyl tosylates through bimolecular nucleophilic (S_N2) ^{18}F-fluorination and the formation of 4-[^{18}F]fluorobenzaldehyde through aromatic nucleophilic (S_NAr) ^{18}F- fluorination.

The secondary goal was to use the improved [^{18}F]fluoride preparation methods in the development of automated microfluidic synthesis procedures for [^{18}F]fluoroalkyl tosylates and [^{18}F]fluorobenzaldehyde and to investigate the net efficiency of radioactivity use in these procedures. [^{18}F]Fluoroalkyl tosylates and [^{18}F]fluorobenzaldehyde are used by our group as building blocks to prepare aminomethylchromane dopamine $D_{2/3}$ receptor tracers described in Chapters 3–5 of the current thesis as well as tracers for other targets [16]. We have performed automated batch syntheses of [^{18}F]fluoroethyl tosylate ([^{18}F]FEtTos) and [^{18}F]fluorobenzaldehyde using both conventional azeotropic distillation and tert-butanolic solutions of TEAB to prepare [^{18}F]fluoride for labeling, and assessed the impact of [^{18}F]fluoride preparation method on the yields of ^{18}F-fluorination reactions and on overall isolated yields of the desired products.

METHODS

Chemistry

Reagents, chemicals, materials and solvents were obtained from commercial sources, and were used as received: Biosolve, Merck for solvents, Aldrich, Acros, ABCR, Merck and Fluka for chemicals, materials and reagents. All solvents were of analytical grade quality.

4-Fluorobenzaldehyde was from Fluka. Trimethylammonium benzaldehyde triflate (TBCHO), 1,2-ethanediol ditosylate (EDT), 1,4-butanediol ditosylate (BDT), 2-fluoroethyl tosylate, and 4-fluorobutyl tosylate were prepared according to procedures described in the literature [17–19].

Analytical thin layer chromatography (TLC) was performed on Kieselgel F-254 precoated silica plates. Non-radioactive compounds were visualised on developed TLC plates by irradiating the plates with a 254 nm UV lamp.

Radiochemistry

General

Non-carrier added [^{18}F]fluoride was produced via the ^{18}O(p,n)^{18}F nuclear reaction in [^{18}O]water in the Scanditronix MC-17F cyclotron (Scanditronix, Uppsala, Sweden) and delivered from the target into a 5 ml V-vial inside the hotcell using helium overpressure.

[^{18}F]Fluoroalkyl tosylates were prepared from ditosylate precursors in acetonitrile (MeCN), [^{18}F]fluorobenzaldehyde was prepared from trimethylammonium triflate precursor in DMSO (Figure 1). Solvents for labeling were dried over molecular sieves and filtered through 0.2 μm PTFE filters. Solid-phase extraction (SPE) cartridges (Sep-Pak Acell Plus QMA Plus Light, Sep-Pak tC18 Plus Short, Oasis HLB Plus Short) were supplied by Waters Corporation (USA), except MP-1 anion-exchange cartridges, which were from ORTG Inc. (USA).

Identity of ^{18}F-labeled products was confirmed by their co-elution with [^{19}F]reference compounds on high performance liquid chromatography (HPLC) columns and/or thin layer chromatography (TLC) plates. Characterization data for [^{18}F]fluoroalkyl tosylates and [^{18}F]fluorobenzaldehyde are presented in Table 1.

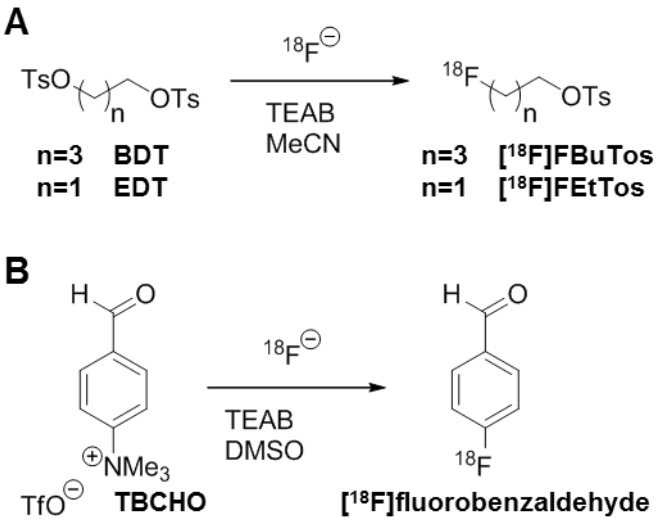

Figure 1. Labelling routes used to obtain [^{18}F]fluoroalkyl tosylates (A) and [^{18}F]fluorobenzaldehyde (B).

Radioactive compounds on TLC plates were visualized by exposing the plates on Cyclone phosphor storage screens (multisensitive, Packard), reading the screens on the Cyclone Plus Storage Phosphor system (PerkinElmer, USA) and quantifying the data with OptiQuant software.

HPLC was run on a system consisting of Hitachi LaChrom L-7100 pump, Hitachi Lachrom Elite L-2400 UV/Vis detector and Bicron Frisk-Tech radiation detector.

This work was carried out on the Advion Nanotek LF microfluidic synthesis system (Advion Biosystems, USA) connected to the PET Tracer Synthesizer (Nuclear Interface GmbH, Münster, Germany).

Advion Nanotek LF Microfluidic Synthesis System

Radiolabeling on the Nanotek system is carried out by pumping the reaction mixture through the heated microfluidic reactor. The reactors are coiled tubes made of fused silica and housed in a silicone polymer bedding inside a brass ring cast. Effective reaction time is equal to the time a particle of the reaction mixture needs to pass the reactor. In this work, reactors with inner diameter of 100 μm and length of 2 m were used (reactor volume 15.7 μl).

Table 1. Characterization data for [^{18}F]fluoroalkyl tosylates and [^{18}F]fluorobenzaldehyde.

Compound	HPLC data[a]	TLC data
2-[^{18}F]fluoroethyl tosylate	Platinum C18 EPS 5 µm 250×5 mm; acetonitrile/10 mM H_3PO_4 70/30; 2.0 ml/min; 229 nm k' = 3.4	Kieselgel F-254 precoated silica plates eluted with hexane/ethyl acetate (2/1 v/v) R_f = 0.6
4-[^{18}F]fluorobutyl tosylate	Platinum C18 EPS 5 µm 250×10 mm; acetonitrile/10 mM H_3PO_4 65/35; 5.0 ml/min; 225 nm k' = 2.5	Same plates eluted with hexane/ethyl acetate (5/1 v/v) R_f = 0.6
4-[^{18}F]fluorobenzaldehyde	Alltima C18 5 µm 250×5 mm; acetonitrile/10 mM H_3PO_4 40/60; 1.5 ml/min; 254 nm k' = 3.6	Same plates eluted with hexane/ethyl acetate (5/1 v/v) R_f = 0.8

a Conditions are listed as: column type, eluent composition; eluent flow; wavelength for absorption monitoring.

The Nanotek system consists of a Concentrator Module (CM), a Pump Module (PM) and a Reactor Module (RM). The CM was used for [^{18}F]fluoride extraction and drying (Figure 2), while PM and RM were used to mix dried [^{18}F]fluoride with precursor solution and pump the mixture through the reactor (Figure 3A). During labeling optimization, boluses of the reacted mixture were collected into Eppendorf vials for radio-TLC analysis. During automated syntheses of [^{18}F]fluoroalkyl tosylates and [^{18}F]fluorobenzaldehyde, the outflow of the reactor was transferred to the Nuclear Interface module (Figure 3B) for purification.

The CM includes a thermostated vial housing, into which a 3-ml or a 5-ml V-vial can be placed, and a low-pressure 2.5 ml syringe pump connected to a 6-way valve. The PM and RM together include three high-pressure (up to 500 psi) syringe pumps connected to 8-way bridged valves: two 0.5 ml syringe pumps on the PM and one 1.0 ml pump on the RM. The pumps of the PM are numbered P1 and P2, the pump on the RM is numbered P3. The valve ports are denoted by letters from A to H. Pump valves have reagent loops made of PEEK tubing (~400 μl volume) attached to them. In this work, the P1 loop was used to store labeling precursor, while the P3 loop was used to store dried [^{18}F]fluoride. The RM also contains a reactor unit with four thermostated reactor slots. Microfluidic reactors (up to four) are mounted on the reactor plate and inserted into the reactor slots. The reactor plate contains slots for tubing lines coming from the pumps and for the reactors themselves. Within the reactor plate, there are channels forming three-way junctions, so that reagents delivered by the pumps can be mixed and directed into the reactor. Thus, labeling precursors and dried [^{18}F]fluoride were first loaded into, respectively, P1 and P3 loops, and then pumped through the reactor (Figure 3A).

The RM also contains an 8-way distribution valve (distribution hub, DH) and three 3/2 way solenoid valves. These valves were used to govern the flow of nitrogen gas and target water in the schemes of [^{18}F]fluoride preparation on the CM.

The Nanotek system also has three semiconductor-based radioactivity detectors, which can be used to monitor radioactivity movement within the system. In this work, one detector was attached to the P3 pump loop, another one – to the vial housing of the CM module, and the third one was used to detect the delivery of the irradiated target water to the receiving V-vial. Auxiliary connection boards present in the Nanotek module allow the coupling of extra input or output devices to the system; we have connected a fourth radioactivity detector to one of the auxiliary port to monitor the absorption of purified ^{18}F-products on SPE cartridges.

The Nanotek system was controlled by a standard laptop with the 1.40 release of the Nanotek software installed. For labeling optimization work, the built-in Automatic Discovery routine was used. For [^{18}F]fluoride drying, batch synthesis and maintenance operations (such as system cleaning), custom macros were written using the coding language built-in into the software.

Before and after each synthesis, all PM and RM tubing and pumps involved in the labeling (Figure 3A) were rinsed with dry reaction solvent (MeCN of DMSO). CM pump and tubing were rinsed with MeCN/water 1/1 mixture. Tubes through which target water was supposed to flow were additionally dried by nitrogen flow.

Nuclear Interface PET Tracer Synthesizer

The Nuclear Interface module consists of a number of reagent vials connected to the thermostated reactor with tubing lines. The reactor contains a movable needle, which can be used to inject the contents of the reactor onto the HPLC column. The movement of reagents around the module is achieved by helium pressure and regulated by solenoid valves installed on the tubing lines. The module is also coupled to an HPLC system consisting of Water 510 pump and Linear UVIS 200 UV/Vis detector (radioactivity detection is done by the built-in detector in the module). Another radioactivity detector is installed near the reactor, which makes it possible to monitor the delivery of radioactivity to the reactor and its withdrawal from it.

In this work, the Nuclear Interface module was used for the HPLC purification of the ^{18}F-labeled products prepared on the Nanotek system and absorption of the purified products on the SPE cartridge. The plumbing scheme of the relevant elements of the Nuclear Interface module is shown in Figure 3B.

The Nuclear Interface module was controlled by a desktop PC with GINA Star SynChrom software installed. A macro for the purification procedure was created using the graphical user interface of the GINA Star software.

Before and after each synthesis, all tubing and vials of the Nuclear Interface module involved in the labeling (Figure 3B) were rinsed with 70% ethanol.

[^{18}F]fluoride extraction and drying

Irradiated target water was passed through the anion-exchange column (MP-1 with 25 mg sorbent or QMA Light with 100 mg sorbent) to trap the [^{18}F]fluoride. Two approaches were used to prepare [^{18}F]fluoride for labeling: conventional approach, where [^{18}F]fluoride was dried by "azeotropic distillation" (AD), and "flushing-elution" (FE) approach devoid of the azeotropic distillation step. In the AD approach, [^{18}F]fluoride was eluted from the anion-exchange column with either 2 mg K_2CO_3 and 10 mg Kryptofix 2.2.2 in 1 ml MeCN/water (9/1 v/v) or 5 mg TEAB in 1 ml methanol, then dried by tri-

ple azeotropic evaporation with MeCN at 110 °C under nitrogen flow and resolubilized in dry reaction solvent. In the FE approach, the anion-exchange column was flushed with dry MeCN, [^{18}F]fluoride was eluted with 5 mg/ml TEAB in 0.45 ml of reaction solvent mixed with tert-butanol (tBuOH) or water, and the eluate was used directly for ^{18}F-labeling.

During the optimization of labeling conditions, trapping, elution and drying of [^{18}F]fluoride was performed manually, and the vial with dry [^{18}F]fluoride solution was then connected to the F port of the P1 pump unit of the Nanotek system. For batch syntheses, both [^{18}F]fluoride approaches were automated using the Advion Nanotek LF Microfluidic Synthesis System.

Automated AD approach (Figure 2A). Irradiated target water was transferred from the "fresh [^{18}O]H_2O" vial through the trap-and-release column (QMA Light or MP-1) into the "used [^{18}O]H_2O" vial by the CM syringe (CS). Then, the SV3 solenoid valve was switched to direct the flow into the 3 ml drying vial (heated to 110 °C), and the trap-and-release column was eluted with 1 ml 5 mg/ml TEAB in methanol. Methanolic solution of [^{18}F]fluoride was added into the drying vial in 100 μl portions, with pauses to let the previous portion evaporate before the next one is added. Evaporation was accelerated by applying nitrogen flow through the vial and was monitored visually using a web-camera installed inside the hotcell. After full evaporation of methanol, 3×100 μl portions of MeCN were added into the drying vial to azeotropically evaporate residual methanol and possible traces of water. Finally, the vial was cooled, dried [^{18}F]fluoride was resolubilized in 0.45 ml dry MeCN or DMSO (the solution was pumped in and out of the loop 3 times to achieve homogeneity and enhance resolubilization).

While this protocol works with both TEAB solutions in methanol and carbonate-Kryptofix solutions in water-MeCN, only the former was used for trap-and-release column elution in batch syntheses. In short reaction runs performed within the Automatic Discovery setup, the system tolerated both bases well, but in prolonged labeling runs, the presence of potassium carbonate in the reaction mixture led to frequent clogging and ruining of the microfluidic reactors.

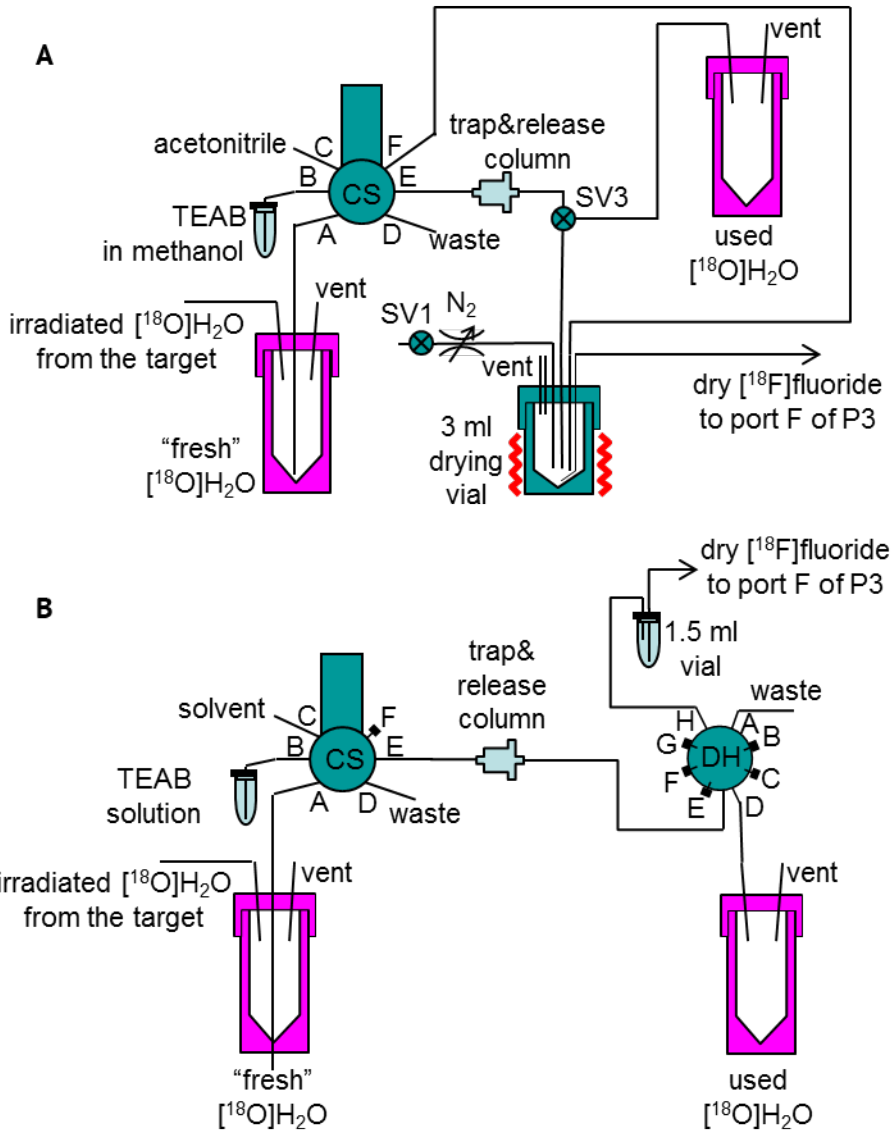

Figure 2. Plumbing schemes of the Nanotek Concentrator Module used for the preparation of [^{18}F]fluoride for labeling.

A – Plumbing scheme for the azeotropic distillation (AD) approach. B – Plumbing scheme for the flushing-elution (FE) approach.

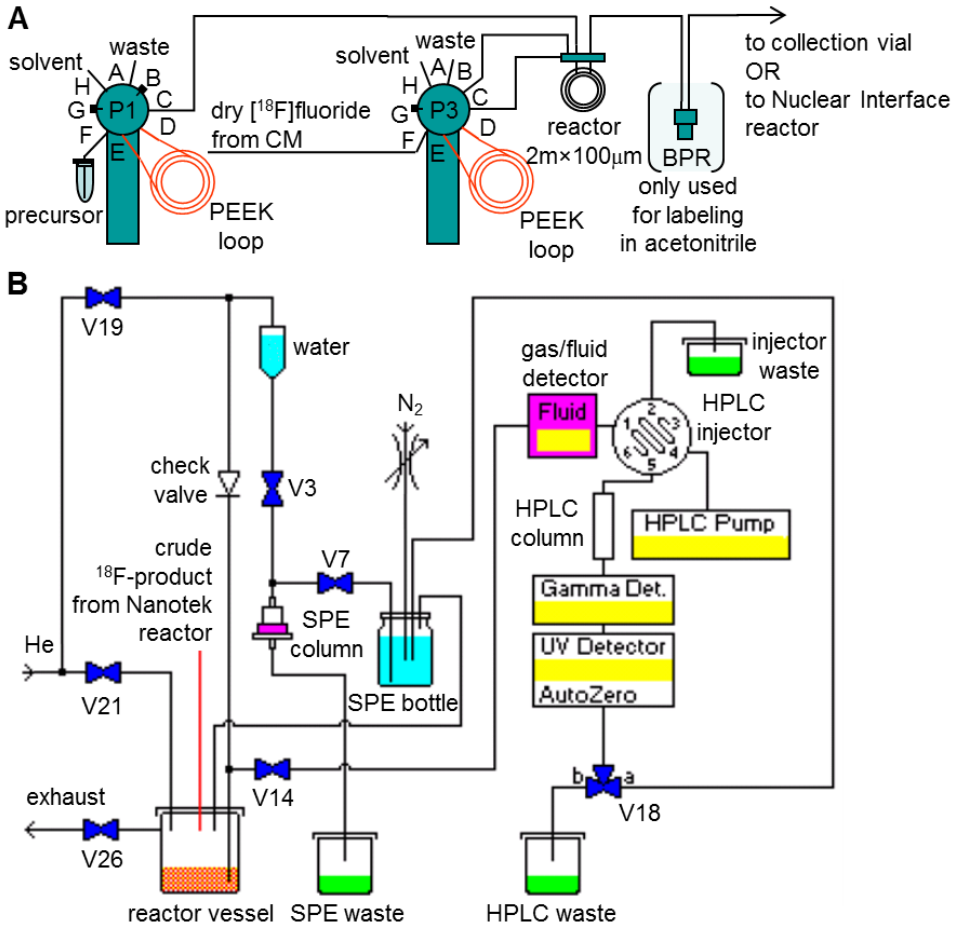

Figure 3. Simplified plumbing schemes of the Nanotek system (A) and the Nuclear Interface module (B).

Automated FE approach (Figure 2B). As in the AD approach, the first step was the trapping of the [^{18}F]fluoride on the trap-and-release column. The column was then rinsed with dry MeCN (directed into the waste by the DH valve), blown with air and eluted with 0.45 ml of 5 mg/ml TEAB in MeCN/tBuOH or DMSO/tBuOH. The tBuOH content was 50% in both cases, which corresponds to 25% tBuOH in the actual reaction mixture. Elution mixtures with other mixing ratios and/or containing water instead of tBuOH were only tried in manual optimization runs. The volume of the eluting solution (0.45 ml) had to match, with some safety margin, the volume of the

P3 reagent loop (~400 μl). Therefore, in this approach, only MP-1 columns with 25 mg sorbent were used, as QMA Light columns with 100 mg sorbent could not be efficiently eluted with such small volumes. Eluted [^{18}F]fluoride was collected at the bottom of an Eppendorf vial placed inside the (unused) V-vial employed in the AD scheme, so elution could again be monitored through the web-camera. To ensure homogeneity, the dry [^{18}F]fluoride was mixed by pumping it in and out of the loop three times.

Automatic Discovery runs on the Nanotek system

The influence of temperature, reactor residence time and co-solvent on the yields of [^{18}F]FBuTos and [^{18}F]fluorobenzaldehyde labeling was investigated using the Automatic Discovery routine of the Nanotek software. Boluses of precursor solution (10 μl) and dried [^{18}F]fluoride (10 μl) were simultaneously dispensed from the P1 and P3 loop by the corresponding pumps to achieve their mixing at 1/1 volume ratio. The speed of pumping was varied to achieve different reactor residence time of 5, 10, 20 or 60 sec. Reactor temperature was set at 90, 120, 150 or 180 °C. Co-solvent, i.e. water or tBuOH, percentage in the reaction mixture was 5%, 10% or 25% v/v (the latter – only with tBuOH). When labeling was performed in MeCN, a backpressure regulator (BPR) set to 200 psi was installed after the reactor to prevent MeCN from boiling (Figure 3A). Precursor concentration in the reaction mixture was fixed at 5 mg/ml (12.6 mM) for butanediol ditosylate ([^{18}F]FBuTos precursor) and at 2 mg/ml (6.4 mM) for trimethylammonium benzaldehyde ([^{18}F]fluorobenzaldehyde precursor). P1 reagent loop was loaded with precursor solution of double concentration, so as to achieve the designated concentration upon 1/1 mixing with [^{18}F]fluoride solution at the entrance of the microfluidic reactor. Portions of reacted mixture were collected into 0.5 ml Eppendorf vials for further analysis. Conversion of [^{18}F]fluoride to [^{18}F]FBuTos and [^{18}F]fluorobenzaldehyde was monitored by TLC on silica plates (hexane/ethyl acetate).

Automated batch synthesis of 2-[^{18}F]fluoroethyl tosylate

[^{18}F]fluoride (5–10 GBq at end of bombardment) was worked up using either AD or EF approach, as described above. The obtained solution of [^{18}F]fluoride in dry MeCN (in case of the AD approach) or MeCN/tBuOH 1/1 (v/v, in case of the EF approach) was loaded into the P3 loop of the Nanotek system. The P1 loop was loaded with 10 mg/ml 1,2-ethanediol ditosylate in dry MeCN.

Contents of both loops were then simultaneously pumped towards the reactor, which was being heated to 180 °C. The pumping speeds were adjusted so that both [^{18}F]fluoride and precursor boluses reached the entrance of the reactor simultaneously. Backpressure regulator set to 200 psi was installed at the outflow of the reactor, so pressure build-up caused by pumping also prevented the solvent inside the reactor from boiling during the heating-up phase. After that, at total speed of 96 μl/min (achieving reactor residence time of 10 s), [^{18}F]fluoride and precursor were pumped through the microfluidic reactor and into the Nuclear Interface reactor vessel (Figure 3B) with 1 ml water in it. The reactor was allowed to cool down as soon as all reagents had passed through it. Organic solution of crude [^{18}F]FEtTos arriving in the Nuclear Interface reactor vessel was mixed with water present in the vessel by bubbling helium through the mix with the aid of the needle. Then, through the same needle, crude [^{18}F]FEtTos was injected onto the HPLC column (Ultracarb ODS 10 μm 250×10 mm). The column was eluted at 5 ml/min with 45% MeCN in water, and radioactivity and 225 nm UV absorption of the eluate were monitored. The [^{18}F]FEtTos fraction (tR 8.3 min) was collected by switching the 3/2 valve V18 to direct the flow from the HPLC column into the SPE bottle containing 80 ml water. Purified [^{18}F]FEtTos was mixed with this water by bubbling nitrogen through it and then, using the pressure of the same nitrogen, the diluted solution of [^{18}F]FEtTos was forced through the SPE column (tC18 Sep-Pak pre-activated with 5 ml 40% ethanol). Finally, using helium pressure, the SPE column was rinsed with 5 ml water in the vial above the V3 valve. The SPE column with [^{18}F]FEtTos adsorbed on it was then available for further use in manual synthesis.

Automated batch synthesis of 4-[^{18}F]fluorobenzaldehyde

[^{18}F]fluorobenzaldehyde was synthesized according to the same procedure as [^{18}F]FEtTos, with the following modifications. [^{18}F]Fluoride solution for labeling was obtained in DMSO when the AD approach was used, and in DMSO/tBuOH 1/1 (v/v) when the EF approach was used. Precursor solution loaded into P1 loop was 4 mg/ml trimethylammoinum benzaldehyde in DMSO. No backpressure regulator was installed on the line connecting the outflow of the Nanotek microfluidic reactor and the reactor vessel of the Nuclear Interface module. HPLC purification conditions were: Ultracarb ODS 10 μm 250×10 mm column, elution at 5 ml/min with 40% MeCN in water, t_R of [^{18}F]fluorobenzaldehyde 6.9 min. Purified [^{18}F]fluorobenzaldehyde was adsorbed on Oasis HLB column (with no pre-activation).

Analysis of efficiency of radioactivity use

In order to assess the efficiency of radioactivity transfer between different steps of the automated synthesis procedures developed in this work and pinpoint "bottlenecks", the amounts of radioactivity found in different wastes generated by the synthesis procedure were measured and corrected for decay. This refers to radioactivity remaining in extracted target water, eluted trap-and-release columns, used [^{18}F]fluoride drying vials, radioactivity rinsed from the Nanotek tubing lines etc.

RESULTS

Optimization of labeling conditions for [^{18}F]FBuTos and [^{18}F]fluorobenzaldehyde. Co-solvent influence

The influence of temperature, reaction time and the presence of water or tBuOH on the conversion yields of [^{18}F]fluoride to 4-[^{18}F]fluorobutyl tosylate ([^{18}F]FBuTos) and 4-[^{18}F]fluorobenzaldehyde [^{18}F]fluorobenzaldehyde is illustrated in Tables 2 and 3, respectively.

Presence of water in the reaction mixture slowed down formation of both [^{18}F]FBuTos and [^{18}F]fluorobenzaldehyde. At 180 °C, the highest temperature investigated, only 27% of ^{18}F-radioactivity corresponded to [^{18}F]FBuTos after 5 sec reaction in the presence of 5% water v/v, compared to 84% in "dry" conditions. For [^{18}F]fluorobenzaldehyde, the presence of 5% water v/v decreased the ^{18}F-fluorination yield to 22%, compared to 70% with azeotropically dried [^{18}F]fluoride. At lower temperatures (<120 °C) ^{18}F-fluorination yields for both [^{18}F]FBuTos and [^{18}F]fluorobenzaldehyde did not exceed 15% even at 60 sec reaction time.

The presence of tBuOH decreased ^{18}F-fluorination yields at temperatures below or equal to 120 °C in a concentration-dependent manner. For [^{18}F]FBuTos, ^{18}F-fluorination yield over 60 sec at 120 °C was 80% with azeotropically dried [^{18}F]fluoride, 41% with 5% v/v tBuOH, 29% with 10% v/v tBuOH and 16% with 25% v/v tBuOH. For [^{18}F]fluorobenzaldehyde, respective figures were 57%, 35%, 29% and 14%. However, at temperatures above or equal to 150 °C tBuOH had little effect on ^{18}F-fluorination yields even at 25% v/v. [^{18}F]FBuTos yield over 10 sec at 180 °C was 83% with "dry" [^{18}F]fluoride and 76% with 25% tBuOH. [^{18}F]fluorobenzaldehyde yield in the same conditions was 75% with "dry" [^{18}F]fluoride and 78% in 25% tBuOH.

Optimization of "dry" [^{18}F]fluoride elution from trap-and-release column

Efficiency of [^{18}F]fluoride elution from MP-1 cartridge was compared for TEAB solutions in MeCN/water, MeCN/tBuOH and DMSO/tBuOH mixtures with varying water or tBuOH percentages. Both co-solvents increased the efficiency of [^{18}F]fluoride elution as their percentage rose (Figure 4). Moreover, in MeCN-based mixtures with co-solvent percentages of 20% v/v or less, tBuOH was even more effective in eluting [^{18}F]fluoride than water. For example, 450 μl (approximately equal to Nanotek reagent loop volume) of

90/10 and 80/20 MeCN/tBuOH mixtures with 5 mg/ml TEAB eluted respectively 73% and 89% trapped [^{18}F]fluoride, compared to 47% and 63% for MeCN/water mixtures with same mixing ratios.

Automated batch syntheses of [^{18}F]FEtTos and [^{18}F]fluorobenzaldehyde

For [^{18}F]fluoroalkyl tosylates as well as for 4-[^{18}F]fluorobenzaldehyde, the temperature of 180 °C and the reactor residence time of 10 sec were chosen as optimal parameters for scaling up to batch synthesis. While [^{18}F]fluorobutyl tosylate was used during optimization of S_N2 ^{18}F-fluorination conditions, the scale-up focused on its shorter homolog, [^{18}F]fluoroethyltosylate ([^{18}F]FEtTos), because the latter was more relevant to PET tracer development.

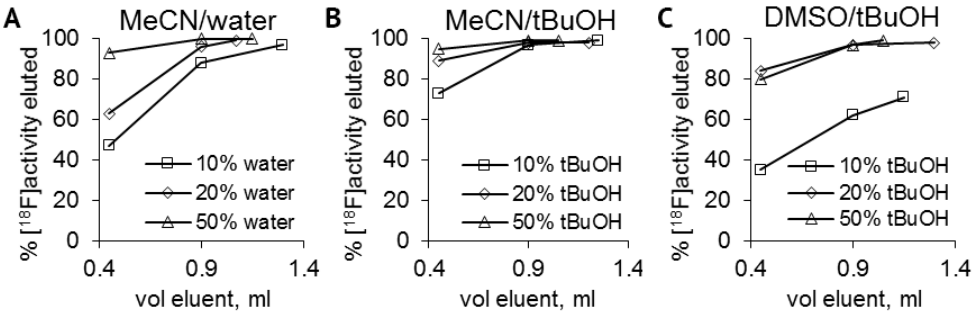

Figure 4. Efficiency of [^{18}F]fluoride elution from MP-1 cartridges with 5 mg/ml TEAB in MeCN/water (A), MeCN/tBuOH (B) and DMSO/tBuOH (C) mixtures.
All values are based on single determinations.

Scaled-up automated batch syntheses of [^{18}F]fluorobenzaldehyde and [^{18}F]FEtTos were carried out with [^{18}F]fluoride prepared via both AD and FE (azeotropic distillation-free) protocols (see Methods). Based on the results of trap-and-release column elution tests, the content of tBuOH in the TEAB solution used for the elution of trap-and-release column in the FE protocol was set to 50% (resulting in 25% tBuOH in the final reaction mixtures).

The syntheses lasted 50–60 min from end-of-bombardment. [^{18}F]Fluoride preparation phase lasted 15 min with the AD protocol and 5 min with the FE protocol. Labelling step (with nominal reactor residence time of 10 s) lasted 8 min. Different phases of the developed automated batch synthesis protocol are compared by their length in Figure 5.

Table 2. Radiochemical yields (non-isolated) of [^{18}F]FBuTos in relation to temperature, time and co-solvent content.

Co-solvent content, % vol	Temperature, °C	Water as co-solvent				tBuOH as co-solvent			
		Reactor residence time, sec				Reactor residence time, sec			
		5	10	20	60	5	10	20	60
0%[a] (neat MeCN)	90	n.i.[b]	n.i.	n.i.	n.i.	n.i.	n.i.	n.i.	n.i.
	120	65	76	79	81	65	76	79	81
	150	81	80	80	81	81	80	80	81
	180	84	83	82	80	84	83	82	80
5%	90	<1	<1	<1	1	<1	1	2	4
	120	1	1	1	5	6	12	29	41
	150	6	10	12	33	27	47	68	66
	180	27	48	62	70	62	60	61	58
10%	90	<1	<1	<1	<1	<1	1	1	3
	120	<1	<1	1	2	4	8	16	29
	150	2	3	4	12	19	35	58	65
	180	13	22	19	41	61	69	67	62
25%	90				n.i.	<1	<1	1	3
	120					3	4	11	16
	150					19	33	47	65
	180					66	76	71	72

All labeling was performed on the Nanotek system using Automatic Discovery routine. Co-solvent content in the final reaction mixture (precursor + [^{18}F]fluoride) is shown. [^{18}F]fluoride was prepared via the "flushing-elution" approach and TEAB was used as phase transfer catalyst in all experiments except no co-solvent experiments (see below). Butanediol ditosylate concentration was 5 mg/ml (13.3 mM) in all experiments. Radiochemical yields were determined by radio-TLC and are single determinations.

a In "0% co-solvent" experiments, potassium-Kryptofix was used as phase-transfer catalyst and [^{18}F]fluoride was dried by azeotropic distillation. Radiochemical yields shown in water and tBuOH columns for no co-solvent experiments represent the same dataset and are averages from 3 independent repetitions.

b Not investigated.

Table 3. Radiochemical yields (non-isolated) of [^{18}F]fluorobenzaldehyde in relation to temperature, time and co-solvent content.

Co-solvent content, % vol	Temperature, °C	Water as co-solvent				tBuOH as co-solvent			
		Reactor residence time, sec				Reactor residence time, sec			
		5	10	20	60	5	10	20	60
0%[a] (neat DMSO)	90	n.i.[b]	n.i.	n.i.	n.i.	n.i.	n.i.	n.i.	n.i.
	120	18	19	34	57	18	19	34	57
	150	45	45	60	66	45	45	60	66
	180	70	75	82	75	70	75	82	75
5%	90	3	6	7	8	1	1	3	10
	120	5	3	2	2	8	12	17	35
	150	11	8	9	13	40	66	68	63
	180	22	24	33	38	78	76	73	57
10%	90				n.i.	1	3	12	30
	120					13	13	19	29
	150					47	56	68	60
	180					80	81	65	68
25%	90				n.i.	<1	<1	2	8
	120					3	5	8	14
	150					27	38	59	60
	180					76	78	71	66

All labeling performed on the Nanotek system using Automatic Discovery routine. Co-solvent content in the final reaction mixture (precursor + [^{18}F]fluoride) is shown. TEAB used as phase transfer catalyst in all experiments. Trimethylammonium benzaldehyde concentration was 2 mg/ml (6.4 mM) in all experiments. Radiochemical yields were determined by radio-TLC and are single determinations.

a In no co-solvent experiments, [^{18}F]fluoride was dried by azeotropic distillation. Radiochemical yields shown in water and tBuOH columns for no co-solvent experiments represent the same dataset.

b Not investigated.

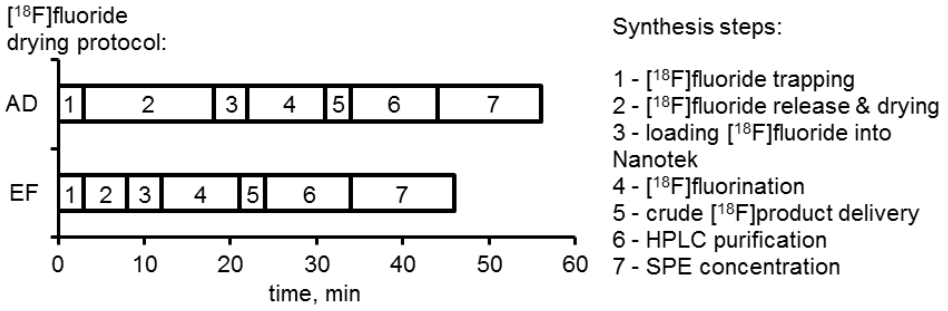

Figure 5. Length of different phases of automated microfluidic batch synthesis protocol used to prepare [^{18}F]FEtTos and [^{18}F]fluorobenzaldehyde.

Losses of radioactivity in different phases of [^{18}F]FEtTos and [^{18}F]fluorobenzaldehyde synthesis are presented in Table 4. The most inefficient synthesis step was [^{18}F]fluoride drying and loop loading in schemes with azeotropic distillation. In the case of [^{18}F]FEtTos labeling in MeCN, 39±15% of radioactivity eluted from trap-and-release cartridge was lost during the drying and loop loading step, and in the case of [^{18}F]fluorobenzaldehyde labeling in DMSO, the losses were 49±13%, mainly because [^{18}F]fluoride got stuck to the drying vessel wall. Without azeotropic distillation, <5% of eluted radioactivity was lost in both cases. Elimination of azeotropic distillation also decreased the losses of radioactivity inside microfluidic module: from 27±7% to 21±5% for [^{18}F]FEtTos labeling and from 39±20% to 24±4% for [^{18}F]fluorobenzaldehyde labeling. Losses at other steps were similar for the two products, with and without azeotropic distillation, except in azeotropic distillation-free [^{18}F]fluorobenzaldehyde syntheses, where on average 89±1% of starting ^{18}F-radioactivity in target water was trapped on the trap-and-release column.

Automated batch procedures produced [^{18}F]FEtTos in 78±16% (n=6) non-isolated and 28±11% (n=6) isolated yield with azeotropic distillation, and in 85±5% (n=3) non-isolated and 53±9% (n=2) isolated yield with flushing-elution protocol. [^{18}F]fluorobenzaldehyde was obtained in 77±13% (n=5) non-isolated and 14±6% (n=5) isolated yield with azeotropic distillation, and in 73±14% (n=4) non-isolated and 28±11% (n=6) isolated yield with flushing-elution protocol. Radiochemical purity of HPLC-purified and SPE concentrated products was >97%. Molar radioactivities of [^{18}F]FEtTos and [^{18}F]fluorobenzaldehyde were 30–90 GBq/μmol and 7–18 GBq/μmol, respectively.

Table 4. Efficiency of radioactivity transfer between different steps of automated [^{18}F]FEtTos and [^{18}F]fluorobenzaldehyde syntheses.

Product	[^{18}F]FEtTos		[^{18}F]fluorobenzaldehyde		Formula for radioactivity transfer efficiency calculation[a]
Conditions	13.5 mM EDT, 5 mg/ml TEAB, 10 sec at 180 °C, MeCN		6.4 mM TBCHO, 5 mg/ml TEAB, 10 sec at 180 °C, DMSO		
[^{18}F]Fluoride preparation approach Step	AD	FE	AD	FE	
[^{18}F]F$^-$ adsorption on trap-and-release column	100±0% (2)	99±1% (4)	98±3% (3)	89±1% (2)	A_1/A_0
[^{18}F]F$^-$ elution from trap-and-release column	99±1% (2)	98±3% (4)	99±1% (3)	98±1% (3)	A_2/A_1
[^{18}F]F$^-$ drying and loop loading[b]	61±15% (8)	97±0% (2)	51±13% (6)	95±1% (3)	$(A_3-D)/A_2$
^{18}F-fluorination yield	78±16% (6)	85±5% (3)	77±13% (5)	73±14% (4)	$A_4/A_3=Y$[c]
crude ^{18}F-product delivery	73±7% (8)	79±5% (2)	61±20% (5)	76±4% (3)	$A_5/(A_3-D)$
HPLC purification	79±8% (8)	87±2% (2)	76±7% (5)	88±4% (3)	A_6/A_5
SPE concentration	96±5% (6)	98±1% (2)	88±1% (4)	98±1% (2)	A_7/A_6
isolated product yield	**28±11% (6)**	**53±9% (*n*=2)**	**14±6% (*n*=5)**	**37±7% (*n*=2)**	A_7/A_0

(continued on the next page)

Table 4 (continuation). Efficiency of radioactivity transfer between different steps of automated [^{18}F]FEtTos and [^{18}F]fluorobenzaldehyde syntheses.

Efficiencies are presented as means±SD. For each determination, number of estimates used for averaging is given in parentheses. Not all parameters were measured in every experiment, so numbers of estimates differ between steps. Radioactivity loss at each step can be calculated as 100% – Efficiency.

a Abbreviations used: A_0 – radioactivity delivered from cyclotron, A_1 – radioactivity absorbed on the trap-and-release column, A_2 – radioactivity extracted from the trap-and-release column, A_3 – radioactivity taken up into the P3 reagent loop, A_4 – radioactivity converted into ^{18}F-product, A_5 – product delivered into the HPLC vial, A_6 – HPLC-purified product, A_7 – purified product adsorbed on the SPE cartridge, D – discrepancy of the radioactivity balance; $D = A_0 - A_8 - \Sigma$ (all radioactivity losses).

b calculations assume that radioactivity that could not be accounted in radioactivity balance calculations (D) was lost primarily during [^{18}F]F^- drying and loop loading, probably due to the formation and evaporation of [^{18}F]HF.

c ^{18}F-fluorination yields (Y) for [^{18}F]FEtTos or [^{18}F]fluorobenzaldehyde were determined by radio-TLC, using radioactivity recovered from Nuclear Interface reactor vessel.

DISCUSSION

This work aimed to optimize [^{18}F]fluoride preparation for microfluidic nucleophilic ^{18}F- fluorination of aliphatic and aromatic substrates by eliminating the azeotropic distillation step, to implement the optimized protocols in the automated microfluidic synthesis procedures for [^{18}F]fluoroalkyl tosylates and [^{18}F]fluorobenzaldehyde and to investigate the efficiency of ^{18}F-radioactivity use at different steps of these procedures.

The compounds chosen as model products for the current study were [^{18}F]fluoroalkyl tosylates (4-[^{18}F]fluorobutyl tosylate and 2-[^{18}F]fluoroethyl tosylate in the first place) and 4-[^{18}F]fluorobenzaldehyde. The synthesis of [^{18}F]fluoroalkyl tosylates from azeotropically dried [^{18}F]fluoride, both in conventional and microfluidic conditions, has been thoroughly investigated both by us and by other groups [6,12]. Moreover, [^{18}F]fluoroalkyl tosylate synthesis is a good example of S_N2 ^{18}F-fluorination. 4-[^{18}F]Fluorobenzaldehyde, meanwhile, is a useful building block for the creation of 4-[^{18}F]fluorobenzylamino moiety and a good example of S_NAr ^{18}F-fluorination. Finally, both [^{18}F]fluoroalkyl tosylates and [^{18}F]fluorobenzaldehyde are used as building blocks for PET radioligand development both in our group [16] (including the research described in the current thesis) and elsewhere [7,20]. Therefore, automation and optimization of their synthesis provided both theoretical insights and practical benefits.

Precursor concentration in 4-[^{18}F]fluorobenzaldehyde preparation protocol was chosen to be 2-fold lower that in the preparation protocol for [^{18}F]fluoroalkyl tosylates (6.4 mM vs 13.3–13.5 mM). The reason was that the triflate precursor for [^{18}F]fluorobenzaldehyde contained ^{19}F-fluorine, which could take part in isotopic exchange reaction with [^{18}F]fluoride used for radiolabeling. Nevertheless, molar radioactivity of [^{18}F]fluorobenzaldehyde turned out to be 5–10 fold lower than that of [^{18}F]FEtTos, despite similar synthesis times and amounts of radioactivity with which the syntheses were started.

Elimination of azeotropic distillation from the radiosynthesis protocol

Drying by azeotropic distillation is known to be a time-consuming procedure that leads to losses of [^{18}F]fluoride radioactivity (through deposition on distillation vessel walls and incomplete resolubilization) and limits the isolated yield of any radiosynthesis based on nucleophilic fluorination. There-

fore, getting rid of this distillation step is a goal that often comes up in the development of radiosyntheses with fluorine-18. Lots of azeotropic distillation-free approaches of [^{18}F]fluoride preparation are known, but many of them require either sophisticated equipment [21] or reagents [22,23]. Good results were reported for organic solutions of KOH-Kryptofix [24], but potassium salts led to frequent clogging of the Nanotek reactor, both in our hands and in reports of others [15]. There are reports of successful microfluidic nucleophilic ^{18}F-labeling [5,25], where [^{18}F]fluoride was introduced into the reaction in irradiated [^{18}O]water without any preparation, but whatever the real versatility and reproducibility of such approach, it is not applicable for batch syntheses because of the high volumes that would need to be reacted.

The method used in this work combined two approaches: (1) replacing potassium carbonate-Kryptofix combination with tetraethylammonium bicarbonate to avoid microreactor clogging [15] and (2) using a tertiary alcohol (tBuOH) as co-solvent to enhance [^{18}F]fluoride ion solvation without impacting its nucleophilicity as much as it happens with water [13,14]. The improvement of [^{18}F]fluoride solvation with the addition of tBuOH was clearly visible in MP- 1 elution studies (Figure 4), where mixtures with greater tBuOH content eluted [^{18}F]fluoride more efficiently. Water also increased the efficiency of [^{18}F]fluoride elution, but it greatly slowed down both [^{18}F]FBuTos (S_N2) ^{18}F-fluorination and [^{18}F]fluorobenzaldehyde (S_NAr) ^{18}F-fluorination reactions at all temperatures investigated, decreasing the yields compared to no co-solvent conditions (Tables 2 and 3). In contrast, while tBuOH did slow down both ^{18}F-fluorination reactions at temperatures of 90 °C and 120 °C, it had little effect on the yields at temperatures of 150 °C and 180 °C. Scaled-up batch syntheses confirmed this finding: ^{18}F-fluorination yields in co-solvent-free conditions and in the presence of 25% tBuOH were very close to each other for both [^{18}F]FEtTos (78±16% co-solvent-free, 85±5% with tBuOH) and [^{18}F]fluorobenzaldehyde (77±13% co-solvent-free, 74±14% with tBuOH). These results demonstrate that our method is sufficiently versatile to achieve efficient radiofluorination of both aliphatic and aromatic substrates.

Two recently published reports describe the successful use of TEAB solutions in water-organic mixtures for [^{18}F]fluoride elution from QMA and MP-1 columns with subsequent ^{18}F- fluorinations in conventional setup [26,27]. Both groups successfully performed S_N2 ^{18}F- fluorinations with TEAB as phase transfer catalyst and up to 5% water in the reaction mixtures, and one of the groups performed S_NAr ^{18}F-fluorinations as well. These results imply that

azeotropic distillation-free ^{18}F-fluorinations can be successfully carried out even using water as co-solvent, but our findings suggest that the product yields could probably be even better if tBuOH were used instead.

Radiosynthesis automation on the Nanotek microfluidic synthesis system

The small volume of microreactors enables low expenses of reagents per test reaction run. Tolerance of microreactors to high pressure means that reaction mixture can be heated to temperatures high above the boiling point of the solvent used. Due to the low overall heat capacity and high surface-to-volume ratio, the designated temperature is reached instantaneously, which results in dramatically decreased reaction times compared to conventional setup. These factors give microchannel systems a lot of flexibility and allow quick optimization of the labeling conditions for the product being investigated. However, scaling up the discovered optimal conditions to batch procedures is connected with a number of important drawbacks.

First, the total volume of [^{18}F]fluoride and precursor solutions (hundreds of microliters) does not fit into the microfluidic reactor (a few tens of microliters) at once, so reagents have to be pumped through the reactor portion by portion. For instance, reacting a test bolus of 20 μl for 60 sec by pumping it through a 2 m Nanotek reactor takes 2.25 min, but reacting 800 μl (total volume of [^{18}F]fluoride and precursor loops in our setup) under the same conditions would take 52.25 min. In our batch synthesis procedure, with effective labeling time of 10 sec, 8 min were needed to pump all reagents through the reactor. Therefore, in batch syntheses, the use of microfluidic setup does not decrease total labeling time compared to conventional setup. In order to cut total labeling time further, the degree of [^{18}F]fluoride concentration before labeling has to be enhanced.

Second, in microfluidic labeling, the drying of [^{18}F]fluoride and the actual labeling takes place in different locations, and the transfer of radioactivity incurs extra losses, decreasing overall isolated yield. The biggest losses are connected with azeotropic distillation of [^{18}F]fluoride, but some radioactivity is also retained in the loops and tubing lines of the microfluidic system. In our work we observed both types of radioactivity loss, and as a result, the isolated yields of [^{18}F]FEtTos and [^{18}F]fluorobenzaldehyde obtained via automated batch protocols with azeotropic distillation were quite low: 28±11% and 14±6%, respectively.

However, eliminating azeotropic distillation and adding tBuOH as co-solvent almost doubled the isolated yields of [^{18}F]FEtTos (to 53±9%) and [^{18}F]fluorobenzaldehyde (to 37±7%). Such yields are comparable to isolated yields of the same compounds prepared in our laboratory via manual procedures with azeotropic distillation (30–40% for [^{18}F]FEtTos and 40–60% for [^{18}F]fluorobenzaldehyde, see Chapters 4 and 5). The observed increase in isolated yields was not the consequence of improved conversion of [^{18}F]fluoride to products, but of improved efficiency of ^{18}F-radioactivity transfer through consecutive steps of the synthesis procedure. Switching from AD to FE protocol for [^{18}F]fluoride preparation decreased the losses during [^{18}F]fluoride radioactivity transfer from the drying step to the labeling step from 39±15% to 3±0% for [^{18}F]FEtTos labeling and from 49±13% to 5±1% for [^{18}F]fluorobenzaldehyde labeling. Losses during radioactivity transfer from the labeling step to the purification step in the same syntheses were also decreased, respectively, from 27±7% to 21±5% and from 39±20% to 24±4%. These results highlight the usefulness of azeotropic distillation-free schemes.

Even if automated batch microfluidic syntheses do not provide advantage in synthesis time or isolated yields of the product compared to manual procedures, they still have an advantage in decreasing personnel exposure to radioactivity and enabling the use of higher starting amounts of radioactivity, as is the case for any automated procedures including those implemented on conventional synthesis modules. [^{18}F]FEtTos and [^{18}F]fluorobenzaldehyde obtained by automated synthesis procedures developed in this work were successfully used as building blocks for the preparation of candidate PET tracers, including ^{18}F-labeled aminomethylchromanes described in Chapters 3–5 of the current thesis and ^{18}F-labeled pyrazolo-triazolo-pyrimidines [28] for the imaging of adenosine receptors in the central nervous system.

CONCLUSION

We have demonstrated that both S_N2 and S_NAr ^{18}F-fluorination can be carried out in mixtures of tBuOH and polar aprotic solvents inside the microfluidic reactor using tetraethylammonium bicarbonate as phase transfer agent. Substituting the flushing-elution procedure of [^{18}F]fluoride preparation for conventional azeotropic distillation increased the efficiency of [^{18}F]fluoride use and reduced synthesis time. Our findings are corroborated by the more recent reports of successful ^{18}F-fluorinations performed in water-containing solutions of tetraethylammonium bicarbonate under conventional conditions, and suggest that switching from water to tertiary alcohols may increase the yields of ^{18}F-labeled radiopharmaceuticals even further. We have also successfully automated the syntheses of 4-[^{18}F]fluorobenzaldehyde and 2-[^{18}F]fluoroethyl tosylate, ^{18}F-synthons relevant for our research work, implementing the developed azeotropic distillation-free approach to [^{18}F]fluoride preparation.

REFERENCES

1. Watts P, Pascali G, Salvadori PA. Positron Emission Tomography Radiosynthesis in Microreactors. J. Flow Chem. 2012;2:37–42.

2. Pascali G, Watts P, Salvadori PA. Microfluidics in radiopharmaceutical chemistry. Nucl. Med. Biol. 2013;40:776–87.

3. Gaja V, Gómez-Vallejo V, Cuadrado-Tejedor M, Borrell JI, Llop J. Synthesis of ^{13}N-labeled radiotracers by using microfluidic technology. J. Label. Compd. Radiopharm. 2012;55:332–8.

4. Liang SH, Collier TL, Rotstein BH, Lewis R, Steck M, Vasdev N. Rapid microfluidic flow hydrogenation for reduction or deprotection of ^{18}F-labeled compounds. Chem. Commun. (Camb). 2013;49:8755–7.

5. Chun J-H, Telu S, Lu S, Pike VW. Radiofluorination of diaryliodonium tosylates under aqueous–organic and cryptand-free conditions. Org. Biomol. Chem. 2013;11:5094.

6. Pascali G, Nannavecchia G, Pitzianti S, Salvadori PA. Dose-on-demand of diverse [^{18}F]-fluorocholine derivatives through a two-step microfluidic approach. Nucl. Med. Biol. Elsevier Inc.; 2011;38:637–44.

7. Dahl K, Schou M, Halldin C. Radiofluorination and reductive amination using a microfluidic device. J. Label. Compd. Radiopharm. 2012;55:455–9.

8. Bois F, Gallezot J-D, Zheng M-Q, Lin S-F, Esterlis I, Cosgrove KP, et al. Evaluation of [^{18}F]-(–)-norchlorofluorohomoepibatidine ([^{18}F]-(–)-NCFHEB) as a PET radioligand to image the nicotinic acetylcholine receptors in non-human primates. Nucl. Med. Biol. Elsevier Inc.; 2015;42:570–7.

9. Liang SH, Yokell DL, Normandin MD, Rice PA, Jackson RN, Shoup TM, et al. First human use of a radiopharmaceutical prepared by continuous-flow microfluidic radiofluorination: Proof of concept with the tau imaging agent [^{18}F]T807. Mol. Imaging. 2014;13:1–5.

10. Liang SH, Yokell DL, Jackson RN, Rice PA, Callahan R, Johnson KA, et al. Microfluidic continuous-flow radiosynthesis of [^{18}F]FPEB suitable for human PET imaging. Medchemcomm. 2014;5:432–5.

11. Neumann KD, Qin L, Vavere AL, Shen B, Miao Z, Chin FT, et al. Efficient automated syntheses of high specific activity 6-[^{18}F]fluorodopamine using a diaryliodonium salt precursor. J. Label. Compd. Radiopharm. 2016;59:30–4.

12. Shalgunov V, de Vries EFJ, Dierckx RAJO, Elsinga PH. Vial-based and microfluidic synthesis of 4-[^{18}F]fluorobutyl tosylate – a comparative study. 16th Eur. Symp. Radiopharm. Radiopharm. 2012.

13. Kim DW, Ahn D-S, Oh Y-H, Lee S, Kil HS, Oh SJ, et al. A new class of S_N2 reactions catalyzed by protic solvents: Facile fluorination for isotopic labeling of diagnostic molecules. J. Am. Chem. Soc. 2006;128:16394–7.

14. Aerts J, Lemaire C, Lignon S, Luxen A, Morelle J-L, Philippart G, et al. Method for the elution of [^{18}F]fluoride trapped on an anion-exchange phase in a form suitable for efficient radiolabeling without any evaporation step. 2008.

15. Reed CD, Launay GG, Carroll MA. Evaluation of tetraethylammonium bicarbonate as a phase-transfer agent in the formation of [^{18}F]fluoroarenes. J. Fluor. Chem. Elsevier B.V.; 2012;143:231–7.

16. Khanapur S, Paul S, Shah A, Vatakuti S, Koole MJB, Zijlma R, et al. Development of ^{18}F-Labeled Pyrazolo[4,3-e]-1,2,4- triazolo[1,5-c]pyrimidine (SCH442416) Analogs for the Imaging of Cerebral Adenosine A_{2A} Receptors with Positron Emission Tomography. J. Med. Chem. 2014;57:6765–80.

17. Wilson AA, Dannals RF, Ravert HT, Wagner HN. Reductive amination of [^{18}F]fluorobenzaldehydes: Radiosyntheses of 2-[^{18}F]- and 4-[^{18}F]fluorodexetimides. J. Label. Compd. Radiopharm. 1990;28:1189–99.

18. van Wieringen J-P, Shalgunov V, Janssen HM, Fransen PM, Janssen AGM, Michel MC, et al. Synthesis and Characterization of a Novel Series of Agonist Compounds as Potential Radiopharmaceuticals for Imaging Dopamine $D_{2/3}$ Receptors in Their High-Affinity State. J. Med. Chem. 2014;57:391–410.

19. Kämäräinen E-L, Kyllönen T, Airaksinen A, Lundkvist C, Yu M, Någren K, et al. Preparation of [^{18}F]β-CFT-FP and [^{11}C]β-CFT-FP, selective radioligands for visualisation of the dopamine transporter using positron emission tomography (PET). J. Label. Compd. Radiopharm. 2000;43:1235–44.

20. Wadsak W, Mien L-K, Ettlinger DE, Eidherr H, Haeusler D, Sindelar K-M, et al. [^{18}F]Fluoroethylations: different strategies for the rapid translation of ^{11}C-methylated radiotracers. Nucl. Med. Biol. 2007;34:1019–28.

21. Sadeghi S, Liang V, Cheung S, Woo S, Wu C, Ly J, et al. Reusable electrochemical cell for rapid separation of [^{18}F]fluoride from [^{18}O]water for flow-through synthesis of ^{18}F-labeled tracers. Appl. Radiat. Isot. 2013;75:85–94.

22. Lemaire CF, Aerts JJ, Voccia S, Libert LC, Mercier F, Goblet D, et al. Fast production of highly reactive no-carrier-added [^{18}F]fluoride for the labeling of radiopharmaceuticals. Angew. Chem. Int. Ed. Engl. 2010;49:3161–4.

23. Aerts JJ, Voccia S, Lemaire C, Giacomelli F, Goblet D, Thonon D, et al. Fast production of highly concentrated reactive [^{18}F] fluoride for aliphatic and aromatic nucleophilic radiolabeling. Tetrahedron Lett. Elsevier Ltd; 2010;51:64–6.

24. Wessmann SH, Henriksen G, Wester H-J. Cryptate mediated nucleophilic ^{18}F-fluorination without azeotropic drying. Nuklearmedizin. 2011;50:1–8.

25. Pascali G, Del Carlo S, Saccomanni G, Manera C, Macchia M, Salvadori P. Use of non-azeotropically dried complex in microfluidic radiofluorinations. J. Nucl. Med. . 2012;53:578.

26. Brichard L, Aigbirhio FI. An efficient method for enhancing the reactivity and flexibility of [^{18}F]fluoride towards nucleophilic substitution using tetraethylammonium bicarbonate. European J. Org. Chem. 2014;2014:6145–9.

27. Inkster J, Akurathi V, Chen Y, Sromek A, Neumeyer J, Packard A. ^{18}F chemistry without azeotropic distillations: tetraethylammonium salts as combined anion exchange reagents and phase transfer catalysts. J. Nucl. Med. . 2016;57:328.

28. Shalgunov V, de Vries EFJ, Dierckx RAJO, Elsinga PH. Development and automation of multi-step in situ microfluidic ^{18}F-labeling procedures using a combination of Advion Nanotek and Nuclear Interface modules. Q. J. Nucl. Med. Mol. Imaging. 2014;58:61.

Chapter 7

Summary

Motivation and aim of the work

Dopamine is an important neurotransmitter involved in the regulation of numerous functions of the brain. Alterations of central dopamine signaling are thought to underlie movement disorders, cognitive disorders and addiction [1–7]. In the brain, dopamine binds to receptors which belong to the G-protein coupled receptor (GPCR) superfamily. Dopamine receptors belonging to D_2 and D_3 subtypes ($D_{2/3}$) have received a lot of attention in neuroscience, and, of all neuroreceptors, have been most thoroughly investigated by non-invasive positron emission tomography (PET) imaging [8].

In vitro data show that GPCRs (including $D_{2/3}$) exist in states of high- and low affinity for the agonists (including dopamine itself), depending on whether G-proteins are bound to them or not. Antagonists do not distinguish between these two affinity states. Because the high-affinity state is a subset of receptors to which G-proteins are pre-coupled, it arguably can be thought of as the functional subpopulation of receptors [9,10].

By virtue of selective binding to this "functional" subset of receptors, agonist may be superior to antagonist tracers in such applications as neurotransmitter release measurement and agonist drug occupancy studies. Also, the use of agonist tracers may improve our understanding of the pathogenesis of neuropsychiatric disorders presumably caused by dysregulation of the relative abundance of the high-affinity state and possibly facilitate the diagnosis of these disorders.

Chapter 2 discusses the concept of the high-affinity state and potential advantages of agonist tracers over antagonist tracers for the imaging of neuroreceptors belonging to the GPCR family. It also reviews experimental paradigms aiming to demonstrate these advantages and experimental evidence gathered using such paradigms. Although it is doubtful whether $D_{2/3}$ agonist tracers really image a subset of all receptors recognized by $D_{2/3}$ antagonist tracers, in one application, measurement of changes in intrasynaptic dopamine levels, $D_{2/3}$ agonist tracers are indeed superior to $D_{2/3}$ antagonist tracers.

A common liability of all $D_{2/3}$ agonist PET tracers available for use in humans at the time of the initiation of this work was the isotope they were labeled with, namely carbon-11. The short half-life of carbon-11 (20.4 min) restricts the use of ^{11}C-labeled tracers to institutions with on-site cyclo-

trons. Fluorine-18-labeled tracers are much better suited for widespread use, because the longer half-life of fluorine-18 (109.8 min) makes it possible to deliver the radiopharmaceutical to numerous imaging institutions from a single production hub.

This work aimed to develop and evaluate fluorine-18-labeled agonist radiopharmaceuticals that could be used for the imaging of the functional state of dopamine $D_{2/3}$ receptors in humans.

Design of candidate compounds

At the time that this work was initiated, the most popular scaffolds for the development of $D_{2/3}$ agonist PET tracers were naphtoxazine, apomorphine and 2-aminotetraline scaffolds (see [11] and Figure 1). Naphtoxazine and apomorphine-derived radioligands with the ^{18}F-label introduced into one of the substituents at the main amino nitrogen atom were not successful [12,13]. One ^{18}F-labeled 2-aminotetraline derivative, capable of visualizing $D_{2/3}$ receptors in the brain with a moderate signal-to-noise ratio, was reported [14], but there did not appear to be a lot of room for further optimization, as similar compounds with somewhat more complex structures had inferior imaging characteristics [15,16]. Therefore, the decision was taken to develop tracers "from scratch" instead of further modifying the structures of existing ^{11}C-labeled tracers. An additional benefit of this decision was that it provided the opportunity to patent and license the newly developed compounds for the market if they turned out to be successful as PET imaging agents.

Aminomethylchromanes (AMCs), a class of high-affinity $D_{2/3}$ agonists that had not been previously evaluated as radioligands, were chosen for the development of new ^{18}F-labeled tracers.

Chapter 3 describes the design of candidate compounds based on this scaffold. A PET tracer for brain imaging should be lipophilic enough to penetrate the blood-brain-barrier by passive diffusion, but should also have high enough affinity towards its target so that its specific binding in brain tissue would be distinguishable from non-specific binding. The tracer should also be metabolically stable to be able to penetrate into the brain tissue from the blood before being metabolized. When the tracer is eventually metabolized, the label should go off the molecule in fragments sufficiently hydrophilic so as not to penetrate the blood-brain-barrier.

The $D_{2/3}$ agonist pharmacophore, to which AMCs also conform, consists of an aromatic core, hydrogen-bonding hydroxyl groups attached to it, and a positively charged nitrogen (Figure 1). The advantage of the AMC scaffold for radioligand development is that the substituent at the nitrogen atom is directed towards a relatively spacious ancillary binding pocket. Therefore, the structure of the N-substituent can be modified with considerable freedom in order to achieve the necessary lipophilicity and accommodate the radiolabel without much impact on the $D_{2/3}$ affinity or agonism.

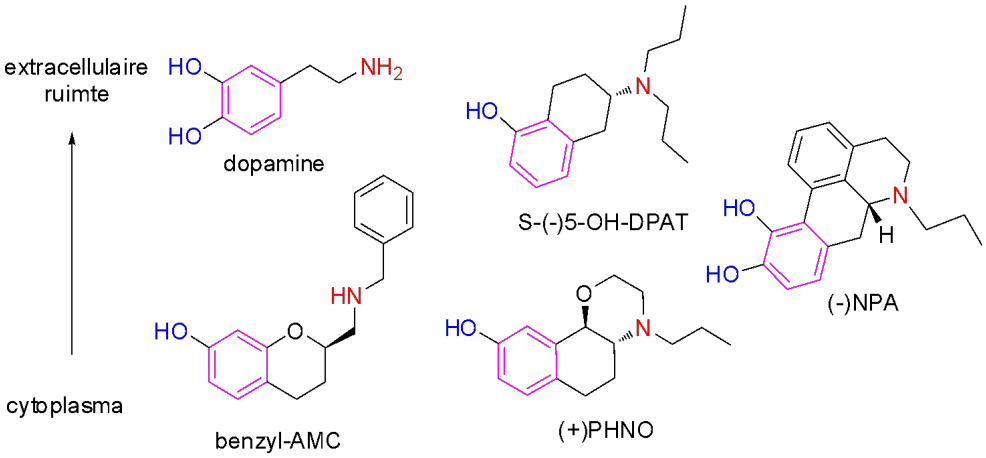

Figure 1. Comparison of the molecular structures of dopamine, aminomethyl chromane, aminotetraline, naphtoxazine and apomorphine ligands.

Aryl cores, basic nitrogens and H-bond donating hydroxyls are marked with color. Ligands are oriented in a rough representation of their putative receptor-bound conformations. The "upward-looking" benzyl substituent of benzyl-AMC and propyl substituent of S-(−)5-OH-DPAT can access the spacious ancillary binding pocket of the D_2 receptor, while the "downward-looking" propyl substituents of S-(−)5-OH-DPAT, (+)PHNO and (−)NPA are pointed towards a minor binding pocket that cannot accommodate groups greater than propyl. Adapted from Chapter 3.

Alkyl-, benzyl- and arylpiperazino-substituted AMCs were developed in this work (Figure 2). Structures of candidate compounds were designed to possess predicted lipophilicities ($LogP_{7.4}$ = LogD) between 1 and 3, which is the preferred range for brain radiopharmaceuticals [17]. In the majority of candidate compounds, the fluorine label was introduced in fluoroalkoxy groups, and the lengths of the alkyl chains were adjusted to obtain the right LogD values. Nevertheless, the AMC moiety remained the main hydrophobic core in all candidate compounds. The radioactive fluorine atom was incorporated

far from the AMC moiety in groups likely to be cleaved from the molecule core by metabolic enzymes. This was done to ensure that radioactive metabolites formed from the candidate tracers would not be lipophilic and would not include the $D_{2/3}$-pharmacophore, because lipophilic radiometabolites, especially those possessing $D_{2/3}$ affinity, could interfere with the quantification of the specific uptake of candidate tracers in the brain.

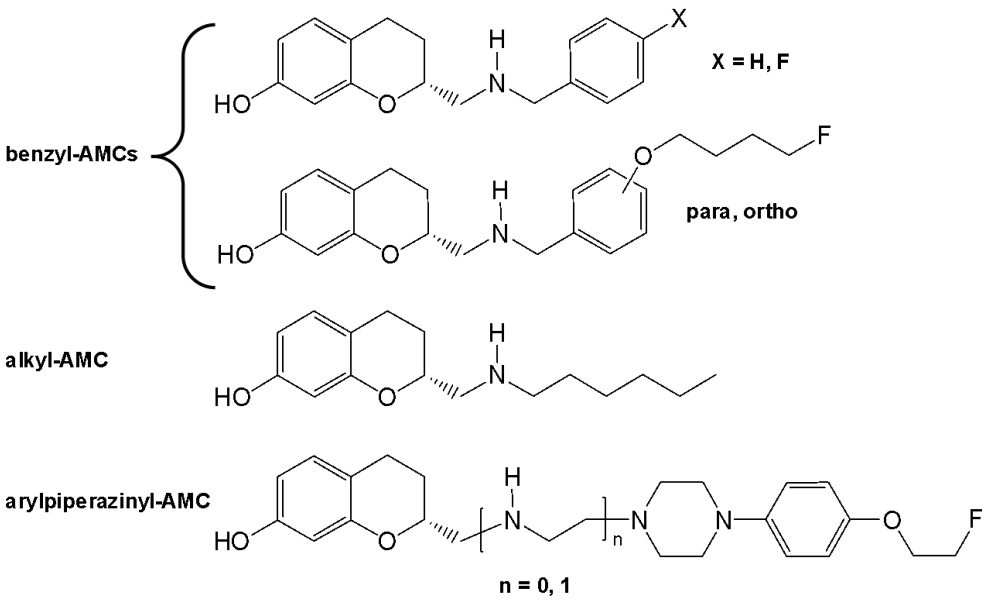

Figure 2. Structures of candidate AMCs (fluorinated and reference compounds) prepared in this work.

Synthesis and pharmacological characterization of candidate compounds

Chapters 3 and **4** describe the preparation of candidate AMCs and their evaluation in vitro. Chirality of AMCs plays a decisive role in their affinity towards D_2 and D_3 receptors, with (*R*)-enantiomers being the eutomers. An enantiomerically pure (*R*)-7-hydroxy-2-ethoxycarbonyl chromane building block was prepared from its racemate using a kinetic lipase resolution procedure. This building block was further modified to eventually obtain alkyl-, benzyl- and arylpiperazino-substituted AMCs, with and without fluorine atoms in their structure.

The pharmacological properties of synthesized compounds were evaluated in radioligand competition assays in membrane homogenates from human embryonic kidney (HEK) and Chinese hamster ovary (CHO) cells expressing various human dopamine receptor subtypes and in functional assays such as adenylate cyclase inhibition and β-arrestin recruitment. Two benzyl- and one arylpiperazino-substituted AMC, codenamed AMC20, FBu-AMC13and FEt-AMC15, respectively, were recognized as good candidates for radiolabeling (in Chapter 3, the latter two compounds are denoted as **12a** and **12d**, respectively). In membrane homogenates with D_2 receptors, these compounds distinguished between high- and low-affinity binding sites (D_2high and D_2low), having 10–1000-fold preference for the former over the latter. Their affinities towards D_2high were in the subnanomolar to nanomolar range: from 85 pM for AMC20 to 6.7 nM for FEt-AMC15. In addition, they bound with high affinity to D_3 receptors (from 0.6 nM for AMC20 to 12.1 nM for FBu-AMC13), did not bind significantly to D_1 receptors and showed almost full agonism in functional assays at D_2 receptors.

Preparing radiolabeled candidate tracers and assessing their lipophilicity

The radiolabeling of AMC20 is described in **Chapter 4**, while the radiolabeling of FBu-AMC13 and FEt-AMC15 is described in **Chapters 3** and **5**. For the latter two compounds, several homologues with varying fluoroalkyl chain lengths were prepared in order to find out what length resulted in the highest signal-to-noise ratios in real brain tissue.

In the AMC20 structure, the fluorine atom was directly attached to the benzyl group. Because the benzyl group has an electron-rich aryl ring that cannot be directly labeled by nucleophilic fluorination, synthesis of this compound started from the preparation of 4-[^{18}F]fluorobenzaldehyde which was then coupled with AMC-amine and converted to [^{18}F]fluorobenzyl group by reductive amination. In FBu-AMC13 and FEt-AMC15, the fluorine atom was part of a fluoroalkoxy group. These compounds were obtained by fluoroalkylation of phenol precursors (Figure 3).

Radiolabeling procedures for the production of the first [^{18}F]AMCs were selected so as to maximize ease and flexibility. Radiosynthetic procedures lasted for 2–2.5 hours. [^{18}F]fluoroalkyl-AMCs were obtained in isolated radiochemical yields of 3–15%, while average isolated radiochemical yield of [^{18}F]AMC20 was 24%. Molar radioactivities of [^{18}F]AMCs were in the range of

10–100 GBq/μmol, which was high enough to carry out in vivo PET imaging at tracer doses. Production of [^{18}F]fluoroalkyl tosylates and 4-[^{18}F]fluorobenzaldehyde was automated at later stages of the work (**Chapter 6**), further simplifying the production of tracers for in vitro and in vivo evaluation.

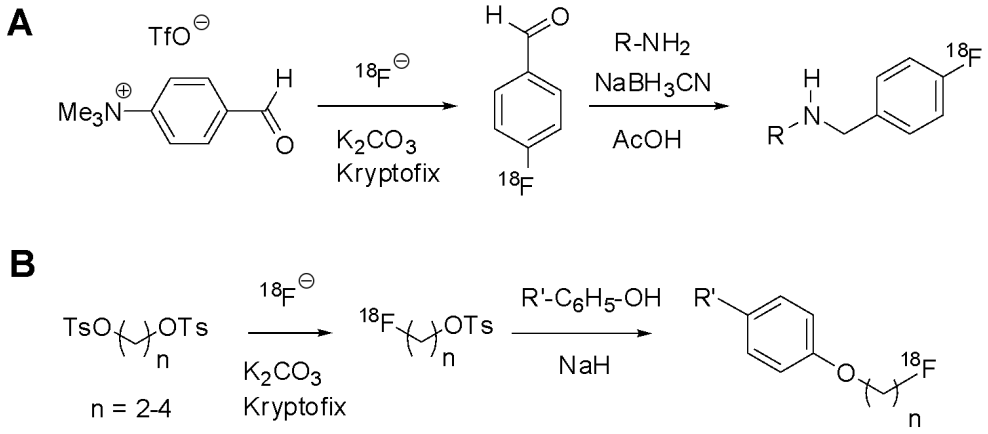

Figure 3. Radiolabeling schemes used for the preparation of [^{18}F]AMCs.

A – reductive amination of 4-[^{18}F]fluorobenzaldehyde with the amine precursor of AMC20; B – [^{18}F]fluoroalkylation of phenol precursors for AMC13 and AMC15 homologues. For simplicity, the actual aminomethyl chromane moieties and the final deprotection of their 7-OH group are not shown.

The experimentally determined LogD value of [^{18}F]AMC20 was 2.33. For AMC13 homologues LogD varied from 1.67 ([^{18}F]FEt-AMC13) to 2.50 ([^{18}F]FBu-AMC13). For AMC15 homologues, LogD varied from 1.48 ([^{18}F]FEt-AMC15) to 2.71 ([^{18}F]FBu-AMC15). All LogD values fall within the range considered optimal for passive diffusion from the plasma into the brain tissue [17].

In vitro and in vivo evaluation of radiolabeled candidate tracers

Results of in vitro and in vivo evaluation of radiolabeled candidate tracers are described in **Chapters 4** and **5**. All radiolabeled compounds were evaluated by in vitro autoradiography in rat brain slices to assess the signal-to-noise ratios of their binding to $D_{2/3}$ receptors in real tissue. Specific binding ratios (SBRs) were calculated from radioactivity concentrations

in striatal ($D_{2/3}$-rich) and cerebellar ($D_{2/3}$-poor) regions. For [^{18}F]AMC20, a fluorobenzyl-substituted AMC with the highest measured affinity towards D_2high (85 pM), striatal SBR reached 6.27 at a concentration of 1.7 nM (**Chapter 4**). Among [^{18}F]fluoroalkoxy-labeled AMCs, the highest SBRs were shown by fluoroethoxybenzyl-substituted [^{18}F]FEt-AMC13 and (fluoroethoxy)phenylpiperazino-substituted [^{18}F]FEt-AMC15: 3.40 at 0.9 nM and 1.64 at 5.8 nM, respectively (**Chapter 5**). For all radioligands, co-incubation with the $D_{2/3}$ antagonist raclopride or guanosine triphosphate (GTP) decreased SBRs by 60–80%, confirming that their striatal binding is specific to the high-affinity state of $D_{2/3}$ receptors.

[^{18}F]AMC20, [^{18}F]FBu-AMC13, [^{18}F]FEt-AMC13 and [^{18}F]FEt-AMC15 were evaluated in Sprague-Dawley rats. In living rats, [^{18}F]FEt-AMC15 showed very low penetration into the brain, which could be due to its relatively high hydrophilicity and the presence of two basic nitrogens or possibly because it interacted with pump proteins like P-glycoprotein (P-gp). On the contrary, [^{18}F]AMC20, [^{18}F]FBu-AMC13, and [^{18}F]FEt-AMC13 penetrated into the brain in good amounts: brain uptake peaked at 1.7%, 0.9% and 0.7% injected dose, respectively. For [^{18}F]FBu-AMC13, the brain region with the highest uptake was the brainstem, but [^{18}F]FEt-AMC13 and [^{18}F]AMC20 preferentially accumulated in the striatum, resulting in striatum-to-cerebellum ratios of about 2 for both tracers. All radioactive metabolites of [^{18}F]FEt-AMC13 and [^{18}F]AMC20 were considerably less lipophilic than their parent tracers and did not penetrate the blood-brain barrier. Finally, for both tracers, a 20–40% decrease (depending on the measurement method) of preferential striatal binding in response to pre-treatment with 1 mg/kg raclopride was detectable in PET measurements, ex vivo biodistribution and ex vivo autoradiography (**Chapters 4** and **5**).

Although in vivo and ex vivo data obtained for [^{18}F]FEt-AMC13 and [^{18}F]AMC20 were consistent with specific binding of these two tracers to $D_{2/3}$ receptors in rat striatum, these radioligands had two common drawbacks. One was that the difference between striatal and cerebellar uptake, typically used as a surrogate measure of $D_{2/3}$ specific binding, was not decreased by more than 40% by pre-treatment with raclopride. This is less than half of reported decreases for existing ^{11}C-labeled agonists at the same (1 mg/kg) or lower raclopride doses (at least 80% decrease [18–20]). This could be a result of either insufficient raclopride dosage or imperfect pharmacological selectivity of the tracers. Based on the available data it is impossible to choose between the two explanations.

Another, more important drawback, was that the baseline signal-to-noise ratios of [^{18}F]FEt-AMC13 and [^{18}F]AMC20 were lower than what was reported in rats for existing ^{11}C-labeled $D_{2/3}$ agonist tracers. Striatal BP_{ND} values for our tracers were ~0.5 compared to 0.9 for [^{11}C]MNPA [18], while striatum-to-cerebellum ratios were ~2 compared to 3 or more for [^{11}C](−)NPA and [^{11}C](+)PHNO [19,20]. So, even if absolute selectivity for $D_{2/3}$ receptors can be proven for [^{18}F]FEt-AMC13 and [^{18}F]AMC20, and >90% decrease of striatal BP_{ND} can be achieved by increasing raclopride dose, they will still be less suitable for the measurement of striatal $D_{2/3}$ receptor availability in vivo than [^{11}C]MNPA, [^{11}C](−)NPA or [^{11}C](+)PHNO.

Conclusion

We have designed and prepared a series of fluorinated aminomethylchromane derivatives and evaluated them as potential agonist radiotracers for the imaging of dopamine $D_{2/3}$ receptors with PET.

The best two compounds of those investigated by us, [^{18}F]AMC20 and [^{18}F]FEt-AMC13, distinguished between high- and low- affinity states of $D_{2/3}$ receptors, did not form lipophilic metabolites in vivo, penetrated well into the rat brain, preferentially accumulated in the striatum and were sensitive to $D_{2/3}$ blockade by raclopride. Although the signal-to-noise ratios of [^{18}F]AMC20 and [^{18}F]FEt-AMC13 are lower than those of existing ^{11}C-labeled $D_{2/3}$ agonist tracers, our results demonstrate that aminomethylchromanes are a viable scaffold for the development of $D_{2/3}$ agonist radioligands.

REFERENCES

1. Bernheimer H, Birkmayer W, Hornykiewicz O, Jellinger K, Seitelberger F. Brain dopamine and the syndromes of Parkinson and Huntington Clinical, morphological and neurochemical correlations. J. Neurol. Sci. 1973;20:415–55.

2. Schwab LC, Garas SN, Drouin-Ouellet J, Mason SL, Stott SR, Barker RA. Dopamine and Huntington's disease. Expert Rev. Neurother. 2015;15:445–58.

3. Sulzer D. How Addictive Drugs Disrupt Presynaptic Dopamine Neurotransmission. Neuron. Elsevier Inc.; 2011;69:628–49.

4. Meyer JH, McNeely HE, Sagrati S, Boovariwala A, Martin K, Verhoeff NPLG, et al. Elevated putamen D_2 receptor binding potential in major depression with motor retardation: an [^{11}C]raclopride positron emission tomography study. Am. J. Psychiatry. 2006;163:1594–602.

5. Tatsumi M, Groshan K, Blakely RD, Richelson E. Pharmacological profile of antidepressants and related compounds at human monoamine transporters. Eur. J. Pharmacol. 1997;340:249–58.

6. van Rossum JM. The significance of dopamine-receptor blockade for the action of neuroleptic drugs. In: Brill H, Cole J, Deniker P, Hippius H, Bradley PB, editors. Neuropsychopharmacol. Proc 5th Coll. Int Neuropsychopharmacol. Excerpta Medica Foundation; 1967. p. 321–9.

7. van Kammen DP. The dopamine hypothesis of schizophrenia revisited. Psychoneuroendocrinology. 1979;4:37–46.

8. Gunn RN, Slifstein M, Searle GE, Price JC. Quantitative imaging of protein targets in the human brain with PET. Phys. Med. Biol. IOP Publishing; 2015;60:R363–411.

9. De Lean A, Stadel JM, Lefkowitz RJ. A ternary complex model explains the agonist-specific binding properties of the adenylate cyclase-coupled beta-adrenergic receptor. J. Biol. Chem. 1980;255:7108–17.

10. Kent RS, De Lean a, Lefkowitz RJ. A quantitative analysis of beta-adrenergic receptor interactions: resolution of high and low affinity states of the receptor by computer modeling of ligand binding data. Mol. Pharmacol. 1980;17:14–23.

11. Finnema SJ, Bang-Andersen B, Wikström H V, Halldin C. Current state of agonist radioligands for imaging of brain dopamine D_2/D_3 receptors in vivo with positron emission tomography. Curr. Top. Med. Chem. 2010;10:1477–98.

12. Zijlstra S, Visser GM, Korf J, Vaalburg W. Synthesis and in vivo distribution in the rat of several fluorine-18 labeled N-fluoroalkylaporphines. Appl. Radiat. Isot. 1993;44:651–8.

13. Vasdev N, Seeman P, Garcia A, Stableford WT, Nobrega JN, Houle S, et al. Syntheses and in vitro evaluation of fluorinated naphthoxazines as dopamine D_2/D_3 receptor agonists: radiosynthesis, ex vivo biodistribution and autoradiography of [^{18}F]F-PHNO. Nucl. Med. Biol. 2007;34:195–203.

14. Shi B, Narayanan TK, Christian BT, Chattopadhyay S, Mukherjee J. Synthesis and biological evaluation of the binding of dopamine D_2/D_3 receptor agonist, (R,S)-5-hydroxy-2-(N-propyl-N-(5'-[^{18}F]-fluoropentyl)aminotetralin ([^{18}F]-5-OH-FPPAT) in rodents and nonhuman primates. Nucl. Med. Biol. 2004;31:303–11.

15. Zijlstra S, Visser GMM, Korf J, Vaalburg W, Elsinga PHH, Oosterhuis EZZ. Synthesis and in vivo distribution in the rat of several fluorine-18 labeled 5-hydroxy-2-aminotetralin derivatives. Appl. Radiat. Isot. 1993;44:473–80.

16. Mukherjee J, Narayanan TK, Christian BT, Shi B, Yang Z-Y. Binding characteristics of high-affinity dopamine D_2/D_3 receptor agonists, [^{11}C]-PPHT and [^{11}C]-ZYY-339 in rodents and imaging in non-human primates by PET. Synapse. 2004;54:83–91.

17. Waterhouse R. Determination of lipophilicity and its use as a predictor of blood–brain barrier penetration of molecular imaging agents. Mol. Imaging Biol. 2003;5:376–89.

18. Seneca N, Zoghbi SS, Skinbjerg M, Liow J-S, Hong J, Sibley DR, et al. Occupancy of dopamine $D_{2/3}$ receptors in rat brain by endogenous dopamine measured with the agonist positron emission tomography radioligand [^{11}C]MNPA. Synapse. 2008;62:756–63.

19. Egerton A, Hirani E, Ahmad R, Turton DR, Brickute D, Rosso L, et al. Further evaluation of the carbon-11-labeled $D_{2/3}$ agonist PET radiotracer PHNO: Reproducibility in tracer characteristics and characterization of extrastriatal binding. Synapse. 2010;64:301–12.

20. Hwang DR, Kegeles LS, Laruelle M. (–)-N-[^{11}C]propyl-norapomorphine: a positron-labeled dopamine agonist for PET imaging of D_2 receptors. Nucl. Med. Biol. 2000;27:533–9.

Chapter 8

Future perspectives

Quest for ^{18}F-labeled dopamine $D_{2/3}$ receptor agonists

As our research into ^{18}F-labeled aminomethylchromanes was being carried out, other research groups were pursuing the development of ^{18}F-labeled $D_{2/3}$ agonists based on other scaffolds. In particular, for the apomorphine scaffold, the focus of ^{18}F-labeling attempts shifted from the substituents at the amino nitrogen to the substituents at the oxygen atoms attached to the apomorphine core. This has yielded [^{18}F]MCL-524, a ^{18}F-labeled dopamine $D_{2/3}$ agonist tracer with a structure very similar to [^{11}C]MNPA [1]. In cynomolgus monkeys, mean striatal binding potential (BP_{ND}) measured for [^{18}F]MCL-524 was 2.0, which is higher than the value of 1.5 measured for [^{11}C]MNPA [2]. [^{18}F]MCL-524 was also sensitive to changes in endogenous dopamine levels, so there is a chance that implementation of this tracer in clinical research will result in wider application of $D_{2/3}$ imaging than is currently feasible with ^{11}C-labeled $D_{2/3}$ agonist tracers and allow more precise measurement of fluctuations in synaptic dopamine levels than is currently achievable with $D_{2/3}$ antagonist tracers.

It would be beneficial, though, to have ^{18}F-labeled agonist tracers from different scaffolds available to be able to distinguish between their general and scaffold-specific properties. Modifications of other scaffolds popular in $D_{2/3}$ agonist tracer development to accommodate an ^{18}F atom have not been successful (see [3] for review). In naphtoxazines like (+)PHNO, the only suitable place for the ^{18}F-label is the N-propyl substituent. [^{18}F]fluoropropyl-(+)HNO showed a homogeneous distribution in rat brain with no discernible specific binding despite 0.4 nM affinity towards D_2high measured in vitro [4]. Possible reason for this is decreased basicity of the nitrogen atom resulting from the negative inductive effect of fluorine, but elongation of the N-propyl substituent in the PHNO structure adversely affects D_2high binding affinity, because this substituent points into a restricted ancillary pocket of the D_2 receptor, which is unable to accommodate greater moieties.

Aminotetralins are more flexible than naphtoxazines regarding possible locations for radiolabeling. Like in aminomethylchromanes, one of the substituents at the nitrogen atom of the aminotetralins can access the spacious ancillary binding pocket (while the second still cannot be greater than propyl, see Figure 1 in Chapter 7) [5,6]. Optimizing the N-substituent led to the development of aminotetralin derivatives with affinities towards D_2 receptors as high as 10 pM in case of the aminotetralin ZYY-339 [7]. However, this compound was also relatively lipophilic (LogD 3.0), and apparently

because of that, [^{11}C]ZYY-339 showed striatum-to-cerebellum ratios of only 1.5 in rats [8]. Less lipophilic aminotetralins with less bulky N-substituents had lower D_2 affinities but showed somewhat greater striatum-to-cerebellum ratios: 1.8 for the ^{11}C-labeled N,N'-dipropyl aminotetralin [^{11}C]5-OH-DPAT (D_2 affinity of 2.5 nM, LogD of 1.4) [9] and up to 2.0 for the ^{18}F-fluoropentyl-substituted aminotetralin [^{18}F]5-OH-FPPAT (LogD 1.60, IC_{50} 6.95 nM at rat $D_{2/3}$ receptors) [10]. Recently reported [^{18}F]fluorohexyl-substituted aminotetralins [^{18}F]5-OH-FHXPAT (logD 1.8, affinity not reported) and [^{18}F]7-OH-FHXPAT also showed striatum-to-cerebellum ratios around 2 in rats and mice [11]. All these tracers, to sum up, are inferior to [^{11}C](+)PHNO or [^{11}C](−)NPA in their signal-to-noise ratios, but comparable to the AMC tracers developed in the current work. It should be noted that all aminotetraline tracers were tested in their racemic form, so converting them to eutomers may increase signal-to-noise ratios. It's unlikely, however, that the gain will be more than 2-fold: assuming only non-specific binding for the distomers, striatal specific binding ratios (SBRs) relative to cerebellum could increase from 1 to 2 (equivalent to striatum-cerebellum ratios of 3) after switching to pure eutomers, but not greater. Therefore, the prospects of aminotetralin-based $D_{2/3}$-agonist tracers are arguably similar to the prospects of aminomethylchromane-based ones.

The main problem with aminomethylchromane ligands obtained in this work is their low signal-to-noise ratios: in living rat brain, striatal SBRs for these ligands did not exceed 1.5, and binding potential (BP_{ND} [12]) values did not exceed 0.6. Specific binding ("signal") of the radioligands results from their affinity to their target, while non-specific binding ("noise") results mainly from the ligands' lipophilicity. It can be claimed, therefore, that low signal-to-noise ratios of aminomethylchromane ligands are a consequence of suboptimal combinations of their affinities and lipophilicities.

On the one hand, the affinity of [^{18}F]AMC20 (investigated in Chapter 4) towards D_2high was considerably high, 0.03–0.14 nM, 85 pM on average, but its signal-to-noise ratio had probably been limited by its non-specific binding. The LogD value of [^{18}F]AMC20 was 2.33, which is close to the middle of the 2.0–3.0 range that corresponds to the maximum brain penetration by passive diffusion [13]. Indeed, 1.7% of injected [^{18}F]AMC20 dose penetrated into the rat brain, but apparently for the AMC scaffold such LogD values also result in too much non-specific binding in the brain. Optimization of radioligands starting from [^{18}F]AMC20 should involve decreasing lipophilicity while keeping the affinity at the same level.

On the other hand, [^{18}F]FEt-AMC13 (investigated in Chapter 5) had much lower LogD value (1.67), but approximately the same signal-to-noise ratio as [^{18}F]AMC20. Apparently, the reason was its rather low D_2high affinity (not measured directly for FEt-AMC13, average of 5.6 nM measured for FBu-AMC13) compared to [^{18}F]AMC20. Brain penetration of [^{18}F]FEt-AMC13 was 0.7% injected dose. Therefore, if [^{18}F]FEt-AMC13 is considered as a starting point for the development of new radioligands, an improvement in affinity is clearly more desirable than a further decrease in lipophilicity.

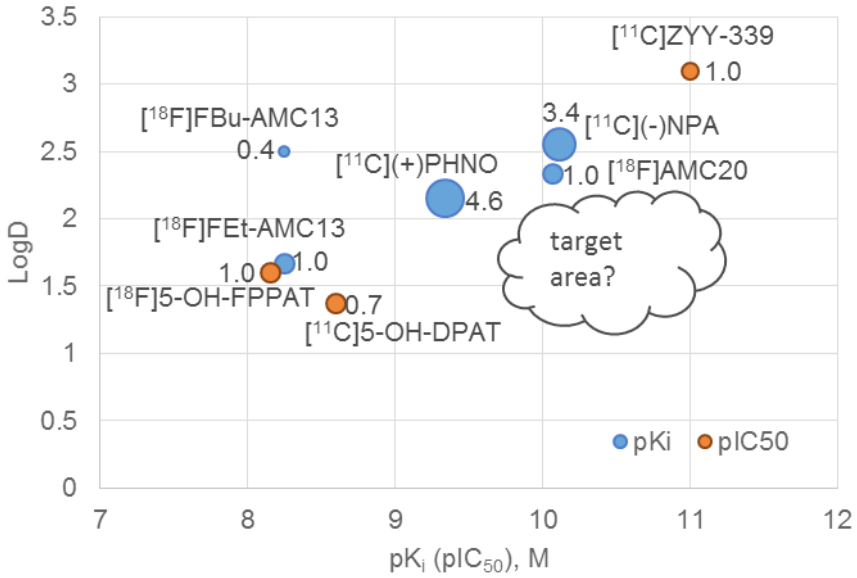

Figure 1. Relationship between affinities, lipophilicities and in vivo striatal SBRs for AMC tracers, aminotetraline tracers, (–)NPA and (+)PHNO.

Affinities for AMCs, (–)NPA and (+)PHNO are expressed as pK_i at the high-affinity state of recombinant human D_2 receptor (Long isoform). Affinities for aminotetralins are expressed as pIC_{50} at rat striatal $D_{2/3}$ receptors (aggregate values without distinction by subtype, isoform or affinity state). Circle areas are proportional to maximum ex vivo SBRs in rats, actual SBR values shown beside. All data for AMC tracers and pK_i values for (-)NPA and (+)PHNO were obtained in the current work (see Chapters 3, 4 and 5); pK_i of FEt-AMC13 is assumed to be equal to pK_i of FBu-AMC13. All the other data are taken from the literature (see [3]).

Affinity, lipophilicity and striatal SBR values obtained in rats for selected aminomethylchromanes, aminotetralins, [^{11}C](–)NPA and [^{11}C](+)PHNO are compared in Figure 1. Note that IC_{50} and K_i values are prone to experimental variation and are not directly comparable to each other [14], while the

relationship between LogD value and non-specific binding is not uniform, especially when tracers being compared are based on different scaffolds. Therefore, the relative placement of different tracers on affinity and lipophilicity scales should be taken with a grain of salt. Nevertheless, presented results suggest that aminomethylchromane and aminotetralin ligands with optimal characteristics for imaging should be located around the "target area" shown in Figure 1: ligands with sub-nanomolar D_2high affinities and LogD values of 1.5–2. Creating such ligands will probably be easier using the aminomethylchromane scaffold. This scaffold has an oxygen atom in the bicyclic core, which lowers its inherent lipophilicity, and many high-affinity D_2 agonist derivatives with a secondary nitrogen atom (not tertiary, as is typical, though not necessary, for aminotetralins [5]) are already described.

Mewshaw's research into aminomethylchromanes eventually branched out into tricyclic derivatives [15], the best of which had 3-fold higher affinity to the high-affinity state of D_2 receptors than (*R*)-2-((benzylamino)methyl) chroman-7-ol, while also being less lipophilic (Figure 2). During the design of the candidate AMC tracers, we aimed for relatively lipophilic compounds to ensure high brain penetration, therefore these tricyclic scaffolds were not considered for development. However, for benzyl-substituted AMCs, brain penetration turned out to be a lesser problem than affinity and non-specific binding, so shifting the focus to intrinsically more hydrophilic derivatives may be reasonable. If further research into ^{18}F-labeled $D_{2/3}$ agonist PET tracers is to be done on Mewshaw's compounds, evaluating the newer tricyclic derivatives will be worthwhile. Before labeling, however, the pharmacological selectivity of these compounds should be investigated in more detail. While the D_2-over-D_1 dopamine receptor selectivity of Mewshaw's compounds is beyond doubt (see Chapters 3 and 4), their selectivity towards D_2-like dopamine receptors versus other monoamine receptors abundant in the striatum has to be conclusively confirmed. For instance, racemic AMC20 was reported to possess 5-HT1$_A$ affinity of 71.5 nM [16]. This is a relatively low value, but it suggests that D_2-over-5-HT$_1$ selectivity of AMCs might be lower than their D_2-over–D_1 selectivity. Meanwhile, serotonergic 5-HT$_1$ receptors are 5–6 times more abundant in rat striatum than $D_{2/3}$ receptors (1200–3400 pmol/g vs 111–522 pmol/g, respectively [17,18]).

If selectivity for $D_{2/3,}$ at least within the striatum, is successfully established, an obvious first option would be to attach the ^{18}F-atom to the benzyl ring of structure shown in Figure 2. Recently developed approaches to high-molar-radioactivity ^{18}F-fluorination, like nucleophilic fluorination with aryliodo-

nium moieties as leaving groups [19] or transition metal-catalyzed fluorination [20–23], mean that even compounds with ^{18}F-label in the electron-rich aromatic ring can potentially be prepared via short radiosynthetic routes suitable for commercial production.

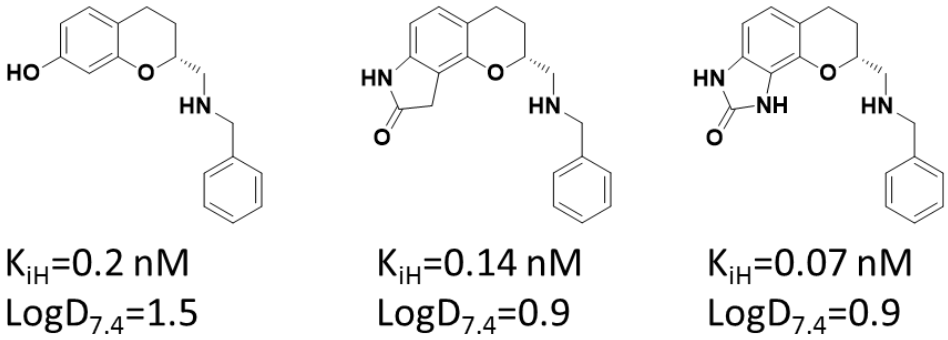

Figure 2. Comparison of D_2 affinities and lipophilicities of (*R*)-2-((benzylamino) methyl) chroman-7-ol and its later derivatives developed by Mewshaw and coworkers.

Inhibition constants for the high-affinity state of D_2 receptors are taken from [15]. LogD values at pH 7.4 are calculated using the web application at www.chemicalize.org (Chemaxon, Hungary).

Value of agonist tracers for neuroreceptor PET imaging

Whether [^{18}F]MCL-524 and hypothetical new ^{18}F-labeled aminotetralins and aminomethylchromanes will be superior to $D_{2/3}$ antagonist tracers in applications beyond the measurement of intrasynaptic dopamine levels, and whether agonist tracers for other neuroreceptors will be superior to corresponding antagonist tracers in any application, is not clear at the moment. The development of agonist tracers for neuroreceptors was inspired by the hypothesis that GPCRs in the living brain are separated into high and low-affinity subpopulations, but this hypothesis is not supported by existing preclinical experimental evidence.

In the clinic, the imaging of subjects in whom alterations in the relative abundance of the high-affinity state were hypothesized, such as patients with neuropsychiatric disorders or drug users, also provided results disappointing for the “high-low-affinity state” theory. There was either no difference between studied groups [24–27], or the difference could be well explained by factors other than the agonist’s preference for the high affinity

state. For instance, a lot of alterations in $D_{2/3}$ receptor availability in neuropathological states were discovered with the $D_{2/3}$ agonist [^{11}C](+)PHNO, but these successes can be attributed to the fact that [^{11}C](+)PHNO is a D_3-preferring tracer in vivo [28]. From a clinical point of view, therefore, dopaminergic receptor imaging should benefit more from novel tracers of any intrinsic activity that are selective for the D_2 or the D_3 receptor subtype than from novel agonist tracers that bind to several D_2-like receptor subtypes at once. This is especially true for the D_3 subtype, given the findings with [^{11}C](+)PHNO [28]. Also, D_3 receptors have the highest affinity towards dopamine of all dopamine receptor subtypes [29], so selective imaging of D_3 may provide more sensitivity to changes in intrasynaptic levels of endogenous dopamine than selective imaging of D_2 (and non-selective imaging of $D_{2/3}$).

Structure-activity relationships for D_2 and D_3 selectivity are especially well researched for the arylpiperazine scaffold (see e.g. [30–32]) and D_2 and D_3-selective arylpiperazine radioligands with partial agonist activity have already been reported [33]. [^{11}C]SV-III-120, a D_2-selective arylpiperazine, showed promising results in monkeys [34]. The usefulness of this tracer for clinical imaging of dopamine receptors remains to be evaluated. Candidate D_3-selective arylpiperazines and related arylimidazolidinones, both agonists [35–37] and antagonists [38–41], suffer from low or zero specific binding levels. For some of these ligands [37], but not for all [42], low specific binding could be caused by high competition with endogenous dopamine. [^{18}F]7-OH-FHXPAT, a recently reported aminotetralin tracer, showed results consistent with preferential binding to D_3 receptors in rat and mouse brain [11], but its signal-to-noise ratio is moderate, while its D_3-selectivity has yet to be confirmed using conventional in vitro methods. Therefore, [^{11}C](+)PHNO remains the best currently available tool for D_3 imaging.

For other neuroreceptors, the relative merits of agonist and antagonist tracers have not been investigated as extensively as for dopamine receptors. New evidence in this regard is most likely to appear for neuroreceptors for which both agonist and antagonist tracers with similar receptor subtype selectivity profiles are available. Such are serotonin 5-HT_{1A} ([^{11}C]CUMI-101 vs [^{11}C]WAY100635), serotonin 5-HT_{2A} ([^{11}C]CIMBI-36 vs [^{11}C]MDL100907) and kappa-opioid ([^{11}C]GR103545 vs [^{11}C]LY2975050) receptors. Agonist tracers for these three receptors have only undergone preliminary evaluations in humans [43–48]. Time will tell if there are any applications in which these agonists are superior to corresponding antagonist tracers.

Fate of the high-affinity state hypothesis

As discussed in **Chapter 2**, there is a gap between ample evidence for the existence of high-affinity state as a separate subpopulation of receptors in membrane homogenates and lack of such evidence in the living brain (Figure 3). What can be done to bridge that gap?

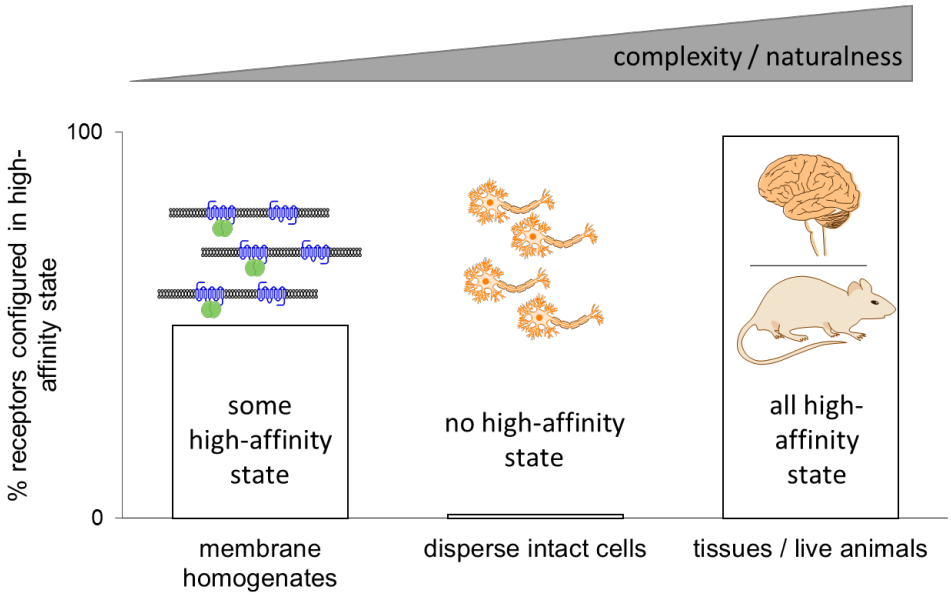

Figure 3. Lack of agreement and contiguousness between assessments of the abundance of receptors configured in high-affinity state in different setups.

For $D_{2/3}$ receptors, a certain percentage of receptors (considerably less than 100%) is known to exist in high-affinity state in membrane homogenates [49]. However, no high-affinity state can be detected at equilibrium in intact cells [50–52], while in tissues and living animals all receptors appear to be configured in the high-affinity state [18,53].
Reproduced from Chapter 2.

High-affinity state imaging beyond $D_{2/3}$ receptors

Obviously, in-depth head-to-head comparisons of agonist and antagonist PET tracers for non-dopaminergic receptors are very valuable for the refinement of our understanding of the high-affinity state in vivo. The first head-to-head comparisons of 5-HT_{1A} and 5-HT_{2A} receptor tracers have only recently been published [46,54–56]. Agonist and antagonist tracers with

matching pharmacological selectivities (i.e. same relative affinities towards various receptor subtypes in vivo) are also available for κ-opioid receptors [57–59], but there are no reports of their head-to-head comparisons yet.

The ternary complex model of GPCR signaling was first validated on β-adrenergic receptors [60], and the mode of receptor-G-protein coupling for adrenergic receptors in general is very well investigated (see e.g. [61]). It would be interesting to attempt to detect the high-affinity state of these receptors by PET imaging. Currently, there are no agonist tracers for adrenergic receptors suitable for in vivo CNS imaging, but non-subtype-selective tracers for α_2-adrenoceptors like [^{11}C]yohimbine and the selective α_{2C}-adrenoceptor tracer [^{11}C]ORM13070 are available and have been used for brain imaging in several animal species and humans [62–64]. Non-subtype selective β-adrenoceptor antagonists S-1'-[^{18}F]fluorocarazolol and [^{18}F]fluoroethylcarazolol can also be used for brain imaging, though only in preclinical settings due to their mutagenicity [65–68]. Building in vivo displacement curves using adrenoceptor antagonist tracers and unlabeled adrenergic drugs of varying intrinsic activity (agonists in the first place) will further our understanding of the fate of GPCR high-affinity state in vivo, although the effects of drugs used for displacement on heart and lung functioning is a potential concern.

"Vertical integration" of in vitro and in vivo setups

Although reviewing the data obtained by separate research groups reveals a discrepancy between the relative abundances of the high-affinity state found in membrane homogenates, intact cells and tissues (see Figure 3), few studies featured attempts to detect high-affinity state in the same receptor population using several experimental set-ups at once [50,51,69–71].

For example, more data are necessary to clarify the relationship between measurements of high-affinity state on disperse intact cells and in living tissues. Studies looking for the high-affinity state of $D_{2/3}$ receptors naturally expressed on intact cells have been carried out with cells from bovine pituitary [50] and rat pituitary adenoma [72], but never with striatal cells, though the latter are most often used in attempts to detect the high-affinity state in vivo.

New studies that would assess the relative abundance of the high-affinity state in the same receptor population (region of interest in the brain of a certain species) using membrane homogenates, dispersed intact cells, and

live animals, would shed more light on the reasons behind the current confusion regarding the existence of the high-affinity state.

Further investigation of the role of kinetic factors on the outcome of pharmacological experiments

As discussed in Chapter 2, two hypotheses have been proposed to explain why high-affinity state cannot be detected in vivo:

(1) All receptors are constantly coupled to G-proteins in vivo and thus are all in the high-affinity state (see [53])

(2) Receptors readily couple to G-proteins in vivo and can become fully coupled (i.e. fully converted to the high-affinity state) if the agonist concentration is high enough. As almost all experimental paradigms used to detect the high-affinity state in vivo involve high concentrations of agonists (tracers/drugs/neurotransmitters), the apparent relative abundance of the high-affinity state is inflated to values close to 100%, even if it is less than that at baseline (see [73,74]).

The first hypothesis is conceptually simpler than the second. However, given the growing understanding that kinetics is an important factor in GPCR signaling [75], the second hypothesis is also worth investigating.

For instance, while many studies found $D_{2/3}$ agonist and antagonist radioligands to be equally vulnerable to displacement by $D_{2/3}$ agonist drugs [73,76,71], Seeman reported that both in vitro and in vivo, the $D_{2/3}$ agonist [^{3}H](+)PHNO showed higher vulnerability than the antagonist [^{3}H]raclopride to displacement by the unlabeled agonist (−)NPA as long as the radioligands reached the receptors before (−)NPA [77]. It will be interesting to see if these findings can be replicated, and in particular to investigate the influence of the relative timing of tracer and drug administration on the outcome of competition experiments.

Alternatively, if agonist tracers can influence the relative abundance of the high-affinity state by their very presence, preparation of ultra-high-molar-radioactivity radioligands [78] may help minimize this effect. Data on agonist and antagonist tracer binding at “normal” and “ultra-high” molar radioactivities can then be analyzed by a conventional Scatchard plot to compare binding site densities and/or to look for non-linearities in the plot itself if more than two molar radioactivity values (i.e. injected doses) per tracer are used.

The high-affinity state of adrenergic receptors could be detected by studying the time course of agonist ligand binding to intact cells [79]. This paradigm could be expanded into a systematic in vitro study of the relationship between the concentration and intrinsic activity of radioligands and the kinetics of their binding to receptors in membrane homogenates, intact cells or tissues. The degree of a ligand's influence on the receptor-G-protein binding equilibrium is dependent on receptor occupancy, and there is a feedback loop between ligand binding to the receptors and G-protein recruitment to or decoupling from them, so both the intrinsic activity and the ligand concentration will influence the shape of the binding curve (Figure 4). Mathematical simulations and kinetic modeling not unlike that used for in vivo PET data analysis would be of great help there.

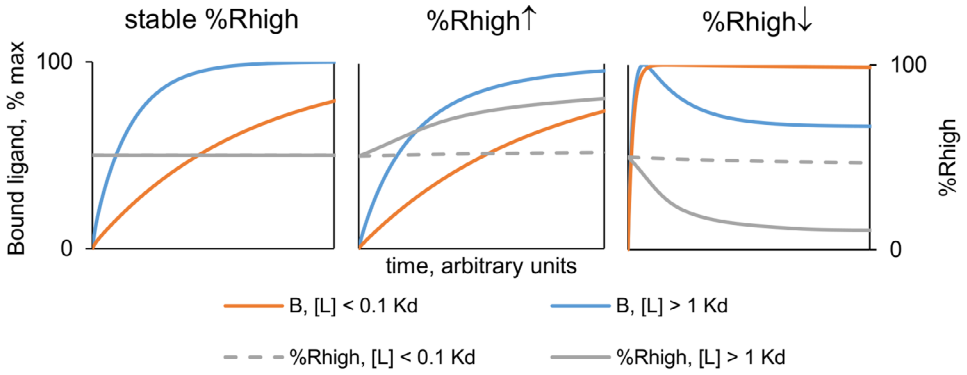

Figure 4. Hypothetical influence of ligand-receptor and receptor-G-protein binding cooperativity on ligand binding time course.

Lines show changes with time of the two parameters: receptor occupancy B by the ligand L and the percentage %Rhigh of receptors configured in the high-affinity state. Changes are shown for high (blue and solid grey lines) and low (orange and dashed grey lines) ligand concentrations [L]. "High" concentration is defined as greater than the ligand's dissociation constant K_d (equilibrium occupancy >50%), while "low" concentration is defined as less than 0.1 K_d (equilibrium occupancy <10%).

Left panel: if %Rhigh is stable throughout the experiment, binding time courses for the ligand at any concentration should be described well by first-order saturation curves.

Middle panel: if ligand binding promotes high-affinity state formation (increase in %Rhigh), it should result in a more complex, multi-order saturation curve shape at high [L], but when [L] and B are low, %Rhigh is stable, so the binding curve should stay first-order.

Right panel: if ligand binding promotes high-affinity state disintegration (fall in %Rhigh), at high [L] the binding curve should have a prominent peak. The same peak can be expected to be much less pronounced at low [L].

Receptor imaging beyond agonist and antagonist tracers

Imaging of GPCRs with agonist tracers was conceived as an approach to assess the availability of functional receptors in the living brain in a simple and non-invasive manner. If the baseline degree of G-protein pre-coupling to receptors is not what determines the ability of receptors to function, how can one assess this ability?

Given that GPCR homo- and hetero-oligomerization is a factor that influences the pharmacological properties of GPCRs, including their affinity towards the ligands (see Chapter 2), development of oligomer-specific tracers for non-invasive in vivo imaging could be a great step forward. A lot of work has been done on the development of ligands targeting homo- and heterodimers of GPCRs (see [80] for review), but few of them were radiolabeled for use as radiopharmaceuticals. Nevertheless, a high-affinity bivalent PET ligand for serotonin 5-HT_{1A} receptor homodimers has recently been successfully evaluated in rats [81].

Another path potentially providing big insights into receptor signaling is imaging of second messenger pathways activated by receptors instead of receptors themselves. A number of tracers is available for the imaging of the activity of phosphodiesterase enzymes and of membrane phospholipid turnover (see reviews [82,83]). However, attempts to directly spot visible alterations in neuropathological states with these tracers have been disappointing [84].

REFERENCES

1. Sromek AW, Si Y-G, Zhang T, George SR, Seeman P, Neumeyer JL. Synthesis and Biological Evaluation of N-Fluoroalkyl and 2-Fluoroalkoxy Substituted Aporphines: Potential PET Ligands for Dopamine D_2 Receptors. ACS Med. Chem. Lett. ACS Publications; 2011;2:189–94.

2. Finnema SJ, Stepanov V, Nakao R, Sromek AW, Zhang T, Neumeyer JL, et al. [^{18}F]-MCL-524, an ^{18}F-Labelled Dopamine D_2 and D_3 Receptor Agonist Sensitive to Dopamine: A Preliminary PET Study. J. Nucl. Med. 2014;55:1164–70.

3. Finnema SJ, Bang-Andersen B, Wikström H V, Halldin C. Current state of agonist radioligands for imaging of brain dopamine D_2/D_3 receptors in vivo with positron emission tomography. Curr. Top. Med. Chem. 2010;10:1477–98.

4. Vasdev N, Seeman P, Garcia A, Stableford WT, Nobrega JN, Houle S, et al. Syntheses and in vitro evaluation of fluorinated naphthoxazines as dopamine D_2/D_3 receptor agonists: radiosynthesis, ex vivo biodistribution and autoradiography of [^{18}F]F-PHNO. Nucl. Med. Biol. 2007;34:195–203.

5. McDermed JD, McKenzie GM, Phillips AP. Synthesis and pharmacology of some 2-aminotetralins. Dopamine receptor agonists. J. Med. Chem. 1975;18:362–7.

6. Seiler MP, Stoll AP, Closse A, Frick W, Jaton A, Vigouret JM. Structure-activity relationships of dopaminergic 5-hydroxy-2-aminotetralin derivatives with functionalized N-alkyl substituents. J. Med. Chem. 1986;29:912–7.

7. Shi B, Narayanan TK, Yang ZY, Christian BT, Mukherjee J. Radiosynthesis and in vitro evaluation of 2-(N-alkyl-N-1'-[^{11}C]-propyl)amino-5-hydroxytetralin analogs as high affinity agonists for dopamine D_2 receptors. Nucl. Med. Biol. 1999;26:725–35.

8. Mukherjee J, Narayanan TK, Christian BT, Shi B, Yang Z-Y. Binding characteristics of high-affinity dopamine D_2/D_3 receptor agonists, [^{11}C]-PPHT and [^{11}C]-ZYY-339 in rodents and imaging in non-human primates by PET. Synapse. 2004;54:83–91.

9. Mukherjee J, Narayanan TK, Christian BT, Shi B, Dunigan KA, Mantil J. In vitro and in vivo evaluation of the binding of the dopamine D_2 receptor agonist [^{11}C]-(R,S)-5-hydroxy-2-(di-n-propylamino)tetralin in rodents and nonhuman primate. Synapse. 2000;37:64–70.

10. Shi B, Narayanan TK, Christian BT, Chattopadhyay S, Mukherjee J. Synthesis and biological evaluation of the binding of dopamine D_2/D_3 receptor agonist,

(R,S)-5-hydroxy-2-(N-propyl-N-(5'-[^{18}F]-fluoropentyl)aminotetralin ([^{18}F]-5-OH-FPPAT) in rodents and nonhuman primates. Nucl. Med. Biol. 2004;31:303–11.

11. Mukherjee J, Majji D, Kaur J, Constantinescu CC, Narayanan TK, Shi B, et al. PET radiotracer development for imaging high-affinity state of dopamine D_2 and D_3 receptors: Binding studies of fluorine-18 labeled aminotetralins in rodents. Synapse. 2016 Nov 19;1–15.

12. Innis RB, Cunningham VJ, Delforge J, Fujita M, Gjedde A, Gunn RN, et al. Consensus nomenclature for in vivo imaging of reversibly binding radioligands. J. Cereb. Blood Flow Metab. 2007;27:1533–9.

13. Waterhouse R. Determination of lipophilicity and its use as a predictor of blood–brain barrier penetration of molecular imaging agents. Mol. Imaging Biol. 2003;5:376–89.

14. Cheng Y, Prusoff WH. Relationship between the inhibition constant (K_I) and the concentration of inhibitor which causes 50 per cent inhibition (I_{50}) of an enzymatic reaction. Biochem. Pharmacol. 1973;22:3099–108.

15. Mewshaw RE, Zhao R, Shi X, Marquis K, Brennan JA, Mazandarani H, et al. New generation dopaminergic agents. Part 8: heterocyclic bioisosteres that exploit the 7-OH-2-(aminomethyl)chroman D_2 template. Bioorg. Med. Chem. Lett. 2002;12:271–4.

16. Mewshaw RE, Kavanagh J, Stack G, Marquis KL, Shi X, Kagan MZ, et al. New generation dopaminergic agents. 1. Discovery of a novel scaffold which embraces the D_2 agonist pharmacophore. Structure-activity relationships of a series of 2-(aminomethyl)chromans. J. Med. Chem. 1997;40:4235–56.

17. Pazos A, Palacios JM. Quantitative autoradiographic mapping of serotonin receptors in the rat brain. I. Serotonin-1 receptors. Brain Res. 1985;346:205–30.

18. Cumming P. Absolute abundances and affinity states of dopamine receptors in mammalian brain: A review. Synapse. 2011;65:892–909.

19. Ross TL. Direct no-carrier-added ^{18}F-labeling of arenes via nucleophilic substitution on aryl(2-thienyl)iodonium salts. University of Cologne; 2005.

20. Lee E, Kamlet AS, Powers DC, Neumann CN, Boursalian GB, Furuya T, et al. A fluoride-derived electrophilic late-stage fluorination reagent for PET imaging. Science. 2011;334:639–42.

21. Ichiishi N, Brooks AF, Topczewski JJ, Rodnick ME, Sanford MS, Scott PJH.

Copper-Catalyzed [^{18}F]Fluorination of (Mesityl)(aryl)iodonium Salts. Org. Lett. 2014;16:3224–7.

22. Tredwell M, Preshlock SM, Taylor NJ, Gruber S, Huiban M, Passchier J, et al. A General Copper-Mediated Nucleophilic ^{18}F Fluorination of Arenes. Angew. Chemie. 2014;126:7885–9.

23. Lee E, Hooker JM, Ritter T. Nickel-Mediated Oxidative Fluorination for PET with Aqueous [^{18}F] Fluoride. J. Am. Chem. Soc. 2012;134:17456–8.

24. Suridjan I, Rusjan P, Addington J, Wilson AA, Houle S, Mizrahi R. Dopamine D_2 and D_3 binding in people at clinical high risk for schizophrenia, antipsychotic-naive patients and healthy controls while performing a cognitive task. J. Psychiatry Neurosci. 2013;38:98–106.

25. Mizrahi R, Suridjan I, Kenk M, George TP, Wilson A, Houle S, et al. Dopamine response to psychosocial stress in chronic cannabis users: a PET study with [^{11}C]-(+)-PHNO. Neuropsychopharmacology. 2013;38:673–82.

26. Graff-Guerrero A, Mizrahi R, Agid O, Marcon H, Barsoum P, Rusjan P, et al. The dopamine D_2 receptors in high-affinity state and D_3 receptors in schizophrenia: a clinical [^{11}C]-(+)-PHNO PET study. Neuropsychopharmacology. 2009;34:1078–86.

27. Narendran R, Martinez D, Mason NS, Lopresti BJ, Himes ML, Chen C-M, et al. Imaging of dopamine $D_{2/3}$ agonist binding in cocaine dependence: A [^{11}C]NPA positron emission tomography study. Synapse. 2011;65:1344–9.

28. Boileau I, Nakajima S, Payer D. Imaging the D_3 dopamine receptor across behavioral and drug addictions: Positron emission tomography studies with [^{11}C]-(+)-PHNO. Eur. Neuropsychopharmacol. Elsevier; 2015;25:1410–20.

29. Richtand NM. Behavioral Sensitization, Alternative Splicing, and D_3 Dopamine Receptor-Mediated Inhibitory Function. Neuropsychopharmacology. 2006;31:2368–75.

30. Salama I, Schlotter K, Utz W, Hübner H, Gmeiner P, Boeckler F. CoMFA and CoMSIA investigations of dopamine D_3 receptor ligands leading to the prediction, synthesis, and evaluation of rigidized FAUC 365 analogues. Bioorg. Med. Chem. 2006;14:5898–912.

31. Salama I, Hocke C, Utz W, Prante O, Boeckler F, Hübner H, et al. Structure-selectivity investigations of D_2-like receptor ligands by CoMFA and

CoMSIA guiding the discovery of D_3 selective PET radioligands. J. Med. Chem. 2007;50:489–500.

32. Newman AH, Beuming T, Banala A, Donthamsetti P, Pongetti K, Labounty A, et al. Molecular Determinants of Selectivity and Efficacy at the Dopamine D_3 Receptor. J. Med. Chem. 2012.

33. Banerjee A, Prante O. Subtype-Selective Dopamine Receptor Radioligands for PET Imaging: Current Status and Recent Developments. Curr. Med. Chem. 2012;19:3957–66.

34. Xu J, Vangveravong S, Li S, Fan J, Jones LA, Cui J, et al. Positron emission tomography imaging of dopamine D_2 receptors using a highly selective radiolabeled D_2 receptor partial agonist. Neuroimage. Elsevier Inc.; 2013;71:168–74.

35. Hocke C, Maschauer S, Hübner H, Löber S, Utz W, Kuwert T, et al. A series of ^{18}F-labeled pyridinylphenyl amides as subtype-selective radioligands for the dopamine D_3 receptor. ChemMedChem. 2010;5:941–8.

36. Hocke C, Cumming P, Maschauer S, Kuwert T, Gmeiner P, Prante O. Biodistribution studies of two ^{18}F-labeled pyridinylphenyl amides as subtype selective radioligands for the dopamine D_3 receptor. Nucl. Med. Biol. Elsevier Inc.; 2014;41:223–8.

37. Mach RH, Tu Z, Xu J, Li S, Jones LA, Taylor M, et al. Endogenous dopamine (DA) competes with the binding of a radiolabeled D_3 receptor partial agonist in vivo: a positron emission tomography study. Synapse. 2011;65:724–32.

38. Bennacef I, Salinas CA, Bonasera TA, Gunn RN, Audrain H, Jakobsen S, et al. Dopamine D_3 receptor antagonists: The quest for a potentially selective PET ligand. Part 3: Radiosynthesis and in vivo studies. Bioorganic Med. Chem. Lett. 2009;19:5056–9.

39. Tu Z, Li S, Xu J, Chu W, Jones L a, Luedtke RR, et al. Effect of cyclosporin A on the uptake of D_3-selective PET radiotracers in rat brain. Nucl. Med. Biol. Elsevier Inc.; 2011;38:725–39.

40. Sóvágó J, Farde L, Halldin C, Langer O, Laszlovszky I, Kiss B, et al. Positron emission tomographic evaluation of the putative dopamine-D_3 receptor ligand, [^{11}C]RGH-1756 in the monkey brain. Neurochem. Int. 2004;45:609–17.

41. Turolla EA, Matarrese M, Belloli S, Moresco RM, Simonelli P, Todde S, et al. ^{11}C-labeling of n-[4-[4-(2,3-dichlorophenyl)piperazin-1-yl]butyl]arylcarboxam-

ide derivatives and evaluation as potential radioligands for PET imaging of dopamine D_3 receptors. J. Med. Chem. 2005;48:7018–23.

42. Sóvágó J, Farde L, Halldin C, Schukin E, Schou M, Laszlovszky I, et al. Lack of effect of reserpine-induced dopamine depletion on the binding of the dopamine-D_3 selective radioligand, [^{11}C]RGH-1756. Brain Res. Bull. 2005;67:219–24.

43. Milak MS, DeLorenzo C, Zanderigo F, Prabhakaran J, Kumar JSD, Majo VJ, et al. In vivo quantification of human serotonin 1A receptor using [^{11}C]-CUMI-101, an agonist PET radiotracer. J. Nucl. Med. 2010;51:1892–900.

44. Hines CS, Liow J-S, Zanotti-Fregonara P, Hirvonen J, Morse C, Pike VW, et al. Human Biodistribution and Dosimetry of [^{11}C]-CUMI-101, an Agonist Radioligand for Serotonin-1A Receptors in Brain. PLoS One. 2011;6:e25309.

45. Ettrup A, da Cunha-Bang S, McMahon B, Lehel S, Dyssegaard A, Skibsted AW, et al. Serotonin 2A receptor agonist binding in the human brain with [^{11}C]Cimbi-36. J. Cereb. Blood Flow Metab. 2014;34:1188–96.

46. Ettrup A, Svarer C, McMahon B, da Cunha-Bang S, Lehel S, Møller K, et al. Serotonin 2A receptor agonist binding in the human brain with [^{11}C]Cimbi-36: Test-retest reproducibility and head-to-head comparison with the antagonist [^{18}F]altanserin. Neuroimage. Elsevier B.V.; 2016;130:167–74.

47. Tomasi G, Zheng M-Q, Weinzimmer D, Lin S, Nabulsi N, Williams W, et al. Kinetic modeling of the kappa agonist tracer [^{11}C]GR103545 in humans. J. Nucl. Med. 2010;51:1293.

48. Naganawa M, Jacobsen LK, Zheng M-Q, Lin S-F, Banerjee A, Byon W, et al. Evaluation of the agonist PET radioligand [^{11}C]GR103545 to image kappa opioid receptor in humans: Kinetic model selection, test–retest reproducibility and receptor occupancy by the antagonist PF-04455242. Neuroimage. 2014;99:69–79.

49. van Wieringen J-P, Booij J, Shalgunov V, Elsinga P, Michel MC. Agonist high- and low-affinity states of dopamine D_2 receptors: methods of detection and clinical implications. Naunyn. Schmiedebergs. Arch. Pharmacol. 2013;386:135–54.

50. Sibley DR, Mahan LC, Creese I. Dopamine receptor binding on intact cells. Absence of a high-affinity agonist-receptor binding state. Mol. Pharmacol. 1983;23:295–302.

51. Skinbjerg M, Namkung Y, Halldin C, Innis RB, Sibley DR. Pharmacological characterization of 2-methoxy-N-propylnorapomorphine's interactions with D_2 and D_3 dopamine receptors. Synapse. 2009;63:462–75.

52. Guo N, Guo W, Kralikova M, Jiang M, Schieren I, Narendran R, et al. Impact of D_2 Receptor Internalization on Binding Affinity of Neuroimaging Radiotracers. Neuropsychopharmacology. Nature Publishing Group; 2009;35:806–17.

53. Skinbjerg M, Sibley DR, Javitch JA, Abi-Dargham A. Imaging the high-affinity state of the dopamine D_2 receptor in vivo: Fact or fiction? Biochem. Pharmacol. Elsevier Inc.; 2012;83:193–8.

54. Finnema SJ, Ettrup A, Stepanov V, Varrone A, Knudsen GM, Halldin C. First evaluation of the 5-HT_{2A} receptor agonist radioligand [^{11}C]Cimbi-36 in primate brain. Brain 2011. 2011. p. 3–4.

55. Kumar JSD, Milak MS, Majo VJ, Prabhakaran J, Mali P, Savenkova L, et al. Comparison of High and Low Affinity Serotonin 1A Receptors by PET In Vivo in Nonhuman Primates. J. Pharmacol. Sci. 2012;0:1–4.

56. Yokoyama C, Mawatari A, Kawasaki A, Takeda C, Onoe K, Doi H, et al. Marmoset Serotonin 5-HT_{1A} Receptor Mapping with a Biased Agonist PET Probe [^{18}F]-F13714: Comparison with an Antagonist Tracer [^{18}F]-MPPF in Awake and Anesthetized States. Int. J. Neuropsychopharmacol. 2016;pyw079.

57. Talbot PS, Narendran R, Butelman ER, Huang Y, Ngo K, Slifstein M, et al. a Radiotracer for Imaging -Opioid Receptors In Vivo with PET : Synthesis and Evaluation in Baboons. 2005;46:484–94.

58. Tauscher JT, Vandenhende F, Witcher J, Ranganathan M, Zheng M-Q, Naganawa M, et al. Assessment of Brain Kappa Opioid Receptor Occupancy after Single Oral Doses of LY2456302 as Measured by PET with the Radioligand LY2879788 in Healthy Subjects. Neuropsychopharmacology. 2012;38:S247.

59. Zheng M-Q, Nabulsi N, Kim SJ, Tomasi G, Lin S-F, Mitch C, et al. Synthesis and evaluation of [^{11}C]-LY2795050 as a κ-opioid receptor antagonist radiotracer for PET imaging. J. Nucl. Med. 2013;54:455–63.

60. De Lean A, Stadel JM, Lefkowitz RJ. A ternary complex model explains the agonist-specific binding properties of the adenylate cyclase-coupled beta-adrenergic receptor. J. Biol. Chem. 1980;255:7108–17.

61. Hein P, Bünemann M. Coupling mode of receptors and G proteins. Naunyn. Schmiedebergs. Arch. Pharmacol. 2009;379:435–43.

62. Jakobsen S, Pedersen K, Smith DF, Jensen SB, Munk OL, Cumming P. Detection of alpha2-adrenergic receptors in brain of living pig with [^{11}C]-yohimbine. J. Nucl. Med. 2006;47:2008–15.

63. Arponen E, Helin S, Marjamäki P, Grönroos T, Holm P, Löyttyniemi E, et al. A PET Tracer for Brain α_{2C} Adrenoceptors, [^{11}C]-ORM-13070: Radiosynthesis and Preclinical Evaluation in Rats and Knockout Mice. J. Nucl. Med. 2014;55:1171–7.

64. Finnema SJ, Scheinin M, Shahid M, Lehto J, Borroni E, Bang-Andersen B, et al. Application of cross-species PET imaging to assess neurotransmitter release in brain. Psychopharmacology (Berl). 2015;232:4129–57.

65. Doze P, Van Waarde A, Elsinga PH, Van-Loenen Weemaes AM, Willemsen AT, Vaalburg W. Validation of S-1'-[^{18}F]fluorocarazolol for in vivo imaging and quantification of cerebral beta-adrenoceptors. Eur. J. Pharmacol. 1998;353:215–26.

66. Doze P, Elsinga PH, de Vries EF, Van Waarde A, Vaalburg W. Mutagenic activity of a fluorinated analog of the beta-adrenoceptor ligand carazolol in the Ames test. Nucl. Med. Biol. 2000;27:315–9.

67. Doze P, van Waarde A, Tewson TJ, Vaalburg W, Elsinga PH. Synthesis and evaluation of (*S*)-[^{18}F]-fluoroethylcarazolol for in vivo beta-adrenoceptor imaging in the brain. Neurochem. Int. 2002;41:17–27.

68. van Waarde A, Vaalburg W, Doze P, Bosker FJ, Elsinga PH. PET imaging of beta-adrenoceptors in human brain: a realistic goal or a mirage? Curr. Pharm. Des. 2004;10:1519–36.

69. Skinbjerg M, Seneca N, Liow J-S, Hong J, Weinshenker D, Pike VW, et al. Dopamine beta-hydroxylase-deficient mice have normal densities of D_2 dopamine receptors in the high-affinity state based on in vivo PET imaging and in vitro radioligand binding. Synapse. 2010;64:699–703.

70. McCormick PN, Kapur S, Reckless G, Wilson AA. Ex vivo [^{11}C]-(+)-PHNO binding is unchanged in animal models displaying increased high-affinity states of the D_2 receptor in vitro. Synapse. 2009;63:998–1009.

71. Peng T, Zysk J, Dorff P, Elmore CS, Ström P, Malmquist J, et al. D_2 receptor occupancy in conscious rat brain is not significantly distinguished with [^{3}H]-MNPA, [^{3}H]-(+)-PHNO, and [^{3}H]-raclopride. Synapse. 2010;64:624–33.

72. Seeman P. Dopamine D_2 High Receptors on Intact Cells. Synapse. 2008;318:314–8.

73. McCormick PN, Kapur S, Seeman P, Wilson AA. Dopamine D_2 receptor radiotracers [^{11}C](+)-PHNO and [^{3}H]raclopride are indistinguishably inhibited by D_2 agonists and antagonists ex vivo. Nucl. Med. Biol. 2008;35:11–7.

74. Slifstein M, Suckow RF, Javitch JA, Cooper T, Lieberman J, Abi-Dargham A. Characterization of in vivo pharmacokinetic properties of the dopamine D_1 receptor agonist DAR-0100A in nonhuman primates using PET with [^{11}C] NNC112 and [^{11}C] raclopride. J. Cereb. Blood Flow Metab. 2011;31:293–304.

75. Shea LD, Neubig RR, Linderman JJ. Timing is everything the role of kinetics in G protein activation. Life Sci. 2000;68:647–58.

76. Finnema SJ, Halldin C, Bang-Andersen B, Gulyás B, Bundgaard C, Wikström H V, et al. Dopamine $D_{2/3}$ receptor occupancy of apomorphine in the nonhuman primate brain - a comparative PET study with [^{11}C]raclopride and [^{11}C]MNPA. Synapse. 2009;63:378–89.

77. Seeman P. Dopamine D_2High receptors measured ex vivo are elevated in amphetamine-sensitized animals. Synapse. 2009;63:186–92.

78. Fujimura Y, Ito H, Takahashi H, Yasuno F, Ikoma Y, Zhang M-R, et al. Measurement of dopamine D_2 receptors in living human brain using [^{11}C]raclopride with ultra-high specific radioactivity. Nucl. Med. Biol. Elsevier Inc.; 2010;37:831–5.

79. Insel PA, Mahan LC, Motulsky HJ, Stoolman LM, Koachman AM. Time-dependent decreases in binding affinity of agonists for beta-adrenergic receptors of intact S49 lymphoma cells. A mechanism of desensitization. J. Biol. Chem. 1983;258:13597–605.

80. Hiller C, Kühhorn J, Gmeiner P. Class A G-protein-coupled receptor (GPCR) dimers and bivalent ligands. J. Med. Chem. 2013;56:6542–59.

81. Hazari PP, Schulz J, Vimont D, Chadha N, Allard M, Szlosek-Pinaud M, et al. A New SiF-Dipropargyl Glycerol Scaffold as a Versatile Prosthetic Group to Design Dimeric Radioligands: Synthesis of the [^{18}F]BMPPSiF Tracer to Image Serotonin Receptors. ChemMedChem. 2014;9:337–49.

82. Cumming P, Vasdev N. Molecular Imaging Studies of Second Messenger Pathways: Looking Deeper than the Membrane. Neuromethods. 2012. p. 137–48.

83. Holland JP, Cumming P, Vasdev N. PET radiopharmaceuticals for probing enzymes in the brain. Am. J. Nucl. Med. Mol. Imaging. 2013;3:194–216.

84. Reis Marques T, Natesan S, Niccolini F, Politis M, Gunn R, Searle G, et al. The role of Phosphodiesterase 10A in Schizophrenia: A Positron Emission Tomography study using [^{11}C]IMA107. J. Nucl. Med. . 2015;56:1622.

Chapter 9

Nederlandse samenvatting

Motivatie en doel van het werk

Dopamine is een belangrijke neurotransmitter, die betrokken is bij de regulatie van talloze functies van de hersenen. Er wordt verondersteld dat ontregelingen van dopaminesignalering in het centrale zenuwstelsel ten grondslag te liggen aan bewegingsstoornissen, cognitieve stoornissen en verslaving. Receptoren, waaraan dopamine in de hersenen bindt, behoren tot de superfamilie van G-proteïnegekoppelde receptoren (GPCR). Dopaminereceptoren van de subtypes D_2 en D_3 ($D_{2/3}$) hebben veel aandacht gekregen in neurologisch onderzoek. Van alle neuroreceptoren, zijn ze ook meest uitgebreid onderzocht door middel van positron emissie tomografie (PET).

Gegevens uit in vitro onderzoek tonen aan dat GPCRs (dus ook $D_{2/3}$ receptoren) bestaan als twee subpopulaties met hoge en lage affiniteit voor de agonisten (verbindingen die in staat zijn om de receptoren te activeren, bijvoorbeeld dopamine). De affiniteit van een gegeven receptor voor de agonist is afhankelijk van het feit of er ook een G-eiwit aan deze receptor is gebonden. Antagonisten (verbindingen die aan de receptoren wel kunnen binden, maar ze niet kunnen activeren) maken geen onderscheid tussen deze twee affiniteitstoestanden. Omdat de hoge affiniteitstoestand een verzameling is van receptoren waaraan G-eiwitten zijn gekoppeld, kan de hoge affiniteitstoestand worden beschouwd als de functionele deelverzameling van de receptoren.

Voor toepassingen zoals receptorbezettingstudies van agonistische geneesmiddelen en meting en beeldvorming van de afgifte neurotransmitters wordt verondersteld dat agonistische tracers geschikter zijn dan antagonistische tracers, want ze binden op een selectieve manier aan de “functionele” deelverzameling van de receptoren.. Het gebruik van agonistische tracers kan ook onze kennis verbeteren van de pathogenese van neuropsychiatrische aandoeningen welke vermoedelijk veroorzaakt worden door de ontregeling van de relatieve abundantie van receptoren in de hoge affiniteitstoestand, en mogelijk de diagnose van deze aandoeningen vergemakkelijken.

Hoofdstuk 2 legt bestaande concepten van de hoge affiniteitstoestand uit en somt op potentiële voordelen van agonistische tracers in vergelijking met antagonistische tracers met betrekking tot de beeldvorming van neuroreceptoren behorende tot de GPCR-familie. Hetzelfde hoofdstuk geeft ook een overzicht van experimentele paradigma’s ontwikkeld om deze voordelen te demonstreren en van experimenteel bewijs verzameld met behulp van deze paradigma’s. Hoewel het te betwijfelen valt of $D_{2/3}$-agonistische tracers

inderdaad een deelverzameling herkennen van alle receptoren herkend door $D_{2/3}$-antagonistische tracers, zijn in één toepassing, namelijk het detecteren van veranderingen in de intrasynaptische concentratie dopamine, $D_{2/3}$-agonistische tracers inderdaad superieur aan $D_{2/3}$-antagonistische tracers.

Het algemene nadeel van alle $D_{2/3}$-agonistische PET tracers die beschikbaar waren voor het gebruik in mensen op het moment dat het werk beschreven in dit proefschrift werd begonnen is dat ze allemaal gelabeld zijn met koolstof-11. Door de korte halfwaardetijd van koolstof-11 (20.4 min) kunnen ^{11}C-gelabelde tracers alleen gebruikt worden op instellingen die hun eigen cyclotron hebben. Tracers gelabeld met fluor-18 zijn veel beter geschikt voor het wijdverbreide gebruik, want de langere halfwaardetijd van fluor-18 (109,8 min) maakt het mogelijk om de radiofarmaca uit één productiehub (in bezit van een cyclotron) naar talrijke "satellietcentra" (zonder cyclotron) te leveren voor beeldvorming.

Het werk beschreven in dit proefschrift had als doel de ontwikkeling en evaluatie van ^{18}F-gelabelde agonistische radiofarmaca welke zouden kunnen worden gebruikt voor de beeldvorming van de functionele subpopulatie (d.w.z. hoge affiniteitstoestand) van $D_{2/3}$ dopaminereceptoren bij de mens.

Het ontwerpen van de kandidaatverbindingen

Op het moment dat dit onderzoeksproject werd gestart, waren de meest populaire scaffolds voor de ontwikkeling van $D_{2/3}$-agonistische PET-tracers naphtoxazine, apomorfine en 2-aminotetraline (zie Figuur 1). Radioliganden afgeleid van naphtoxazine en apomorfine met het ^{18}F-label geïntroduceerd in één van de substituenten op het primaire amino-stikstofatoom bleken ongeschikt te zijn voor in vivo beeldvorming. Met één ^{18}F-gelabelde derivaat van 2-aminotetraline wist men $D_{2/3}$-receptoren in de hersenen van ratten te visualiseren met een matige signaal-ruisverhouding, maar er leek niet veel ruimte beschikbaar te zijn voor verdere optimalisatie, want gelijkaardige verbindingen met wat complexere structuren had nog lagere beeldvormingsprestaties. Daardoor was de beslissing door ons genomen om de nieuwe tracers vanuit een andere scaffold te ontwikkelen in plaats van verdere modificaties van de structuren van bestaande ^{11}C-gelabelde tracers. Een bijkomend voordeel van deze beslissing was dat die de gelegenheid gaf om de ontwikkelde verbindingen te patenteren en op de markt te brengen in het geval dat ze succesvol zouden bleken als agenten voor PET-beeldvorming.

Aminomethylchromanen (AMC), een klasse van $D_{2/3}$-agonisten met hoge affiniteit, die vroeger niet geëvalueerd waren als radioliganden, werden gekozen als het startpunt voor de ontwikkeling van nieuwe ^{18}F-gelabelde tracers.

Hoofdstuk 3 beschrijft het ontwerpen van kandidaatverbindingen op basis van de AMC scaffold. Een PET-tracer voor de beeldvorming van de hersenen moet lipofiel genoeg zijn om de bloed-hersenbarrière door passieve diffusie te kunnen doordringen, maar moet ook niet te lipofiel zijn zodat de specifieke binding in het hersenweefsel onderscheiden kan worden van de niet-specifieke binding. Natuurlijk moet de tracer voldoende affiniteit voor de doelreceptoren hebben om meetbare specifieke binding te laten zien. Nog één eis is dat de tracer het metabolisme goed genoeg moet weerstaan om naar het hersenweefsel vanuit het bloed te kunnen diffunderen voordat die gemetaboliseerd wordt. Wanneer de metabolisering uiteindelijk toch zou gebeuren, moet het radioactieve label van het tracermolecuul gaan in fragmenten die hydrofiel zijn en de bloed-hersenbarrière niet kunnen doordringen.

De structuur van de $D_{2/3}$-agonistische farmacofoor, waaraan AMCs ook voldoen, bestaat uit een aromatische kern, waterstofbrugvormende hydroxylgroepen daaraan gekoppeld, en een positief geladen stikstofatoom (Figuur 1). Een eigenschap van de AMC-scaffold die handig is bij de ontwikkeling van radioliganden is dat de substituent op het primaire amino-stikstofatoom is gericht naar een betrekkelijk ruim onderdeel van de bindingsholte van de dopaminereceptor. Daarom kan de structuur van de N-substituent met veel vrijheid worden gemodificeerd om de noodzakelijke lipofiliciteit te bereiken en de radioactieve label te introduceren zonder veel effect op de $D_{2/3}$-affiniteit of agonisme.

In dit werk waren AMCs ontwikkeld met alkyl-, benzyl- en arylpiperazino-substituenten (Figuur 2). Structuren van kandidaatverbindingen waren ontworpen om voorspelde lipofiliteitswaarden ($LogP_{7.4}$ = LogD) tussen 1 en 3 te hebben, wat het voorkeursbereik is bij de radiofarmaca voor hersenbeeldvorming. Bij meeste kandidaat-verbindingen werd het fluor-label geïntroduceerd in fluoroalkoxy groepen, terwijl de lengten van de alkylketens werden aangepast om de juiste LogD waarden te verkrijgen. De AMC-kern bleef echter de belangrijkste hydrofobe kern in alle kandidaat-verbindingen. Het radioactieve fluoratoom werd bewust geïntroduceerd op afstand van de AMC-kern, in groepen die relatief gemakkelijk gesplitst konden wor-

den van het molecuul door de werking van metabolische enzymen. Dit werd gedaan om te verzekeren dat radioactieve metabolieten gevormd uit kandidaat-tracers niet lipofiel zouden zijn en de $D_{2/3}$-farmacofoor niet zouden bevatten, want lipofiele radiometabolieten, met name die met $D_{2/3}$ affiniteit, kunnen interfereren met de kwantificering van de specifieke opname van kandidaat-tracers in de hersenen.

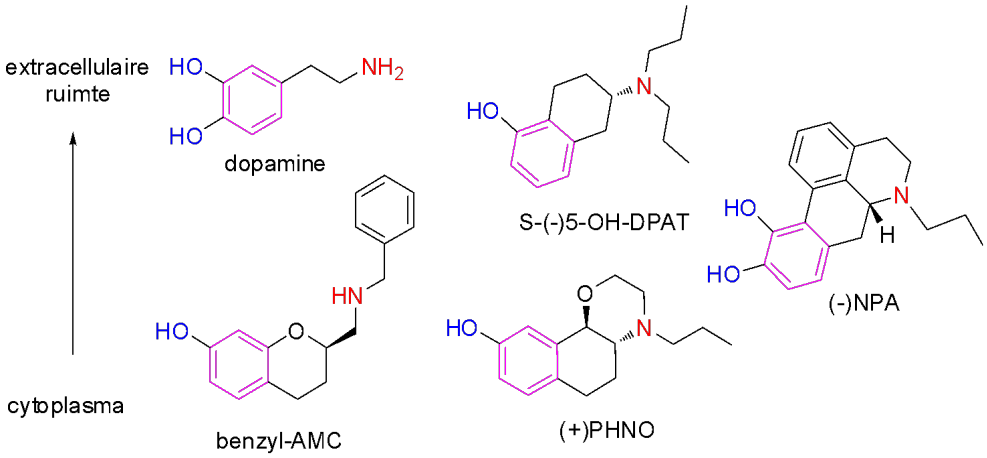

Figuur 1. Vergelijking van de moleculaire structuren van dopamine en dopaminerge liganden afgeleid van de structuren van aminomethylchromaan (links beneden), aminotetraline (midden boven) naphtoxazine (midden beneden) en apomorfine (rechts).

Aromatische kernen, basische stikstofatomen en waterstofbugdonerende hydroxylgroepen zijn in kleur weergegeven. Liganden zijn georiënteerd in een ruwe representatie van de vermoedelijke receptorgebonden conformaties. De “opwaarts gerichte” benzyl substituent van benzyl-AMC en de propyl substituent van S-(–)5-OH-DPAT hebben toegang tot het ruime onderdeel van de bindingsholte van de D2-receptor, terwijl de “neerwaarts gerichte” propyl substituenten van S-(–)5-OH-DPAT, (+)PHNO en (–)NPA wijzen in de richting van een en gedeelte van de bindingsholte waar er slechts genoeg ruimte is voor groepen niet groter dan propyl. Aangepast van Hoofdstuk 3.

Synthese en farmacologische karakterisering van kandidaat-verbindingen

Hoofdstukken 3 en **4** beschrijven de bereiding van kandidaat-verbindingen afgeleid van de AMC scaffold en hun evaluatie in vitro. Chiraliteit van de AMCs speelt een beslissende rol in hun affiniteit voor D_2 en D_3-recep-

toren, en (*R*)-enantiomeren zijn de eutomeren. De enantiomerisch zuivere (*R*)-7-hydroxy-2-ethoxycarbonylchromaan bouwsteen werd bereid uit het racemische vorm van dezelfde stof door het kinetische resolutiemethode met gebruik van lipase-enzyme. Deze bouwsteen werd verder gemodificeerd om uiteindelijk alkyl-, benzyl- en arylpiperazinyl-gesubstitueerde AMCs te verkrijgen, met en zonder fluoratomen in hun structuur.

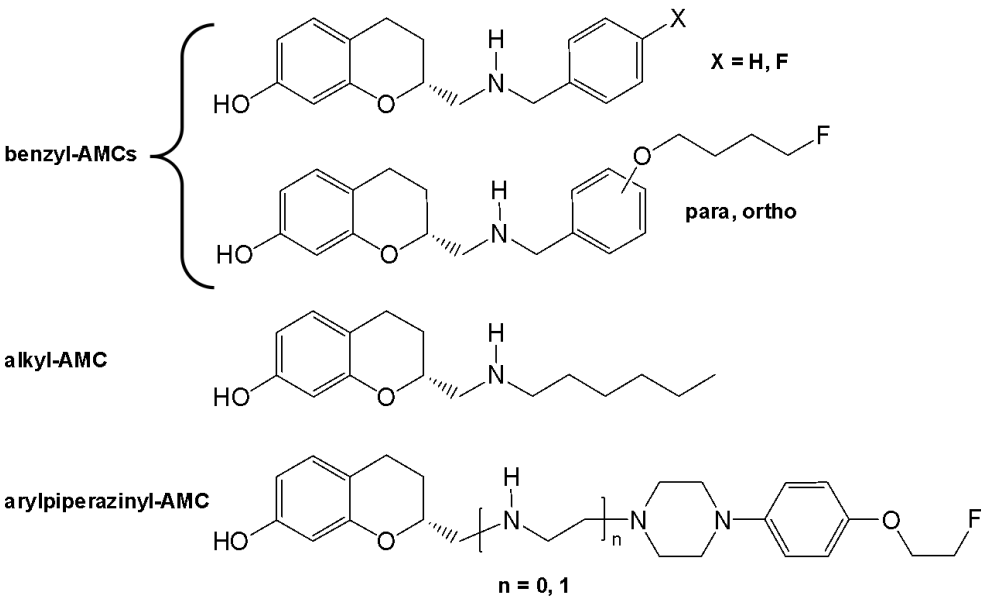

Figuur 2. Structuren van gefluorideerde kandidaat-AMCs en referentieverbindingen bereid in dit werk.

De farmacologische eigenschappen van de gesynthetiseerde verbindingen werden geëvalueerd in competitie-assays met radioliganden in membraanhomogenaten van humane embryonale nierencellen (HEK) en Chinese hamster-eierstokcellen (CHO) cellen, die verschillende subtypen van humane dopaminereceptoren tot expressie brachten. Ook werden met gesynthetiseerde verbindingen functionele testen uitgevoerd zoals remming van adenylaatcyclase en rekrutering van β-arrestine. Twee benzyl- en één arylpiperazinyl-gesubstitueerde AMCs, genoemd, in respective volgorde, AMC20, FBu-AMC13 en FEt-AMC15, werden beschouwd als goede kandidaten voor de radiolabeling (in Hoofdstuk 3 zijn de laatste twee verbindingen aangeduid als **12a** en respectievelijk **12d**). In membraanhomogenaten

maakten deze verbindingen goed onderscheid tussen hoge en lage affiniteitstoestanden van D_2-receptoren (D_2high en D_2low), zodat de affiniteit voor de hoge affiniteittoestand 10 tot 1000 maal groter was dan voor de lage affiniteitstoestand. Affiniteiten van de verbindingen voor D_2high lagen in het subnanomolaire of nanomolaire bereik: van 85 pM voor AMC20 tot 6.7 nM voor FEt-AMC15. Bovendien bonden ze met hoge affiniteit aan D_3-receptoren (gemeten affiniteitswaarden van 0.6 nM voor AMC20 tot 12.1 nM voor FBu-AMC13), lieten geen significante binding aan D_1 receptoren zien en toonden bijna volledig agonisme in functionele testen op D_2 receptoren.

Synthese van radioactief gelabelde kandidaat-tracers en beoordeling van hun lipofiliteit

De radiolabeling van AMC20 wordt beschreven in **Hoofdstuk 4**, terwijl de radiolabeling van FBu-AMC13 en FEt-AMC15 wordt beschreven in **Hoofdstukken 3** en **5**. Voor die laatste twee verbindingen, een aantal homologen met variërende fluoralkylketenlengtes werd bereid om na te gaan welke ketenlengte een ligand met de hoogste signaal-ruisverhouding in het werkelijke hersenweefsel zou opleveren.

In de structuur van AMC20 is het radioactieve fluoratoom direct aan de benzylgroep gehecht. Omdat de benzylgroep een elektronrijke arylgroep is die niet rechtstreeks door nucleofiele fluoridering gelabeld kan worden, werd deze verbinding bereid uitgaande van 4-[^{18}F]fluorbenzaldehyde, welke vervolgens tot een [^{18}F]fluorbenzyl groep werd omgezet via een reductieve amineringsreactie met AMC-amine. Bij FBu-AMC13 en FEt-AMC15 maakt het fluoratoom deel uit van een fluoroalkoxy groep. Deze verbindingen werden bereid door fluoroalkylering van fenol-precursoren (Figuur 3).

Bij het ontwerpen van de radiolabelingsproceduren voor het verkrijgen van de eerste [^{18}F]AMCs wilden we bovenal gemak en flexibiliteit te bereiken. Radiosyntheses duurden 2–2.5 uur. [^{18}F]fluoralkyl-AMC's werden verkregen in radiochemische opbrengsten van 3–15% (gecorrigeerd voor radioactief verval), terwijl de gemiddelde radiochemische opbrengst van [^{18}F]AMC20 24% was. Molaire radioactiviteit van [^{18}F]AMCs was in de range van 10 tot 100 GBq/μmol, wat hoog genoeg is om in vivo PET-beeldvorming uit te voeren met gebruikelijke geïnjecteerde doseringen. In de latere stadia van dit werk werd de bereiding van [^{18}F]fluoralkyltosylaten en 4-[^{18}F]fluorbenzaldehyde geautomatiseerd (**Hoofdstuk 6**), wat de de productie van tracers voor in vitro en in vivo onderzoek verder vereenvoudigde.

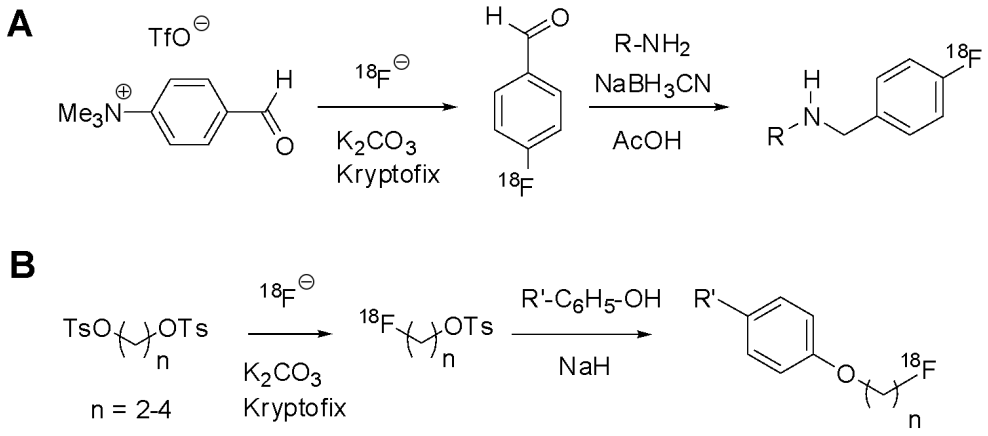

Figuur 3. Radiosynthetische schema's gebruikt voor de bereiding van [^{18}F]AMC's.

A – reductieve aminering van 4-[^{18}F]fluorbenzaldehyde met de amineprecursor van AMC20; B – ^{18}F-fluoroalkylering van fenolprecursoren om de homologen van AMC13 en AMC15 te verkrijgen. Eenvoudigheidshalve worden de aminomethylchromaangroepen en de uiteindelijke ontscherming van de 7-OH-groep niet getoond.

De experimenteel bepaalde LogD-waarde van [^{18}F]AMC20 was 2.33. Voor de homologen van AMC13 varieerden de LogD-waarden van 1.67 ([^{18}F]FEt-AMC13) tot 2.50 ([^{18}F]FBu-AMC13). Voor AMC15 homologen, lagen de LogD-waarden in het traject van 1.48 ([^{18}F]FEt-AMC15) tot 2.71 ([^{18}F]FBu-AMC15). Alle LogD-waarden vallen binnen het bereik dat als optimaal wordt beschouwd voor passieve diffusie vanuit het bloedplasma naar het hersenweefsel.

In vitro en in vivo evaluatie van radioactief gelabelde kandidaat-tracers

Resultaten van de in vitro en in vivo evaluatie van radioactief gelabelde kandidaat-tracers zijn beschreven in **Hoofdstukken 4** en **5**. Alle radioactief gelabelde verbindingen werden geëvalueerd door middel van in vitro autoradiografie in plakjes rattehersenen om de signaal-ruisverhouding van hun binding aan $D_{2/3}$ receptoren in het hersenweefsel te beoordelen. Specifieke bindingverhoudingswaarden (specific binding ratios, SBRs) werden berekend op basis van concentraties radioactiviteit gemeten in de gebieden van het striatum (rijk aan $D_{2/3}$-receptoren) en het cerebellum (kleine

hersenen, arm aan $D_{2/3}$-receptoren). Voor [^{18}F]AMC20, een fluorobenzyl-gesubstitueerd AMC met de hoogste gemeten affiniteit voor D_2high (85 pM), bereikte de striatale SBR de waarde van 6.27 bij de ligandsconcentratie van 1.7 nM (**Hoofdstuk 4**). Onder AMC's met een [^{18}F]fluoroalkoxygroep waren de hoogste SBR-waarden getoond door de fluoroethoxybenzyl-gesubstitueerde [^{18}F]FEt-AMC13 en de (fluorethoxy)-phenylpiperazinyl-gesubstitueerde [^{18}F]FEt-AMC15: SBR 3.40 bij 0.9 nM en respectievelijk SBR 1.64 bij 5.8 nM (**Hoofdstuk 5**). Co-incubatie met de $D_{2/3}$-antagonist raclopride of met guanosinetrifosfaat (GTP), die de ontkoppeling van G-eiwitten van de receptoren stimuleert, heeft voor alle radioliganden in een 60–80% daling van SBR-waarden geresulteerd, hetgeen een bewijs is dat de opname van de AMCs in het striatum door hun specifieke binding aan de hoge affiniteitstoestand van $D_{2/3}$ receptoren is veroorzaakt.

[^{18}F]AMC20, [^{18}F]FBu-AMC13, [^{18}F]FEt-AMC13 en [^{18}F]FEt-AMC15 waren verder geëvalueerd in Sprague-Dawley ratten. [^{18}F]FEt-AMC15 liet zeer lage opname in de hersenen van levende ratten zien, hetgeen mogelijk veroorzaakt was door de relatief hoge hydrofiliciteit van deze tracer (het molecuul heeft ook twee basische stikstofatomen), door een interactie van de tracer met pompeiwitten zoals P-glycoproteïne (P-gp) of misschien door beide redenen. [^{18}F]AMC20, [^{18}F]FBu-AMC13 en [^{18}F]FEt-AMC13 drongen daarentegen in ruim voldoende mate de hersenen binnen: piekopname in de hersenen was 1,7%, 0,9% en 0,7% geïnjecteerde dosis, respectievelijk voor de drie genoemde tracers. De opname van [^{18}F]FBu-AMC13 was het hoogste in de hersenstam, maar [^{18}F]FEt-AMC13 en [^{18}F]AMC20 werden voornamelijk opgenomen in het striatum, resulterend in striatum-tot-cerebellum verhoudingen van ongeveer 2 voor beide tracers. Alle radioactieve metabolieten van [^{18}F]FEt-AMC13 en [^{18}F]AMC20 waren aanzienlijk minder lipofiel dan hun moederstoffen en drongen de bloed-hersenbarrière niet door. Tot slot, voorbehandeling van ratten met 1 mg/kg raclopride resulteerde in 20–40% daling (afhankelijk van de meetmethode) in $D_{2/3}$-specifieke striatale opname van beide tracers, wat te detecteren was met PET-beeldvorming, ex vivo biodistributie en ex vivo autoradiografie (**Hoofdstukken 4** en **5**).

Hoewel de verkregen in vivo en ex vivo gegevens voor [^{18}F]FEt-AMC13 en [^{18}F]AMC20 in overeenstemming zijn met specifieke binding van deze twee tracers aan $D_{2/3}$-receptoren in de striata van ratten, hadden deze radioliganden twee algemene nadelen. Het eerste was dat het verschil tussen de striatale en cerebellaire opname, meestal gebruikt als een surrogaatmeting voor $D_{2/3}$-specifieke binding, met niet meer dan 40% verlaagd werd door voorbe-

handeling met raclopride. Dit is minder dan de helft van de dalingswaarden gemeld in de literatuur voor de bestaande ^{11}C-gelabelde agonisten na voorbehandeling met dezelfde (1 mg/kg) of lagere doseringen raclopride (ten minste 80% daling). Dit kan het gevolg zijn geweest van onvoldoende dosering raclopride of van onvolkomen farmacologische selectiviteit van onze tracers. Op basis van de beschikbare gegevens is het niet mogelijk om tussen die twee mogelijke oorzaken te onderscheiden.

Een ander belangrijker nadeel is dat de signaal-ruisverhoudingswaarden van [^{18}F]FEt-AMC13 en [^{18}F]AMC20 in controleratten lager waren dan de waarden gemeld voor bestaande ^{11}C-gelabelde $D_{2/3}$ agonistische tracers. Onze tracers toonden striatale BP_{ND}-waarden van circa 0.5, vergeleken met 0.9 gemeld voor [^{11}C]MNPA; striatum-tot-cerebellum verhoudingswaarden van onze tracers waren ongeveer 2, terwijl voor [^{11}C](−)NPA en [^{11}C](+)PHNO zijn verhoudingswaarden van 3 of meer gemeld. Daarom, zelfs als voor [^{18}F]FEt-AMC13 en [^{18}F]AMC20 een hoge selectiviteit voor $D_{2/3}$-receptoren kon worden bewezen en >90% afname van de striatale BP_{ND}-waarden kon worden bereikt door verhoging van de geïnjecteerde dosis raclopride, zouden deze twee tracers toch minder geschikt zijn voor het beeldvormen van striatale $D_{2/3}$-receptoren in vivo dan [^{11}C]MNPA, [^{11}C](−)NPA en [^{11}C](+)PHNO.

Conclusie

Wij hebben een reeks gefluorideerde derivaten van aminomethylchromaan ontworpen en bereid en deze derivaten geëvalueerd als potentiële agonistische radioliganden voor de beeldvorming van dopamine $D_{2/3}$-receptoren door middel van positronemissietomografie.

De twee beste verbindingen uit de door ons onderzochte reeks, [^{18}F]AMC20 en [^{18}F]FEt-AMC13, konden onderscheid maken tussen hoge en lage affiniteitstoestanden van $D_{2/3}$-receptoren, vormden geen lipofiele metabolieten in vivo, drongen goed tot de hersenen door, werden voornamelijk opgenomen in het striatum van levende ratten en waren gevoelig voor $D_{2/3}$-blokkade veroorzaakt door injectie van raclopride. Alhoewel de signaal-ruisverhoudingen van [^{18}F]AMC20 en [^{18}F]FEt-AMC13 lager zijn dan die van bestaande ^{11}C-gelabelde $D_{2/3}$-agonistische tracers, bewijzen onze resultaten dat aminomethylchromanen een geschikte scaffold zijn voor de ontwikkeling van $D_{2/3}$-agonistische radioliganden.

Chapter 10

Acknowledgements

In the last chapter of my thesis, I would like to express my gratitude to people who made it possible for me to achieve this milestone in my life.

First of all, I ought to thank my primary supervisor, **Philip Elsinga**, for inviting me to Groningen and introducing me to the world of radiochemistry, PET imaging and drug development. I learned a lot from my discussions with him and grew to appreciate his hands-off approach to supervision.

I would also like to thank **Rudi Dierckx**, head of the department of the Nuclear Medicine and Molecular Imaging (NGMB) of the University Medical Center Groningen (UMCG), for giving me the opportunity to do research at his department.

Thanks to **GE Healthcare** and **Dutch Foundation for Technical Sciences (STW)** for co-funding the research project I was involved in. Also thanks to **Alexander Popkov**, who in 2008 told me about a PhD student position available in Groningen. If it were not for him, this thesis would not happen.

It is necessary to acknowledge those with whom I collaborated in my PhD research project.

Thanks to **Henk Janssen**, **Michel Fransen** and others from the Technical University of Eindhoven for shouldering the burden of preparing enantiomerically pure reference compounds and labeling precursors for my research. Their work was crucial for all subsequent progress.

Thanks to **Martin Michel** from the Academic Medical Center of the University of Amsterdam, and his PhD student **Jan-Peter van Wieringen**, for designing and performing sophisticated in vitro tests on the compounds synthesized in Eindhoven to make sure they satisfy our requirements. On top of that, special thanks to them for teaching me the basics of in vitro pharmacology and introducing me to reference management software, which very much simplified my further work with literature.

Thanks to my second supervisor, **Jan Booij** from the University of Amsterdam, for his critical comments on my manuscripts and for connecting my research to the problems of clinical PET imaging.

Thanks to the staff of the NGMB department for providing me with a work environment: **Chantal Kwizera**, **Gert Luurtsema**, **Hilde Dekens**, **Janet Hessels-Scheper**, **Marianne Schepers**, **Michel de Vries**, **Rolf Zijlma** and others. It is worthwhile to single out **Bram Maas** for his maintenance of the radiochemistry lab, **Hans Pol** for taking care of the gamma-counter

and **Jurgen Sijbesma** for making sure that the PET camera worked, and the workplace for animal handling was ready. Also thanks to the administrative staff, **Annie van Zanten**, **Annegriet Wijker** and **Sarita Evers** for arranging lab supplies and navigating the bureaucracy for me.

Of the research staff at the NGMB department, I am especially grateful to **Erik de Vries** for helping me get familiar with radiochemistry, to **Aren van Waarde** for helpful input on the parts of my work concerning in vivo pharmacology, and to **Antoon Willemsen** for discussions regarding PET data interpretation.

I ought to thank my fellow PhD students and postdocs – people with whom I worked in the lab side by side, and who helped me carry out my in vivo experiments, even when I sounded outright needy. Thanks to **Alexandre Shoji** for his extremely quick and efficient cannulation of rats and **Andrea Parente** for his precise timing of blood sample withdrawals (later I managed to I create a computer-aided system to match his precision). Thanks to **Anna de Bruyn** for teaching me cell culturing. Thanks to **Chao Wu** for solving ligand binding equations for me, even though it was the software on his computer that did the bulk of the work. Thanks to **David Vallez-Garcia** for telling me about the Mendeley software package, which I still use to generate reference lists in my work. Thanks to **Anniek Visser** for valuable discussions and to **Ate Boerema** for helpful conversations during the last months of my PhD contract about what to do next. Thanks to the people whose contribution to my work and self-development cannot be clearly and briefly formulated at the moment of writing, but who nevertheless helped: **Heli Savolainen**, **Inês Farinha-Antunes**, **Janine Doorduin**, **Leila Mirfeizi**, **Marcel Benadiba**, **Mehrsima Abdoli**, **Nisha Ramakrishnan**, **Shivashankar Khanapur**, **Siddesh Hartimath**, **Vinneet Kumar**, **Willem-Jan Kuik**, **Xiaoyun Zhou** and whomever I forgot to mention. Special thanks to **Mohamed Abdul Khayum** for his ever-present helpfulness and inexhaustible optimism.

Apart from the NGMB department, I need to thank the Research School of Behavioral and Cognitive Neurosciences (BCN). Thanks to **Erik Boddeke**, **Michiel Hooiveld**, **Diana Koopmans**, **Janine Wieringa** and other people working here. The BCN educational program allowed me to learn a lot about neuroscience (special thanks to **Ruud Kortekaas** for his Human Neuroanatomy course), and their travel grants let me attend conferences to present the results of my research and network with other scientists.

Thanks to **Amarins Heeringa**, **David Vallez-Garcia**, **Emi Saliasi**, **Jonathan Mall** and **Stefan Wierda**, the members of the BCN PhD council, for their efforts in making me get out of my shell and do something useful.

Also thanks to **Jan Keijser** from the Neurobiology Research Unit of the University of Groningen for providing advice on arranging in vitro autoradiography experiments. Thanks to **Frank Dekker** from the Groningen Research Institute of Pharmacy for advising me in my studies of the binding mode of dopamine receptor ligands. Thanks to **Annemieke Smit-van Oosten**, **Alex Kluppel**, **Michel Weij**, **Wiebe Hofstra** and other personnel of the Central Animal Facility of the UMCG for taking care of my experimental animals and teaching me animal handling and minor surgery. Thanks to **Hetty Timmer-Bosscha** from the department of Medical Oncology for letting me grow cells in her lab.

I would very much like to thank the staff of BIND RUS LLC, where I had a wonderful research job for two years after returning home from the Netherlands. Arguably, it slowed down my thesis writing, but this extra time gave me the opportunity to take a different perspective on my work, not to mention all the valuable experience I got during that time. Moreover, the severance package I got from the company allowed me to finish my thesis in comfort. **Elmira Safarova**, **Daria Zaytseva-Zotova**, **Arkady Zinchenko**, **Tatiana Levada**, **Tatiana Sitnova**, **Dmitry Andreyev**, **Yuri Shilov**, **Natalia Samsonenko**, **Natalia Morozova**, **Yulia Mironova** and **Dzhangar Dzhumashev** from Moscow, and also **Kevin McDonnell**, **Greg Troiano**, **Steve Zale**, **Mir Ali** and **Scott Lentini** from Cambridge, Massachusetts, I had great time with you all.

I guess it is worthwhile to acknowledge the influence on this thesis of **Sjoerd Finnema**, **Patrick McCormick**, **Mikael Palner** and **Mette Skinbjerg**. Although I have never met or talked to three of the four mentioned people, in my work I drew heavily on the materials of their research and used their PhD theses as examples when writing mine.

Finally, thanks to my parents for supporting me in the beginning and right after the end of my stint in Groningen, to my friends who did not abandon me while I was working (or procrastinating working) on my thesis, and to my wife who even agreed to marry me during the time.

Experiences and interactions I had in Groningen have shaped me as a scientist. When I look back on my years there, I feel that I could (and should)

have done much more if I knew right from the start what I wanted and how to achieve it. However, understanding what you want and learning what to do to get it is by itself a valuable acquisition. I hope I will be able to use the acquired knowledge to maximum efficiency in my future endeavors.